Hydrodynamics below a closed fallpipe system

The profile of a rock berm acquired with rock placement operations

M.D.J. Kevelam

Delft University of Technology

Hydrodynamics below a fallpipe

The profile of a rock berm acquired with rock placement operations

MASTER OF SCIENCE THESIS

For obtaining the degree of Master of Science in Civil Engineering at Delft University of Technology

M.D.J. Kevelam, BSc

Faculty of Civil Engineering and Geosciences • Delft University of Technology

Photo cover image:

The fallpipe vessel the Flintstone.
Internal image Tideway Offshore Solutions ©.

DELFT UNIVERSITY OF TECHNOLOGY
DEPARTMENT OF
Civil Engineering and Geosciences
SECTION OF
Dredging Engineering

In cooperation with

TIDEWAY OFFSHORE SOLUTIONS

Dated: September 5th, 2016

Thesis committee

Prof. dr. ir. C. van Rhee	Delft University of Technology Hydraulic Engineering, Section of Dredging Engineering
Dr. ir. G.H. Keetels	Delft University of Technology Offshore Engineering, Section of Dredging Engineering
Dr. ir. D.L. Schott	Delft University of Technology Maritime & Transport Technology, Section Transport Engineering and Logistics
Ir. M. Hovestad	Tideway Offshore Solutions Engineering Department
Ir. C. Visser	Tideway Offshore Solutions Engineering Department

Abstract

In the offshore industry rock is used for different kind of applications, such as scour protection, pipeline protection and upheaval buckling prevention. In deep water operations, but also increasingly in shallow water operations, use is made of the method by guiding the rock from the water surface to the seabed with a fallpipe.

During a rock placement operation the water level inside the closed fallpipe system will drop. In order to prevent the water level falling too far, water is let into the fallpipe. As a result, a current through the fallpipe and subsequently a jet below the fallpipe is created. However, it is not well understood when stones leave the fallpipe how they interact with the surrounding water, what happens when the mixture hits the seabed, the strength of the currents along the seabed and where the stones eventually will settle. Therefore the goal of this study is to get a better understanding of the hydrodynamic processes below a closed fallpipe system.

"To assess the relevant processes of settling stones towards the seabed and to predict the occurrence of irregular berm shapes due to jet formation below a fallpipe."

First the literature was explored to get a better understanding of the processes involved in rock placement operations and to determine the governing parameters thereon. After this, the research phase was started and consists of a threefold. First of all the possibility to use empirical relations, in comparison with computational fluid dynamics (CFD) simulations, for the description of the velocity field below a fallpipe system is looked at. With this velocity field the spreading and displacement of rock is determined, taking into account different parameters, such as the grading and stone size. The last step is to combine this spreading with the transport of stones by the impinging jet to predict the berm built-up.

It was found that the velocity field described with empirical relations are comparable with the velocity field simulated with CFD. However, it was concluded that without a proper turbulent kinetic energy field it is impossible to get matching relations between the empirical approach and the CFD approach. Although an effort was made by adding turbulence to the empirical approach no realistic, or comparable to the CFD approach, results were found. It is therefore concluded that a proper turbulent kinetic energy field is needed for predicting the trajectory behaviour of stones in a turbulent impinging jet.

The research also shows that the spreading of rock below the fallpipe is bounded quite close to the centre of the jet, however being significantly dependent on various parameters. However, further research is required to validate the used stone transport relations for this application. Also, future research is required to overall validate the berm profile modelled within this study. Nevertheless a better insight in the hydrodynamic processes below the closed fallpipe system is given in this report.

Preface

This thesis is submitted in partial fulfilment of the requirements for the degree of MSc. in Civil Engineering at Delft University of Technology. The research was carried out in cooperation with the Engineering department of Tideway Offshore Solutions. The study began with the desire of Tideway Offshore Solutions to get a better understanding of the hydrodynamics below a closed fallpipe system. This report shows the possibility to determine the shape of a rock berm obtained with a deep water rock placement operation.

Acknowledgement
First of all I would like to thank my graduation committee for their guidance and support during this research. Without their input, experience and knowledge I would not have been able to deliver this report. I would like to thank Prof. dr. ir. Cees van Rhee for helping me during the search for a graduation subject, and after this for his numerous input on how to approach and tackle problems such as the influence of turbulence on the trajectory of stones; Dr. ir. Geert Keetels for his feedback during this research, especially on the software package OpenFOAM. As well a special thanks to ir. Frans van Grunsven for also helping me out with OpenFOAM.

Furthermore, I would like to acknowledge Tideway Offshore Solutions for providing me the opportunity to perform this research. A special thanks to Ir. Martijn Hovestad and Ir. Connie Visser for their inspiration and constructive feedback that was needed to realize this thesis.

Additionally, I am very grateful of my girlfriend for bearing me during the time of my graduation. Every time I encountered a problem she supported me and listened to my endless talks on the subject of this thesis. Finally, I would like to thank my fellow graduate students at Tideway Offshore Solutions for the nice lunch break walks.

Marten Kevelam
Delft, September 5, 2016

Main Report

Master Thesis

Part I

Delft University of Technology | Tideway Offshore Solutions

Contents

Abstract V

Preface VII

Contents XI

1 Introduction 1

1.1 General Introduction 1

1.2 Tideway Offshore Solutions 2

1.3 Problem Description 2

1.4 Thesis Objective 3

1.5 Problem Analysis 4

1.6 Thesis Approach 5

1.7 Main Report Outline 6

2 Description of Rock Placement Processes 9

2.1 Rock Placement Operations 9

2.2 Circular Turbulent Jets 10

2.2.1 Large stand-off distance 11

2.2.2 Small stand-off distance 13

2.3 Threshold of Motion 14

2.4 Rock Properties 15

2.5 Dumping of a Single Stone 16

2.6 Dumping of Multiple Stones 17

2.7 Dumping of Stones through a Fallpipe 18

3 Methodology of the Numerical Modelling 21

3.1 Numerical Modelling 21

3.2 Computational Fluid Dynamics 21

3.2.1 The $k-\varepsilon$ model 22

3.2.2 The $k-\omega SST$ model 23

3.2.3 The *driftFlux* model 25

3.3 Set-up of the Numerical Models 26

4 Prediction of the Jet Profile below a Fallpipe ... 27
4.1 Empirical Approach ... 28
4.2 Computational Fluid Dynamics Approach ... 29
4.2.1 Input velocity ... 29
4.2.2 Boundary roughness ... 31
4.3 Comparison ... 32
4.3.1 Small stand-off distance ... 34
4.3.2 Large stand-off distance ... 35
4.4 Concluding Remarks ... 36
5 Prediction of Settling Stone Path ... 37
5.1 Calculation Method of the Stone Trajectory Model ... 39
5.1.1 Discretization of the differential equations ... 40
5.1.2 Influence of the turbulence ... 40
5.2 Empirical Approach ... 44
5.3 Computational Fluid Dynamics Approach ... 46
5.4 Comparison ... 47
5.4.1 Influence of the stand-off distance ... 48
5.4.2 Influence of the grading ... 49
5.4.3 Influence of the stone diameter ... 50
5.4.4 Influence of the hindered settling ... 51
5.4.5 Influence of the outflow velocity ... 51
5.4.6 Influence of the release location ... 52
5.5 Concluding Remarks ... 53
6 Assessment of Berm Formation Processes ... 55
6.1 Height Increase ... 55
6.2 Stone Transport ... 58
6.3 Berm Built-up ... 63
6.4 Concluding remarks ... 65
7 Conclusions and Recommendations ... 67
7.1 Conclusions ... 67
7.1.1 Velocity field ... 67

7.1.2 Rock spreading 68
7.1.3 Berm built-up 68
7.2 Recommendations 69
Appendix A: Numerical Modelling 71
A.1 Introduction 71
A.2 Near wall treatment 72
Appendix B: OpenFOAM 75
B.1 The '0' directory 75
B.2 The 'constant' directory 76
B.3 The 'system' directory 77
Appendix C: Model Set-up 79
C.1 Algorithms 79
C.2 Initial and boundary conditions 80
Appendix D: Mesh Generation 83
Appendix E: Results 85
E.1 Circular Turbulent Jet 85
E.2 Stone Trajectory 90
G.3 Berm built-up 94
List of Figures 95
List of Tables 97

1 Introduction

In this chapter the subject of a rock placement operation with a closed fallpipe system will be introduced. The motive of this thesis will be discussed on the basis of the problem description, the objective and the research questions. After this the problem will be further analysed. Finally the approach of the study and the outline of the report is given.

1.1 General Introduction

For different applications, such as scour protection, pipeline protection and upheaval buckling prevention subsea rock placement operations are used. For such rock placement operations two different types can be distinguished. Shallow water rock placement up to 50 m depth and rock placement for greater water depths, usually ranging from 50 to around 2000 m.

For shallow water operations conventional side stone dumping vessels are sometimes applied. Although an easy solution, their placement precision rapidly decreases with increasing depth. Therefore in deep water operations, but also increasingly in shallow water operations, use is made of the method by guiding the rock from the water surface to the seabed with a fallpipe. For this end two different systems are currently employed in the field, a closed and open fallpipe system.

This study will focus on deep water rock placement operations with the use of a closed fallpipe system.

A closed fallpipe system consists of various steel, aluminium or plastic standard sections which are mounted on top of each other. On top of the standard sections the water inlet section is placed. The upper telescope, on top of the water inlet section, consists of two pipe sections whereby one section can slide into the other. The upper part is connected with wires to the fallpipe vessel and the lower part rests on the water inlet section. At the downward end of the fallpipe a lower telescope is located which fits through the Remote Operated Vehicle (ROV). The function of the ROV is to steer the outer end of the fallpipe, serve as a survey platform and to monitor the rock installation process.

1.2 Tideway Offshore Solutions

Tideway Offshore Solutions are a company dedicated to serving the oil and gas industry. Tideway BV is based in Breda the Netherlands and part of the Belgium based Dredging, Environmental and Marine Engineering (DEME) group of companies. The company is an expert in landfall construction, scour protection and pre- and post-dredging for the support of pipe laying operations. A second line of activity is the precision stone dumping for pipeline crossings, platform approach and offshore ballasting. Operating currently three state-of-the-art fallpipe vessels, Tideway executes precision stone dumping up to depths of 2000 m.

These three state-of-the-art fallpipe vessels are the DP2 Fallpipe Vessel Seahorse (18,500 t), Rollingstone (11,500 t) and the Ice Class Vessel Flintstone (20,000 t).

1.3 Problem Description

In Figure 1 three different berm profiles as result of a rock placement operation are shown. The solid line shows the theoretical profile whereby the least amount of rock is used to assure the minimum coverage of a pipeline or cable. The dotted line illustrates the practical profile which is mostly observed in the field, it satisfies the minimum coverage but uses more rock than the ideal profile. The third profile, the dashed line, is an example of a profile whereby the coverage is not satisfied. This must be corrected and leads to extra use of rock, which is not desirable. Insight into when which type of berm occurs is the basis and main motivation of this thesis.

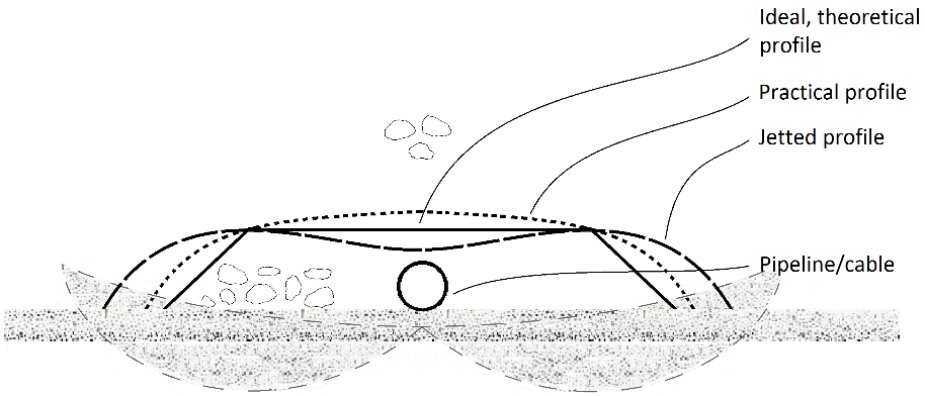

FIGURE 1: BUILT-UP OF A ROCK PROTECTION BERM

During a rock placement operation, when rock is dumped into the fallpipe, the density of the rock & water mixture inside the fallpipe is greater with reference to the surrounding water body. Therefore the water level inside the fallpipe will drop. In order to prevent the water level falling too far, water is let into the fallpipe by means of a water inlet section located in the upper end of the fallpipe. As a result, a current through the fallpipe and subsequently a jet below the fallpipe is created.

The current below a fallpipe may have an important influence on the final shape of the berm. A low current velocity and a large distance of the fallpipe from the seabed will yield in a completely different result than a high current velocity and a small distance of the fallpipe from the seabed. Another contributing factor may be the load of the placed rock onto the seabed. This can cause failure of the soil, depicted by the two greyed shear circles in Figure 1, however not under investigation within this thesis.

By this, the situation just below the fallpipe is known to a limited extent. It is not well understood when stones leave the fallpipe how they interact with the surrounding water, what happens when the mixture hits the seabed, the strength of the currents along the seabed and where the stones eventually will settle. Still, the rock has to be placed in a pre-determined profile. And therefore, especially the arbitrarily occurrence of the jetted profile berm, is subjected to questions. Hence the problem is defined as:

> *"A limited extent of knowledge on the hydrodynamic processes below a fallpipe and their influence on the occurrence of a jetted profile berm."*

1.4 Thesis Objective

All the processes involved in a rock placement operation, from dumping the rocks in the chute, stones falling through the fallpipe until reaching the seabed are interesting. However, because of the extent of this subject it has been decided to only focus on the descent of stones from the moment they leave the fallpipe until they find their resting place.

Hence, the main objective is to get a better understanding of the hydrodynamic processes which exists below the fallpipe. In Figure 2 the region of interest of the objective is shown.

Operational parameters, which will be used as input parameters for this research, such as exit velocity, rock supply, stand-off distance and rock grading will be supplied either from practical experience or theory. It is especially under interest of the possible influence of these operational parameters on the occurrence of a jetted profile berm. Ideally, this shall lead to a prediction tool that can determine the berm shape acquired with a rock placement operation.

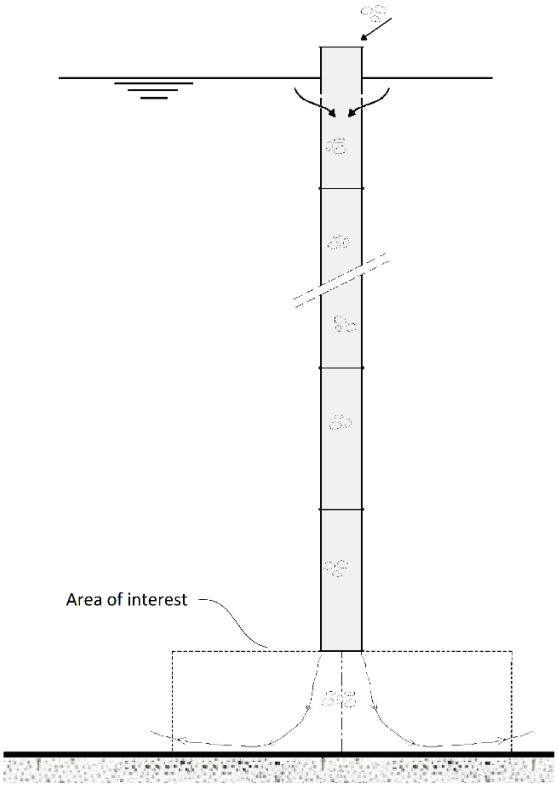

FIGURE 2: AREA OF INTEREST OF THIS THESIS

Therefore the research objective of this thesis will be:

> *"To assess the relevant processes of settling stones towards the seabed and to predict the occurrence of irregular berm shapes due to jet formation below a fallpipe."*

The objective is supported by the following main research question:

- *What is the influence of the hydrodynamic processes below a fallpipe on the occurrence of a jetted profile berm?*

To fulfil the objective and to answer the main research question the following sub questions will be answered in this report:

- *Is it possible to describe the velocity profile below the fallpipe with empirical relations found in literature when compared with computational fluid dynamics simulations?*
- *What is the influence of this velocity profile on the spreading and displacement of rock, taking into account the different parameters, such as the grading and stone size?*
- *What is the influence of this velocity profile on the threshold of motion and accordingly the transport of stones?*

1.5 Problem Analysis

The created current in the fallpipe, of the rock & water mixture, will reach the end of the fallpipe with a certain velocity and enters the ambient fluid. From the orifice of the fallpipe this jet will develop from the Zone of Flow Establishment (ZFE) to the fully developed jet or Zone of Established Flow (ZEF) and when it reaches the seabed a horizontal spreading or impingement region will develop. The zone close to the seabed is called the wall jet region, see Figure 3. The point at the centre of the wall jet region, the point where the radial distance from the centre of the jet is zero, is called the stagnation point.

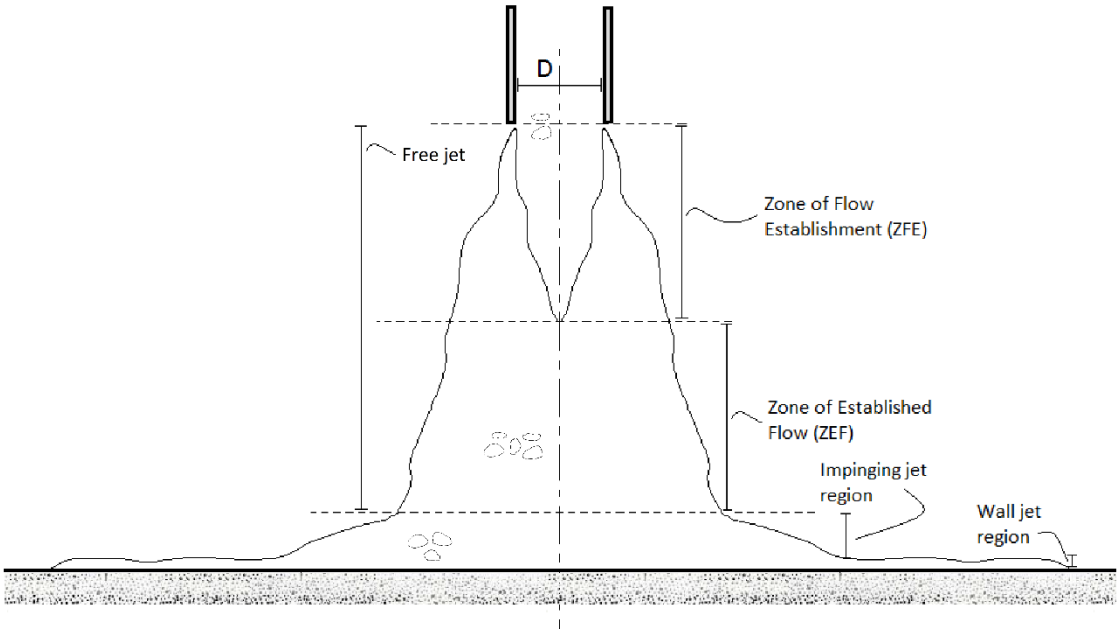

FIGURE 3: FLOW REGIMES BELOW A FALLPIPE

These different flow regimes have an influence on the rock placement operation and the shape of the resulting berm. The flow velocity of the mixture will decrease from the exit of the fallpipe to the bed due to turbulence. One can imagine when the distance from the orifice of the fallpipe to the bed is higher, a greater spreading of rock will be observed.

On the other hand, when this distance is too small the flow velocity of the impinging jet region will be quite large and could exceed the threshold of motion of the rock already placed on the bed. Subsequently, a certain amount of transport of stones may be noticed to the side of the jet.

Furthermore this exceedance of the threshold of motion, and therefore the transport of stones, is not only depending on the stand-off distance but also on the exit velocity from the fallpipe. This exit velocity on its turn depends on the dump rate of rock into the chute and the flow rate through the water inlet sections.

1.6 Thesis Approach

The approach to tackle the problem, described by the problem description, can be divided into two phases. These two phases correspond to the two parts of the report. The first phase (Part II of the report) is the literature study to get a better understanding of the processes involved in a rock placement operation and the governing parameters thereon. In the second phase (Part I of the report) use will be made of computational fluid dynamics (CFD) to make a comparison with the relations found in literature and to predict the occurrence of irregular berms shapes due to the jet formation below a fallpipe.

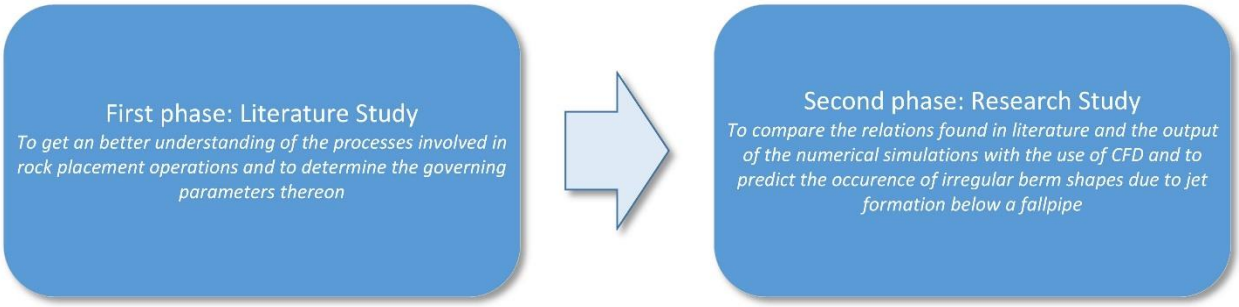

FIGURE 4: THE APPROACH

In Figure 5 the road map of this thesis is shown. On the one hand a theoretical approach is used to determine the velocity profile, the trajectory of the particles and the transport of stones. On the other hand a numerical approach is used to also determine these processes. Ideally, this shall lead to a prediction tool that can determine the berm shape acquired with a rock placement operation by comparing the two approaches and using input from practical experience.

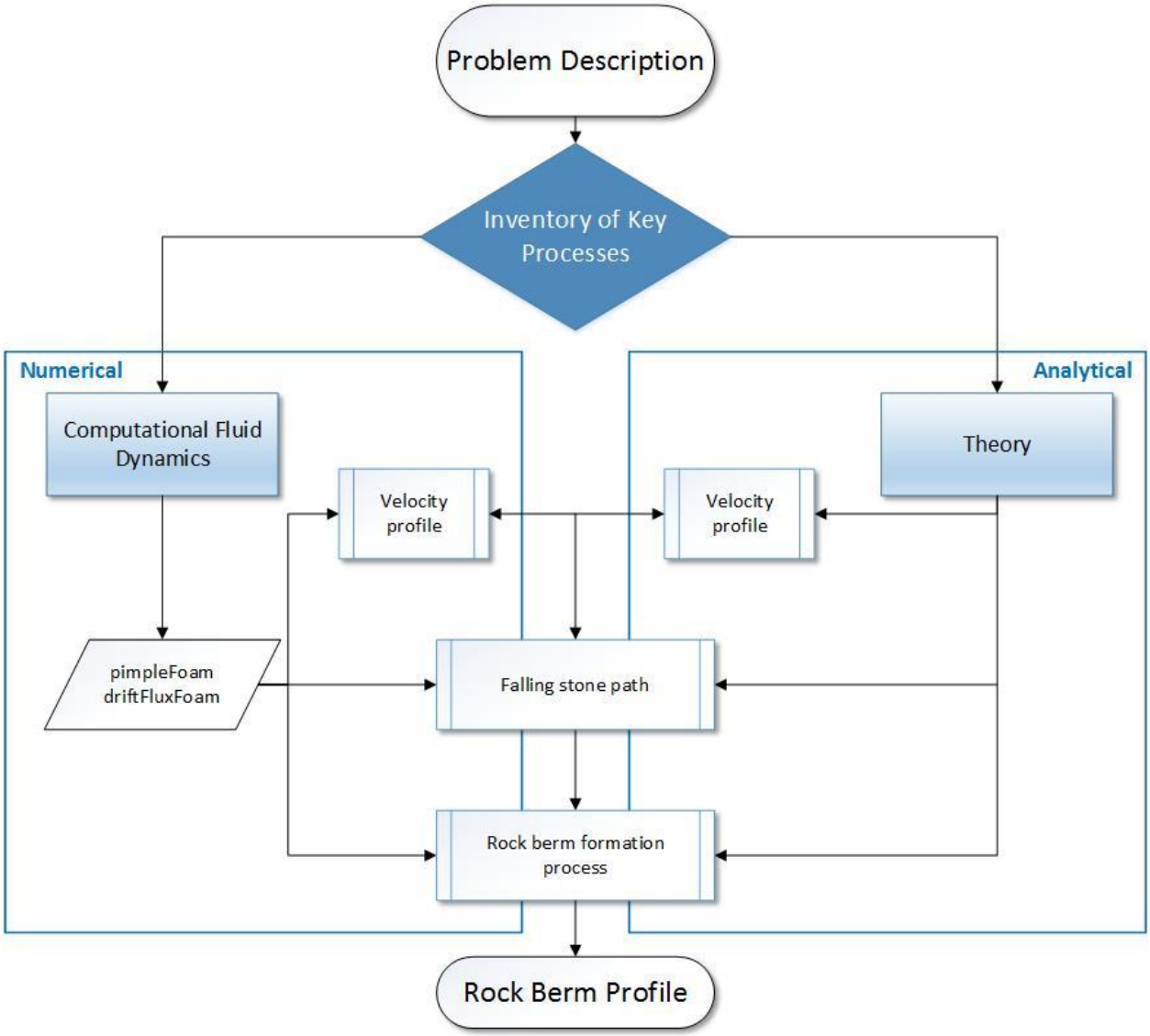

FIGURE 5: ROADMAP OF THIS THESIS

1.7 Main Report Outline

The main report is a description of the research phase of the thesis and contains answers to the questions stated in section 1.4. The content of every chapter is briefly explained:

- *In chapter 2,* an inventory of the key processes, found in literature, involved in a rock placement operation and the governing parameters thereon is stated. This contains, among other things, an explanation on circular turbulent jets, the dumping of stones and the built-up of a rock berm seen in practice.
- *In chapter 3,* the methodology of the numerical modelling with the use of CFD will be explained, including different turbulence models to close the Reynolds-averaged Navier-Stokes (RANS) equations. Furthermore, the basics for the *driftFlux* model are given.

- *In chapter 4,* the prediction of the velocity profile below a fallpipe on the basis of empirical relations is stated. This prediction of the velocity profile is also given by the numerical modelling. A comparison of the both methods is made whereby the possibility to describe the velocity profile with empirical relations when compared with CFD simulations is assessed.
- *In chapter 5,* the prediction of the path of settling stones below the fallpipe is explained.
- *In chapter 6,* the prediction and assessment of the berm formation process is given. Consisting of the increase in height of the rock berm due the dumping process and the degradation due to the stone transport by the turbulent jet.
- *In chapter 7,* the conclusions of the research will be presented as well as recommendations for further research.

2

Description of Rock Placement Processes

As explained in the introduction this thesis consists of two main phases. In phase one, research is done to find all the different processes involved of a rock placement operation. So a brief summary is given in this chapter with the relations and key processes found in literature which will be used for the research phase of this thesis. For the full in depth literature study into the key processes of a rock placement operation, one is referred to the corresponding chapters of Part II.

2.1 Rock Placement Operations

For offshore subsea rock placement operations two different types can be distinguished. Shallow water rock placement up to 50 m and rock placement for greater water depths, usually ranging from 50 to around 2000 m. There are currently two different fallpipe systems in operation for deep water, one with a flexible fallpipe and one with a closed fallpipe. In order to prevent the water level in the closed fallpipe, under research in this thesis, falling too far, water is let into the fallpipe by means of a water inlet section located at the upper end. The main advantage of the closed fallpipe system over a flexible fallpipe system is that the current through this fallpipe can be better regulated by means of opening or closing the water inlet sections. By opening or closing water inlet sections the amount of water which will enter the fallpipe, and thus the downward directed flow can be regulated.

Subsea rock placement operations are used for all kinds of applications. The main applications for these operations are pre-lay seabed preparation works, scour protection, pipeline protection, upheaval buckling prevention, insulation and rock placement operations for crossings. In Figure 6 a single long berm as foundation for a pipeline is shown.

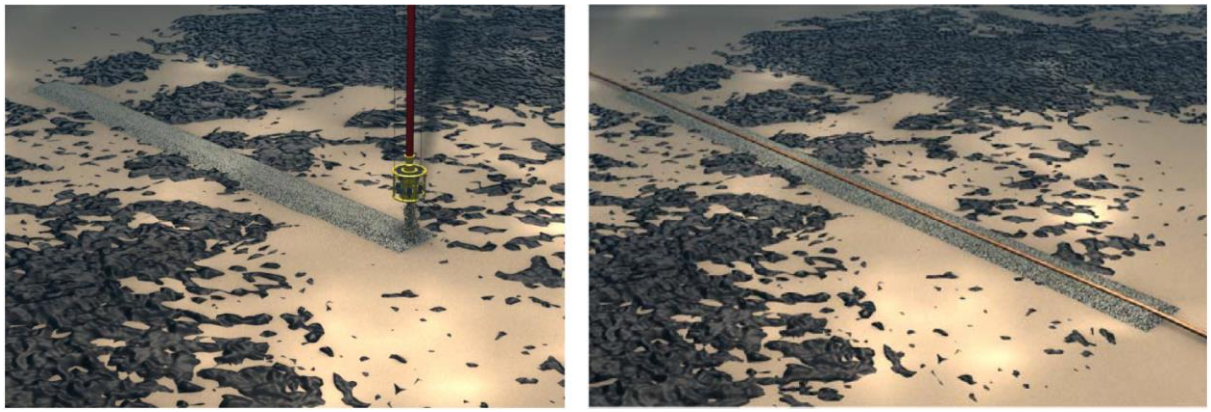

FIGURE 6: SINGLE LONG ROCK BERM

2.2 Circular Turbulent Jets

In Figure 3 the flow below a fallpipe is divided into four regions, the ZFE, the ZEF, the impinging jet region and the wall jet region. The ZFE and ZEF together, with a transitional zone between them, form the free jet region. In literature little can be found on the transitional zone because it is usually neglected. The reason for this is because the influence and length of this zone is rather small. Besides this, the free jet remains a free jet when the flow is not restricted by a boundary, i.e. when the orifice has enough height above the bed, see also Figure 3.

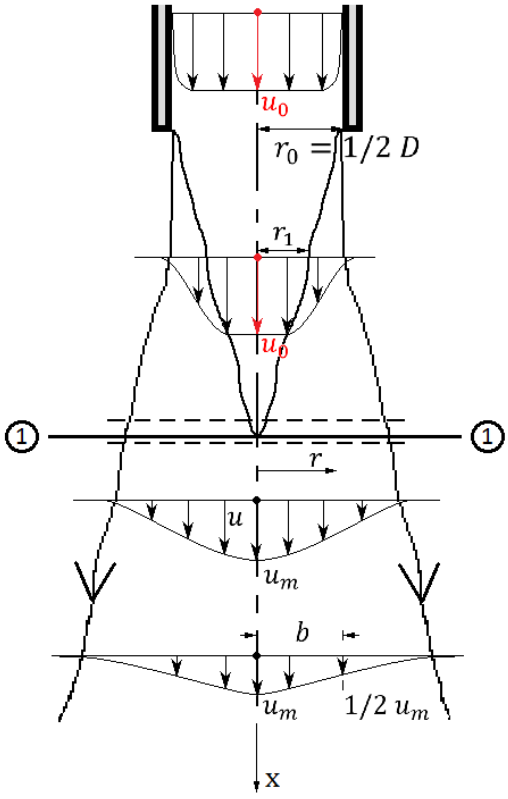

FIGURE 7: FREE JET VELOCITY PROFILE

This distance between de jet and seabed is called the stand-off distance (SOD). A distinction is made between large and small stand-off distances by [BELTAOS AND RAJARATNAM, 1977]. It was proposed in their research values of the SOD less than approximately $5.5D$ be considered small. For a SOD greater than $8.3D$ the distance is considered large, with the range $5.5D \lesssim SOD \lesssim 8.3D$ being transitional. Before section 1 – 1 in Figure 7, a core of fluid, in the form of a cone, is situated. This cone is known as the potential core and within this core the velocity is undiminished.

From the different empirical relations which describe the velocity field of a circular turbulent jet found in literature those of [RAJARATNAM, 1976], [BELTAOS AND RAJARATNAM, 1977] and [RAJARATNAM AND MAZUREK, 2005] will be used in this thesis. Because no expressions were found for the transitional zone, with the range of $5.5D \lesssim SOD \lesssim 8.3D$, the relations for a large SOD will be used to describe this velocity field. The first part of the velocity field is described with the same relations for both large and small stand-off distances.

$$u = u_0 * e^{-0.693\left(\frac{r-r_1}{b}\right)^2} \tag{2.1}$$

With:			
	u	vertical velocity	$[m/s]$
	u_0	initial velocity	$[m/s]$
	r	radial coordinate	$[m]$
	r_1	distance from centre to the edge of the core	$[m]$
	b	spreading width	$[m]$

The distance from the centre to the edge of the potential core and the spreading width of the jet are both described by different empirical relations for large or small $SODs$.

2.2.1 Large stand-off distance

As explained, a large stand-off distance is defined as when the SOD is larger than $8.3D$. The centreline velocity, and therefore the maximum velocity, decreases in the zone after section 1 – 1 in Figure 7. This decreasing centreline velocity is expressed by:

$$u_m = 12.6u_0 * \frac{r_0}{x} \tag{2.2}$$

With:			
	u_m	maximum velocity	$[m/s]$
	r_0	radius of the jet	$[m]$
	x	vertical distance from the nozzle	$[m]$

Now, with the use of the maximum velocities the jet velocity for the ZEF can be calculated, again with a different empirical relation for the spreading width:

$$u = u_m * e^{-0.693\left(\frac{r}{b}\right)^2} \tag{2.3}$$

For an impinging jet with a large SOD the free jet region extends from the orifice up to about 0.86 x/SOD. Or, in other words, the impinging jet starts at a height of 0.14 SOD above the seabed.

When the jet reaches this impinging region the corresponding maximum velocity can be approximated with the following expression:

$$\frac{u_m}{u_{mf}} = 3.10\eta_i\sqrt{1-\eta_i} \tag{2.4}$$

With:

u_{mf}	corresponding centreline velocity of free jet without boundary	$[m/s]$
η_i	factor for impinging jet	$[-]$

With the use of this new maximum velocity the velocity field in this region can again be calculated with the use of equation (2.3). The reduction factor is expressed by:

$$\eta_i = \frac{x}{SOD} \tag{2.5}$$

In the wall jet region the maximum radial velocity is given as:

$$v_m = u_0 * \frac{1.03}{r/D} \tag{2.6}$$

With:

v_m	maximum radial velocity	$[m/s]$

With this maximum radial velocity an expression for the flow field is noted as:

$$v = v_m * 1.48\eta_w^{1/7}[1 - erf(0.68\eta_w)] \tag{2.7}$$

With:

v	radial velocity	$[m/s]$
η_w	factor for wall jet	$[-]$

The factor of the wall jet and the spreading width can be determined with:

$$\eta_w = \frac{z}{b} \tag{2.8}$$

$$b = 0.087r \tag{2.9}$$

The different empirical relations given in this section do not describe the entire velocity field below the fallpipe due to the fact that they have a region of validity. Accordingly, it is impossible to receive a closing velocity field with the use of the empirical relations. However, to make a comparison between the theory and CFD simulations and to use the velocity field later on in the study, use is made of interpolation between the different relations. By the interpolation the "gaps" within the velocity field are filled, or better said, a closing velocity field below the fallpipe is received.

2.2.2 Small stand-off distance

As explained, a small stand-off distance is defined as when the SOD is smaller than $5.5D$. As can be seen in Figure 8, in comparison to the flow field of the free jet or for an impinging jet with a large SOD, the maximum velocity is not found at the centre of the jet.

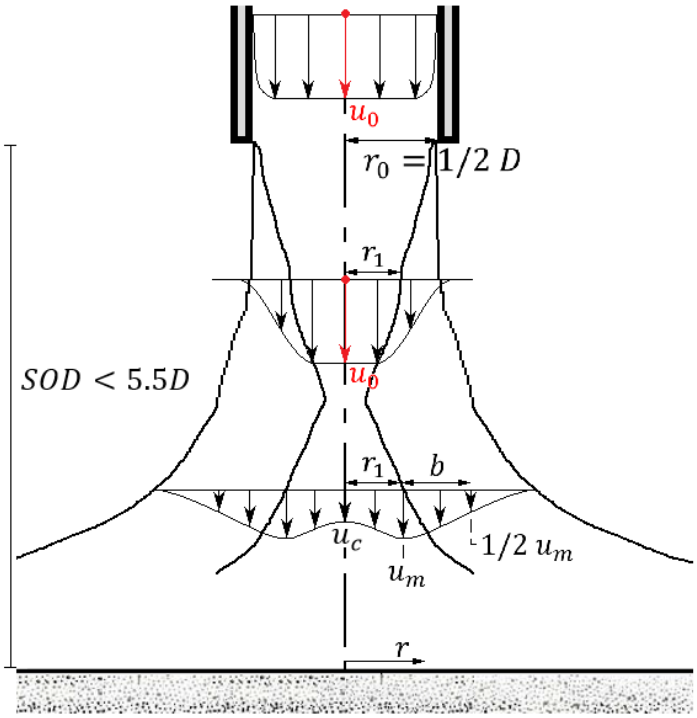

FIGURE 8: IMPINGING JET VELOCITY PROFILE

For an impinging jet with a small SOD the impinging region starts, and therefore the centreline velocity starts to decrease, at $z/D = 1.1$. This centreline velocity is now equal to:

$$u_c = u_0 * \frac{z/D}{1.1}\left(2 - \frac{z/D}{1.1}\right) \tag{2.10}$$

With: z vertical distance from the seabed $[m]$

The relation between the centreline velocity and maximum velocity is roughly proportional to:

$$u_m = 1.15 u_c \tag{2.11}$$

With this maximum velocity, the jet velocity in the shear layer can be determined with equation (2.3). In the core of the jet a rough approximation of the velocity field is expressed as:

$$u = \lambda^2(2 - \lambda^2)(u_m - u_c) + u_c \tag{2.12}$$

With: $\lambda = \frac{r}{r_1}$

Just as for the approximation of the velocity field for large $SODs$ different empirical relations are given for the spreading width and the distance from the centre to the edge of the core.

The radial component of the velocity in the impingement region is given as:

$$v = v_1 * \frac{\lambda}{1.15}[1 + 0.15\lambda^2(2 - \lambda^2)] \tag{2.13}$$

With: v_1 radial velocity at $r = r_1$ $[m/s]$

Whereby the radial velocity at $r = r_1$ is defined as:

$$v_1 = \frac{u_0 * r_1}{D} * \frac{0.294}{\sqrt{(z/D) - 0.07}} \tag{2.14}$$

In the wall jet region the maximum radial velocities are expressed by:

$$v_m = u_0 * \frac{1}{r/D} \tag{2.15}$$

With this maximum radial velocity the flow field can again be calculated with equation (2.7). Again, the expressions given in this section again do not describe a closing relation for the velocity field below the fallpipe. However, to make a comparison between the theory and CFD simulations and to use the velocity field later on in the study, use is made of interpolation between the different relations.

2.3 Threshold of Motion

A critical or threshold condition for flow over an erodible bed has been reached when the hydrodynamic force is balanced by the resisting force. Already for various times the threshold of motion of particles and the corresponding transport formula have been researched. This has been proven to be a very difficult task because still no conclusive physical relation and formula have been found. Accordingly, numerous experiments have been performed to find an empirical formula for this transport.

In this thesis use will be made of a 3D RANS model for the numerical simulations. [HOFLAND, 2005] proposed a method for evaluating the stability of bed protections under non-uniform flow using output of a 3D RANS model, accordingly this stability parameter will be used in this thesis and is expressed as:

$$\Psi_{Lm} = \frac{max\left[\langle \bar{u} + \alpha * \sqrt{k} \rangle_{Lm} \frac{L_m}{z}\right]^2}{\Delta * g * d_{n50}} \tag{2.16}$$

With:			
	Ψ_{Lm}	Hofland stability parameter	$[-]$
	$\bar{u}$	stationary mean part of u	$[m/s]$
	α	empirical turbulence coefficient	$[-]$
	k	turbulent kinetic energy	$[m^2/s^2]$
	L_m	Bakhmetev mixing length $= \kappa z\sqrt{1 - z/h}$	$[m]$
	κ	Von Karman constant	$[-]$
	h	water depth	$[m]$
	Δ	relative density	$[-]$
	g	gravitational acceleration	$[m/s^2]$
	d_{n50}	median nominal diameter	$[m]$

The Bakhmetev mixing length is a function of the distance above the seabed, z. By this, the moving average of the term $\bar{u} + \alpha * \sqrt{k}$ is taken and a distribution of the hydraulic load is calculated. To determine the Hofland stability parameter the maximum value of this distribution is used, see Figure 9.

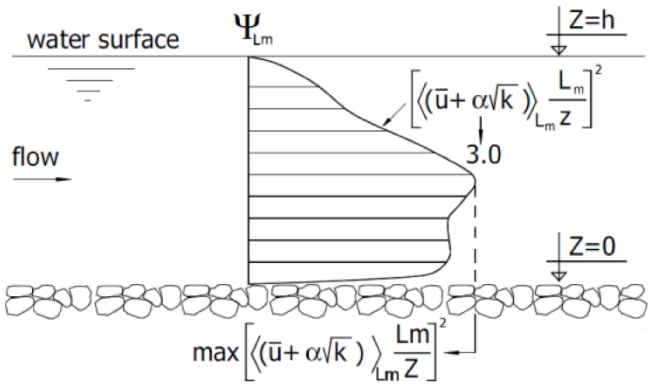

FIGURE 9: DISTRIBUTION OF THE KEY PARAMETERS FOR THE HOFLAND STABILITY PARAMETER

[Hoan, 2008] used a correlation analysis which led to the following stone entrainment function for the Hofland stability parameter:

$$\Phi_E = 1.15 * 10^{-9} * \Psi_{Lm}^{4.53} \qquad for\ 1.3 < \Psi_{Lm} < 3.2 \tag{2.17}$$

With: Φ_E entrainment parameter $[-]$

With the use of the dimensionless entrainment parameter the entrainment rate can be calculated with [HOFLAND, 2005]:

$$E = \Phi_E * \sqrt{\Delta * g * d_{n50}} \tag{2.18}$$

With: E entrainment rate $[m/s]$

2.4 Rock Properties

All materials can be characterized by their properties, for rock this is the same. A lot of different characteristics of rock can be recognised. However, in the literature study the focus lies on rock types, mass and sizes, grading, and shapes. As this thesis is part of a research in the offshore rock placement operations use is made of the grading mainly used in the offshore industry. These different requirements for rock grading are set by [Statoil TR1370, 2009] and are intended for subsea rock installation. In Table 1 the size of the stones within the grading are given by their median diameter. However, often the median nominal diameter of stones is used in design formulas such as an equation for the threshold of motion and transport of stones. Because the shape of most rock is more-or-less the same, a relation between the median and median nominal diameter exists.

This relation can be noted as a shape factor times the diameter:

$$d_{n50} = F_s * d_{50} \tag{2.19}$$

With:
- F_s shape factor $[-]$
- d_{50} median diameter $[m]$

According to [LAAN, 1982] this shape factor is around 0.84, and this value is widely applied in hydraulic engineering practice. In this thesis therefore the factor of 0.84 will also be used to converse from the median diameter to the median nominal diameter.

TABLE 1: ROCK GRADING BY [STATOIL TR1370, 2009]

Class	Rock size	Target (mm)	Min (mm)	Max (mm)
1 – 3" $(75\ mm\ rock)$	d_m	--	--	100
	d_{90}	75	60	90
	d_{50}	50	40	60
	d_5	22	16	32
1 – 4" $(100\ mm\ rock)$	d_m	--	--	125
	d_{90}	100	90	115
	d_{50}	60	50	70
	d_5	22	16	32
1 – 5" $(125\ mm\ rock)$	d_m	--	--	150
	d_{90}	125	110	135
	d_{50}	75	60	90
	d_5	22	16	32

2.5 Dumping of a Single Stone

When a single rock is falling through stagnant water it will be subjected to an acceleration due to the gravitational force. The settling velocity of a single rock will increase until the terminal, or equilibrium, velocity is reached. This equilibrium velocity is caused by the fact that the resisting force will increase with an increasing settling velocity and thus the acceleration decreases. Therefore this equilibrium will be reached when the gravitational force is the same as the resistance force. The combination of the three vertical forces and with the help of Newton's law of motion the differential equation is noted as:

$$F_z + F_b + F_D = M * a_v \tag{2.20}$$

With:
- F_z gravitational force $[kgm/s^2]$
- F_b buoyancy force $[kgm/s^2]$
- F_D drag force $[kgm/s^2]$
- M mass $[kg]$
- a_v vertical acceleration of a particle $[m/s^2]$

The drag force for a stone falling through water is the main unknown in equation (2.20), because the drag coefficient for rock needs to be determined. This is quite an ambitious process because even for a sphere this is rather difficult. Nonetheless, several empirical relations have been found in literature. To have the possibility to contain the shape of a stone as part of the research it is chosen to use the relations derived by [VAN DER WAL, 2002] for the determination of the drag coefficient.

$$f_{C_D}(C_D) = \frac{1}{\sqrt{2\pi} * \sigma_{C_D}} * e^{-\frac{\left(C_D - \mu_{C_D}\right)^2}{2\sigma_{C_D}^2}} \tag{2.21}$$

With:

f_{C_D}	probability density function of the drag coefficient	
μ_{C_D}	mean value of the drag coefficient	$[-]$
σ_{C_D}	standard deviation of the drag coefficient	$[-]$
C_D	drag coefficient	$[-]$

The mean value and standard deviation of the drag coefficient are evaluated as:

$$\mu_{C_D} = 0.54 * \frac{l}{d} + 0.42 \tag{2.22}$$

$$\sigma_{C_D} = 0.30 \tag{2.23}$$

Now, with the drag coefficient the equilibrium settling velocity of a single stone can be calculated with the following formula:

$$u_e = \sqrt{2 * \Delta * d_n * \frac{g}{C_D}} \tag{2.24}$$

With:

u_e	equilibrium settling velocity	$[m/s]$

This method for calculating the equilibrium settling velocity assumes that the surface exposed to the drag is equal to the square of the nominal diameter.

2.6 Dumping of Multiple Stones

In practice, when a rock placement operation with a fallpipe vessel is executed a large amount of rock is dumped. Production rates of $2300\ t/h$ are not uncommon for industrial purposes. [VAN DER WAL, 2002] defined five different phases, based on his experiments, for the settling process of rock groups. The five phases include all possible mechanisms which can occur, however not all phases actually have to occur during the settling process. The five phases are defined as:

- **Phase 1:** Acceleration of the stone group.
- **Phase 2:** Deceleration of the stone group.
- **Phase 3:** Rock front of larger stones.
- **Phase 4:** Settling process according to the Single Stone Model, see Chapter 9 Part II
- **Phase 5:** Radial runoff.

Besides the five phases of the settling process of rock groups, when particles are continuously dumped in stagnant water the mutual influence of the particles decreases the settling velocity. This effect is called hindered settling and is caused by an increased drag coefficient, particle collision and a returning water flow. In literature a series of empirical formulae is found to describe the hindered settling velocity. These formulae are all based on the particle Reynolds number. The particle Reynolds number for stones used in rock placement operations is in the order of $(\mathcal{O}4)$. Because the research done by Garside in 1977 [VAN RHEE, 2002] covers this range the following relation will be used:

$$u_{hs} = u_e * (1 - C_v)^{\beta} \tag{2.25}$$

With:	u_{hs}	hindered settling velocity	$[m/s]$
	C_v	volume concentration	$[-]$
	β	coefficient $=$ 2.7 by Garside, 1977 [VAN RHEE, 2002]	$[-]$

2.7 Dumping of Stones through a Fallpipe

In the previous two sections the dumping of a single stone and multiple stones is elaborated. Yet, for rock placement operations in practice the stones are dumped through the fallpipe and not at the water surface. For this, different methods for determining the exit velocity of the stone and water mixture out of the fallpipe have been found in literature, such as the method by Tideway and van Oord. However, the area of interest of this research lies below the orifice of the fallpipe, as shown in Figure 2. As starting point for the different models an assumption is made on different parameters based on practical experience, see Table 2.

TABLE 2: STANDARD PARAMATERS

Parameter	Value
Density water	$1025\ kg/m^3$
Density rock	$2650\ kg/m^3$
Exit velocity	$5\ m/s$
Viscosity	$1.42 * 10^{-6}$
Diameter fallpipe, D	$0.65\ m$

3

Methodology of the Numerical Modelling

In this chapter the methodology of the numerical modelling used in the modelling phase of this thesis will be treated. The first part is a brief introduction and the basis on numerical modelling. In the second part of this chapter an elaboration will be given on computational fluid dynamics including the used program and different turbulence models.

3.1 Numerical Modelling

Fluid flows are governed by partial differential equations (PDE's) which represent conservation laws. In engineering practice the real world often gets approximated by models. This is done because the boundary value problems often cannot be solved analytically, especially when nonlinear terms are included. Therefore numerical modelling is introduced and is defined as the study of the methods of numerically approximating solutions of mathematical equations with finite computational processes [Zijlema, 2012]. To solve a problem, the continuous abstract number space of the model is projected on a grid containing a finite number of grid points. In Appendix D the mesh independency study for this thesis is treated. The main objective of the mesh independency study is to reduce computational time by setting a cell size, however, securing independency of the solution on the grid size.

As mentioned numerical models are only an approximation of the real solution. For this reason in Appendix A possible disadvantages of numerical modelling are treated. For example, the discretization and the use of computers give rise to errors.

3.2 Computational Fluid Dynamics

As said, fluid flows are governed by PDE's. Computational fluid dynamics (CFD) replaces such PDE systems by a set of algebraic equations which can be solved by using a computer. The CFD simulation part of this thesis will be carried out with a full 3D model. Consequently, the simulated velocity profile will not be completely axisymmetric, however it was quickly discovered from some first simulations that no significant deviations from an axisymmetric velocity profile were noticeable. By this, just as with the empirical relations, the velocity profile is assumed completely axisymmetric.

Within the 3D domain a part of the fallpipe with the length of $2D$ is modelled to receive a realistic input velocity distribution. The software used for this 3D modelling is the open source software package OpenFOAM. Detailed information on the OpenFOAM case structure and settings is given in Appendix B.

In this thesis use will be made of the Reynolds-averaged Navier-Stokes (RANS) equations for the turbulence modelling. The RANS equations are the oldest approach to turbulence modelling and are time-averaged equations of motion for fluid flow. By Reynolds averaging of the Navier-Stokes equations new apparent stresses are introduced, the so-called Reynold stresses. To solve the RANS equations additional equations are necessary to approximate these Reynold stresses. Hence, to close the system, i.e. get an equal number of unknowns and equations, the Reynold stresses have to be modelled in some way. For closing the system use will be made of the $k-\varepsilon$ and $k-\omega SST$ models, whereby the ω *and* ε stand for the specific– and turbulent dissipation rate respectively.

Both the $k-\varepsilon$ and $k-\omega SST$ models are a single phase approach and therefore only assume a circular turbulent water jet below the fallpipe. This is considered because quite large stones are dumped with a rather large terminal settling velocity and no real homogenous mixture can be assumed. Though, looking at the real situation the stones within the water jet clearly have an influence. Hence, also the *driftFlux* model is used to get an idea of the influence of the mixture. In this model both water and the stones are considered. Therefore the model is a two phase approach, although considering the mixture as a whole, rather than two phases separately. The *driftFlux* model also uses the $k-\varepsilon$ turbulence model to close the RANS equations.

The influence of a mixture on the velocity field of an impinging jet can be clarified with a simple example. Imagine a lock with on both sides of the closed lock gate a fluid with the same depth. However, the fluid on one side has a higher density compared to the density of the fluid on the other side. On a certain moment the slide gate is lifted with a certain height. Now, due to the higher pressure on the side of the fluid with a higher density, a density current from one to the other side will be observed. This phenomena is well described in literature and is known as the lock-exchange process.

In the coming three sections a more in depth explanation is given on the two turbulence models and the *driftFlux* model.

3.2.1 The $k-\varepsilon$ model

The $k-\varepsilon$ model is probably the most well-known, used and researched turbulence model, hence also used in this thesis, and is a two-equation model. Since it was proposed by Launder and Spalding [ANSYS, 2013] the model has become the go-to model because of its robustness, economy and reasonable accuracy for a wide range of turbulent flows [ANSYS, 2013]. It is a semi-empirical model and the derivation of the model equations relies on considerations and empiricism. The turbulence kinetic energy and its rate of dissipation are obtained from the following transport equations [ANSYS, 2013]:

$$\frac{\partial k}{\partial t}+\frac{\partial k u_j}{\partial x_j}=\frac{\partial}{\partial x_j}\left[\left(\nu+\frac{\nu_t}{\sigma_k}\right)\frac{\partial k}{\partial x_j}\right]+G_k-\varepsilon \tag{3.1}$$

$$\frac{\partial \varepsilon}{\partial t}+\frac{\partial \varepsilon u_j}{\partial x_j}=\frac{\partial}{\partial x_j}\left[\left(\nu+\frac{\nu_t}{\sigma_\varepsilon}\right)\frac{\partial \varepsilon}{\partial x_j}\right]+C_{\varepsilon 1}\frac{\varepsilon}{k}G_k-C_{\varepsilon 2}\frac{\varepsilon^2}{k} \tag{3.2}$$

In the two equations (3.1) and (3.2) the term G_k represents the generation of turbulent kinetic energy due to the mean velocity gradients and is defined as [FURBO, 2010]:

$$G_k = \nu_t \left(\frac{\partial \overline{u}_i}{\partial x_j} + \frac{\partial \overline{u}_j}{\partial x_i} \right) \frac{\partial \overline{u}_i}{\partial x_j} \tag{3.3}$$

By combining the turbulent kinetic energy and its rate of dissipation the turbulent (or eddy) viscosity can be computed [FURBO, 2010]:

$$\nu_t = C_\mu \frac{k^2}{\varepsilon} \tag{3.4}$$

For a full derivation of the transport equations see for example [ANSYS, 2013] and [FURBO, 2010].

Due to its popularity, the strength and weaknesses have become known and variants of this model have been proposed. Nonetheless, in this thesis the standard $k-\varepsilon$ model will be used with the model constants noted in Table 3.

TABLE 3: STANDARD MODEL CONSTANT $k-\varepsilon$ MODEL

Coefficient	Value
C_μ	0.09
$C_{\varepsilon 1}$	1.44
$C_{\varepsilon 2}$	1.92
σ_k	1.0
σ_ε	1.3

The main advantages of the $k-\varepsilon$ model are:

- **Robustness:** Due the robustness this model has a high popularity in industrial flow and heat transfer simulations.
- **Accuracy:** The $k-\varepsilon$ is known for its reasonable accuracy for a wide range of turbulent flows.
- **Well-tested:** Since it was proposed by Launder and Spalding [ANSYS, 2013] it is a well-used model and therefore the strengths and weaknesses have become known.

A common known disadvantage of the $k-\varepsilon$ model is the possible build-up of turbulent kinetic energy in stagnation regions.

3.2.2 The $k-\omega SST$ model

The method of turbulence closure in the $k-\omega SST$ model is proposed by [MENTER, 1994] and is an adaptation of the $k-\omega$ model by Wilcox [ANSYS, 2013]. This is done to effectively blend the robust and accurate formulation of the $k-\omega$ model in the near wall-region with the freestream independence of the $k-\varepsilon$ model in the far field. Hence, the $k-\omega SST$ (Shear Stress Transport) model is a hybrid model which uses the best of both worlds. To link both the models use is made of a blending function and the $k-\varepsilon$ model is converted into a $k-\omega$ formulation.

The main difference between the standard $k-\omega$ model by Wilcox is that the absolute value of the transport of shear stress (the strain rate) S is now used in the definition of the eddy viscosity instead of the vorticity [STEENSTRA, 2014]. This eddy viscosity is used in the RANS equations for calculating the mean flow properties. Transport equations of the turbulent kinetic energy and the specific turbulent dissipation rate are expressed in equations (3.5) and (3.6) [ANSYS, 2013].

$$\frac{\partial k}{\partial t}+\frac{\partial k u_j}{\partial x_j}= \frac{\partial}{\partial x_j}\left[\left(\nu+\frac{\nu_t}{\sigma_k}\right)\frac{\partial k}{\partial x_j}\right]+G_k-\beta^*\omega k \tag{3.5}$$

$$\frac{\partial \omega}{\partial t}+\frac{\partial \omega u_j}{\partial x_j}= \frac{\partial}{\partial x_j}\left[\left(\nu+\frac{\nu_t}{\sigma_\omega}\right)\frac{\partial \omega}{\partial x_j}\right]+\frac{\omega}{k}G_k+2(1-F_1)\sigma_\omega\frac{1}{\omega}\frac{\partial k}{\partial x_j}\frac{\partial \omega}{\partial x_j}-\beta\omega^2 \tag{3.6}$$

The turbulent (or eddy) viscosity can now be calculated with [FURBO, 2010]:

$$\nu_t=\frac{a_1 k}{max(a_1\omega, SF_2)} \tag{3.7}$$

As said, the $k-\omega SST$ model is a hybrid model and therefore uses a blending function (F_1) to determine the coefficients in the equations above. The blending function has a value of one near surfaces (resulting in $\varphi=\varphi_1$) and a value of zero in the outer part of the boundary layer and for free shear flows (resulting in $\varphi=\varphi_2$). Equation (3.8) shows this blending function [STEENSTRA, 2014].

$$\varphi = F_1\varphi_1+(1-F_2)\varphi_2 \tag{3.8}$$

For a full derivation of the transport equations see for example [ANSYS, 2013] and [FURBO, 2010]. The different constants used by OpenFOAM for this model are denoted in Table 4.

TABLE 4: STANDARD MODEL CONSTANTS $k-\omega SST$ MODEL

Coefficient (φ_1)	Value	Coefficient (φ_2)	Value
σ_{k1}	0.85	σ_{k2}	1.0
$\sigma_{\omega1}$	0.5	$\alpha_{\omega2}$	0.856
κ	0.41	κ	0.41
γ_1	0.555556	γ_2	0.44
β_1	0.075	β_2	0.0828
β^*	0.09	β^*	0.09
a_1	0.31	a_1	0.31

Just as the $k-\varepsilon$ turbulence model the $k-\omega SST$ model has it capabilities and limitations. The main advantages of the $k-\omega SST$ model are noted by [ANSYS, 2013] as:

- **Hybrid:** Both the $k-\varepsilon$ and $k-\omega$ model are multiplied by a blending function and both models are added together. Therefore the $k-\omega SST$ model uses the best of both models.
- **Cross-diffusion:** A damped cross-diffusion derivative term is incorporated.

- **Turbulent shear stress:** The definition of the turbulent viscosity is modified to account for the transport of the turbulent shear stress.

Due to the fact that the $k-\omega SST$ model uses a blending function which is dependent on the distance from a wall, errors may arise.

3.2.3 The *driftFlux* model

For the formulation of the *driftFlux* model some drastic constitutive assumptions are required causing some of the important characteristics to be lost. However, it is exactly this simplicity that makes the model very useful in many engineering applications [ISHII AND HIBIKI, 2006]. In the *driftFlux* model one energy and one momentum equation have been eliminated and hence only four field equations are left. By doing this, the two eliminated equations have to be replaced by additional constitutive equations. The precise derivation of the model, including the field equations, model constitutive laws and model formulation is extensively discussed by [ISHII AND HIBIKI, 2006] or [BRENNAN, 2001] and therefore not repeated here.

Still, the system has to be closed and, as explained, for this end this thesis uses the buoyant $k-\varepsilon$ model. The buoyant version of the $k-\varepsilon$ turbulence model uses the same transport equations as expressed in section 3.2.1, however the density and concentration of both water and stones is implemented. Besides this, an extra buoyancy term is added and is given as [ANSYS, 2013]:

$$G_b = -g_i C_{g_t} \nu_t \frac{\partial \rho}{\partial x_i} \tag{3.9}$$

Because the same transport equations are used, besides the added term, the same standard values of the model constants are used by OpenFOAM as stated in Table 5. Nonetheless, for the buoyancy term another constant is needed and is set as [OPENFOAM, 2012]:

TABLE 5: STANDARD MODEL CONSTANTS DRIFTFLUX MODEL

Coefficient	Value
C_{g_t}	0.85

The main advantages of the *driftFlux* model are [ISHII AND HIBIKI, 2006]:

- **Simplicity:** A rather simple model compared to the two-fluid model.
- **Mixture:** The possibility to include both water and stones, as a mixture, for the simulation.
- **Turbulence model:** This model uses the same transport equations as used for the $k-\varepsilon$ model and therefore give rise to the same advantages.

The main disadvantage of the *driftFlux* model is that some drastic constitutive assumptions are required causing some of the important characteristics to be lost. Besides this, in this thesis the stones considered are rather large whereas the model assumes, and therefore is based on, small particles.

3.3 Set-up of the Numerical Models

OpenFOAM has a wide variety of solvers divided by category of continuum mechanics, such as incompressible flow and multiphase. For the $k-\varepsilon$ and $k-\omega SST$ model the *simpleFoam* solver is used. This is a steady-state solver for incompressible flows with turbulence modelling and uses the SIMPLE algorithm. The *driftFlux* model, on the other hand, uses the *driftFluxFoam* solver, which is a solver for 2 incompressible fluids using the mixture approach with the drift-flux approximation for relative motion of phases [OpenFOAM, 2012]. This solver uses the PIMPLE algorithm. For the specifics on the two algorithms see Appendix C.1.

Besides a solver, every numerical model needs initial and boundary conditions. However, for the simulations the initial conditions are not of great concern [OpenFOAM, 2012]. The initial conditions are only used as an initial guess and therefore one is referred to Appendix C.2 for an elaboration hereon.

4

Prediction of the Jet Profile below a Fallpipe

In this chapter the simulations of the circular turbulent jet below a fallpipe system will be discussed. In section 4.1 the velocity profile found with empirical relations for different $SODs$ will be treated. After this the velocity profile simulated by numerical modelling will be elaborated. For the CFD simulations the same $SODs$ are modelled as for the empirical relations, according to large, small and transitional $SODs$, see Table 6.

TABLE 6: MODELLING CONSIDERATIONS STAND-OFF DISTANCE

Empirical	*CFD*
$4D$	$4D$
$5.5D$	$5.5D$
$7D$	$7D$
$8.3D$	$8.3D$
$10D$	$10D$
$15D$	$15D$
$20D$	$20D$

Besides this, different input velocities and certain bottom roughness are taken into account. In Table 7 the standard input parameters are shown which will be used for all simulations except when explained otherwise.

TABLE 7: STANDARD INPUT PARAMETERS FOR THE FLOW FIELD MODELLING

Parameter	Input
SOD	$0.65\ m$
Velocity	$5\ m/s$
Gravitational constant	$9.81\ m/s^2$
Viscosity	$1.42 * 10^{-6}$
Roughness	smooth

The *driftFlux* model requires some extra parameters compared to the $k-\varepsilon$ and $k-\omega SST$ models. As explained in section 3.3, the density of both water and rock are included in the transport equations and thus must be supplied. Additionally, the input concentration and terminal settling velocity of the stones in the mixture needs to be defined. In practice it is noticed that the density of the mixture inside the fallpipe is roughly $1150\ kg/m^3$. With the considered density for water and rock an input concentration of 8% is assumed. When using equation (2.24) the terminal settling for a stone with median nominal diameter found in the $1-5\ inch$ grading can be calculated roughly on $1.25\ m/s$, therefore this value is used.

TABLE 8: INPUT VALUES FOR THE DRIFTFLUX MODEL

parameter	*Value*
Density of rock	$2650\ kg/m^3$
Density of water	$1025\ kg/m^3$
Density of mixture	$1150\ kg/m^3$
Concentration	8 %
Terminal settling velocity	$1.25\ m/s$

4.1 Empirical Approach

In literature it was found that a distinction for a turbulent impinging jet can made in accordance to the SOD. This is, an impinging jet with a small SOD or a large SOD with in between a transitional range. For an impinging jet all the velocities, vertical as well radial, are based on the input velocity, u_0. Besides this, the vertical velocities of both a jet with a small SOD and large SOD follow the same relation in the ZFE, with the highest velocity at the centreline. Near the seabed however, for a jet with a small SOD the highest velocity is not found at the centreline anymore, yet this is still the case for a jet with a large SOD. Furthermore, as already remarked in 2.2, with the empirical relations it is impossible to describe a complete velocity profile below the fallpipe due to the fact that they have a region of validity. However, in this research use is made of interpolation between these different relations to receive a description of a closing flow field.

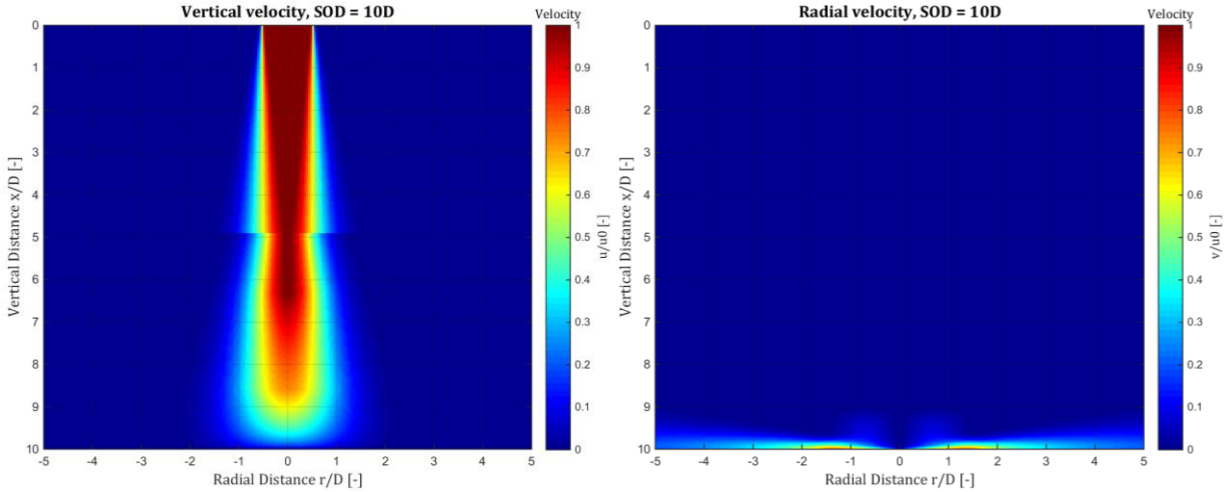

FIGURE 10: NORMALIZED VERTICAL AND RADIAL VELOCITY PROFILE OF IMPINGING JET WITH SOD = 10D, EMPIRICAL APPROACH

In Figure 10 an example of the normalized vertical and radial velocity profiles of an impinging jet with a SOD of $10D$ is shown. The transitional zone between de ZFE and ZEF in the free jet region of the vertical velocity profile can be clearly seen, or better said, the lack of definition for this zone. When looking at the vertical velocity fields for an impinging jet with a small SOD this lack of definition is not observed due to the fact that the impinging jet is still in the ZFE zone. Furthermore, in the radial velocity profile it is clearly noticeable that the flow is bounded quite close to the seabed with at the stagnation point of course a zero velocity magnitude.

4.2 Computational Fluid Dynamics Approach

In Figure 11 an example of the normalized vertical and radial velocity profiles, with a SOD of $10D$, as output of the numerical simulations are shown.

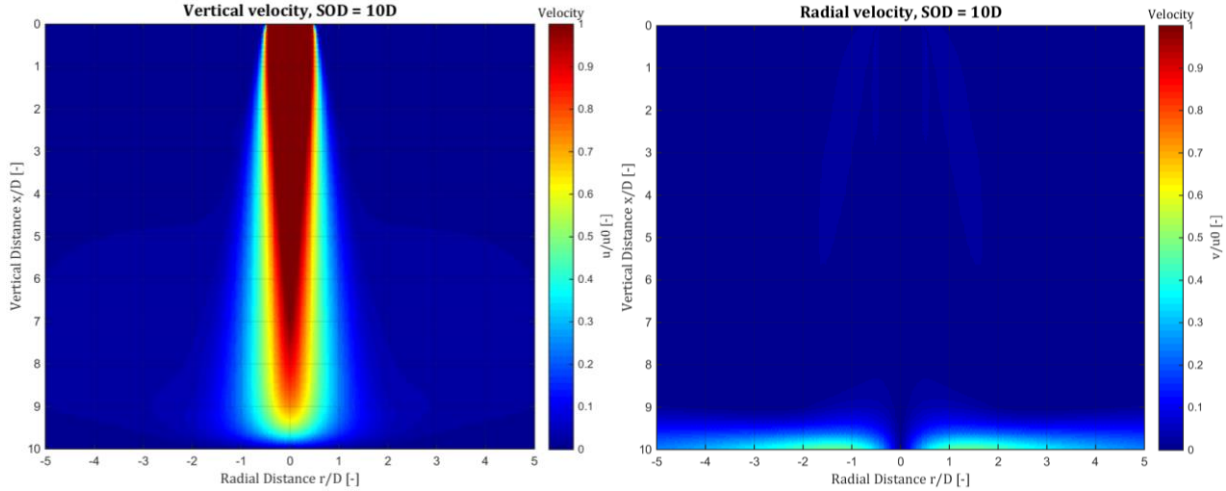

FIGURE 11: NORMALIZED VERTICAL AND RADIAL VELOCITY PROFILE OF IMPINGING JET WITH SOD = 10D, CFD APPROACH

The radial velocity is, just as with the empirical relations, quite bounded close to the seabed. Although also some radial velocities can be seen higher in the domain.

4.2.1 Input velocity

The empirical relations for a circular turbulent impinging jet suggest that the velocity field is completely depended on the input velocity. As explained, the input velocity for all simulations is set on $5\ m/s$ due to experience from practice. Nonetheless, for a large and small SOD also an input velocity of 3 and $7\ m/s$ is simulated with the $k-\varepsilon$ and $k-\omega SST$ model to check this dependency, see Table 9.

TABLE 9: MODELLING CONSIDERATIONS INPUT VELOCITY

SOD	$k-\varepsilon$	$k-\omega SST$
$4D$	3 m/s	3 m/s
	7 m/s	7 m/s
$10D$	3 m/s	3 m/s
	7 m/s	7 m/s

In left window of Figure 12 the normalized centreline velocity for different input velocities and $SODs$ of $4D$ and $10D$ is shown. The right panel shows the normalized radial velocity at a radial distance of $1D$ and $3D$, for an impinging jet with a $10D$ distance above the seabed along with different input velocities. It can indeed be seen, at least for the range tested that the velocity field is completely depended on the input velocity because the results from the simulations with a different input velocity overlap.

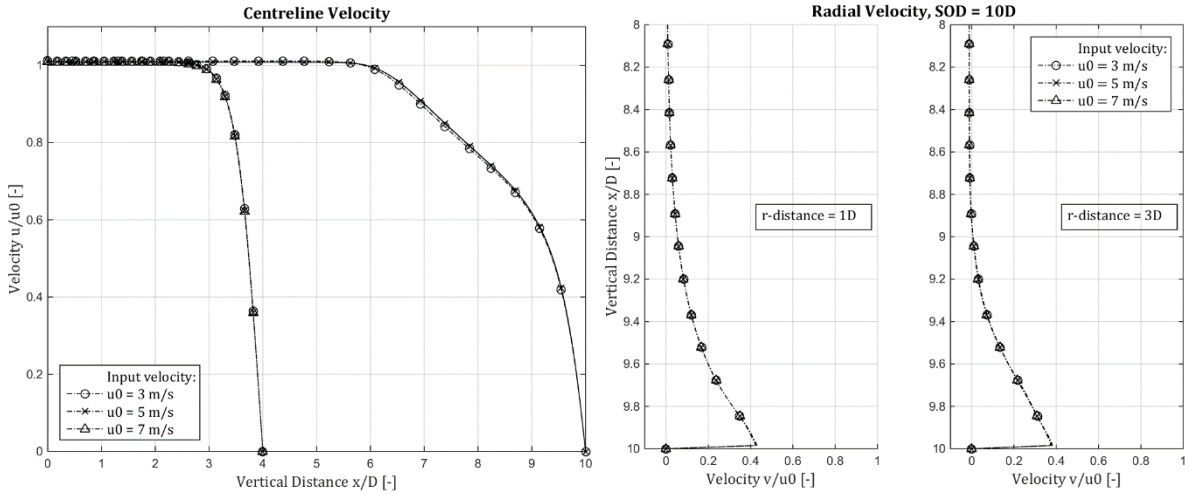

FIGURE 12: A) NORMALIZED CENTRELINE VELOCITY B) NORMALIZED RADIAL VELOCITY, $k-\omega SST$ TURBULENCE MODEL

For the illustrative purpose of Figure 12 use was made of the $k-\omega SST$ turbulence model, however the $k-\varepsilon$ model shows similar results. Furthermore, also the turbulence field of both the $k-\varepsilon$ and $k-\omega SST$ turbulence model show comparable results throughout the domain when the turbulence is normalized with the input velocity squared. However, indeed as expected and explained in section 3.2, the $k-\varepsilon$ turbulence model overall shows a higher built up of turbulence near the seabed and at the stagnation point, see Figure 13.

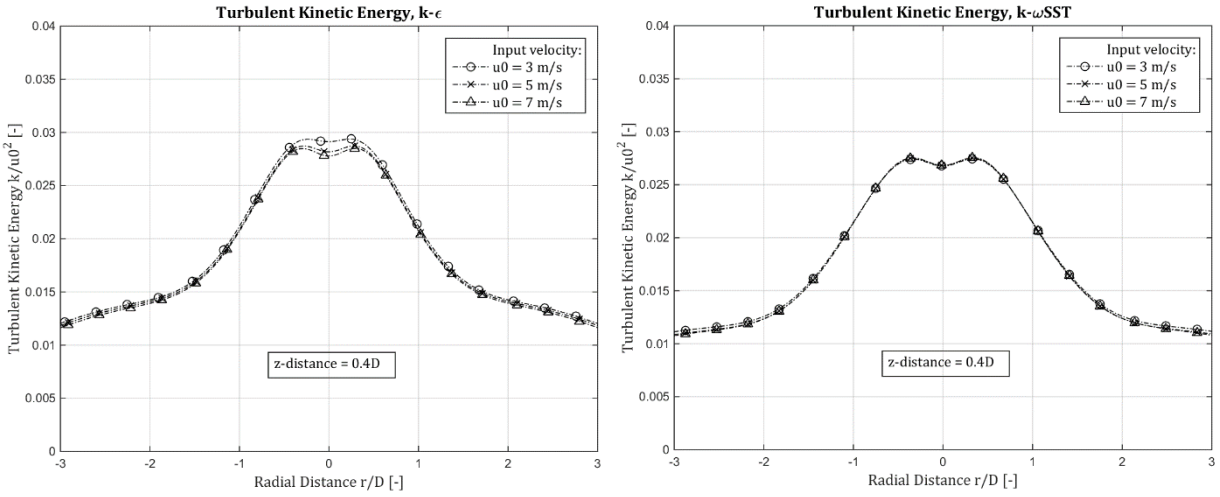

FIGURE 13: NORMALIZED TURBULENT KINETIC ENERGY, SOD = 10D

4.2.2 Boundary roughness

All empirical relations which describe the velocity field of a circular turbulent jet are based on experiments carried with an impinging jet on a smooth plate. Therefore the majority of the simulations executed as part of this research were carried out with a smooth boundary condition. In a real situation the seabed is however not a smooth plate. Hence, some simulations were run with a different boundary roughness to check the influence. The roughness used corresponds to sediment on the seabed with a nominal median diameter of $200\ \mu, 400\ \mu$ *and* $5\ mm$, see Table 10. This material roughly resembles fine sand, coarse sand and gravel respectively.

TABLE 10: MODELLING CONSIDERATIONS BOUNDARY ROUGHNESS

SOD	$k-\varepsilon$	$k-\omega SST$
$4D$	$200\ \mu m$	$200\ \mu m$
	$400\ \mu m$	$400\ \mu m$
	$5\ mm$	$5\ mm$
$7D$	$200\ \mu m$	$200\ \mu m$
	$400\ \mu m$	$400\ \mu m$
	$5\ mm$	$5\ mm$
$10D$	$200\ \mu m$	$200\ \mu m$
	$400\ \mu m$	$400\ \mu m$
	$5mm$	$5\ mm$

A certain roughness can be implemented in an OpenFOAM model by instead of using the *nutkWallFunction* using the *nutkRoughWallFunction* boundary condition. This wall function requires the input of the Nikuradse roughness as parameter. The value of k_s is usually taken as 1 to 3 times the nominal median diameter [SCHIERECK, 2001]. In this thesis two times the d_{n50} will be used and thus the k_s parameter becomes:

TABLE 11: NIKURADSE ROUGHNESS

d_{n50}	k_s
$200\ \mu$	0.0004
$400\ \mu$	0.0008
$5\ mm$	0.01

In the left window of Figure 14 the reduction of the maximal radial velocity for a SOD of $4D$ is shown. The right panel shows this reduction factor against the radial distance from the stagnation point for an impinging jet with a SOD of $10D$. The velocity reduction factor is defined as the maximum radial velocity at a certain dimensionless radial distance as result of simulations with a rough boundary divided by the maximum radial velocity at the same radial distance as result of simulations with the smooth boundary. Or in formula form:

$$F_v = \frac{v_{r,max}}{v_{s,max}} \tag{4.1}$$

With:

F_v	velocity reduction factor	$[-]$
$v_{r,max}$	maximum radial velocity with rough boundary	$[m/s]$
r_{L_1}	maximum radial velocity with smooth boundary	$[m/s]$

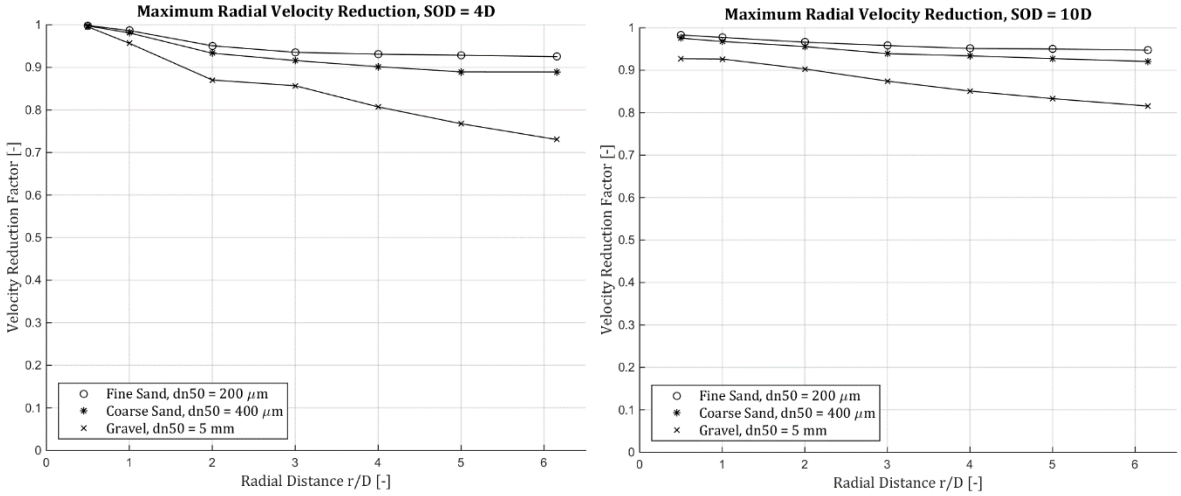

FIGURE 14: MAXIMUM RADIAL VELOCITY REDUCTION DUE TO BOUNDARY ROUGHNESS, $k-\varepsilon$ TURBULENCE MODEL

A clear pattern is noticeable in Figure 14. The maximum radial velocity is more reduced by both an increasing roughness and increasing radial distance. The SOD is of minor influence, although a larger distance gives rise to a lower value of the reduction factor. As can be seen in Table 10, these simulations were also carried out for the $k-\omega SST$ model whereby similar results were found.

4.3 Comparison

In this section a comparison between the different approaches for determining the flow field below the fallpipe is treated. The coming three figures display the centreline velocity, the vertical velocity and the radial velocity. The centreline velocity is shown for an impinging jet with a SOD of $4D$ and $10D$. For the illustrative purpose the vertical and radial velocity are shown for both two different $x-$ and $r-distances$ with a SOD of $10D$.

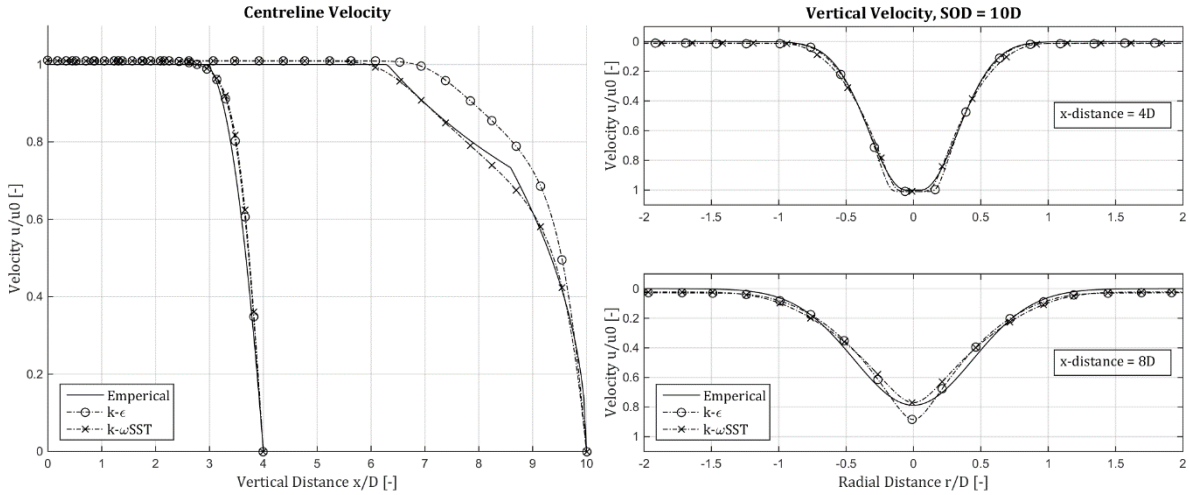

FIGURE 15: CENTRELINE AND VERTICAL VELOCITY FOR THE DIFFERENT APPROACHES

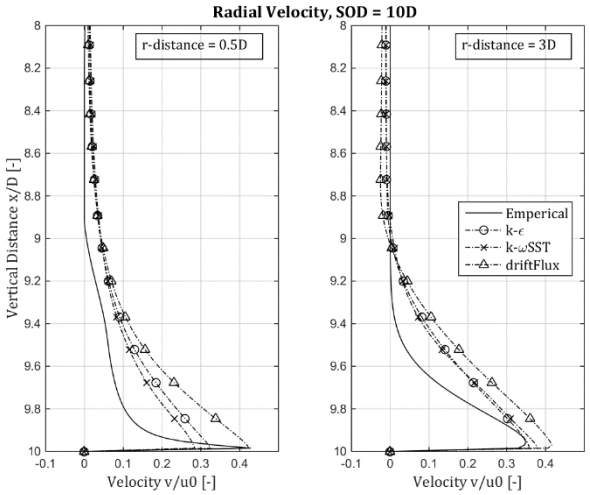

FIGURE 16: RADIAL VELOCITY FOR THE DIFFERENT APPROACHES

First of all, as explained, no empirical relations were found for the determination of the flow field for an impinging jet with a SOD in the transitional range, the range $5.5D \lesssim SOD \lesssim 8.3D$. It was therefore assumed that this flow field can be described with the empirical relations for large $SODs$ due the fact that the relations for a small SOD show a considerable deviation in the vertical velocity profile near the bed. This is because near the seabed, for a jet with a small SOD, the highest velocity is not found at the centreline anymore, yet this is still the case for a jet with large SOD, see Figure 8. As can be seen in Figure 17, this assumption is appropriate considering that with the numerical simulations the maximum vertical velocity near the seabed is indeed found at the centre of the jet for an impinging jet in the transitional range.

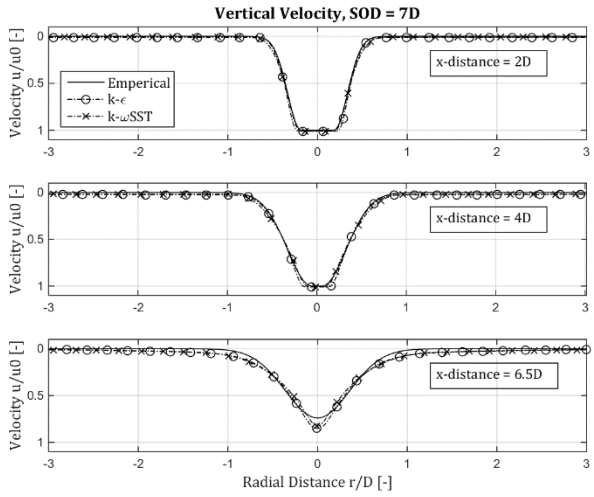

FIGURE 17: VERTICAL VELOCITY FOR THE DIFFERENT APPROACHES

Even for the simulations with a SOD of $5.5D$ this maximum is still found at the centreline, suggesting the classification of an impinging jet with small SOD is indeed below $5.5D$. Correspondingly, in the coming two sections the comparison between the different approaches for the remaining two classifications of the SOD will be treated.

4.3.1 Small stand-off distance

In the centreline velocity graph, Figure 15, it can be clearly seen that similar results are shown for the different methods when looking at a small SOD. Figure 18 also shows that the results of the spreading width of the jet matches. Besides this, as stated in the empirical relations for an impinging jet with a small SOD the maximum vertical velocity, after the ZFE, is not found at the centre of the jet. When looking at the flow field predictions conducted with the numerical simulations this same behaviour is noticeable, again see Figure 18.

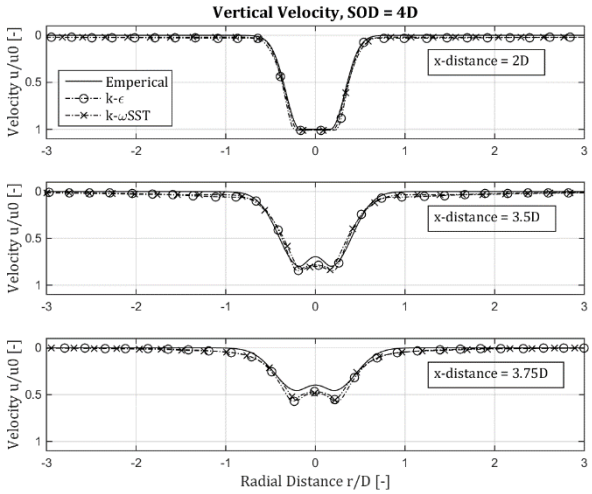

FIGURE 18: VERTICAL VELOCITY FOR THE DIFFERENT APPROACHES

The radial velocity in the wall jet region show high similarities for the different approaches including the spreading height above the bed. Nonetheless, the maximum radial velocity expressed by the empirical relation predicts a lower value in comparison with the numerical simulations. The radial velocity in the impinging jet region however, calculated with the empirical approach, shows largely different results. The spreading height above the seabed is less and the maximum radial velocity is calculated considerably larger.

Besides this, an influence of the density current, simulated by the *driftFlux* model, on the radial velocity in the impinging jet region is noticed. This difference is relative small compared to the $k-\omega SST$ model, however, the *driftFlux* model uses the same turbulence model as the $k-\varepsilon$ model and compared with this a higher difference is observed. On the contrary in the wall jet region, the increase in radial velocity is nearly diminished. The decrease in influence can be explained with the fact that the stones used in the *driftFlux* model are quite large. These large stones consequently have a large terminal settling velocity and thus the concentration in the layer above the bed decreases rapidly with radial distance. Therefore, with increasing radial distance, the radial jet velocity is increasingly similar with the radial velocity of a water jet.

It must again be noted that the *driftFlux* model is based on small particles and therefore only valid for mixtures whereby the particles are small. Nonetheless, simulations were carried out with the *driftFlux* model to get an idea of the influence of the mixture on the velocity profile.

4.3.2 Large stand-off distance

In contrary to the simulations with a small SOD clearly some differences between the different turbulence models can be seen. When looking at Figure 19 the $k-\omega SST$ model predicts roughly the same potential core length as the empirical expressions were as the $k-\varepsilon$ model predicts a longer potential core length.

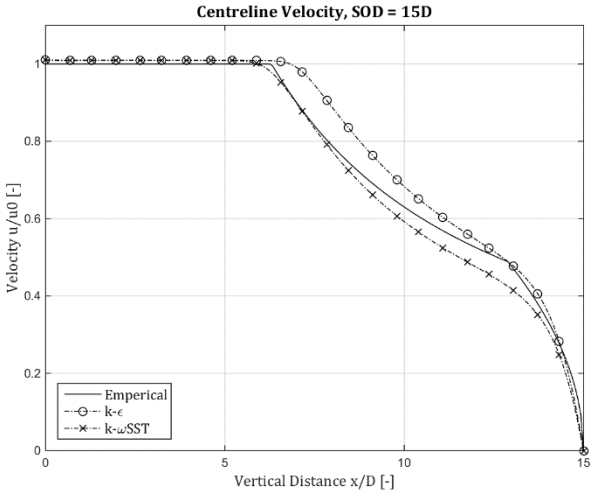

FIGURE 19: CENTRELINE VELOCITY FOR THE DIFFERENT APPROACHES

After the potential core, considering even larger $SODs$ than the $15D$ used for the illustrative purpose in this section, both the $k-\varepsilon$ and $k-\omega SST$ model show a similar dissipation of the centreline velocity in the ZEF. Although due to the different potential core length the centreline velocity is deviating from one another. The empirical approach on the contrary, shows less dissipation of the centreline velocity. Despite the difference in centreline velocity the spreading width of the different approaches is almost identical. In addition, when approaching the bed the vertical velocity field defined with the different approaches also agree with each other once again.

The velocities in the radial field show roughly the same behaviour and differences between the approaches as in section 4.3.1. The spreading height in the impinging jet region is still predicted lower with the empirical approach as compared with the numerical simulations. In this region also a larger maximum velocity is calculated with the empirical formulas. In the wall jet region the velocity fields roughly agree with one another again.

The influence of the density current simulated with the *driftFlux* model showed to be relatively small for a small SOD. This influence is considerably larger in the impinging jet region for a jet with a large distance to the seabed. Just as explained in section 4.3.1, in the wall jet region this difference in radial velocity decreases with increasing radial distance.

For more graphical results of the comparison between the different approaches, one is referred to Appendix E.1.

4.4 Concluding Remarks

First of all, as can be seen in Table 6 the empirical approach as well as the numerical simulations were carried out for a range of $SODs$. The remarks on the differences and/or similarities of the flow fields in the previous two sections are based on all these modelling considerations. Comparable results were found for intermediate $SODs$ and a trend with increasing SOD was noticed. Therefore, in Appendix E only the full results of an impinging jet with a small, transitional and a large SOD are shown.

Secondly the empirical relations for determining the flow field are based on multiple experiments carried out for circular turbulent jets with different $SODs$. Whether a fluid flow is turbulent depends on the Reynolds number. The Reynolds number used in the experiments was high, including experiments with $Re \approx 5 * 10^4$. In this thesis however, the Reynolds number of the jet caused by the closed fallpipe system is approximately $Re \approx 2.3 * 10^6$. This being said, the flow field calculated with the empirical expressions, closed with interpolations, show generally similar results as the flow field determined with the numerical simulation. Although the deviating order of Reynolds number it is adopted that it is possible to describe the flow field with the empirical relations, with the acknowledgement that a more fitting description for the radial velocity in the impinging jet region needs to be found.

As last, both the empirical relations as well as the numerical simulations give a zero velocity at the stagnation point due to the steady state approximation. For the time averaged values this is approximately true. In a real life situation this stagnation point is however not at a fixed location but alternating between sides of the centre of the jet, or better said, the real life situation is not a steady state but a time dependent situation.

5

Prediction of Settling Stone Path

In this chapter the trajectory of single stone below a closed fall pipe system will be treated. For each of the simulation and modelling considerations a bin of 1000 stones will be used. A single stone will be tracked from the starting location until it reaches the seabed. With the trajectory of the stones, the displacement and therefore the spreading of rock below a fallpipe can be determined. To determine the trajectory of a stone use is made of an iterative process whereby the equations of motion are solved for each time step. Figure 20 illustrates the calculation method used in this model. The starting location of the stone is denoted as L_1 and the used coordinate system is shown. With this model the influence of the turbulence, SOD, stone diameter or grading, hindered settling and jet velocity is researched.

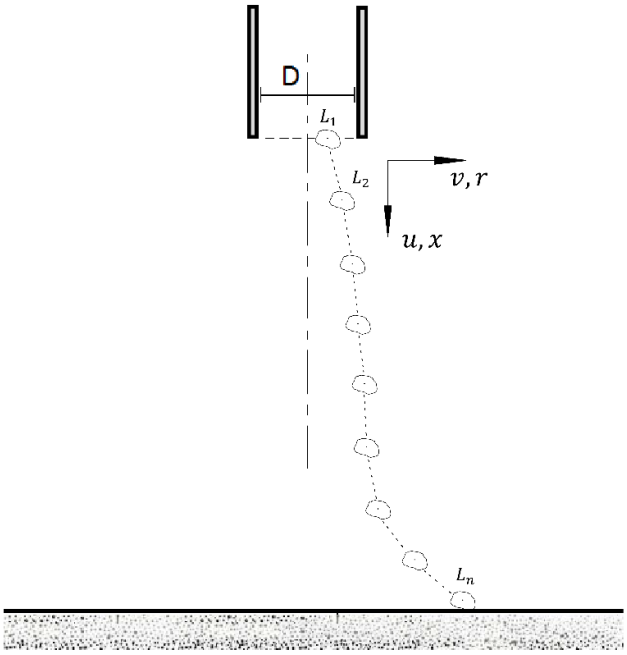

FIGURE 20: STONE LOCATION AND USED COORDINATE SYSTEM

To determine the trajectory of a single stone a set of input parameters is needed. The input used in this model are the starting location, the jet velocity field and stone properties & velocity. The iterative process of the model starts at the moment a stone exits the orifice of the fallpipe. The horizontal starting location in $x - direction$ is at the end of the fallpipe. The radial starting location of the stone, in $r - direction$, is of course bounded by the pipe diameter from which it exits. In the model it is possible to set a fixed radial starting location or to choose a distribution over the pipe diameter, such as a uniform distribution or a bounded "normal" distribution. The next input parameter is the velocity field of a circular turbulent jet below the fallpipe. In Figure 21 an example of such a velocity field is shown. For the illustrative purposes use is made of the velocity field below a fallpipe with a SOD of $15D$. As mentioned, within the domain of all numerical simulations a part of the fallpipe with the length of $2D$ is modelled, therefore the $x - position$ starts at $1.3\ m$.

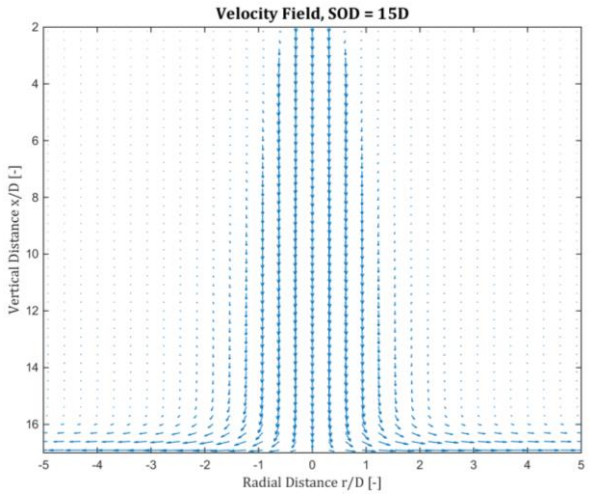

FIGURE 21: VELOCITY FIELD, $k - \varepsilon$ TURBULENCE MODEL

In this trajectory model a single stone has the density of $2650\ kg/m^3$ and the density of water is set on $1025\ kg/m^3$. As this thesis is part of research in the offshore rock placement operations use is primarily made of the grading mainly used in the offshore industry. These different requirements for rock grading are set by [STATOIL TR1370, 2009], see Table 1, and are intended for subsea rock installation. The main grading used is the $1 - 5\ inch$ class.

To determine the input velocity, the drag coefficient of a single stones needs to be derived. For this purpose equation (2.21) will be used. With the drag coefficient determined for a certain stone size and shape, the terminal settling velocity is known. The initial horizontal velocity of a single stone is set on zero. The initial vertical velocity is defined as the jet velocity plus the terminal settling velocity, or both, horizontal and vertical, velocities in formal form:

$$v_s = 0 \tag{5.1}$$

$$u_s = u_f + u_e \tag{5.2}$$

With:	u_s	stone velocity	$[m/s]$
	u_f	fluid velocity	$[m/s]$

Table 12 is an overview of the different standard input parameters needed for the two different approaches.

TABLE 12: POSSIBLE INPUT PARAMETERS FOR THE STONE TRACKER

Parameter	Empirical analyses	CFD analyses
Starting Location, L_1	Fixed value or distribution	Fixed value or distribution
Velocity field	Empirical relations	OpenFOAM output
Density of rock, ρ_s	$2650\ kg/m^3$	$2650\ kg/m^3$
Density of water, ρ_f	$1025\ kg/m^3$	$1025\ kg/m^3$
d_{n50} *or Grading*	Fixed value or grading	Fixed value or grading
Length-to-thickness ratio, l/d	Fixed value or distribution	Fixed value or distribution
Drag coefficient, C_D	Calculated by (2.21)	Calculated by (2.21)

5.1 Calculation Method of the Stone Trajectory Model

In Chapter 6 of Part II of this report a stone was simplified as a sphere and its equation of motion was already derived, see equation (2.20). However, this was a sphere falling through stagnant water but during its descend below the fallpipe the stone is no longer surrounded by a steady fluid and thus its velocity is not constant anymore. Therefore an additional term was introduced in the equation of motion: the added mass. The added mass is used to add extra inertia to the system because an accelerating body moves or deflects some volume of surrounding fluid as it moves through it. For simplicity this is modelled as some volume of fluid moving with the object [RAVELLI, 2012]:

$$M_a = \frac{1}{12}\pi\rho_f d^3 \tag{5.3}$$

With: M_a added mass $[kg]$

Therefore the new equation of motion of a sphere in the jet velocity field becomes:

$$(M + M_a)a_v = F_D + F_b + F_z \tag{5.4}$$

When substituting the corresponding forces derived in Chapter 6 of Part II in equation (5.4) the two differential equations for the stone velocity in horizontal and vertical direction become:

$$(M + M_a)\frac{du_s}{dt} = \frac{1}{8}\pi d^2 C_D \rho_f |\vec{u}|(\overline{u_f} - u_s) + \frac{1}{6}\pi d^3(\rho_s - \rho_f)g \tag{5.5}$$

$$(M + M_a)\frac{dv_s}{dt} = \frac{1}{8}\pi d^2 C_D \rho_f |\vec{u}|(\overline{v_f} - v_s) \tag{5.6}$$

With: ρ_s density of rock $[kg/m^3]$

ρ_f density of water $[kg/m^3]$

Whereby $\vec{u}$ is defined as:

$$\vec{u} = \sqrt{\left(u_f - u_s\right)^2 + \left(v_f - v_s\right)^2} \tag{5.7}$$

Give notice to $\overline{u_f}$ and $\overline{v_f}$, these velocities are the mean part of the horizontal and vertical velocities as expressed in the velocity field below a fallpipe.

5.1.1 Discretization of the differential equations

Both equation (5.5) and (5.6) can be discretized to get the horizontal and vertical velocity of the stone at the next time step. In the equation for the radial velocity both the gravity and buoyancy are not present. Besides this, also the lift force was neglected as part of the equations of motion. This was done because the determination of the lift coefficient for a stone is rather difficult and in literature no substantiated relations were found. Furthermore, the direction of the force depends, among others, on the shape of a stone. Due to the fact stones have a highly irregular shape also the direction of the force is rather difficult to determine. It has therefore been decided to neglect the lift force and let the horizontal displacement be only a result of the drag force and flow field. The coming two equations give the discretized formula to determine the horizontal and vertical velocity of the stone at the next time step.

$$u_s^{n+1} = \left(\frac{1}{8} A_s C_D \rho_f \left|\vec{u}^n\right| \left(u_f^n - u_s^n\right) + V\left(\rho_s - \rho_f\right) g\right) * \frac{\Delta t}{(M + M_a)} + u_s^n \tag{5.8}$$

$$v_s^{n+1} = \left(\frac{1}{2} A_s C_D \rho_f \left|\vec{u}^n\right| \left(v_f^n - v_s^n\right)\right) * \frac{\Delta t}{(M + M_a)} + v_s^n \tag{5.9}$$

With:	n	current time step	$[-]$
	$n+1$	next time step	$[-]$
	Δt	time step	$[s]$

The new position of a stone, in $x-$ *and* $r-$ *direction*, for the next time step can be calculated by eq. (5.10) and (5.11).

$$x_s^{n+1} = x_s^n + u_s^{n+1} * \Delta t \tag{5.10}$$

$$r_s^{n+1} = r_s^n + v_s^{n+1} * \Delta t \tag{5.11}$$

5.1.2 Influence of the turbulence

The influence of turbulence is included with the use of the Discrete Random Walk (DRW) or "eddy lifetime" model, as described by [ANSYS, 2013]. In this model each eddy is characterized by:

- **A Gaussian distributed random velocity fluctuation,** u' *and* v'
- **A time scale:** the eddy lifetime or the eddy crossing time.

The idea of this model is to define a certain time scale whereby the turbulence has the same intensity and direction as can be seen by an eddy in a real situation. The turbulence is defined as a fluctuating velocity around the mean velocity. Hence, not only the mean part of the velocity but also the instantaneous value of the fluctuating velocity is taken into account, as noted in equation (5.12) and (5.13) for the $x\ and\ r-direction$ respectively.

$$u = \overline{u} + u' \tag{5.12}$$

$$v = \overline{v} + v' \tag{5.13}$$

With:			
	u	vertical mean velocity	$[m/s]$
	u'	vertical fluctuating velocity	$[m/s]$
	v	horizontal mean velocity	$[m/s]$
	v'	horizontal fluctuating velocity	$[m/s]$

By this the two new differential equations for the stone velocity in horizontal and vertical direction become:

$$(M + M_a)\frac{du_s}{dt} = \frac{1}{8}\pi d^2 C_D \rho_f |\vec{u}|\left((\overline{u_f} + u') - u_s\right) + \frac{1}{6}\pi d^3(\rho_s - \rho_f)g \tag{5.14}$$

$$(M + M_a)\frac{du_s}{dt} = \frac{1}{8}\pi d^2 C_D \rho_f |\vec{u}|\left((\overline{v_f} + v') - v_s\right) \tag{5.15}$$

The values of u' and v' that prevail during the lifetime of the turbulent eddy are sampled by assuming that they obey a normal probability distribution, so that [TRANG, 2013]:

$$u' = \zeta\sqrt{\overline{u'^2}} \tag{5.16}$$

$$v' = \zeta\sqrt{\overline{v'^2}} \tag{5.17}$$

With:			
	ζ	normal distributed random number	$[-]$

Now, when isotropy is assumed, the fluctuating components of the velocity can be defined as [ANSYS, 2013]:

$$u' = \zeta\sqrt{\frac{2k}{3}} \tag{5.18}$$

$$v' = \zeta\sqrt{\frac{2k}{3}} \tag{5.19}$$

Figure 22 shows a turbulent kinetic energy field as an output from OpenFOAM. For the graphical illustration the turbulent kinetic energy field of a numerical simulation with a fallpipe with a SOD of $15D$ is used.

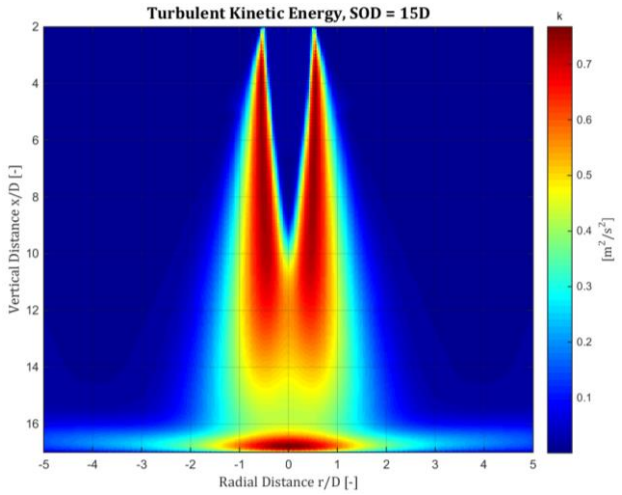

FIGURE 22: TURBULENT KINETIC ENERGY FIELD, $k-\varepsilon$ TURBULENCE MODEL

As said, the eddies in this DRW model are characterized by the eddy lifetime or eddy crossing time. The characteristic lifetime of the eddy is defined as a random variation about fluid Lagrangian integral time, [ANSYS, 2013]. For the $k-\varepsilon$ model, or variants hereof, such as the $k-\omega SST$ model, this time scale can be approximated as [TRANG, 2013]:

$$T_L = 0.30 * \frac{k}{\varepsilon} \tag{5.20}$$

With: T_L Lagrangian integral time $[s]$

Now, with this time scale, the characteristic lifetime of the eddy is defined as [TRANG, 2013]:

$$\tau_e = -T_L ln(r) \tag{5.21}$$

With: τ_e characteristic lifetime of the eddy $[s]$
r random number, $0 < r < 1$ $[-]$

It is chosen to calculate the lifetime of the eddy with a uniform random number, greater than zero and less than one, because this yields a more realistic description of the correlation function [ANSYS, 2013]. The other time scale whereby an eddy is characterized, the particle eddy crossing time, is defined as [CHOI AND TU, 2006]:

$$t_{cross} = -t_p ln\left[1 - \left(\frac{L_e}{t_p|u - u_p|}\right)\right] \tag{5.22}$$

With: t_{cross} particle eddy crossing time $[s]$
t_p particle relaxation time $[s]$
L_e eddy length scale $[m]$

The particle relaxation time and eddy length scale can be calculated with the following formula [CHOI AND TU, 2006]:

$$t_p = \frac{\rho_s * d^2}{18 * \rho_f * \nu} \tag{5.23}$$

$$L_e = C_\mu^{3/4} * \frac{k^{3/2}}{\varepsilon} \tag{5.24}$$

With: C_μ turbulence model constant $[-]$

The shorter lasting time scale is used in this model to determine the particle interaction time with the fluid eddy.

To recap, a stone is situated at a certain location in the flow and turbulence kinetic energy field below a fallpipe. The flow field determines the mean value of the velocities as given in equations (5.12) and (5.13). With the turbulence field and the normal distributed random number the fluctuating part of the velocities is determined. These velocities together are used in the equations of motion to determine the new location of the stone. The normal distributed random number picked at the certain location of the stone is kept constant for a certain time. This time is either the characteristic lifetime of the eddy or the particle eddy crossing time, depending on which one of the two is shorter. Due to ζ is kept constant, the fluctuating part of the velocities is only depended, during the certain characteristic time, on the turbulent kinetic energy as given in the turbulence field. After the characteristic time scale is passed, new normal distributed random numbers are picked and the process repeats itself.

Discretization

Again the, new, two differential equations for the stone velocity in horizontal and vertical direction, given by equation (5.14) and (5.15), can be discretized to determine the horizontal and vertical velocity of the stone at the next time step:

$$u_s^{n+1} = \left(\frac{1}{8} A_s C_D \rho_f |\vec{u}^n| \left((u_f^n + u'^n) - u_s^n\right) + V(\rho_s - \rho_f) g\right) * \frac{\Delta t}{(M + M_a)} + u_s^n \tag{5.25}$$

$$v_s^{n+1} = \left(\frac{1}{2} A_s C_D \rho_f |\vec{u}^n| \left((v_f^n + v'^n) - v_s^n\right)\right) * \frac{\Delta t}{(M + M_a)} + v_s^n \tag{5.26}$$

The new position of a stone, in $x-$ *and* $r-$ *direction*, for the next time step can still be calculated with equations (5.10) and (5.11).

For all simulations, with the stone trajectory model, the mean and standard deviation of the spreading have been determined, which will be used as a measure for the rock spreading below the fallpipe. The spreading is defined as the absolute deflection of a single stone. Additionally the mean and standard deviation of the displacement have been calculated whereby the displacement is defined as:

$$\Delta r_L = r_{L_n} - r_{L_1} \tag{5.27}$$

With:
- Δr_L displacement $[m]$
- r_{L_n} spreading $[m]$
- r_{L_1} starting location in r-direction $[m]$

In Figure 23 an example of the distribution of spreading and displacement as result of simulations with input from a numerical computation is shown. For the graphical illustration use was made of the velocity and turbulent kinetic energy field obtained from a computational fluid dynamics simulation with the use of the $k-\varepsilon$ turbulence model. The distance from the orifice of the fallpipe to the seabed is $10D$.

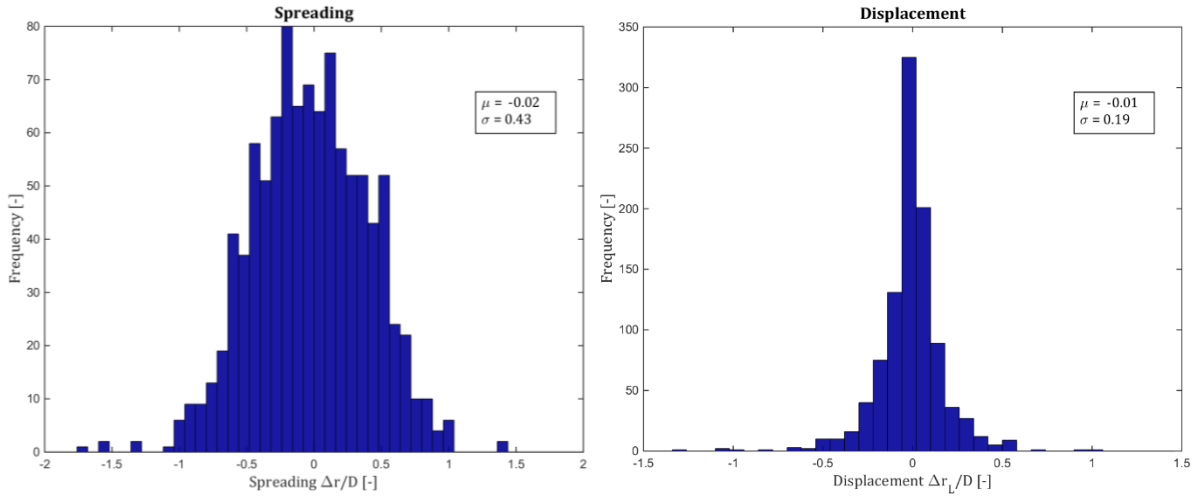

FIGURE 23: EXAMPLES OF SIMULATED ROCK SPREAD AND DISPLACEMENT, $k-\varepsilon$ TURBULENCE MODEL

5.2 Empirical Approach

To get an impression of the path of the settling stones the trajectory of a bin of 80 stones is shown in the figure below. The trajectory is determined with the empirical approach using the trajectory model without turbulence, given by equations (5.8) - (5.11). For this graphical illustration use is made of a fallpipe with a SOD of $10D$. The stones are released within the boundary of the fallpipe diameter and are distributed over this width conform the output velocity profile.

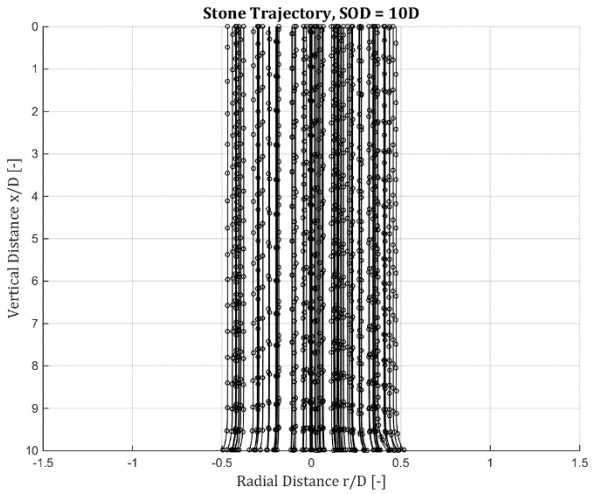

FIGURE 24: TRAJECTORY OF SINGLE STONES DETERMINED WITH THE EMPIRICAL APPROACH, NO TURBULENCE

The coming two figures show the standard deviation of the spreading and displacement of 1000 stones calculated with the preceding mentioned equations of motion, thus without turbulence. To investigate the influence of the distance to the seabed and diameter of a stone, a range of calculations have been performed.

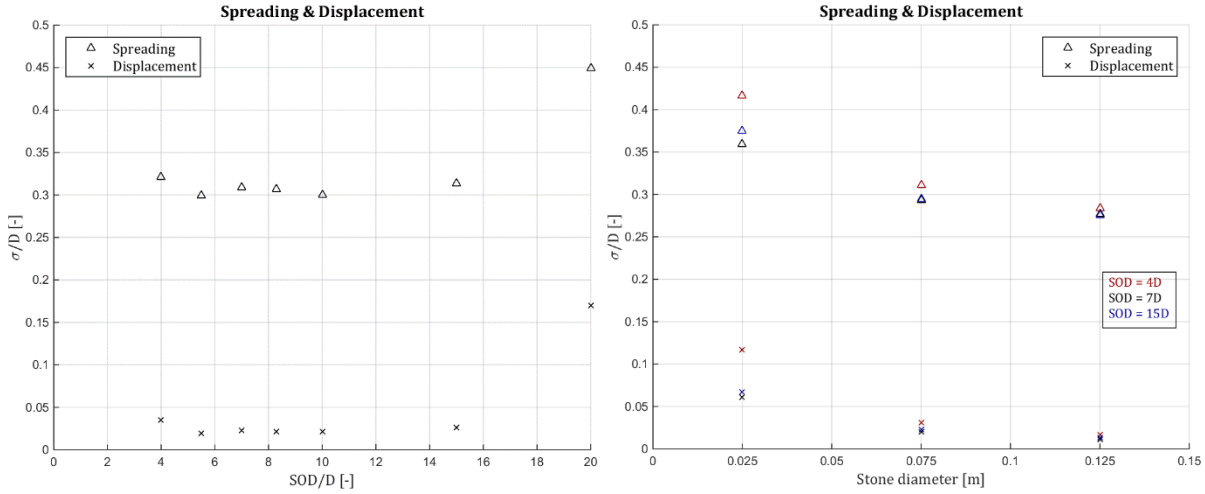

FIGURE 25: SPREADING AND DISPLACEMENT AS FUNCTION OF A) SOD AND B) STONE DIAMETER, EMPIRICAL APPROACH

As clearly can be seen in Figure 25 there is no significant displacement visible. The stones follow the flow field quite closely and due to the fact that the radial velocity field is bounded close to the seabed the small displacements can be explained, as also can be seen in Figure 24. Accordingly, the end location of a stone is mainly determined by the starting location at the orifice of the fallpipe. In a real situation the impinging jet is highly turbulent and greater displacements are expected. For this reason this method for determining the influence of different parameters on the displacement and spreading of stones below a fallpipe was quickly discarded.

In an effort to make the empirical approach for determining the trajectory of a stone viable and comparable to the CFD approach, turbulent kinetic energy was added to the system. The turbulent kinetic energy can be calculated with:

$$k = \frac{3}{2}(U * I)^2 \tag{5.28}$$

With: U mean flow velocity $= \sqrt{u^2 + v^2}$ $[m/s]$

I turbulence intensity $[-]$

The situation below the fallpipe is highly turbulent and a typical turbulence intensity for such cases is 10% [OPENFOAM, 2012]. Even though the turbulence intensity is dependent on the specific location within the impinging jet an overall intensity of 10% is assumed. To use the DRW model the characteristic time scale needs to be determined. The characteristic time scale is dependent on the turbulent dissipation rate which can be calculated with:

$$\varepsilon = C_\mu^{\frac{3}{4}} \frac{k^{\frac{3}{2}}}{l} \tag{5.29}$$

With: l turbulent length scale $[m]$

The turbulent length scale, although valid for fully developed pipe flow, can be estimated with [OPENCFD, 2010]:

$$l = 0.07D \tag{5.30}$$

Now, the path of a stone below the fallpipe can be determined with the trajectory model which includes turbulence, given by equations (5.25), (5.26) and (5.10), (5.11). Again to get an impression of the path of the settling stones the trajectory of a bin of 80 stones is shown in Figure 26. For this graphical illustration use is made of a fallpipe with a SOD of $10D$. The stones are released within the boundary of the fallpipe diameter and are distributed over this width conform the output velocity profile.

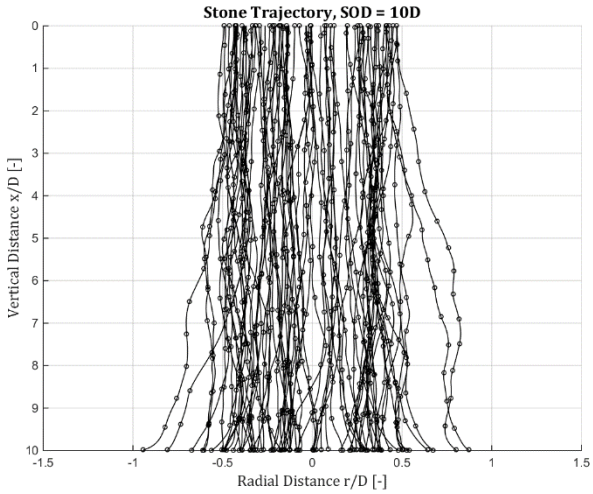

FIGURE 26: TRAJECTORY OF SINGLE STONES DETERMINED WITH THE EMPIRICAL APPROACH, TURBULENCE

5.3 Computational Fluid Dynamics Approach

In the previous section it was determined that the trajectory of a stone cannot be simulated conform reality with only using a velocity field for the highly turbulent cases which are part of this thesis. The CFD simulations however, do not only provide a velocity field but also a turbulent dissipation and kinetic energy field and therefore the trajectory model including turbulence can be used. For illustrative purpose, the path of a bin of 80 stones with the use of this model, given by equations (5.25), (5.26) and (5.10), (5.11), is given in the right panel of Figure 27.

To get an impression how a stone settles below the fallpipe when using the computational fluid dynamics approach without turbulence, given by equations (5.8) - (5.11), this is shown in the left panel of Figure 27. Again, clearly can be seen that there is no significant displacement visible. The stones follow the flow field quite closely and due to the fact that the radial velocity field is bounded close to the seabed the small displacements can be explained. Accordingly, the end location of a stone is mainly determined by the starting location at the orifice of the fallpipe.

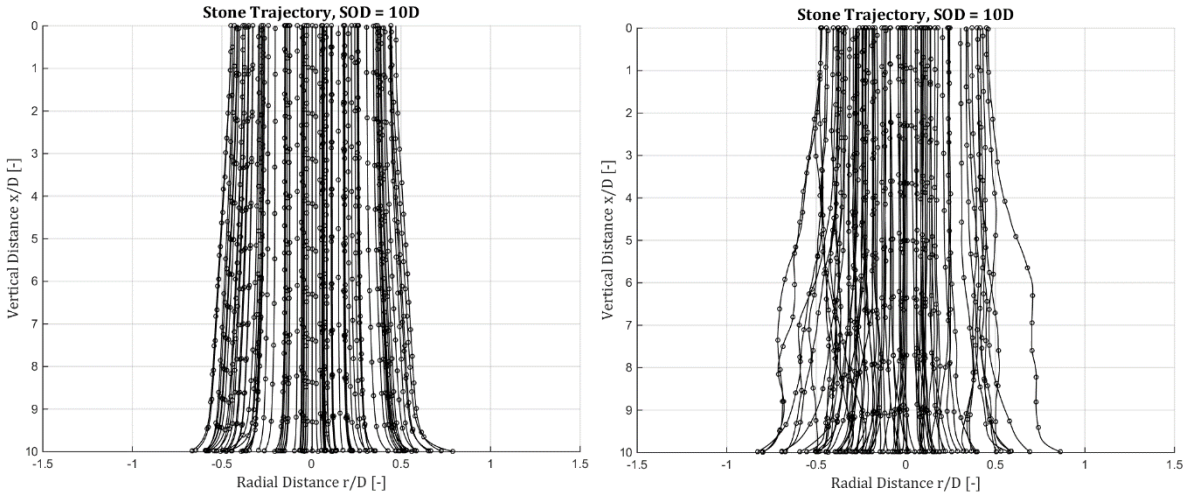

FIGURE 27: TRAJECTORY OF SINGLE STONES, $k-\varepsilon$ TURBULENCE MODEL A) NO TURBULENCE B) TURBULENCE

5.4 Comparison

The influence of the different variables on the spreading below the closed fallpipe system is researched and shown in this section. During the investigation of the different parameters all the other variables are kept constant on the standard value, given in Table 13.

TABLE 13: STANDARD INPUT PARAMETERS STONE TRAJECTORY MODELLING

Parameter	Input
Velocity	$5\ m/s$
Grading	$1-5\ inch$
Starting Location, r_{L_1}	distributed conform u_0 profile
Hindered settling	no

Furthermore, this section gives a comparison between the different approaches for determining the spreading. In section 5.2 and 5.3, however, it was quickly established that for determining the trajectory of a stone conform reality the flow field alone was inadequate. This can clearly be seen when looking at the right panel of Figure 27, CFD approach including turbulence, and comparing this to Figure 24, empirical approach without turbulence. Also in Figure 28 a distinct difference can be seen when turbulence is not included in the model. This figure shows the spreading and displacement for increasing SOD, for the empirical approach without the turbulence and the CFD approach with turbulence.

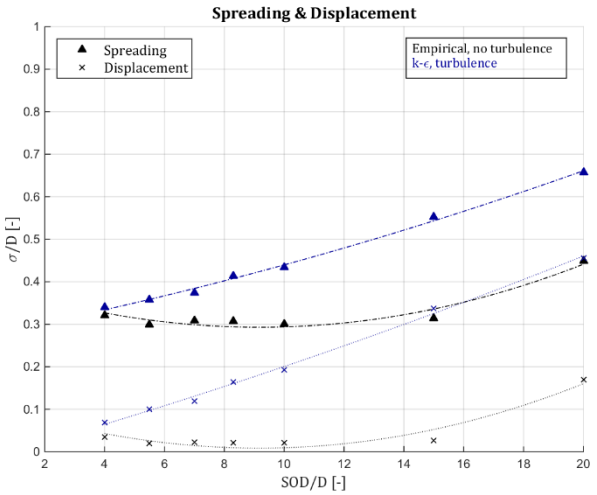

FIGURE 28: SPREADING AND DISPLACEMENT AS FUNCTION OF SOD

Consequently, in an effort for making a viable and sound comparison between the empirical approach and CFD approach, a turbulent kinetic energy was added to the empirical approach, see section 5.2. By doing this the trajectory and motion of a stone showed a similar behaviour as determined with the computational approach, see Figure 26 and right panel of Figure 27. Still, it must be noted that the turbulent kinetic energy was based on the mean flow velocity which is highest in the potential core of the jet. Accordingly, the highest turbulent kinetic energy is found in this region. The CFD simulations however show that the turbulent kinetic energy is very low in the potential core. By this, different results and behaviours of a settling stone were found between the empirical and CFD approach, especially for larger $SODs$. All the graphical illustrations in this section therefore do not show the findings with the empirical approach, for these results one is referred to Appendix E.2.

5.4.1 Influence of the stand-off distance

Just as for the different approaches and simulations for determining the flow field below a closed fallpipe system a range of distances to the seabed is investigated. The $SODs$ tested are the same as simulated for the circular turbulent jet and therefore covering the small, large and transitional SOD, see Table 14.

TABLE 14: MODELLING CONSIDERATIONS STAND-OFF DISTANCE

Empirical	*CFD*
$4D$	$4D$
$5.5D$	$5.5D$
$7D$	$7D$
$8.3D$	$8.3D$
$10D$	$10D$
$15D$	$15D$
$20D$	$20D$

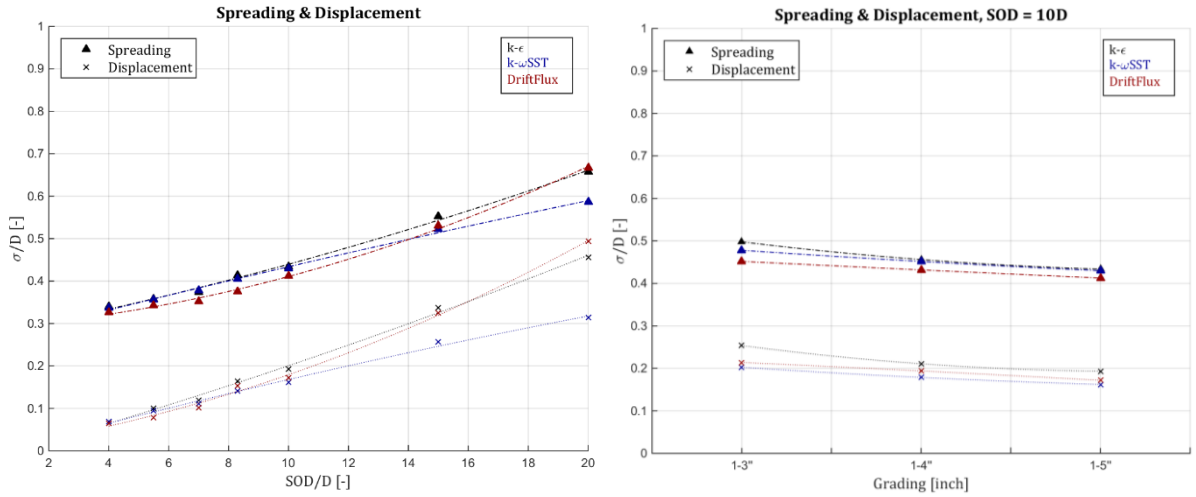

FIGURE 29: SPREADING AND DISPLACEMENT AS FUNCTION OF A) SOD AND B) GRADING

The left panel of Figure 29 displays that the spreading is roughly increasing linear with the stand-off distance for the $k-\varepsilon$ and $k-\omega SST$ model. The *driftFlux* model shows a faster increasing standard deviation of the spreading for increasing $SODs$. When looking at small $SODs$ all the turbulence models give approximately the same results, however with increasing SOD a deviation is noticeable. Two explanations can be given as reason for at first the similarities and later the deviations.

First, the fact that for small $SODs$ the impinging jet is still in the ZFE whereby, as mentioned, a low turbulent kinetic energy is situated in the potential core. Accordingly, the radial velocities, including the turbulent part are low. A second reason is that with small $SODs$ the stones still have a rather high settling velocity. For increasing $SODs$ this settling velocity decreases, which on its turn also give rise to a higher radial displacement due to turbulence.

5.4.2 Influence of the grading

The main grading used for offshore rock placement operations is the $1-5\,inch$ grading. Therefore this grading is kept constant when the influence of other parameters is researched. However, also $1-3$ and $1-4\,inch$ gradings are used in practice and the influence of these different gradings is tested, see Table 15.

TABLE 15: MODELLING CONSIDERATIONS GRADING

SOD	*Empirical*	*CFD*
$4D$	$1-3''$	$1-3''$
	$1-4''$	$1-4''$
$7D$	" "	" "
$10D$	" "	" "
$15D$	" "	" "

The right panel of Figure 29 shows that for a smaller grading the standard deviation of the spreading increases whereby the different turbulence models show a comparable trend. For this graphical illustration a distance to the seabed of $10D$ is used, however also different $SODs$ are tested. These tests show a similar decrease in spreading for a larger grading, with, again, a larger deviation for increasing $SODs$ between the different turbulence models.

5.4.3 Influence of the stone diameter

When rock is produced at a quarry a distribution of the stones is delivered and not a batch with one single diameter. Still in this thesis it is of interest how the spreading is influenced by different stone sizes. As stated in the grading Table 1, the maximum stone diameter has a size of $0.15\ m$ and the minimal diameter is equal to $0.016\ m$. These two stone sizes will be used as the upper and lower boundary of the sampling bin. All the modelling considerations that have been used to check the influence of the stone diameter can be seen in Table 16.

TABLE 16: MODELLING CONSIDERATIONS STONE DIAMETER

SOD	*Empirical*	*k-ε*
$4D$	$0.016, 0.04,$ $0.06, 0.075,$ $0.10, 0.125, 0.15\ m$	$0.016, 0.04,$ $0.06, 0.075,$ $0.10, 0.125, 0.15\ m$
$7D$	" "	" "
$10D$	" "	" "
$15D$	" "	" "

The left panel of Figure 30 shows this influence of the stone diameter, for the $k-\varepsilon$ model, on the spreading and displacement.

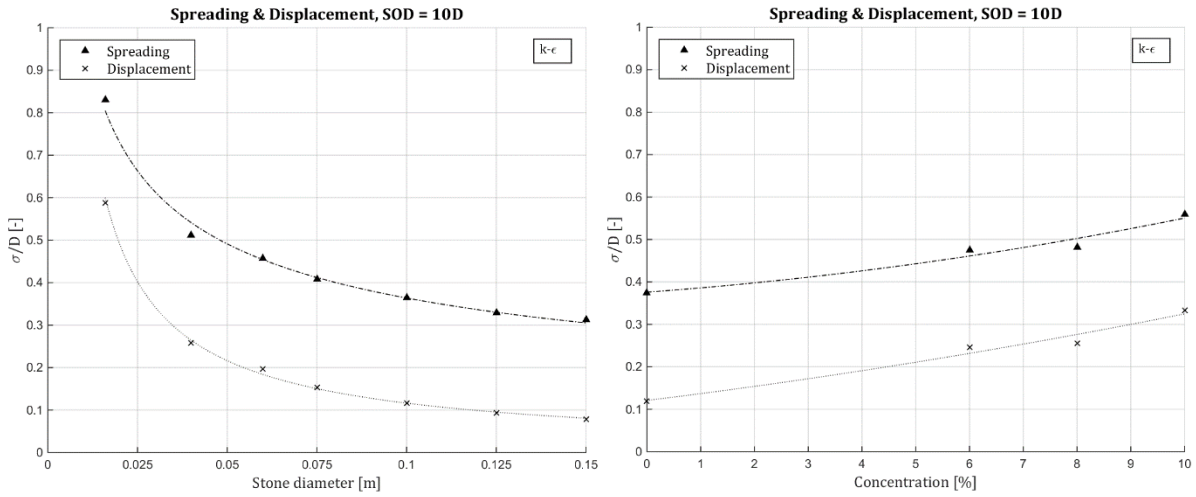

FIGURE 30: SPREADING AND DISPLACEMENT AS FUNCTION OF A) STONE DIAMETER AND B) CONCENTRATION, $k-\varepsilon$ MODEL

The effect of the stone size is easily noticed. The decrease in spreading for increasing stone size can be explained by the fact that large stones have a larger settling velocity and thereby a shorter settling time. Also, a smaller weight gives rise to a faster adaptation of the flow direction. Because the radial velocity was bounded quite close to the seabed possible not enough time was available for the heavier stones to adapt to the radial flow whereby a smaller displacement will be noticed. For different $SODs$ the same behaviour is noticed.

5.4.4 Influence of the hindered settling

When particles are continuously dumped in stagnant water the mutual influence of the particles decreases the settling velocity. This effect is called hindered settling and is caused by an increased drag coefficient, particle collision and a returning water flow. The increased drag coefficient causes a lower terminal settling velocity. To calculate this new terminal settling velocity of a single stone equation (2.25) is used whereby the concentration is needed as input parameter. During rock placement operations different productions are realised which causes a different concentration of stones in the impinging jet. From practical experience this concentration is roughly around 8%. Therefore this concentration have been tested for the $k-\varepsilon$ turbulence model, including a concentration of 6% and 10%, see Table 17. It seems that an increasing concentration causes a linear increasing spread as shown in the right panel of Figure 30. This behaviour is noticed for all $SODs$, although a larger derivative for larger $SODs$.

TABLE 17: MODELLING CONSIDERATIONS CONCENTRATION

SOD	*Empirical*	*k-ε*
$4D$	6 %	6 %
	8 %	8 %
	10 %	10 %
$7D$	" "	" "
$10D$	" "	" "
$15D$	" "	" "

5.4.5 Influence of the outflow velocity

As shown in Table 13 the standard input velocity is set on $5\,m/s$ due to experience from practice. Nonetheless, this exit velocity depends on several factors, such as the production, fallpipe length and number of water inlets and is thereby not constant. In section 4.2.1 it is however shown that the assumption of the empirical expressions that the flow field is completely dependent on the input velocity is confirmed by the numerical simulations. With the normalization of the flow and turbulence field this dependency gives the possibility to obtain the flow and turbulence field for a different velocity input without running new simulations. Therefore the influence of the input jet velocity on the spreading of the stones can be investigated for different cases, see Table 18.

TABLE 18: MODELLING CONSIDERATIONS INPUT VELOCITY

SOD	$k-\omega SST$
$4D$	$3\ m/s$
	$7\ m/s$
$7D$	" "
$10D$	$1\ m/s$
	$3\ m/s$
	$7\ m/s$
	$9\ m/s$
	$11\ m/s$
$15D$	$3\ m/s$
	$7\ m/s$

It was found that the jet velocity barely has an influence on the spreading for smaller $SODs$. For larger $SODs$ an increase in spreading is noticed with higher jet velocities, although the relative increase declines. This difference can be explained because for small $SODs$ the impinging jet is still in the ZFE and the stones will be mainly situated in the potential core. As mentioned, it was found that the turbulent kinetic energy in the potential core is rather small. For larger $SODs$, stones will also pass the other zones in an impinging jet whereby an increased turbulent kinetic energy is found for increasing jet velocities.

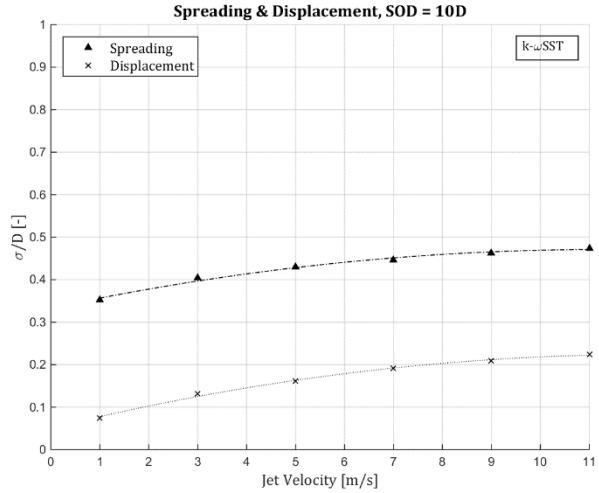

FIGURE 31: SPREADING AND DISPLACEMENT AS FUNCTION OF THE OUTFLOW JET VELOCITY

5.4.6 Influence of the release location

In all the simulations for determining the spreading below a fallpipe the stones have been released within the boundary of the pipe diameter and are distributed over this width conform the output velocity profile. This is done to simulate as realistic as possible. Nonetheless, it has been observed that the horizontal starting location has a large influence on the displacement. In Figure 32 the normalized horizontal starting locations versus the normalized displacement can be seen.

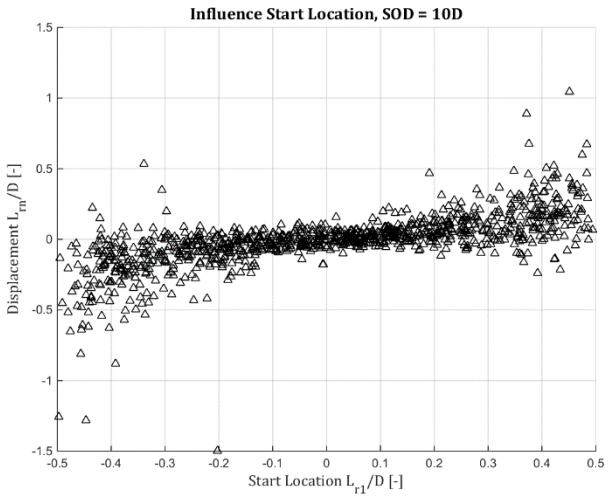

FIGURE 32: NORMALIZED STARTING LOCATION VS. DISPLACEMENT, $k-\varepsilon$ TURBULENCE MODEL

Due to higher vertical velocities and low turbulence in the potential core one would expect a low displacement when the starting location is near the centre of the jet. This is indeed predicted by the simulations. Roughly the same behaviour is seen for all $SODs$ with the acknowledgement that for smaller $SODs$ the data is more bounded to the zero displacement line.

All results predicting the influence of the variables on the spreading can be found in Appendix E.2.

5.5 Concluding Remarks

Chapter 4 showed that the flow fields calculated with the empirical approach were highly similar to the flow fields determined with the numerical simulations, adhering some deviations. Although the similar flow fields, in this chapter it was fast concluded that it is impossible to receive comparing results for the spreading below the fallpipe between the empirical and CFD approach when only taken into account the flow field. Accordingly, turbulent kinetic energy was added to the empirical approach however this also offered no solution. It is therefore concluded a proper turbulent kinetic energy field is needed for simulating a realistic trajectory of a settling stone due the fact that a highly turbulent impinging jet is under investigation in this thesis.

Still, it must be noted that it is possible to receive realistic results with the empirical approach because, as said, the flow fields of the empirical approach and those found by the numerical simulations were highly similar. This can subsequently be done by using the trajectory model with turbulence whereby the turbulent kinetic energy field is obtained with numerical simulations. Although this being a quite devious method because still numerical simulations have to be done and the velocity field obtained with these simulations can as easily be used.

This being said, although the different turbulence models showed some deviations in the flow field generally speaking, largely comparable results were found for the influence of the different parameters on the spreading and displacement of stones. However, not for all turbulence models a range of all variables have been tested because a general trend in the results was noticed. The spreading and displacement increases for an increasing `SOD` and release location and a decreasing stone diameter. It is expected that when all variables are tested for every turbulence model the same general trend is followed.

As last, it must be noted that for determining the trajectory of the stones the lift force was neglected as part of the equations of motion. This was done because the determination of the lift coefficient for a stone is rather difficult and in literature no substantiated relations were found. However, it is possible when the lift force was included larger displacements were found. Besides this, in reality several other effects that are not included in the trajectory model will play a role, such as the natural fall behaviour of a stone.

6

Assessment of Berm Formation Processes

This chapter will elaborate on the built up of a rock berm with a rock placement operation. The built up of a rock berm consists of two components in this research. The first is the increase of height due to the dumping of stones, explained in section 6.1, and the second is the degradation due to the stone transport by the turbulent jet, treated in section 6.2. By combining these two components the built up of a rock berm can be determined, which will be elaborated in 6.3.

6.1 Height Increase

The increase of height of the rock berm is a function of the production, trailing speed and spreading, or better said the probability density distribution below the fallpipe. In the previous chapter the distribution of the spreading was determined for a range of variables, for see also Figure 23. It was found that the different numerical simulation models show comparable results for the distribution of the spreading below the fallpipe. It was furthermore found that a proper turbulent kinetic energy field is needed to receive realistic results from the particle tracking model. Therefore the results given in this chapter regarding the height increase of the rock berm are based on the trajectory model with turbulence included, given by equations (5.25), (5.26). Figure 33 shows the basis for determining the height increase of the rock berm

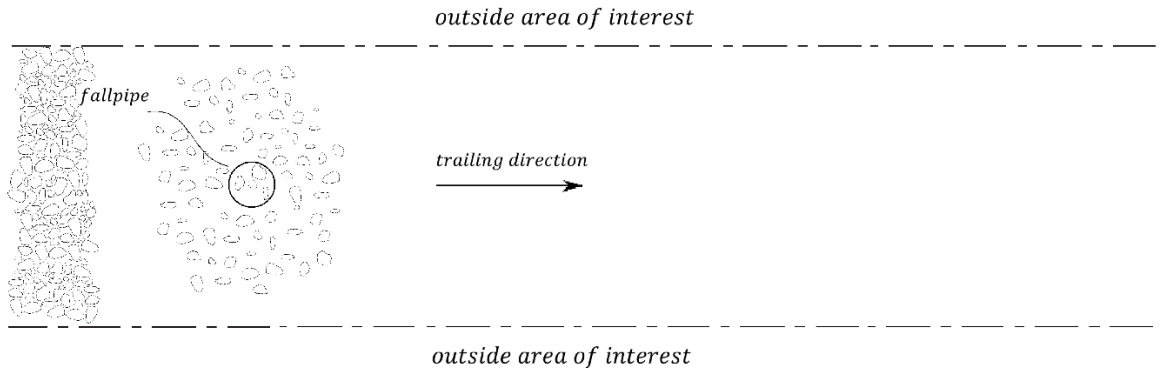

FIGURE 33: BASIS FOR DETERMINING THE HEIGHT INCREASE OF THE ROCK BERM

When dividing the distribution of spreading below the fallpipe by the number of released stones, or the number of simulated stones, the probability density curve is found. Due to the fact that, for the steady state approximation in this thesis, the impinging jet is assumed axisymmetric it is therefore also assumed that this probability density distribution is axisymmetric. Figure 34 displays such a 3-dimensional expended probability distribution.

For the graphical illustration the distribution of the spreading is taken from a simulation with the $k-\varepsilon$ turbulence model, a distance from the orifice of the fallpipe to the seabed of $10D$ and with the standard grading of $1-5\ inch$. As said, the two other numerical simulation models show comparable results when the same input parameters are chosen for the trajectory model.

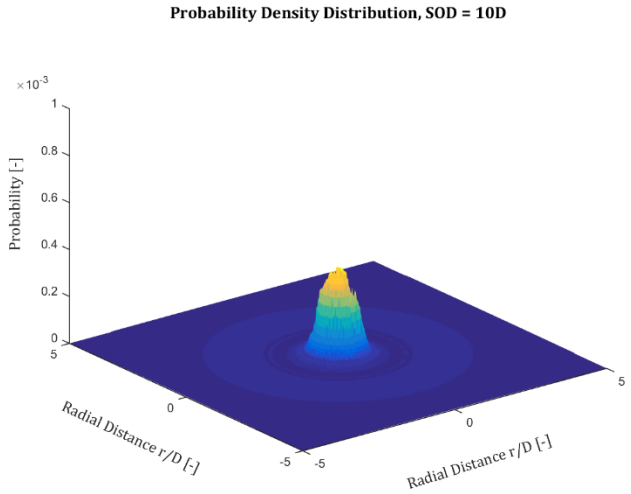

Figure 34: Probability density distribution of rock spreading, $k-\varepsilon$ model

To acquire the most realistic simulation of the rock berm shape the most realistic variables are used for determining the probability density distribution. The simulations are accordingly all performed with a rock grading of $1-5\ inch$. With a certain production the height increase of the rock berm can now be calculated with:

$$\Delta z_b = \left(\frac{1}{1-\epsilon}\sum P_i * D\right) * \Delta t \tag{6.1}$$

With:	Δz_b	bed level change	$[m]$
	ϵ	porosity = 0.4	$[-]$
	P_i	probability density	$[-]$
	D	production	$[m^3/s]$

Figure 35 shows such a height increase of a rock berm with a simulation time of 100 seconds. With a trailing speed of $0.1\ m/s$ the total length of the berm is 10 m. For this graphical illustration a production of $1600\ t/h$ is used and the probability density distribution from Figure 34 is taken.

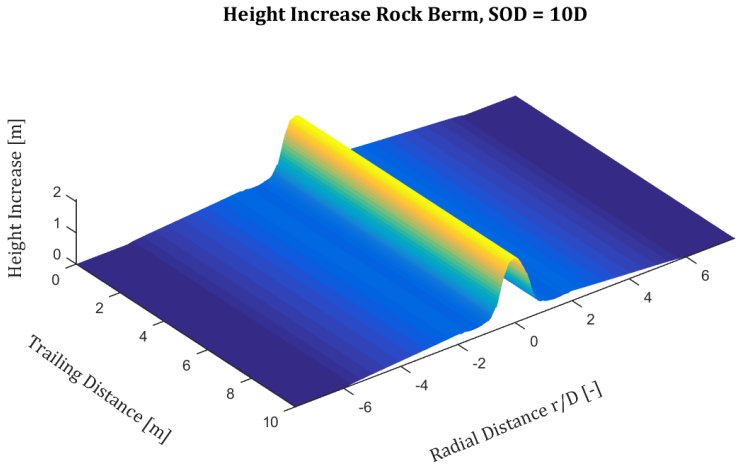

FIGURE 35: HEIGHT INCREASE OF A ROCK BERM

In Figure 36 the height increase of a rock berm by a fallpipe vessel with a trailing speed of $0.1\,m/s$ is shown. The height increase is determined with equation (6.1) and therefore only the spreading below the fallpipe is taken into account. The height increase is shown for different production rates whereby the higher production rates correpsonds to higher outflow velocities, obtained with the method by Tideway for determining the output velocity, see Table 19.

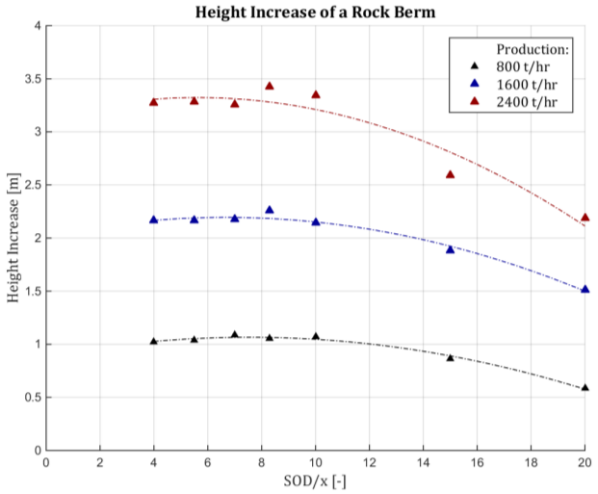

FIGURE 36: HEIGHT INCREASE OF A ROCK BERM

It seems that the height increase is rather constant for the SOD in the range $4D < SOD < 10D$. After this a lower height increase is noticable. Which ofcourse corresponds to the fact that for an increasing SOD an increasing spreading below the fallpipe is simulated, shown in the left panel of Figure 29

TABLE 19: OUTFLOW VELOCITY CORRESPONDING TO PRODUCTION RATE

Production	*Outflow velocity*
–	–
–	–
–	–

Angle of repose

Due to the fact that the spreading of the stones below the fallpipe was bounded rather close to the centre of the jet quite steep slopes were modelled for the determination of the berm shape. In reality this is not possible due to the fact that rock berm has a maximum angle of repose. This maximum angle of repose depends on the internal friction coefficient of the rock. In this thesis it is assumed that the maximum slope of the rock berm is 1:2.

6.2 Stone Transport

The modelling of the stone transport will be performed with the Hofland stability parameter and the corresponding entrainment formula by [HOAN, 2008]. The transport formula is expressed in the dimensionless entrainment parameter. For convenience the Hofland stability parameter and the entrainment functions are given here again.

$$\Psi_{Lm} = \frac{max\left[\langle \bar{u} + \alpha * \sqrt{k} \rangle_{Lm} \frac{L_m}{z}\right]^2}{\Delta * g * d_{n50}} \tag{6.2}$$

$$\Phi_E = 1.15 * 10^{-9} * \Psi_{Lm}^{4.53} \qquad for\ 1.3 < \Psi_{Lm} < 3.2 \tag{6.3}$$

With the use of the dimensionless entrainment parameter the entrainment rate can be calculated with [HOFLAND, 2005]:

$$E = \Phi_E * \sqrt{\Delta * g * d_{n50}} \tag{6.4}$$

Figure 37 shows the basis of this model for determining the stone transport as part of the berm built-up. With u_x given as the velocity component of the radial velocity perpendicular to the trailing direction.

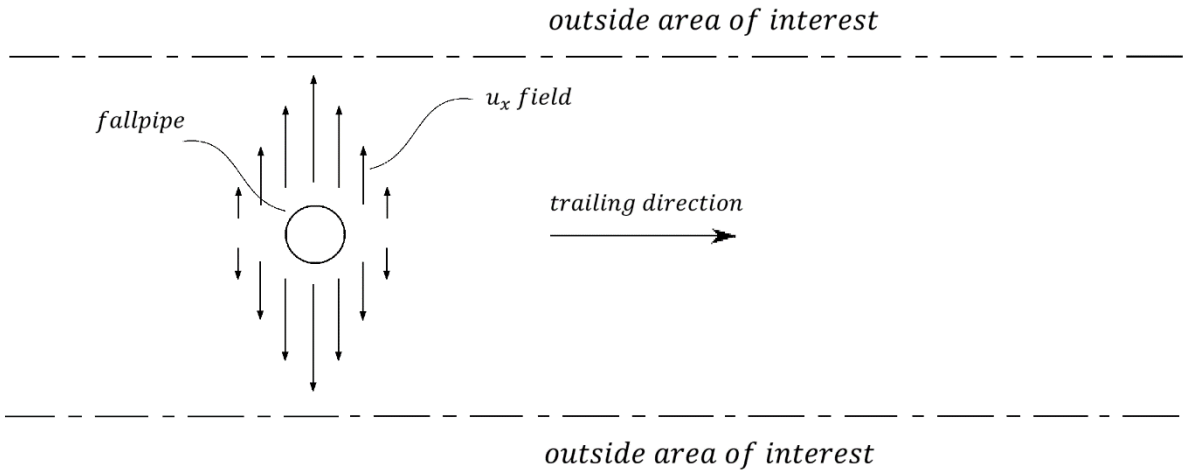

FIGURE 37: BASIS FOR DETERMINING THE STONE TRANSPORT

Now, imagine that the seabed over which the fallpipe vessel is trailing already consists of the distribution of stones used by the said vessel. This is the main assumption, in this research, for determining the bed degradation by an impinging jet. Besides this, several other assumptions have been made.

It can be seen from equation (6.2) that a certain water depth is required for the calculation of the stability parameter. This formula was based on open channel flow whereby a clear water depth can be derived. In this thesis however an impinging jet at great water depths is researched. When taking the total water column into account the stability parameter would become very small and thus this will not be conform reality. Accordingly, a certain water depth needs to be defined and because a clear radial velocity spreading height can be seen, as shown in Figure 11, this height will be used as water depth.

The entrainment, which can be now determined with the stability parameter, is highly dependent on the stone diameter. When considering a rock placement operation the rock dumped has a certain grading instead of stones with a fixed diameter. In consequence it is not conform reality to only assume rock with a certain diameter because stones with a smaller diameter are transported much faster compared to stones with a larger diameter. For this reason the stone transport is determined on the basis of the distribution of the rock grading. The distribution of the rock is conform the input grading, Table 1, and not conform the distribution at the seabed. This has been decided because the distribution of the stone diameter at the seabed highly depends on the spreading of the stones below the fallpipe.

One can imagine, and as shown in section 5.4, that the smaller stones have a higher possibility of settling further from the centre of the jet compared to larger stones. Also, when looking at the stone transport, even if a certain threshold of motion value for the stability parameter can be determined, then still this threshold would be exceeded at different radial distances from the centre for different stone sizes. By these two effects, the distribution of the stone sizes change in radial distance and therefore this distribution would be virtually impossible to determine.

Furthermore, when looking at the steady state radial velocity profile of the impinging jet the direction of the flow is completely radial. However, the impinging jet below the fallpipe is moving in the same direction as the vessel direction. Due to the moving jet, stones are transported both in the same as the opposite direction of the vessel. Thus looking at a fixed point at the trail of the vessel it is expected that an equilibrium of stone transport can be assumed due to the velocity component parallel of the vessels direction. Consequently, it is assumed that only the velocity component perpendicular to the trailing direction has an influence on the profile of the rock berm. Figure 38 shows such a normalized velocity component determined with the numerical simulations.

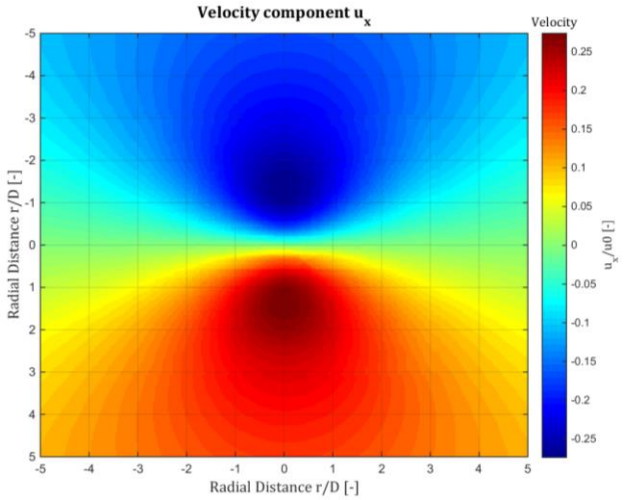

FIGURE 38: PERPENDICULAR VELOCITY COMPONENT BELOW THE FALLPIPE

To summarize the assumptions:

- **Water depth:** The water depth needed in equation (6.2) is taken as the spreading height of the radial velocity field which can be clearly seen in Figure 11.
- **Stone diameter:** For a rock placement operation not rock with a single diameter is used. For determining the stability parameter the distribution of stone diameters is used, given in Table 1. With the probability of each stone size within this distribution the total stability parameter is determined as the sum of each individual stability parameter value.
- **Velocity:** Only the velocity component perpendicular to the trailing direction of the fallpipe vessel is assumed to contribute to the bed degradation.
- **Deposition rate:** The deposition rate is expected to be very small within the area of interest and is therefore neglected. This means that entrained stones some were outside the area of interest will settle causing a bed height increase.

Bearing these assumptions in mind the stability parameter and therefore the corresponding entrainment parameter can be calculated, see Figure 39.

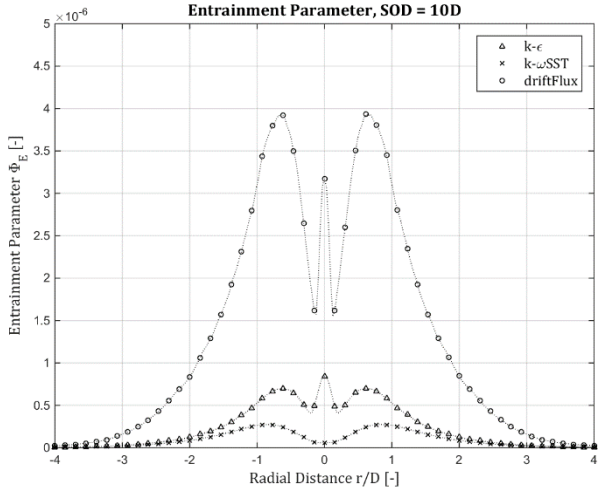

FIGURE 39: ENTRAINMENT PARAMETER FOR DIFFERENT TURBULENCE MODELS AT $r = 0$

As clearly can be seen in Figure 39, the *driftFlux* model shows the highest stone transport. In this research the main research object is to determine the possible occurrence of a jetted profile berm. Accordingly, the simulations for determining the berm built-up in the coming section will be performed with the *driftFlux* model.

In Figure 40 the entrainment parameter at the centre of the jet for different production rates is shown. The entrainment parameter is the cumulative of the dimensionless entrainment rate for a fallpipe vessel with a trailing speed of $0.1\ m/s$.

Author's note: This information is confidential.

FIGURE 40: ENTRAINMENT RATE AT THE CENTRE OF THE JET

Now, with the stability parameter and the corresponding entrainment parameter it is of interest how to quantify the amount of damage [HOFLAND, 2005]. [HOFLAND, 2005] stated that the balance equation for sediment can be used. This equation, when rewritten with the entrainment rate of stones, becomes [HOFLAND, 2005]:

$$\frac{\partial z_b}{\partial t} = -\frac{1}{(1-\epsilon-c_b)}(E - D_r) \tag{6.5}$$

With:			
	z_b	bed level	$[m]$
	D_r	deposition rate	$[m/s]$
	c_b	concentration near bed	$[-]$

Due to the high hydraulic loads within the area of interest, the deposition rate at these locations are expected to be small. Therefore, the deposition rate will be neglected. It is furthermore assumed that the concentration near the bed is rather low due to the same fact that the hydraulic loads are high. Besides this, the settling velocity of the considered stones is also rather high and thus, when the hydraulic load is not high enough anymore, the stones will settle right away instead of staying into suspension.

By this, equation (6.5) can be rewritten with the entrainment rate of stones, and after discretization, becomes:

$$\Delta z_b = \left(-\frac{1}{1-\epsilon}\sum E_{di}\right) * \Delta t \tag{6.6}$$

With: Δz_b bed level change $[m]$

E_{di} distributed stone diameter entrainment rate $[m/s]$

In Chapter 4 it was, quite logically, determined that with a smaller SOD larger radial velocities were predicted. Also the turbulent kinetic energy follows this trend. However it was noticed during the simulations of the stone transport that the maximum entrainment rate for a stand-off distance between $4D$ and $10D$ was roughly the same, or better said, in the same order, see Figure 41. This figure shows the maximum dimensionless entrainment, thus not per se being at the centre of the jet. Again for different production rates whereby the outflow velocity is given by Table 19. Notice must be made to the logarithmic y-axis.

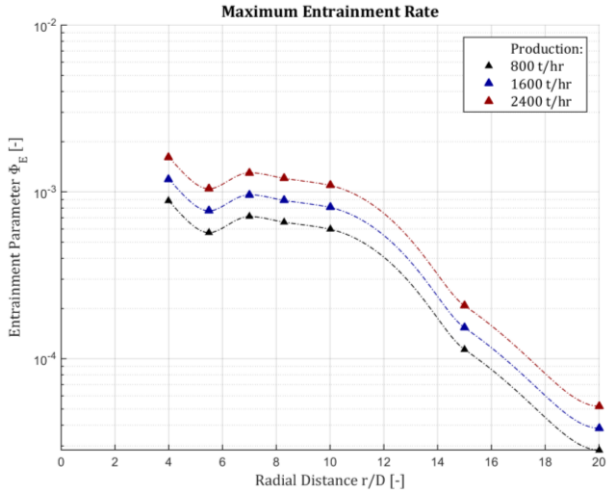

FIGURE 41: MAXIMUM ENTRAINMENT RATE

For larger $SODs$ the entrainment rate declined rapidly to orders lower. It was furthermore noticed during the simulations that for an input velocity of $5\ m/s$ the bed degradation was low, even for the smaller $SODs$. By this, simulations for determining the bed degradation with higher input velocities were run, see Figure 42.

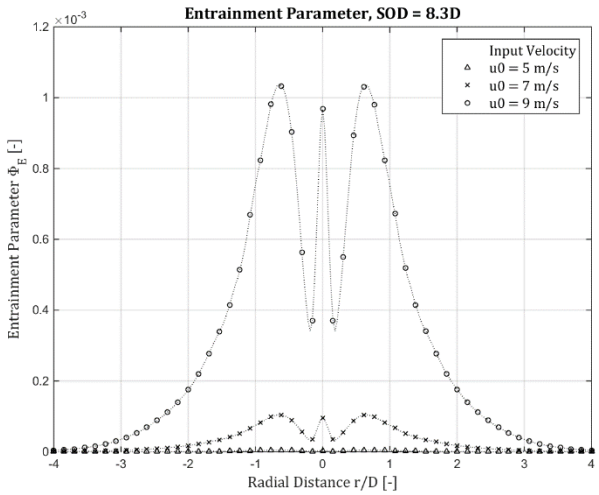

FIGURE 42: ENTRAINMENT RATE FOR DIFFERENT INPUT VELOCITIES

It was found that an input velocity of $9 - 10\,m/s$ was needed to receive significantly bed degradations.

6.3 Berm Built-up

Author's note: This information is confidential.

6.4 Concluding remarks

First of all, it must be stated that the expression used for the determination of the stone transport is based on flume experiments and 3D RANS modelling looking at open channel flow. Therefore they are based on long lasting hydraulic loads whereas the impinging jet caused by a rock placement operation is an incidental, short lasting and abrupt hydraulic load. Consequently, the relations were used outside the applicable range which was determined by [HOAN, 2008].

The main assumption for the stone transport model was that the bed already consists of the distribution of stones. It is concluded that a rather large, $9 - 10\, m/s$, outflow velocity is needed to obtain significant bed degradation by stone transport for these stones. Such high outflow velocities are not noticed in practice thus the irregular shaped berms cannot be explained by this fact. After this, an effort was made by adding sediment transport into the model. This was done because when looking at the spreading below the fallpipe the maximum displacement of stones is quite close to the centre of the jet. For a radial distance larger than the maximum displacement, of the stones, the velocity component perpendicular to the fallpipe vessel was still considerable when considering bed sediment transport.

7

Conclusions and Recommendations

This chapter provides the conclusions of this study. Besides that, recommendations for future research are made.

The aim of this thesis was to get a better understanding of the hydrodynamic processes below a closed fallpipe system. To assess the relevant processes of settling stones towards the seabed and to predict irregular berm shapes due to jet formation below a fallpipe. This research uses a threefold for reaching this objective: determine the possibility to use empirical relations, in comparison with CFD simulations, for the description of the velocity field; determine the spreading and displacement or rock; determine the built-up of the rock berm.

7.1 Conclusions

With regards to the threefold of this thesis, the conclusions are accordingly subdivided into three sections.

7.1.1 Velocity field

- No closing empirical relations were found for the radial velocity field. Consequently, for making a sound comparison between the different approaches, interpolation was used between the found relations to receive a complete flow field.
- In literature it was found that a distinction for a turbulent impinging jet can made in accordance to the distance to the bed. This is, an impinging jet with a small or a large SOD and a transitional region in between. Although this is probably the case when considering different situations, in this research it is concluded that the flow field of the transitional range behaves accordingly to large $SODs$.
- The length of the potential core predicted by the $k-\omega SST$ model is the same as stated by the empirical relations. The $k-\varepsilon$ turbulence model predicted a longer preservation of the potential core.
- Although different predictions were found for the length of the potential core between the different approaches the spreading width of the jet was highly similar for all cases.

- Both the turbulence models predicted the same dissipation of the centreline velocity after the potential core, the empirical relations however stated a slightly lower dissipation.
- When looking at the radial velocities the $k-\varepsilon$ and $k-\omega SST$ turbulence models predicted similar developments with a maximum deviation of the maximum radial velocity of around 15%. The empirical relations also showed comparing results, including the spreading height, for the wall jet region. In the impinging jet region however, the maximum radial velocity and the spreading height is expressed differently.
- The *driftFlux* model shows the influence of the "lock-exchange" effect for the radial velocity field, whereas this process is bounded quite close to the centreline. Nonetheless, in the impinging jet region the increase of the maximum radial velocity ranges from 15% to 30% for small to larger $SODs$ respectively.
- The empirical relations stated that the velocity field is completely dependent on the input velocity of the jet. The numerical simulations predicted indeed this behaviour for both the velocity field as well as the turbulent kinetic energy field. By this, it is concluded different input velocities can be tested by using the velocity and turbulent kinetic energy factor.

Overall it can be concluded that when looking at a purely circular turbulent water jet the empirical relations based on experiments describe the velocity field below this said jet well, when compared to the numerical predictions. The same behaviour and trend is noticed, although with the acknowledgement that a closing and fitting description of the radial velocities in the impinging jet region needs to be found.

7.1.2 Rock spreading

- It is impossible to receive comparable results on the spreading and displacement with the empirical and CFD approach without implementing a proper turbulent kinetic energy field in the empirical approach. Although an effort was made by adding a turbulence intensity to the empirical approach no realistic, or comparable to the CFD approach, results were found.
- The horizontal starting location of a stone has a big influence on the displacement. When a stone is released near the centre of the jet a significantly lower probability on a high displacement is noticed compared with a stone released at the edge of the fallpipe. This influence becomes less for larger $SODs$, although the same trend is followed.
- The three numerical models showed largely comparable results for the influence of the different parameters on the spreading and displacement of stones below the fallpipe.
- The spreading and displacement increases for and increasing SOD and release location and a decreasing stone diameter.

7.1.3 Berm built-up

Author's note: This information is confidential.

7.2 Recommendations

First of all, it was expected from literature that in the free jet region the $k-\varepsilon$ and $k-\omega SST$ models showed the same velocity profile in the free jet region. However, it is noticed from the numerical simulations that this is not the case. An explanation can be that for all the numerical simulations a piece of pipe was modelled to achieve a more realistic input profile. Although this piece of pipe obeys to the law of the wall, this could have an influence on the output of the models. Besides this, the ZFE is a quite sensitive region of the jet, this can also explain the difference in outcome. Nonetheless, a more in depth research is recommended to clarify these differences.

Besides this, the numerical simulations uses a steady state approximation and therefore give a zero velocity at the stagnation point. For the time averaged values this is approximately true. In real life this stagnation point is however not at a fixed location but alternating between sides of the centre of the jet, or better said, the real life situation is not a steady state but a time dependent situation. With further research it is possible to check the influence of this time dependency on the spreading and transport of stones with the use of a Large Eddy Simulation (LES) model.

Additionally, the spreading and displacement of stones below the fallpipe was calculated with the use of the velocity fields obtained from the numerical simulations, whereby the equations of motion were solved. In this model the lift force and natural fall behaviour of stones was however not included. These processes could cause a higher spreading and for further research it is therefore advised to compare the spreading and displacement of stones with experiments and/or more practical data. By doing this, the spreading below the fallpipe can be validated or made comparable by finding, for example, a fitting lift coefficient.

As last, the modelling of the stone transport uses the empirical expression of the stability parameter of [Hofland, 2005] with a fitted stone entrainment function by [Hoan, 2008]. These relations have been based on experiments and numerical simulations when looking at open channel flow. Therefore they are based on long lasting hydraulic loads whereas the impinging jet caused by a rock placement operation is and incidental, short lasting and abrupt hydraulic load. It is thus recommended more applicable and realistic transport relations need to be used for further research.

Appendix A: Numerical Modelling

In Appendix A.1 an introduction is given into numerical modelling and computational fluid dynamics. In the first part of this appendix a more in depth description of numerical modelling is stated, including possible disadvantages. The section A.2 describes the behaviour of the turbulence models near a wall boundary. This is especially of interest because of the importance of the flow velocities near the seabed caused by the impinging jet.

A.1 Introduction

Fluid flows are governed by partial differential equations (PDE's) which represent conservation of laws. CFD replaces such PDE systems by a set of algebraic equations. There is a large number of numerical techniques available to approximate the PDE's with the algebraic equations, often being of a repetitive computation. This is why this method is especially quite good suited with the use of a computer. Examples of methods to discretize these PDE's in space, time and/or combinations of the both are, for example, noted by [Zijlema, 2012] and [Vuik *et al.*, 2006]. The most important characteristics are the stability and order of accuracy. First of all, the numerical scheme has to be stable or in other words, the error has to stay small when time evolves. However, different numerical schemes often have different stability regions. Some numerical schemes are never stable, always stable or has to obey to a certain condition. This conditions is called the Courant-Friedrichs-Lewy (CFL) condition. For a one-dimensional case the CFL condition is defined as:

$$C = \frac{u * \Delta t}{\Delta x} \leq C_{max} \tag{A.1}$$

With:			
	C	Courant number	$[-]$
	Δt	time step	$[s]$
	Δx	length interval	$[m]$

Because quite an extensive elaboration is conducted in the reports by [Zijlema, 2012] and [Vuik *et al.*, 2006], including the different schemes, stability regions and order of accuracy, one is referred to this literature when a more in-depth knowledge is wanted and/or needed.

Besides the stability and order of accuracy, the results from numerical models are only an approximation of the real solution. By this end the discretization and the use of computers give rise to errors. The most well-known causes of errors when using numerical modelling are:

- **Round-off error:** When using numerical modelling the solution is not calculated exactly by the computer. That is, computers do not calculate with infinite precision but use floating point numbers with a fixed length. Therefore the real solution is rounded off at a set precision which means information is lost by this process.
- **Truncation error:** Some functions can be represented by an infinite Taylor series. However computers use a finite sum to approximate this infinite series. By doing this an error will arise, which is called the truncation error.

- **Measurement error:** In this thesis the numerical models solve the RANS equations. To do so the model needs, for example, boundary conditions, initial conditions and uses empirical coefficients. All these input parameters give arise to an error because measurements, assumptions or experiments had to be done to obtain the needed input.

A.2 Near wall treatment

Commonly the near-wall region is subdivided into three different areas, see also [BREDBERG, 2000]:

- **Viscous sub-layer,** $0 < y^+ < 5$**:** Viscous effects are dominant in this layer.
- **Buffer layer,** $5 < y^+ < 30$**:** The buffer layer is a transitional region between de viscous sub-layer and log-law layer and therefore both turbulent and viscous effects are of importance.
- **Log-law layer,** $30 < y^+ < 300$**:** The turbulent shear stresses are dominant in this layer and can be assumed constant.
- **Outer layer,** $y^+ > 300$**:** The layer after the near-wall region. The turbulent shear stresses are still dominant but cannot be considered constant anymore.

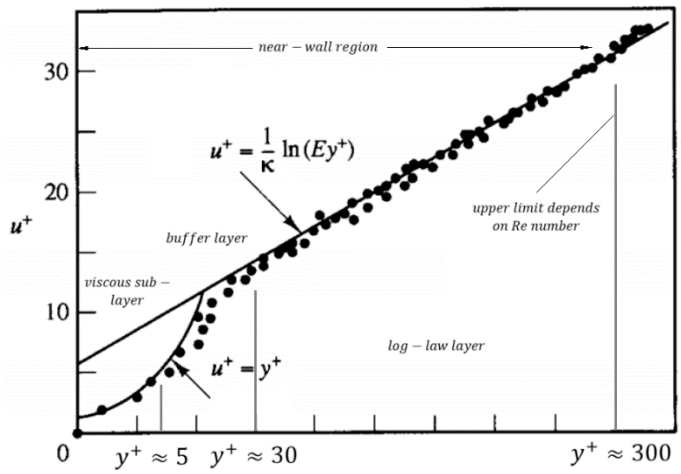

FIGURE 43: VELOCITY DISTRIBUTION NEAR A SOLID WALL (ADAPTED FROM [VERSTEEG AND MALALASEKERA, 1995]).

Traditionally, there are two approaches for modelling the near wall region [ANSYS, 2013]. The first method is to apply a very fine mesh close to the wall to resolve the flow. However, at higher Reynolds numbers the region under the wall influence diminishes. Hence, from an engineering point of view a method which uses 'wall functions' to bridge the viscosity affected region between the wall and fully turbulent region is instead introduced. This method allows the use of much coarser near-wall meshes resulting in shorter computation time and costs. To use wall functions, which are a set of semi-empirical formulas, the velocity has to obey the law of the wall and must therefore be in the log-law layer. The logarithmic relation of the velocity in the log-law layer is given as [STEENSTRA, 2014]:

$$u^+ = \frac{1}{\kappa} ln\, y^+ + B \tag{A.2}$$

With: u^+ dimensionless velocity [−]

y^+ wall coordinate [−]

	B	modelling constant	$[-]$

The values of kappa and B are universal constants valid for all turbulent flows past smooth walls at high Reynolds numbers [VERSTEEG AND MALALASEKERA, 1995]. OpenFOAM uses a value of 5.5 for smooth walls as the modelling constant B, with a certain wall roughness this modelling constant is decreased. This decrease, ΔB, is calculated with [STEENSTRA, 2014]:

$$\Delta B = \frac{1}{\kappa} ln\,(1 + C_s k_s^+) \tag{A.3}$$

With:	C_s	roughness constant	$[-]$
	k_s^+	dimensionless equivalent roughness ($k_s^+ = \frac{k_s u_\tau}{\upsilon}$)	$[-]$
	k_s	Nikuradse roughness	$[-]$

The wall coordinate in equation (A.2) can be calculated as follows [BREDBERG, 2000]:

$$y^+ = \frac{y u_\tau}{\nu} \tag{A.4}$$

With:	y	wall distance	$[m]$
	u_τ	friction velocity	$[m/s]$

Whereby the friction or shear velocity is defined as [OPENFOAM, 2012]:

$$u_\tau = \sqrt{\frac{\tau_w}{\rho}} \tag{A.5}$$

With:	τ_w	wall shear stress	$[kg/ms^2]$

The wall shear stress can be computed with [OPENFOAM, 2012]:

$$\tau_w = \frac{1}{2} C_f \rho u_{freestream}^2 \tag{A.6}$$

With:	C_f	skin friction coefficient	$[-]$

In literature a great deal of approximating formulas can be found for the skin friction coefficient and are all based on the Reynolds number, see for example [SCHLICHTING, 1979].

Appendix B: OpenFOAM

In Chapter 10 of the literature study a short introduction to the software package developed by OpenCFD, OpenFOAM, is given. In this appendix the files needed for an OpenFOAM computation are briefly discussed, for a more in depth description see [OpenFOAM, 2012]. The basic directory structure for an OpenFOAM case used in this thesis is shown in Figure 44.

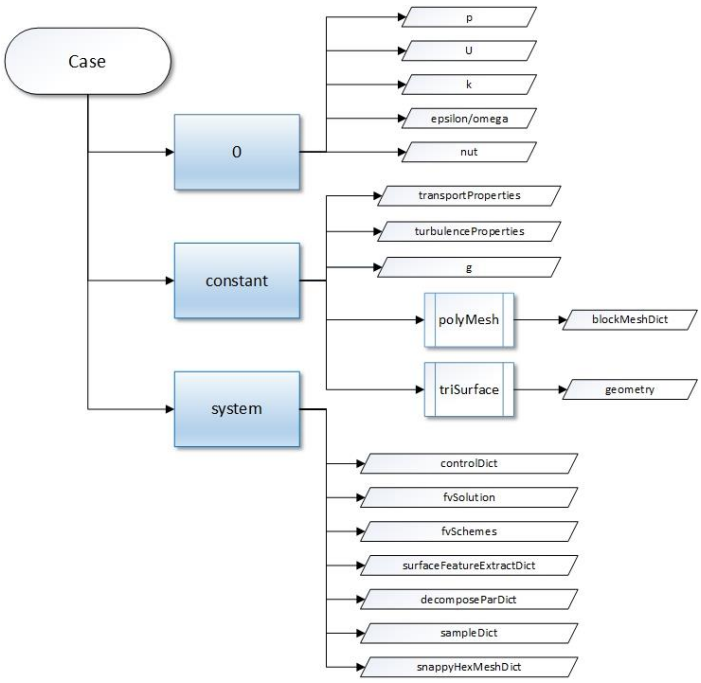

FIGURE 44: OPENFOAM CASE STRUCTURE

B.1 The '0' directory

The '0' directory contains different files stating the initial and boundary conditions for each of the governing variables used in a specific model. When using a RAS turbulence model as used in this thesis, for example the $k-\varepsilon$ turbulence model, these variables are the pressure, velocity, turbulent kinetic energy, turbulent dissipation rate and turbulent viscosity. The files inside the '0' directory are named as the variables itself, therefore in this case respectively: $p, U, k,$ *epsilon* and *nut*, were *nut* stands for ν_t. In the case of the $k-\omega SST$ model the turbulent dissipation rate, *epsilon*, is replaced by the specific turbulent dissipation rate, *omega*.

For the purpose of applying boundary conditions, a boundary is broken up into a set of patches. Therefore in each of the files inside the '0' directory a type of patch is specified for each boundary (see also Table 21):

- **Primitive type:** The base numerical patch condition assigned to a field variable on the patch.
- **Derived type:** A complex patch condition, derived from the primitive type, assigned to a field variable on the patch.

Examples of the patch types used in this thesis are shown in Table 20.

TABLE 20: PRIMITIVE AND DERIVED PATCH TYPES [OPENFOAM, 2012]

Patch type	Description	Data to specify
zeroGradient	Normal gradient of the variable is zero	-
fixedValue	Value of the variable is specified	value
inletOutlet	Switches **U** and **p** between *fixedValue* and	inletValue,
	zeroGradient depending on the direction of **U**	value
epsilonWallFunction	Wall function for $\boldsymbol{\varepsilon}$	value
omegaWallFunction	Wall function for $\boldsymbol{\omega}$	value
kqRWallFunction	Wall function for k, q and R	value
nutkWallFunction	Wall function for $\boldsymbol{\nu_t}$	value
nutkRoughWallFunction	Rough wall function for k	value
fixedFluxPressure	Boundary flux matched to the velocity condition	value

B.2 The 'constant' directory

As can be seen in Figure 44 the 'constant' directory contains multiple folders with information regarding the physical properties and one folder with a full description of the case mesh for the application concerned. In the *transportProperties* file information on the transport model constants is given, e.g. a Newtonian transport model and the value of the viscosity $\boldsymbol{\nu}$. In the file *turbulenceProperties* the method of turbulent closure is defined, either [OPENFOAM, 2012]:

- **Laminar:** Uses no turbulence models.
- **RASModel:** Uses Reynolds-averages stress (RAS) modelling.
- **LESModel:** Uses large-eddy simulation (LES) modelling.

Furthermore, the turbulence model is also specified in this file, e.g. *kEpsilon*, *kOmega* and *kOmegaSST*. The *polyMesh* directory is the folder with the information on the mesh. For the generation of the meshes needed for this thesis first a background hex mesh with the use of the *blockMeshDict* is created. This base mesh defines the extent of the computational domain and a base level mesh density. In addition to the two patch types mentioned in B.1, a basic patch type is specified in the *blockMeshDict*. Table 21 displays the basic patch types considered in this thesis.

TABLE 21: BASIC PATCH TYPES [OPENFOAM, 2012]

Patch type	Description
patch	Generic patch
wall	Wall boundary, used for wall functions in turbulent flows

By executing the *blockMesh* utility additional files are generated containing the mesh data of points, boundary, neighbour, faces and owner. The last file in the 'constant' directory, the *triSurface* directory and its underlying files, are necessary for the mesh generation utility *snappyHexMesh.*

B.3 The 'system' directory

The 'system' directory is used for setting parameters associated with the solution procedure itself. For this end at least three files are necessary, *controlDict, fvSolution* and *fvSchemes*. Furthermore, additional files for specialised mesh generation, files that are related to post-processing and files for parallel computations are also found in this directory. The three necessary files will be briefly explained below, for a more in depth description, including an example of the different files, see for example [OpenFOAM, 2012] and [Steenstra, 2014].

B.3.1. *controlDict*

In the *controlDict* file the solver is defined used for the application concerned. Also, the run control parameters, including start and end time are set. The only two entries which are truly compulsory in this file are the time control and *writeInterval*. For the time control it is possible to set a fixed time step or, for example, set a maximum Courant number, as expressed by equation (A.1), with an automatic adjusted time step. Another example what can be set in the *controlDict* file are the parameters for the data output such as the *writeInterval* and *writePrecision*.

B.3.2. *fvSolution*

The two main parts which are set in the *fvSolution* file are the solvers and the algorithm [Steenstra, 2014]. The solver part specifies the method that is used for number-crunching to solve each discretized equation, i.e. the different variables used in the model. The linear-solvers which can be chosen in OpenFOAM are shown in Table 22.

Table 22: Linear solvers used in OpenFOAM [OpenFOAM, 2012]

Solver	Description
PCG/PBiCG	Preconditioned (bi-)conjugate gradient
smoothsolver	Solver using a smoother
GAMG	Diagonal solver for explicit systems
diagonal	PCG for symmetric matrices, PBiCG for asymmetric

OpenFOAM offers a range of options for preconditioning the matrices of the preconditioned conjugate gradient solvers. The same when a solver is chosen which require a smoother, this needs to be further specified. For the preconditioner and smoother options one is referred to [OpenFOAM, 2012].

The method of the sparse matrix solvers, see [OpenFOAM, 2012], is iterative, i.e. they are based on reducing the equation residual over a succession of solutions. Therefore the boundaries for each variable needs to be set. The solver stops if either of the following conditions are reached [OpenFOAM, 2012]:

- **Tolerance:** The residual error falls below the solver tolerance.
- **relTol:** The ratio of the current to initial residuals falls below the solver relative tolerance.
- **Iterations:** The number of iterations exceeds a maximum number of iterations.

It is possible to define tolerances for the intermediate iterations and for the final iteration. By setting a higher tolerance for the intermediate iterations computational time can be saved and still the wanted final tolerance can be achieved.

The second main part which needs to be specified in the *fvSolution* file is the algorithm. Most fluid dynamics solver applications in OpenFOAM uses the pressure-implicit split-operator (PISO) or semi-implicit method for pressure-linked equations (SIMPLE) algorithms [OpenFOAM, 2012], see also [Versteeg and Malalasekera, 1995]. When using a steady-state algorithm the under-relaxation needs to be set. The under-relaxation is technique used for improving the stability of a computation. The function of this technique is to limit the change of the variable from one iteration to the next. General values for the under-relaxation are [OpenFOAM, 2012]:

Table 23: Under-relaxation factors

Equation	Value
p	0.3
other equations	0.7

B.3.3. *fvSchemes*

The *fvSchemes* dictionary is used to set the numerical schemes for the different terms of the equations. [OpenFOAM, 2012] gives the following terms:

Table 24: Main keywords used in *fvSchemes* [OpenFOAM, 2012]

Term	Category of mathematical terms
ddtSchemes	First and second time derivatives $\boldsymbol{\partial/\partial t, \partial^2/\partial^2 t}$
gradSchemes	Gradient $\boldsymbol{\nabla}$
divSchemes	Divergence $\boldsymbol{\nabla \cdot}$
laplacianSchemes	Laplacian $\boldsymbol{\nabla^2}$
interpolationSchemes	Point-to-point interpolations of values
snGradSchemes	Component of gradient normal to a cell face
fluxRequired	Fields which require the generation of a flux

The aim in OpenFOAM is to offer an unrestricted choice to the user. For example, while linear interpolation is effective in many cases, OpenFOAM offers complete freedom to choose from a wide selection of interpolation schemes for all interpolation terms, for the possibility of the interpolation schemes one is referred to [OpenFOAM, 2012].

Appendix C: Model Set-up

In appendix B the basic directory structure and model set-up is treated. In this appendix a more in-depth elaboration on the model set-up used within this thesis with OpenFOAM will be given. The CFD model used in this thesis is a 3D model. Within this 3D domain a part of the fallpipe with the length of $2D$ is modelled to receive a realistic input velocity distribution. In section C.2 the boundary and initial conditions for the different turbulence models are treated.

C.1 Algorithms

As mentioned before, the two main algorithms used for fluid dynamic applications are the PISO and SIMPLE algorithm. A third possibility is a merged PISO-SIMPLE algorithm, referred to as PIMPLE. In this thesis use is made of the SIMPLE algorithm for the $k-\varepsilon$ and $k-\omega SST$ models. The *driftFlux* model uses the PIMPLE algorithm. A brief explanation on both the algorithms will be given in the coming two sections, for more details one is referred to [Ferziger, 2002].

C.1.1. SIMPLE

The Semi-Implicit Method for Pressure-Linked Equations (SIMPLE) algorithm was originally put forward by Patankar and Spalding in 1972 [Versteeg and Malalasekera, 1995]. This algorithm uses basically a trial and error procedure. If an implicit method is used in time, the discretized momentum equations at the new time step are non-linear. Due to this and that the underlying differential equations are coupled, the equations system resulting from discretization cannot be solved directly [Furbo, 2010]. Therefore the SIMPLE algorithm first constructs the velocity fields that do not satisfy the continuity equation and then correct them and hence using an iterative solution method.

C.1.1. PIMPLE

The Pressure-Implicit with Splitting of Operators (PISO) algorithm of Issa (1986) is a pressure-velocity calculation procedure developed originally for the non-iterative computation of unsteady compressible flows [Ferziger, 2002]. Within the PISO algorithm use is made of one predictor step and two corrector steps and can be seen as an extension of SIMPLE with a further corrector step to enhance it [Versteeg and Malalasekera, 1995]. The PIMPLE algorithm combines the SIMPLE algorithm then uses the PISO algorithm to rectify the second pressure correction and correct both velocities and pressure explicitly [Ong *et al.*, 2011].

For the sequence of operations in a CFD procedure which uses the SIMPLE or PIMPLE algorithm see [Versteeg and Malalasekera, 1995] and [Steenstra, 2014].

C.2 Initial and boundary conditions

Every numerical model needs initial and boundary conditions. However, for the simulations the initial conditions of the turbulent kinetic energy, the (specific) turbulent dissipation rate and turbulent viscosity are not of great concern [OpenFOAM, 2012]. The initial conditions are only used as an initial guess in OpenFOAM. Though, by supplying an educated initial guess the simulation time can be reduced because less time is needed to find the closing values. The initial guess of the turbulent kinetic energy, turbulent viscosity and the (specific) turbulent dissipation rate can be calculated with [OpenCFD, 2010]:

$$k = \frac{3}{2}(uI)^2 \tag{C.1}$$

$$\varepsilon = C_\mu^{\frac{3}{4}} \frac{k^{\frac{3}{2}}}{l} \tag{C.2}$$

$$\omega = C_\mu^{-\frac{1}{4}} \frac{\sqrt{k}}{l} \tag{C.3}$$

$$\nu_t = C_\mu \frac{k^2}{\varepsilon} \tag{C.4}$$

With:

I	turbulence intensity	$[-]$
ε	turbulent dissipation rate	$[m^2/s^3]$
C_μ	turbulence model constant	$[-]$
l	turbulent length scale	$[m]$
ω	specific turbulent dissipation rate	$[s^{-1}]$
ν_t	turbulent viscosity	$[m^2/s]$

The initial guess of the turbulent parameters are calculated with assuming a length scale of $0.65\,m$ and a freestream velocity of $5\,m/s$. The turbulence intensity is assumed on 5% at the bottom boundary and for the other boundaries calculated with [OpenCFD, 2010]:

$$I = 0.16Re^{-\frac{1}{8}} \tag{C.5}$$

Table 25 displays the used initial and boundary conditions for the $k-\varepsilon$ model.

TABLE 25: INITIAL AND BOUNDARY CONDITIONS USED IN THIS THESIS FOR THE $k-\varepsilon$ MODEL

Boundary	U	k	epsilon	p	nut
Inlet	fixedValue	fixedValue	fixedValue	zeroGradient	calculated
	uniform (0 0 -5)	uniform 0.0247	uniform 0.0258		uniform 0.00213
Pipe	fixedValue	kqRWallFunction	epsilonWallFunction	zeroGradient	nutkWallFunction
	uniform (0 0 0)	uniform 0.0247	uniform 0.0258		uniform 0.00213
Bottom	fixedValue	kqRWallFunction	epsilonWallFunction	zeroGradient	nutkWallFunction
	uniform (0 0 0)	uniform 0.0938	uniform 0.1037		uniform 0.00763
Open	inletOutlet	zeroGradient	zeroGradient	fixedValue	zeroGradient
ocean	uniform (0 0 0)			uniform 0	

In Table 26 the initial and boundary conditions for the $k-\omega SST$ are shown.

TABLE 26: INITIAL AND BOUNDARY CONDITIONS USED IN THIS THESIS FOR THE $k-\omega SSt$ MODEL

Boundary	U	k	omega	p	nut
Inlet	fixedValue	fixedValue	fixedValue	zeroGradient	calculated
	uniform (0 0 -5)	uniform 0.0247	uniform 11.613		uniform 0.00213
Pipe	fixedValue	kqRWallFunction	omegaWallFunction	zeroGradient	nutkWallFunction
	uniform (0 0 0)	uniform 0.0247	uniform 11.613		uniform 0.00213
Bottom	fixedValue	kqRWallFunction	omegaWallFunction	zeroGradient	nutkWallFunction
	uniform (0 0 0)	uniform 0.0938	uniform 22.632		uniform 0.00763
Open	inletOutlet	zeroGradient	zeroGradient	fixedValue	zeroGradient
ocean	uniform (0 0 0)			uniform 0	

The *driftFlux* models uses the same initial and boundary conditions for the velocity, turbulent kinetic energy, turbulent dissipation rate and turbulent viscosity. But instead of the pressure parameter the dynamic pressure needs to be defined. Additionally, a new parameter is introduced, *alpha.stone*. This parameter denotes the concentration of the stones present. For the initial and boundary conditions of the dynamic pressure and the new parameter *alpha.stone* see Table 27.

TABLE 27: INITIAL AND BOUNDARY CONDITIONS USED IN THIS THESIS FOR THE *DRIFTFLUX* MODEL

Boundary	*alpha.stone*	*p_rgh*
Inlet	fixedValue	fixedFluxPressure
	uniform 0.094	uniform 0
Pipe	zeroGradient	fixedFluxPressure
		uniform 0
Bottom	zeroGradient	fixedFluxPressure
		uniform 0
Open ocean	zeroGradient	zeroGradient

In Table 8 a different input value for the concentration is noted than in Table 27. This is because the inlet flux is calculated differently than the flux within the domain:

$$Flux\ inlet = alpha.stone * u \tag{C.6}$$

$$Flux\ cell\ 1 = alpha.stone * u + alpha.stone * u_e \tag{C.7}$$

Due to the different calculation of the flux a conservation of mass can only be achieved by reducing the concentration in the first cell. Still, the calculations within the model are correct and mass conservation is kept. By this, the input concentration within the model is calculated with:

$$alpha.stone\ (input) = alpha.stone\ (desired) * \frac{u + u_e}{u} \tag{C.8}$$

Appendix D: Mesh Generation

The generation of the mesh that is used for the different numerical models is discussed in this appendix. In numerical modelling a grid with a finite number of grid cells and points is used and therefore is approximating solutions of mathematical equations. To obtain an infinite small error between the numerical model and mathematical equation; infinite small cells need to be used, which will cause infinite computational time. For this reason the main objective of the mesh independency study is to reduce computational time by setting a cell size, however, securing independency on the solution of the numerical simulation.

For the generation of the mesh the following aspects are taken into account:

- **Mesh independence:** The solution has to be independent of the mesh.
- **Convergence:** The convergence requirement is fulfilled when the (steady state) solution satisfies the following three conditions:
    1. Monitor points of values of interest have reached a steady state solution.
    2. The residual error values have reduced to an acceptable value; acceptable usually differs per case, however typically lower than 10^{-4} to 10^{-5} [OpenCFD, 2010].
    3. The imbalances (spurious oscillations) in the domain should be less than 1%.

The mesh independency study will be carried out for a free jet with the $k-\varepsilon$ turbulence model. The initial simulation is run on a rather coarse initial mesh of $180k$ cells until convergence of the residual error was ensured, the value of interest at the monitor points were steady and the imbalances below 1%. From here on the mesh was refined, roughly around 1.5 times the number of cells of the previous mesh, until the value of interest was the same at the monitor points, within an allowable tolerance.

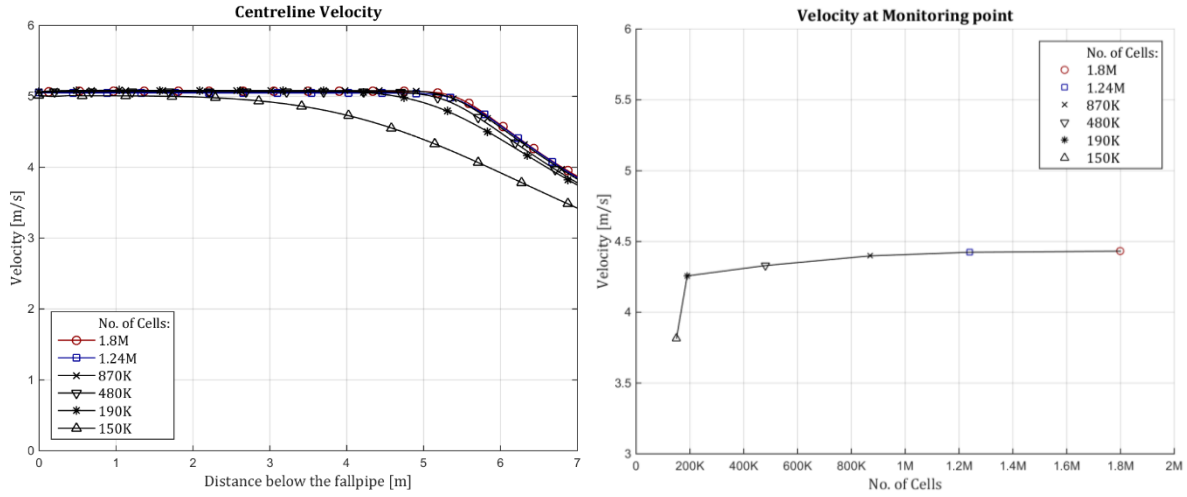

FIGURE 45: THE CENTRELINE AND VELOCITY AT CERTAIN MONITORING POINT VS. NUMBER OF CELLS WITHIN THE MESH

As can be seen from Figure 45 the value of interest is within an allowable tolerance at the monitor points from the mesh with $1.24M$ cells onward. To verify the mesh independency study for different turbulence models it was also carried out on the $k-\omega SST$ model and similar results were found. Accordingly, the corresponding cell size of the $1.24M$ cell mesh will be used for all further numerical model runs. However, the main focus of this thesis lies on the impinging jet. In this thesis use is made of wall functions to save computational time, and as explained in section A.2.4.2, the flow must therefore be in the log-law layer. This can be achieved by obeying the condition of $5 < y^+ < 300$ [BREDBERG, 2000]. For this reason two extra aspects are taken into account:

- **Height of the first cell:** The height of the first cell has to obey to the law of the wall.
- **Cell height expansion factor:** The computational time can be reduced by expanding the height between two consecutive cells from the first cell onward, although within a certain limit.

The height of the first cell can be calculated with [OPENFOAM, 2012]:

$$y = \frac{y^+ \nu}{u_\tau} \tag{D.1}$$

In literature no real rules were found for the determination of the cell height expansion factor. Nonetheless, a rule of thumb from practice gives a maximum expansion factor of around 1.15. Consequently, an expansion factor below the maximum expansion factor is chosen, roughly around 1.14, meaning an increase in cell height of 14% between two consecutive cells.

TABLE 28: USED MESH VARIABLES

parameter	*Value*
First cell height	$2\ mm$
Cell expansion factor	1.14

Appendix E: Results

In this appendix an extensive overview of the different results will be conducted. The first section covers the results of the circular turbulent jet. In section E.2 the stone trajectory and its corresponding spreading and displacement will be treated. In the last section of this appendix the results of the stone transport are presented.

E.1 Circular Turbulent Jet

Input Velocity

The coming figures show the dimensionless vertical and radial velocities for different cross sections.

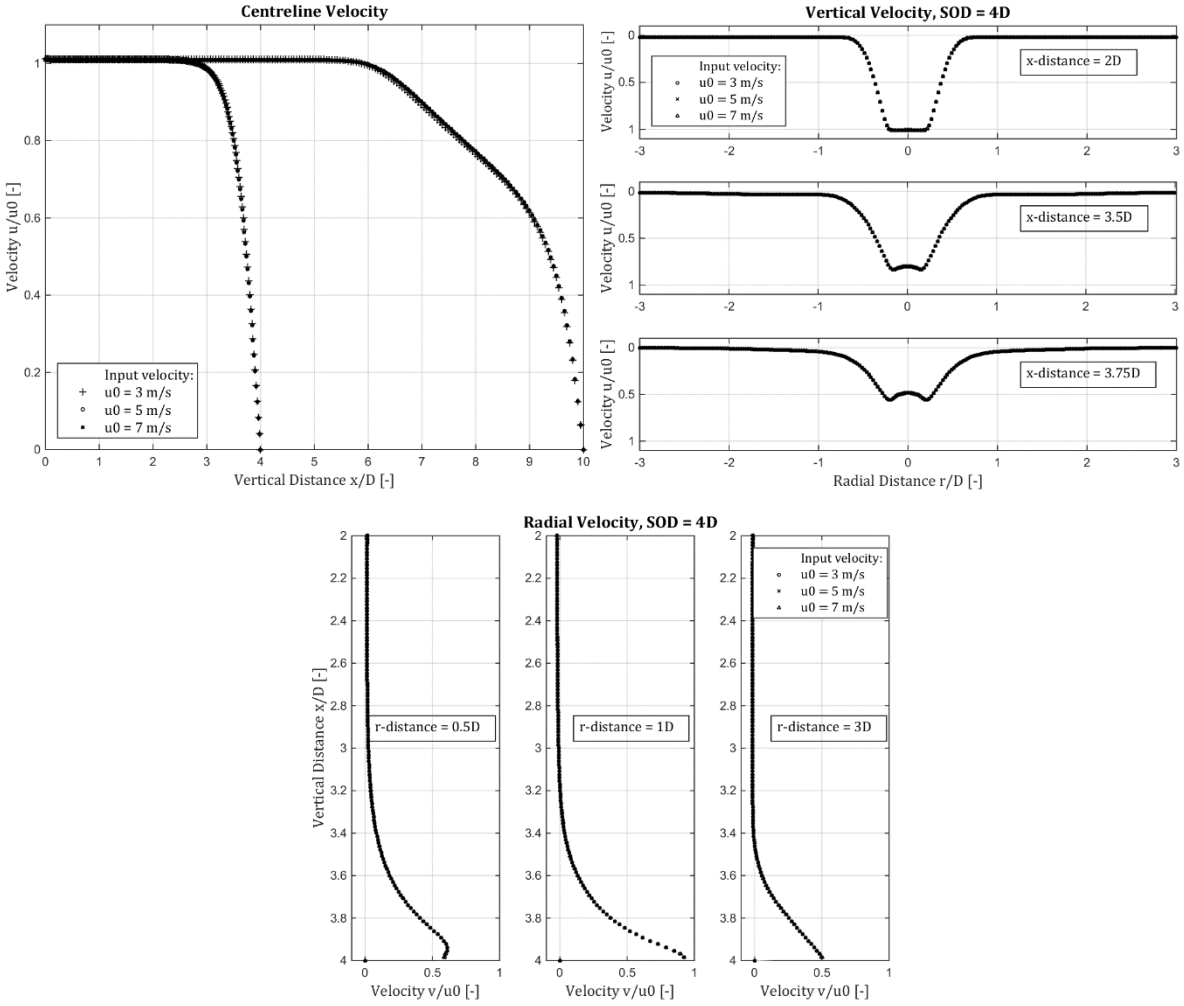

FIGURE 46: CENTRELINE, VERTICAL AND RADIAL VELOCITIES AS FUNCTION OF INPUT VELOCITY

As can be seen, at least for the range tested ($3 - 7\ m/s$), the velocity field is indeed completely depended on the input velocity. Therefore, it is fair to assume a simulation with a certain input velocity can be picked and be multiplied with the velocity factor to receive the velocity field for a different input velocity.

Turbulent Kinetic Energy

In Figure 47 the turbulent kinetic energy can be seen for different input velocities. The left panel shows the numerical simulations done with the k-epsilon model, whereas the right panel displays the k-omegaSST model.

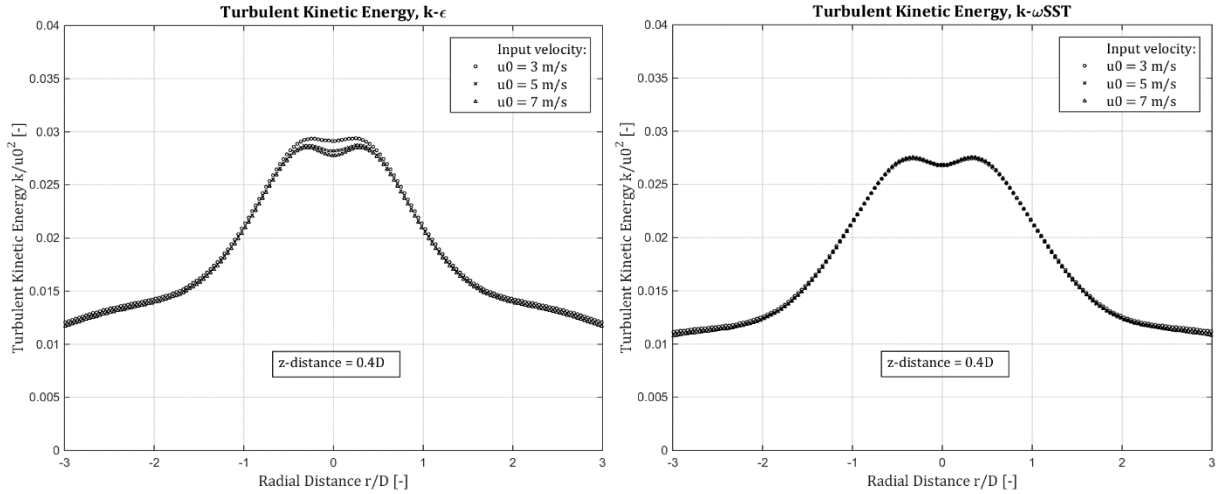

FIGURE 47: TURBULENT KINETIC ENERGY DEPENDING ON THE INPUT VELOCITY

Boundary Roughness

Numerical simulations were run with a different boundary roughness. The influence on the radial velocity can be seen in the figure below.

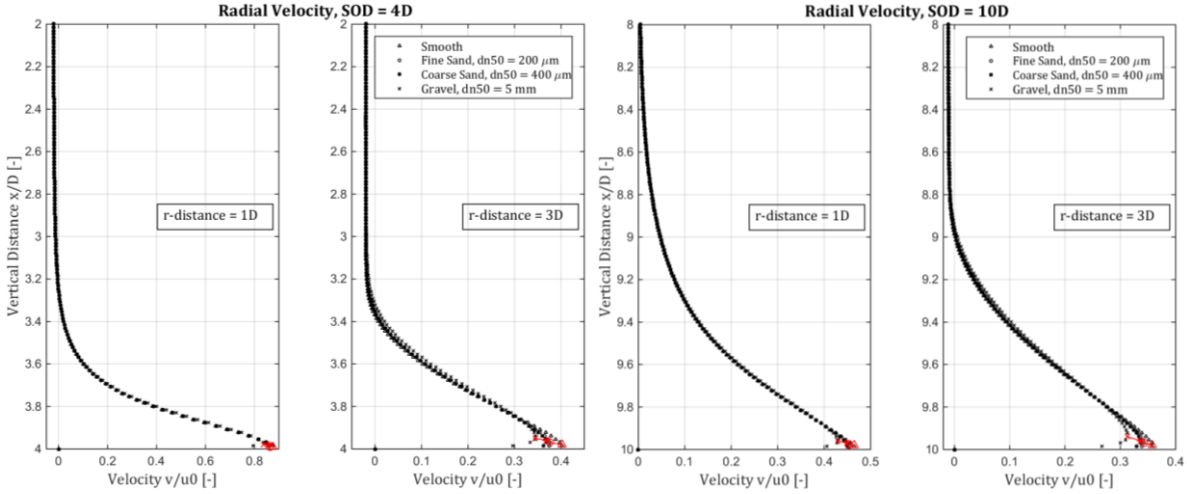

FIGURE 48: RADIAL VELOCITY DEPENDING ON THE BOUNDARY ROUGHNESS

In Figure 49 the reduction of the maximum radial velocity for different SODs and different radial distances is shown.

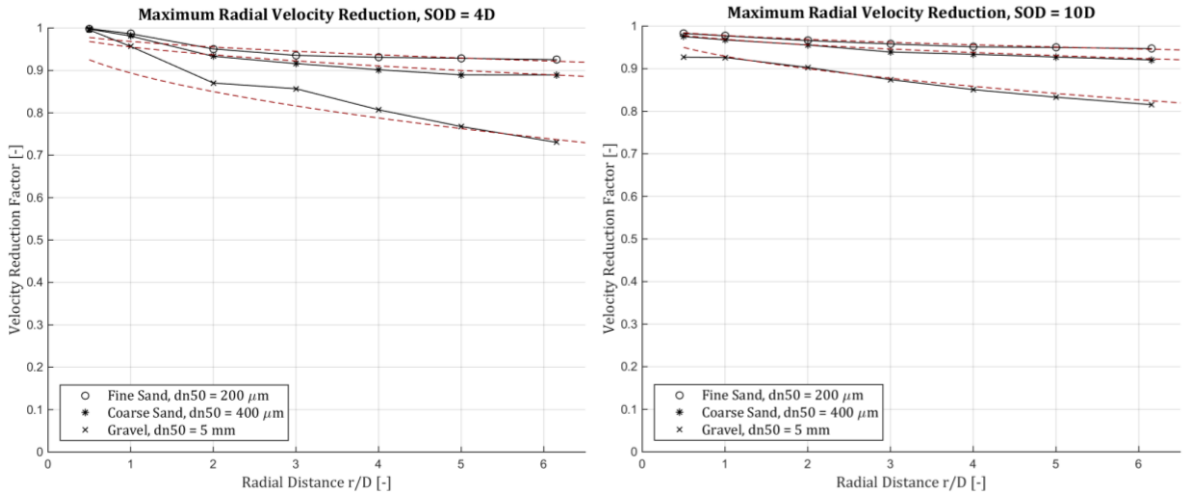

FIGURE 49: MAXIMUM RADIAL VELOCITY REDUCTION DUE TO BOUNDARY ROUGHNESS

The maximum radial velocity reduction factor for both the $k-\varepsilon$ and $k-\omega SST$ model can be roughly approximated for the fine and coarse sand with equation (G.1). For the gravel this reduction factor is expressed as in equation (G.2).

$$F_r = 1 - \sqrt{24 * d_{n50} * \frac{r * D}{SOD}} \tag{G.1}$$

$$F_r = 1 - \sqrt{10 * d_{n50} * \frac{r * D}{SOD}} \tag{G.2}$$

Small stand-off distance

The centreline, vertical and radial velocities of an impinging jet with SOD = 4D.

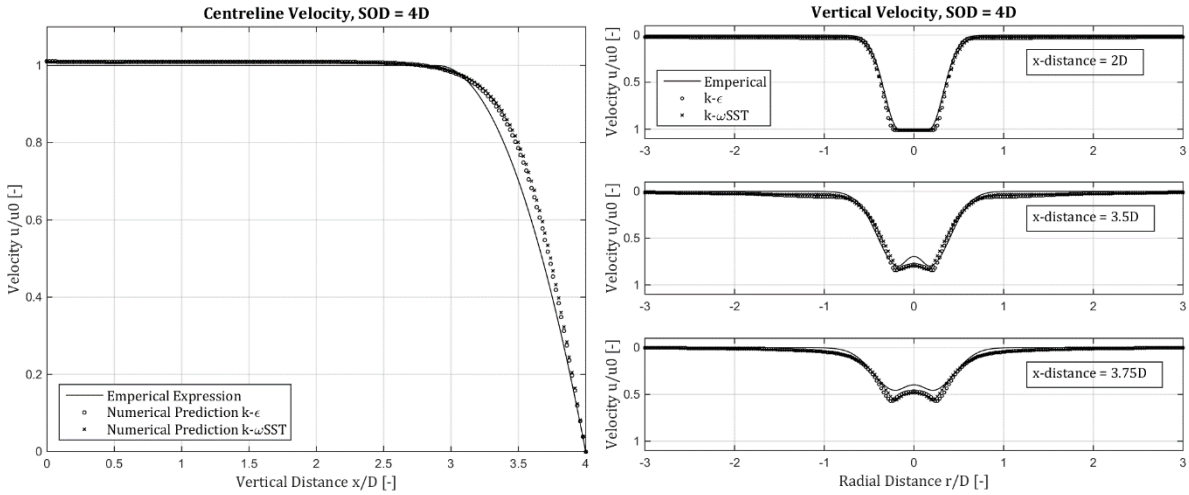

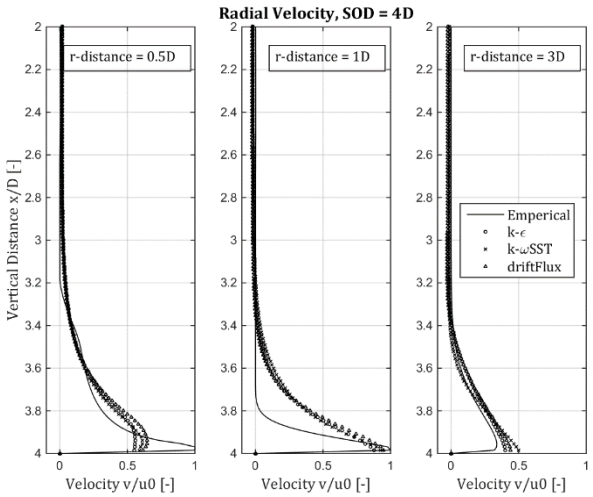

FIGURE 50: CENTRELINE, VERTICAL AND RADIAL VELOCITIES FOR DIFFERENT APPROACHES, $SOD = 4D$

Transitional range stand-off distance

The centreline, vertical and radial velocities of an impinging jet with SOD = 7D.

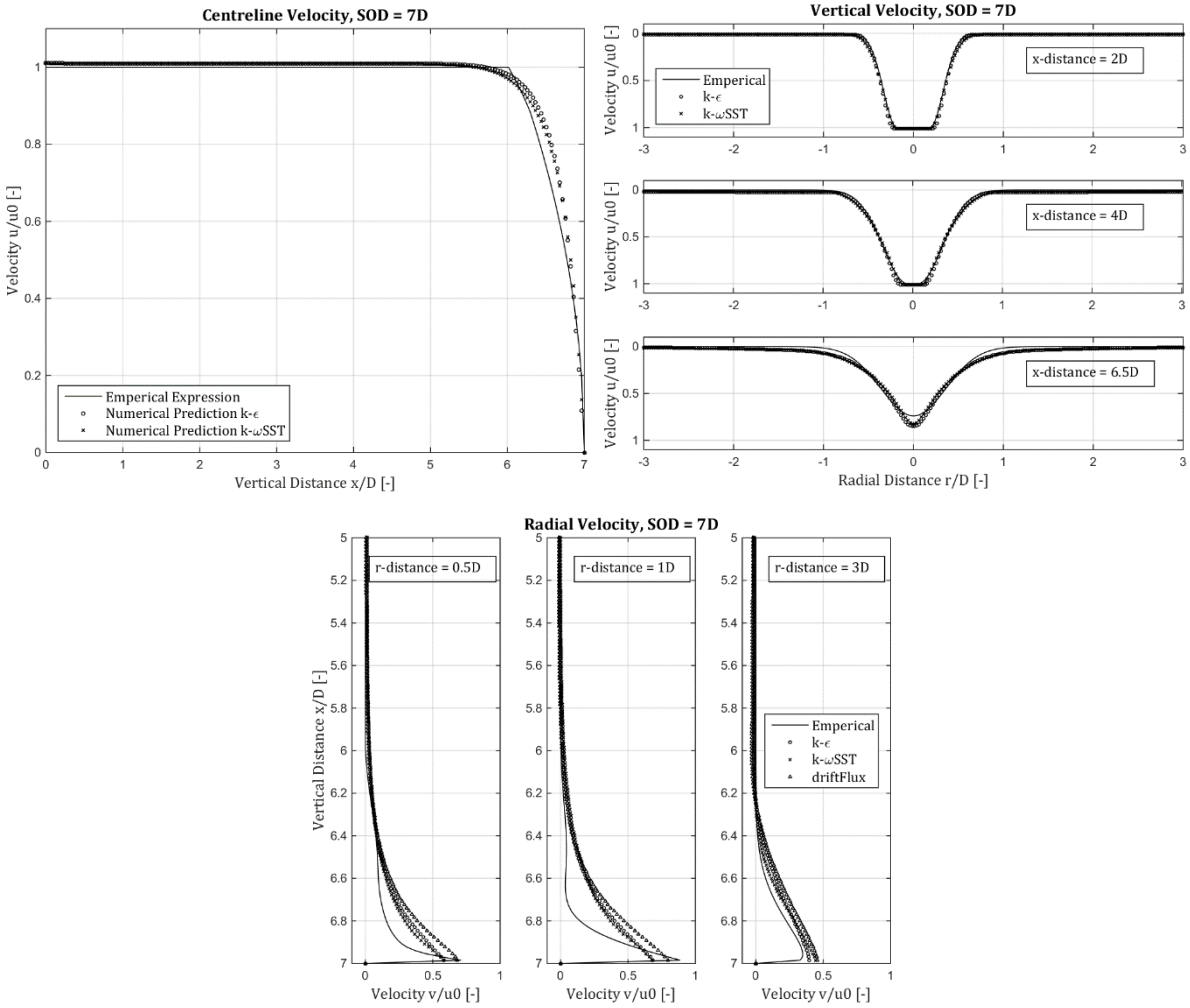

FIGURE 51: CENTRELINE, VERTICAL AND RADIAL VELOCITIES FOR DIFFERENT APPROACHES, $SOD = 7D$

Large stand-off distance

The centreline, vertical and radial velocities of an impinging jet with SOD = 15D.

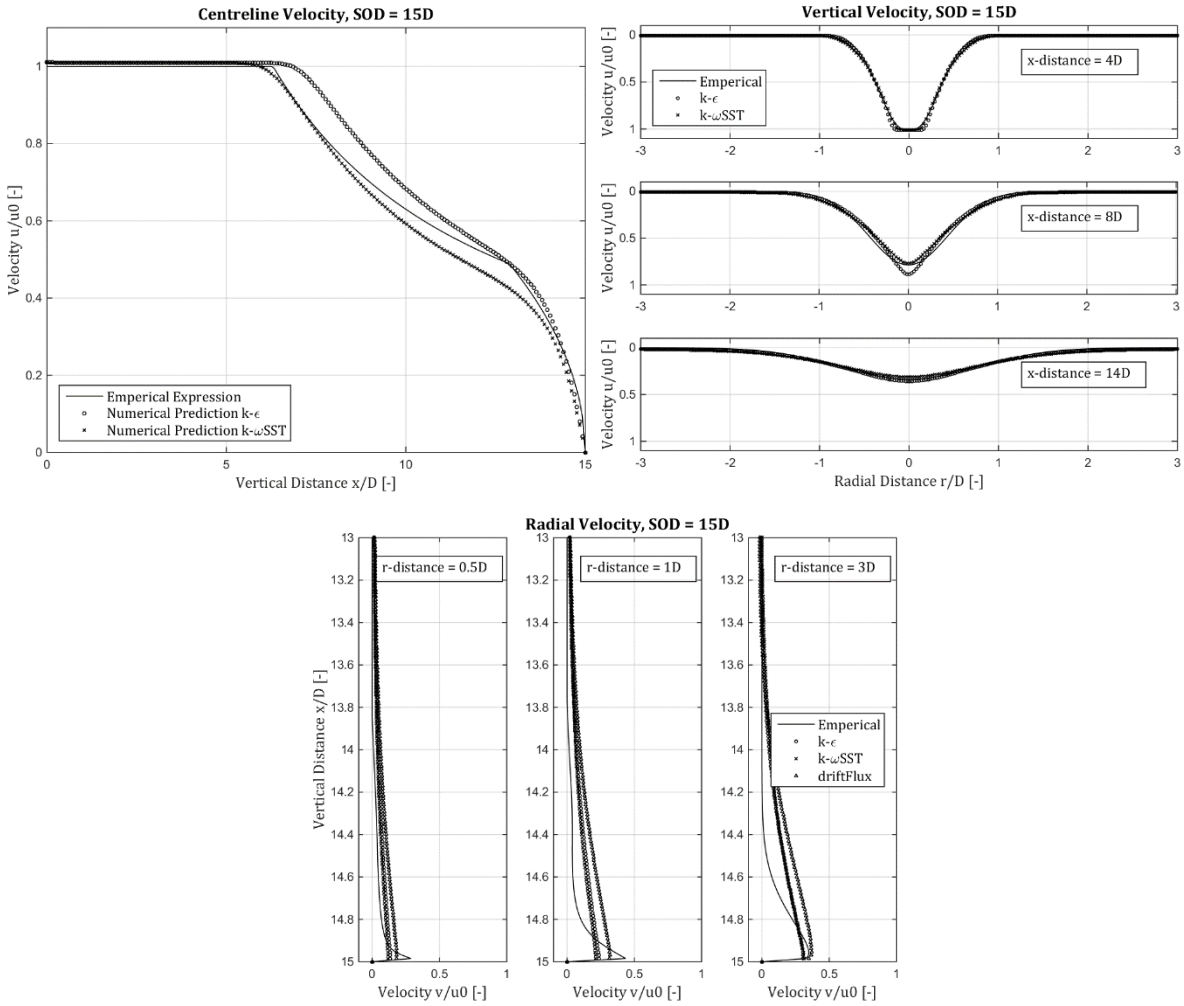

FIGURE 52: CENTRELINE, VERTICAL AND RADIAL VELOCITIES FOR DIFFERENT APPROACHES, $SOD = 15D$

E.2 Stone Trajectory

Settling behaviour

In the coming two graphs the trajectory of a bin of 80 stones determined with the empirical approach are shown. In the left panel of Figure 53 use is made of the equations of motion without a turbulent kinetic energy. The right panel shows the result when this turbulent intensity is included.

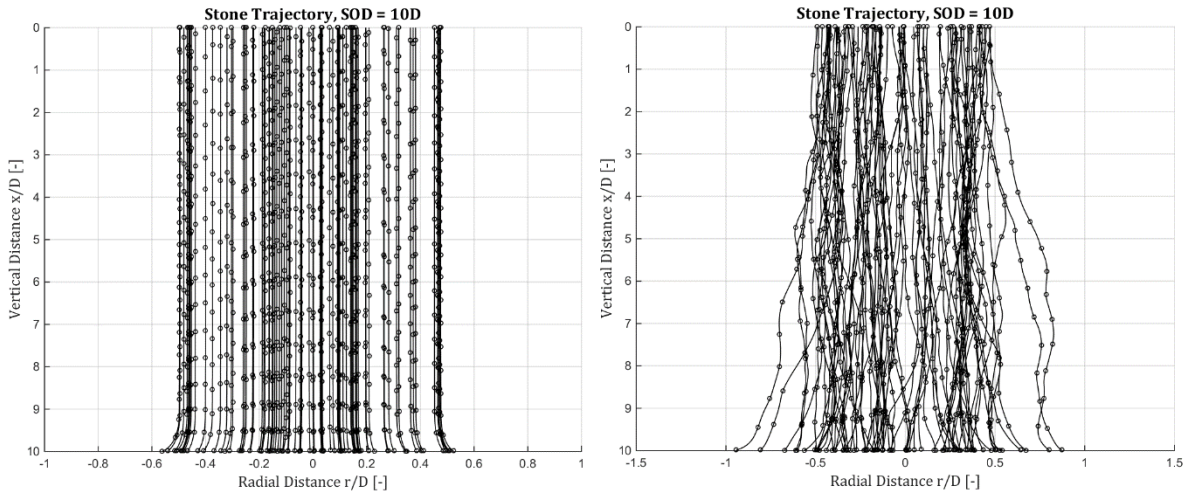

FIGURE 53: STONE TRAJECTORY DETERMINED WITH THE EMPIRICAL APPROACH

Stand-off distance

The influence of the stand-off distance on the spreading and displacement of stones.

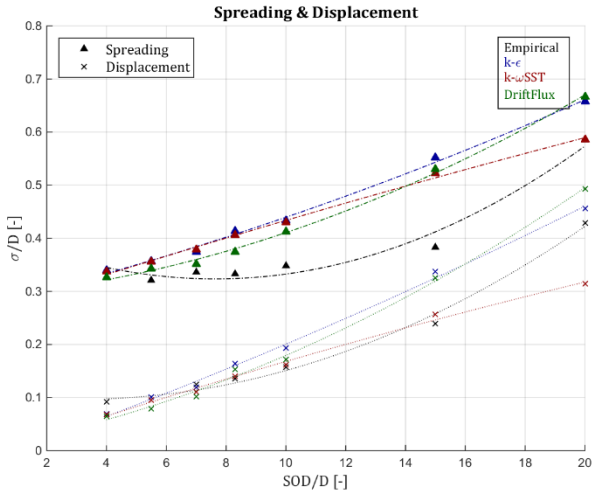

FIGURE 54: SPREADING AND DISPLACEMENT AS FUNCTION OF THE SOD

Grading

The influence of the grading on the spreading and displacement of stones.

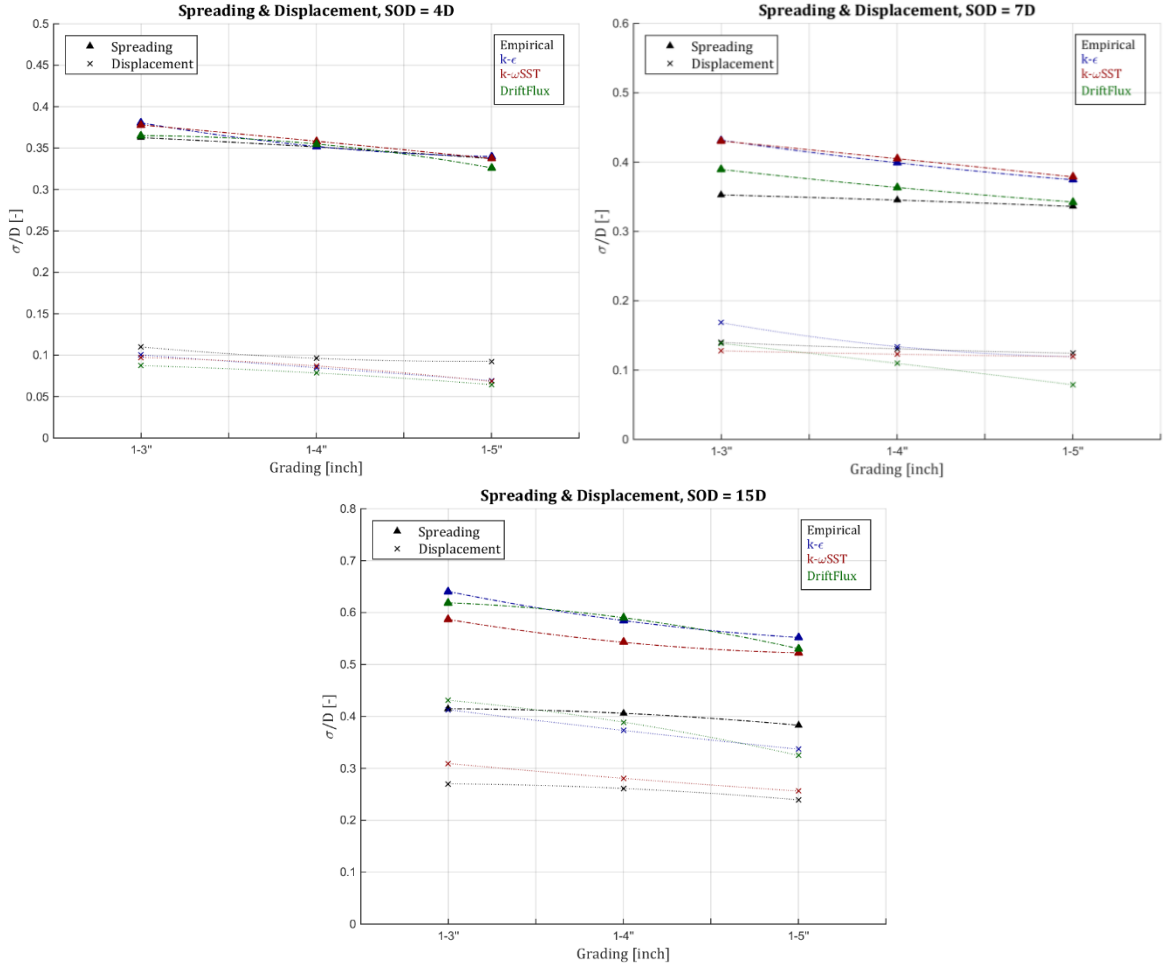

FIGURE 55: SPREADING AND DISPLACEMENT AS FUCNTION OF THE GRADING

Stone diameter

The influence of the stone diameter on the spreading and displacement of stones.

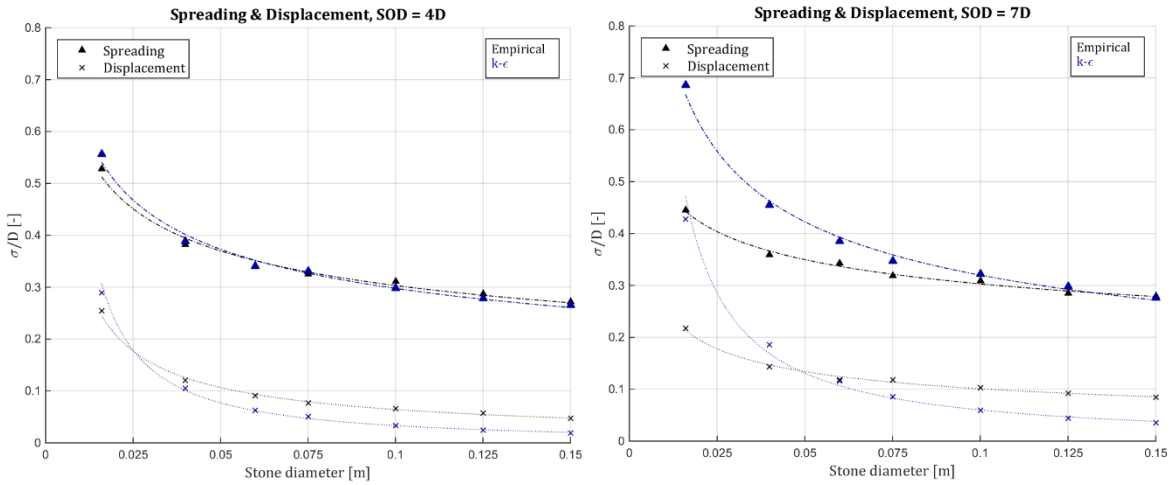

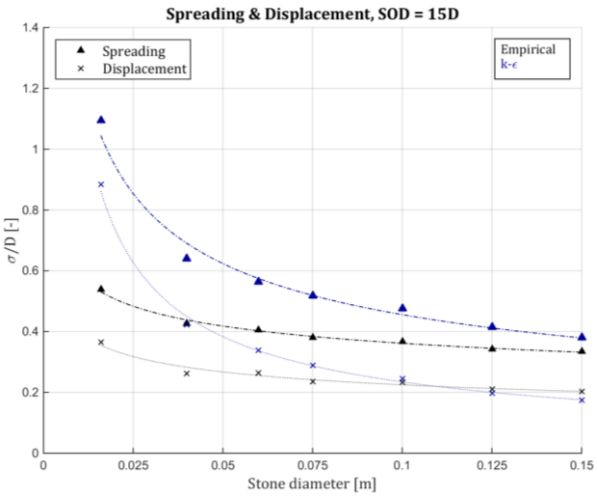

FIGURE 56: SPREADING AND DISPLACEMENT AS FUCNTION OF THE STONE DIAMETER

Hindered settling

The influence of the hindered settling on the spreading and displacement of stones.

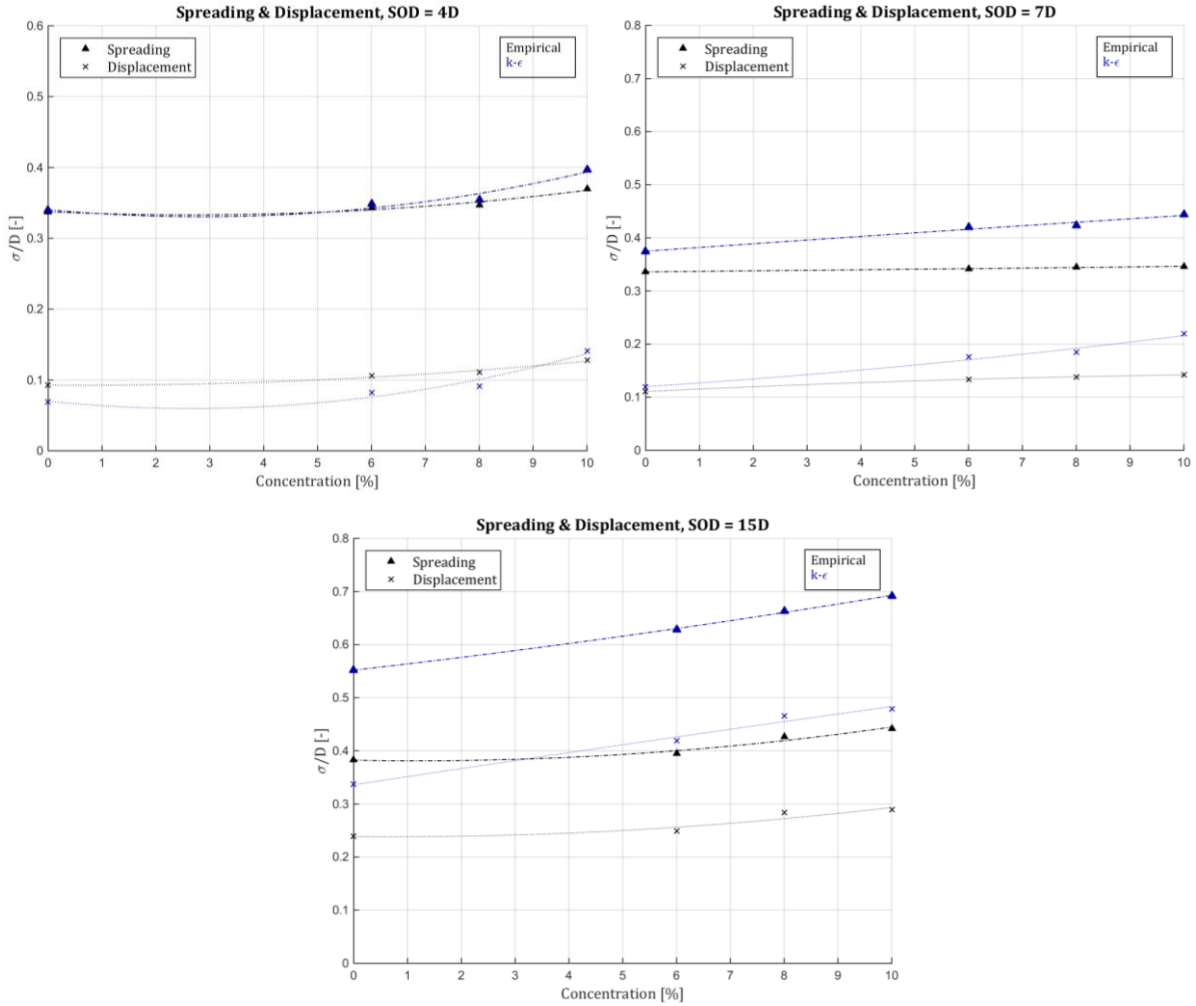

FIGURE 57: SPREADING AND DISPLACEMENT AS FUCNTION OF THE CONCENTRATION

Jet velocity

The influence of the jet velocity on the spreading and displacement of stones.

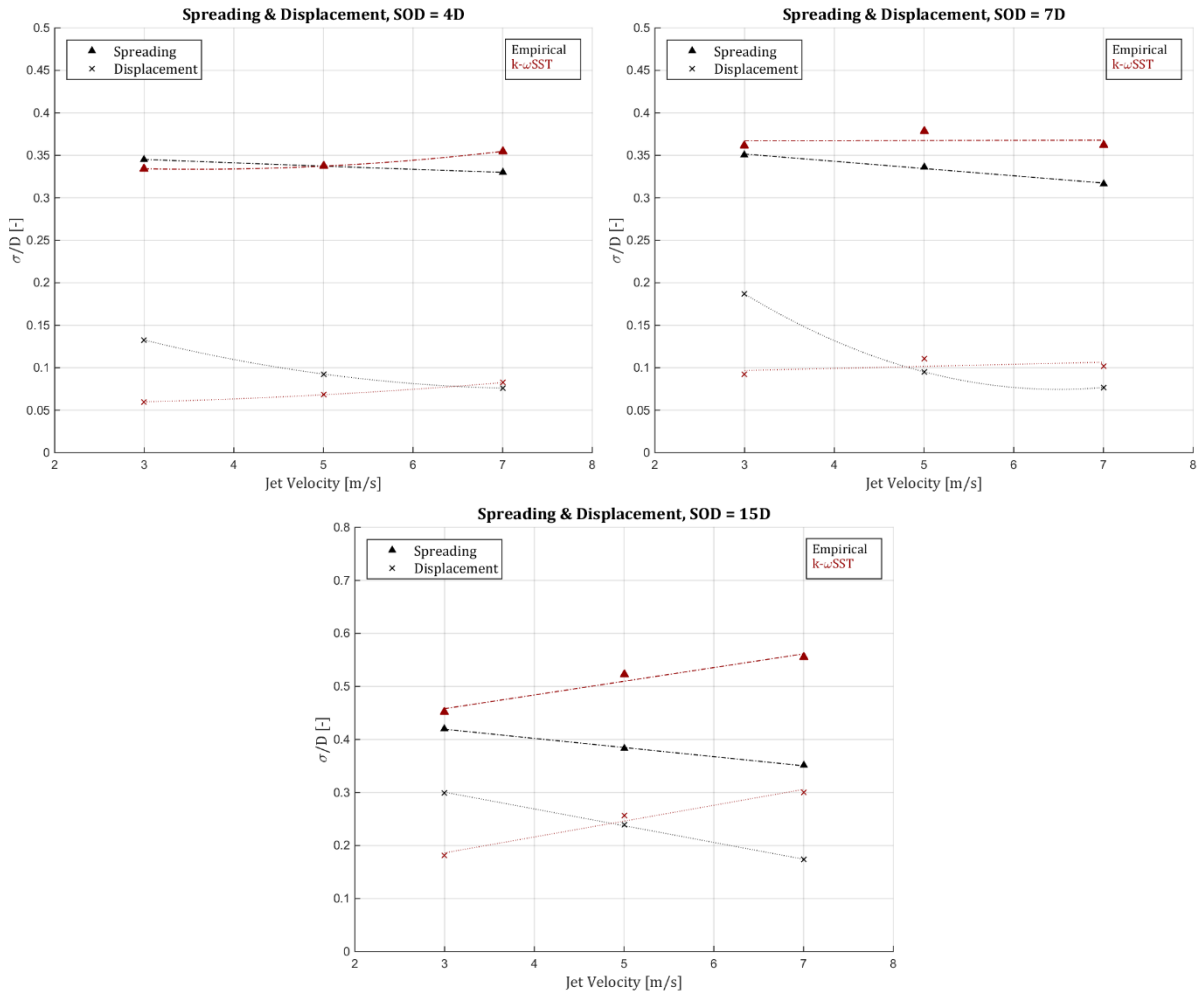

FIGURE 58: SPREADING AND DISPLACEMENT AS FUCNTION OF THE JET VELOCITY

Release location

The influence of the release location on the spreading and displacement of stones.

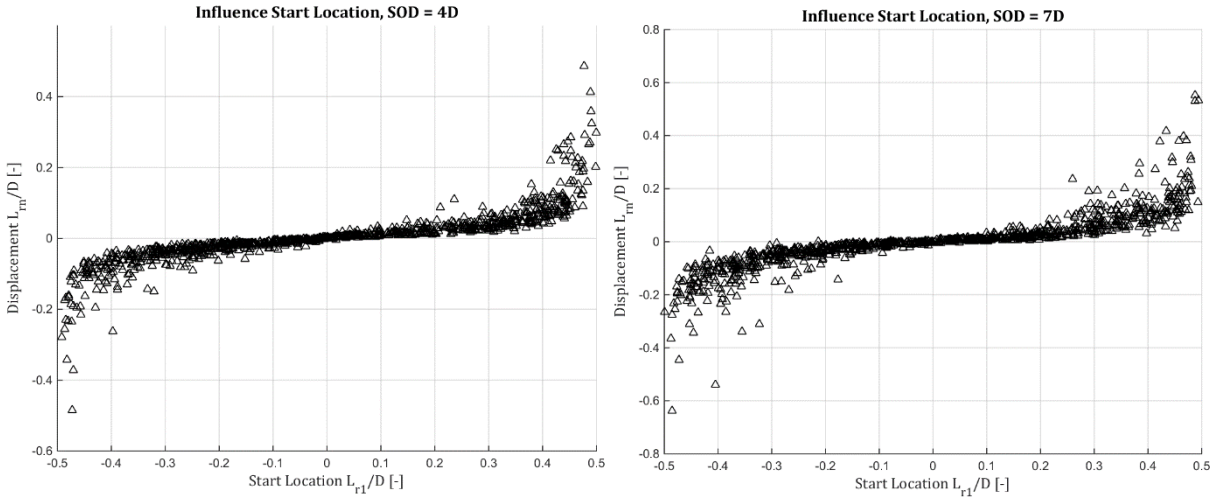

FIGURE 59: SPREADING AND DISPLACEMENT AS FUCNTION OF THE STARTING LOCATION

E.3 Berm built-up

Stone Transport

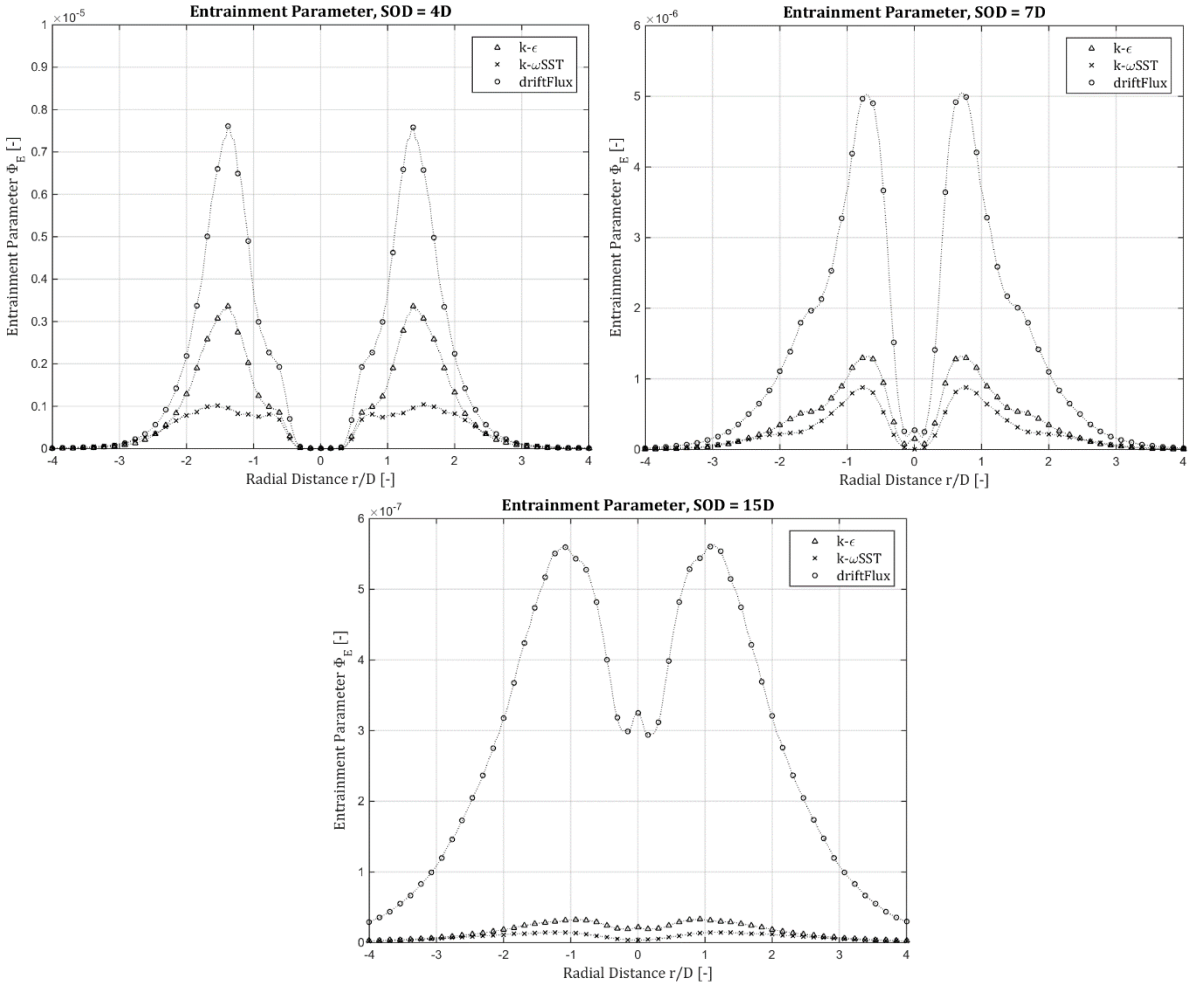

FIGURE 60: ENTRAINMENT PARAMETER FOR DIFFERENT TURBULENCE MODELS

List of Figures

Figure 1: Built-up of a rock protection berm 2
Figure 2: Area of interest of this thesis 3
Figure 3: Flow regimes below a fallpipe 4
Figure 4: The approach 5
Figure 5: Roadmap of this thesis 6
Figure 6: Single long rock berm 10
Figure 7: Free jet velocity profile 10
Figure 8: Impinging jet velocity profile 13
Figure 9: Distribution of the key parameters for the Hofland stability parameter 15
Figure 10: Normalized vertical and radial velocity profile of impinging jet with SOD = 10D, EMP 28
Figure 11: Normalized vertical and radial velocity profile of impinging jet with SOD = 10D, CFD 29
Figure 12: A) Normalized centreline velocity B) Normalized radial velocity, $k-\omega SST$ turbulence model 30
Figure 13: Normalized turbulent kinetic energy, SOD = 10D 30
Figure 14: Maximum radial velocity reduction due to boundary roughness, $k-\varepsilon$ turbulence model 32
Figure 15: Centreline and vertical velocity for the different approaches 32
Figure 16: Radial velocity for the different approaches 33
Figure 17: Vertical velocity for the different approaches 33
Figure 18: Vertical velocity for the different approaches 34
Figure 19: Centreline velocity for the different approaches 35
Figure 20: Stone location and used coordinate system 37
Figure 21: Velocity field, $k-\varepsilon$ turbulence model 38
Figure 22: Turbulent kinetic energy field, $k-\varepsilon$ turbulence model 42
Figure 23: Examples of simulated rock spread and displacement, $k-\varepsilon$ turbulence model 44
Figure 24: Trajectory of single stones determined with the empirical approach, no turbulence 44
Figure 25: Spreading and displacement as function of a) SOD and B) Stone diameter, EMP 45
Figure 26: Trajectory of single stones determined with the empirical approach, turbulence 46
Figure 27: Trajectory of single stones, $k-\varepsilon$ turbulence model A) No turbulence B) Turbulence 47
Figure 28: Spreading and displacement as function of SOD 48
Figure 29: Spreading and displacement as function of a) SOD and b) Grading 49
Figure 30: Spreading and displacement as function of a) Stone diameter and b) Concentration 50
Figure 31: Spreading and displacement as function of the outflow jet velocity 52
Figure 32: Normalized starting location vs. displacement, $k-\varepsilon$ turbulence model 53
Figure 33: Basis for determining the height increase of the rock berm 55
Figure 34: Probability density distribution of rock spreading, $k-\varepsilon$ model 56
Figure 35: Height increase of a rock berm 57
Figure 36: Height increase of a rock berm 57
Figure 37: Basis for determining the stone transport 58
Figure 38: Perpendicular velocity component below the fallpipe 60
Figure 39: Entrainment parameter for different turbulence models at $r=0$ 60

Figure 40: Entrainment rate at the centre of the jet 61
Figure 41: Maximum entrainment rate..... 62
Figure 42: Entrainment rate for different input velocities..... 63
Figure 43: Velocity distribution near a solid wall (adapted from [Versteeg and Malalasekera, 1995]). 72
Figure 44: OpenFOAM case structure..... 75
Figure 45: The centreline and velocity at certain monitoring point vs. number of cells within the mesh... 83
Figure 46: Centreline, vertical and radial velocities as function of input velocity..... 85
Figure 47: Turbulent kinetic energy depending on the input velocity..... 86
Figure 48: Radial velocity depending on the boundary roughness 86
Figure 49: Maximum radial velocity reduction due to boundary roughness..... 87
Figure 50: Centreline, vertical and radial velocities for different approaches, $SOD = 4D$..... 88
Figure 51: Centreline, vertical and radial velocities for different approaches, $SOD = 7D$..... 88
Figure 52: Centreline, vertical and radial velocities for different approaches, $SOD = 15D$..... 89
Figure 53: Stone trajectory determined with the empirical approach 90
Figure 54: Spreading and displacement as function of the SOD..... 90
Figure 55: Spreading and displacement as fucntion of the grading..... 91
Figure 56: Spreading and displacement as fucntion of the stone diameter..... 92
Figure 57: Spreading and displacement as fucntion of the concentration..... 92
Figure 58: Spreading and displacement as fucntion of the jet velocity..... 93
Figure 59: Spreading and displacement as fucntion of the starting location 94
Figure 60: Entrainment parameter for different turbulence models 94

List of Tables

Table 1: Rock grading by [Statoil TR1370, 2009] 16
Table 2: Standard paramaters 18
Table 3: Standard model constant $k-\varepsilon$ model 23
Table 4: Standard model constants $k-\omega SST$ model 24
Table 5: Standard model constants driftFlux model 25
Table 6: Modelling considerations stand-off distance 27
Table 7: Standard input parameters for the flow field modelling 27
Table 8: Input values for the driftFlux model 28
Table 9: Modelling considerations input velocity 29
Table 10: Modelling considerations boundary roughness 31
Table 11: Nikuradse roughness 31
Table 12: Possible input parameters for the stone tracker 39
Table 13: Standard input parameters stone trajectory modelling 47
Table 14: Modelling considerations stand-off distance 48
Table 15: Modelling considerations grading 49
Table 16: Modelling considerations stone diameter 50
Table 17: Modelling considerations concentration 51
Table 18: Modelling considerations input velocity 52
Table 19: Outflow velocity corresponding to production rate 57
Table 20: Primitive and derived patch types [OpenFOAM, 2012] 76
Table 21: Basic patch types [OpenFOAM, 2012] 76
Table 22: Linear solvers used in OpenFOAM [OpenFOAM, 2012] 77
Table 23: Under-relaxation factors 78
Table 24: Main keywords used in *fvSchemes* [OpenFOAM, 2012] 78
Table 25: Initial and boundary conditions used in this thesis for the $k-\varepsilon$ model 80
Table 26: Initial and boundary conditions used in this thesis for the $k-\omega SSt$ model 81
Table 27: Initial and boundary conditions used in this thesis for the *driftFlux* model 81
Table 28: Used mesh variables 84

Literature Study

Master Thesis

Part II

Delft University of Technology | Tideway Offshore Solutions

TU Delft Delft University of Technology

Tideway Offshore Solutions

Readers Guide Literature Study

Chapter 1 Introduction: In this chapter a general introduction to rock placement operations is given. The four main techniques: side stone dumping, dumping stone with a split hopper, rock placement with a fallpipe vessel and rock placement with a dragline, will be elaborated. There are currently two different fallpipe systems in operation in the field, one with a flexible and one with a closed fallpipe. The literature study will further focus on the closed fallpipe system.

Chapter 2 Rock Placement Operations: In this chapter the layout of the fallpipe vessel Flintstone is treated. Three main features of the vessel can be distinguished as, the storage room, the feeding system and the closed fallpipe system. A deeper elaboration of the closed fallpipe system is given and furthermore some considerations with respect to the fallpipe operations of the Flintstone is touched upon.

In the second paragraph of this chapter examples of specific rock placement operations are considered, including: pre-lay seabed preparation works, scour and pipeline protection, upheaval buckling prevention and insulation.

Chapter 3 Circular Turbulent Jets: The beginning of this chapter starts with a general introduction into fluid intrusions into other fluids. The flow below the fallpipe is considered as a buoyant jet because it is both momentum and buoyancy driven. In literature is found that the circular turbulent jet below a fallpipe can be divided into three regions, namely: a free jet region, impinging jet region and wall jet region.

In the first paragraph of this chapter the free zone of the turbulent jet is treated. This free jet can again be divided into three zones: Zone of Flow Establishment (ZFE), transitional zone and Zone of Established Flow (ZEF). [Rajaratnam, 1976] did extensive research on the ZFE and ZEF and derived a formula for the velocity profile of both (3.7) and (3.14). [Lee, 2009] derived in his research an expression for the velocity profile of the entire free zone (3.16).

In the second paragraph the impinging jet region is considered. Impingement occurs when the height of the orifice above the seabed is limited and it was found that a division between large and small stand-off distances (*SOD*) must be made. It was established that the velocity profile for large *SODs* can be determined with the same equation as for the ZEF, however, with the use of a reduction factor given by (3.24). For small *SODs* the radial distribution of the jet velocity is non-uniform, as contrary to the flow distribution for large *SODs*. Now a different expressions for the velocity profile are given, depending on the radial distance from the centreline. For radial distances smaller than the distance from the centre to the edge of the core of the jet this expression is given in (3.29). Otherwise expression (3.31) must be used.

In the last paragraph the wall jet region is treated, again a distinction between large and small *SODs* must be made. An axis symmetric wall jet can be created when the jet below the fallpipe spreads out radially due to a boundary, i.e. the seabed. It is quite noticeable that the flow characteristics in the wall jet region are independent of the height above the seabed, both for large and small *SODs*. The radial velocity profile for large *SODs* can be calculated with the use of (3.35) and the shear velocity for small *SODs* can be determined with (3.38).

Chapter 4 Threshold of Motion: A critical or threshold condition for the flow over an erodible bed has been reached when the hydrodynamic force is balanced by the resisting force. The determination of the threshold of motion of particles has been proven to be a very difficult task, therefore, numerous experiments have been performed to find an empirical formula for particle transport. In 1936 Shields pioneered the dimensionless critical shear stress to define this incipient of motion for a particle. This dimensionless critical shear stress is from then on called the Shields stability parameter. A lot of researchers used a Shields-like stability parameter to define the incipient motion, of which some are given in this chapter. In the first part of the chapter the hydrodynamic forces on stone lying on the seabed exposed to a fluid flow is elaborated.

In the second paragraph of this chapter different stability parameters were considered, whereby [HOAN, 2009] executed a comparative research on different stability parameters, namely: the Jongeling *et al.* stability parameter (4.16) and the Hofland stability parameter (4.17). Also his own stability parameter (4.21) was introduced and it was found that three stability parameters perform similarly well.

With these stability parameters the required stone diameter for design purposes now can be determined with (4.23), (4.24) and (4.25).

Chapter 5 Rock Properties: In this chapter four different characterizations of rock are given: rock types, rock mass and size, rock grading and rock shapes. Rock types can be classified by their mineral and chemical composition, texture of the constituent particles and formation process. In the second paragraph rock mass and size is treated with an elaboration on the distinction between the nominal diameter and diameter of a particle.

Rock from a quarry, of for that matter any kind of rock, comes in all kind of sizes. Therefore it has big advantage to have some sort of grading classes for practical used, these classes are noted in the third paragraph. In the last part of this chapter a description of rock shapes is given. The shape of rock is important, because it has an influence on the stability, shear strength, permeability and filtering properties of a layer of rock. A distinction between the length-to-thickness ratio, blockiness and cubicity is made.

Chapter 6 Dumping of a Single Stone: To get a better understanding of what happens with rock falling through a fallpipe and settling below the fallpipe, the dumping of a single stone in water will be looked at in this chapter. It is found that three different forces work on a single stone. Forces in the same direction as the falling direction and forces in the opposite direction as the falling direction (vertical forces) and forces perpendicular of the falling direction (horizontal forces).

The vertical forces are distinguished as the gravitational force, buoyancy force and the drag force. When the downward force is equal to the upward force. That is, the submerged weight of a particle equal to the drag force, the equilibrium settling velocity is reached. To determine this equilibrium velocity for rock the drag coefficient needs to be known. The determination of the drag coefficient is however quite ambitious because even for a sphere this is rather difficult. Nonetheless, several empirical relationships between the drag coefficient and the particle Reynolds number are compared. With these drag coefficients a comparison of the terminal velocity as function of the length-to-thickness ratio of a stone is illustrated in Figure 39.

The possible horizontal forces are found which act on a stone falling through water, a force due to a horizontal current and the lift force. The lift force, perpendicular to the settling direction, is caused by three different phenomena: vortex shedding, Magnus-effect and asymmetric boundary layer separation. For the current, an equation (6.32) is given which describes the movement of the settling rock for the equilibrium situation. This equilibrium situation is when the horizontal component of the settling velocity of a stone is equal to the current velocity of the surrounding water.

In the last part of this chapter a short overview of the knowledge and research done on the trajectory and motion of stones is given. Additionally, for the interaction of a stone with the seabed three different phenomena are elaborated: bouncing, rolling and sliding.

Chapter 7 Dumping of Multiple Stones: In chapter 6 the dumping of a single stone is elaborated. However, in practice large amount of rock are dumped by a fallpipe vessel when a rock placement operation is executed. Therefore, in chapter 7 will be looked at the dumping of multiple rocks, and the influence on each other.

[VAN DER WAL, 2002] defined five different phases for the settling process of rock groups. The five phases include all possible mechanisms which occur. These five phases are: acceleration of the group, deceleration of the group, a rock front of larger stones, settling process according to the Single Stone Model (SSM) and radial runoff.

In the last paragraph of this chapter hindered settling is treated. A comparison is made between different approaches to determine the coefficient which is needed to calculate the hindered settling velocity. This comparison is given in Figure 50.

Chapter 8 Dumping of Stones through a Fallpipe: For a deep water rock placement operation, rock is not dumped at the water surface but the method used is by guiding the rock to the seabed with a fallpipe. In the first section of this chapter different methods found in literature for determining the exit velocity from the orifice of the fallpipe are explained. There is the van Oord method which uses an iterative process for determining the exit velocity and the Tideway's method which uses a calculation tool whereby the optimal production rate can be established.

The second and last paragraph of this chapter reports on previous research for determining the spreading of rock below a flexible open fallpipe. Whereby the most promising variables were selected and give as: initial jet velocity, height above the seabed and stone diameter.

Chapter 9 Built-up of a Berm: In this chapter first of all an elaboration is given on the built-up of a berm when rock is dumped into stagnant water. In literature different models were found which describe this process, such as the single stone model, ring model and the combination model. Whereby the combination model is a hybrid of the random walk and ring model.

In the last part of this chapter an overview of different berm types seen in practice is given. In practice five different built-up of berms are seen. These are the basic berm, transitory berm, jetted profile berm, teardrop shaped berm and the flat berm.

Chapter 10 <u>Computational Fluid Dynamics:</u> In this chapter a brief introduction of computational fluid dynamics (CFD) is given. Fluid flows are governed by partial differential equations (PDE) which represent conservation laws. CFD replaces such PDE systems by a set of algebraic equations which can be solved by using a computer. The Navier-Stokes equations, which define any single-phase fluid flow, are the fundamental basis of almost all CFD problems.

All approaches for CFD follow the same basic procedure, and can be divided into three stage: pre-processing, simulation and post-processing. For the discretization of the Navier-Stokes equations three numerical methods are mainly used: the finite volume method, the finite element method and the finite difference method. Furthermore, some introduction to computational models for turbulent flows are given, such as: Reynolds-averaged Navier-Stokes (RANS), Large Eddy Simulation (LES) and Direct Numerical Simulation (DNS). In the last paragraph of the chapter some CFD solvers, commercial as-well as open-source, are elaborated.

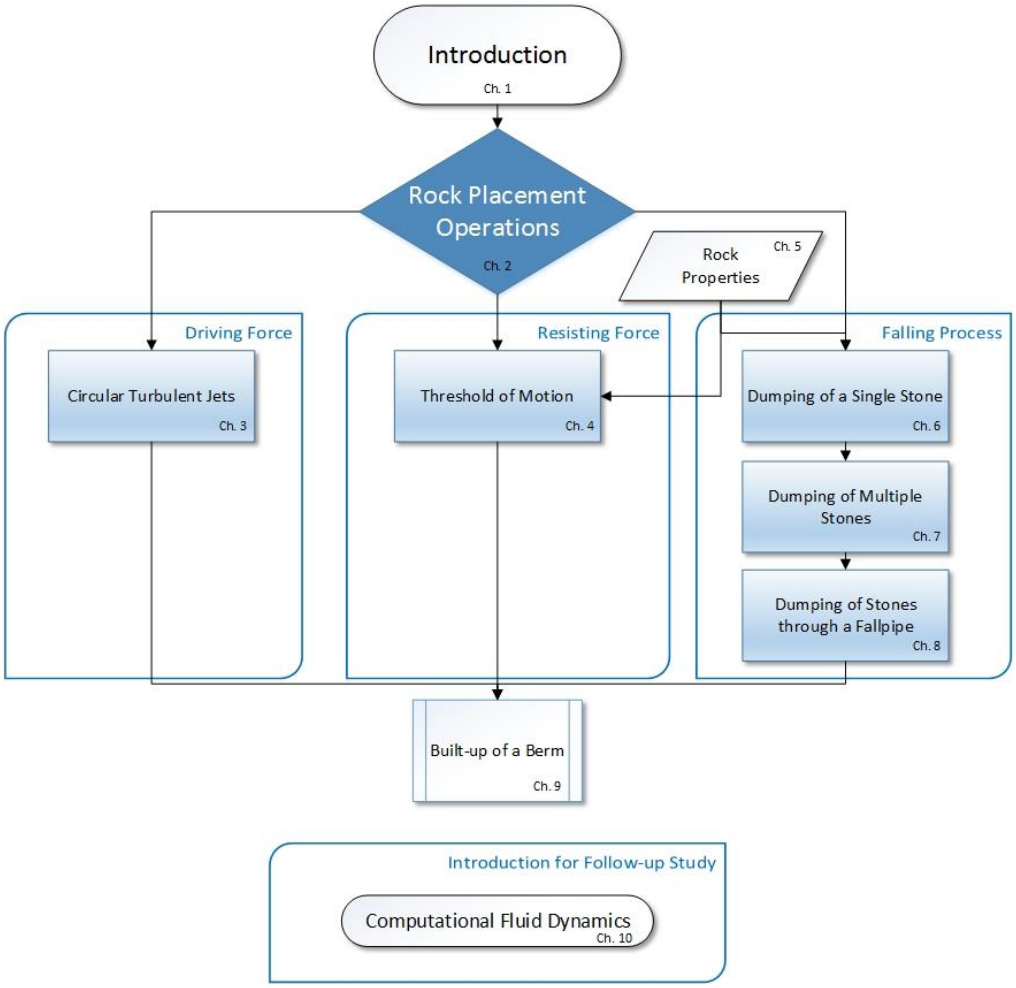

FIGURE 1: FLOWCHART OF THE LAYOUT OF THE LITERATURE STUDY

Contents

Readers Guide Literature Study I
Contents V
Tideway Offshore Solutions IX
1 Introduction 1
2 Rock Placement Operations 3
2.1 The Tideway Flintstone 3
2.2 Rock placement 5
3 Circular Turbulent Jets 9
3.1 Free jet 12
3.1.1 Zone of Flow Establishment 12
3.1.2 Transitional zone 14
3.1.3 Zone of Established Flow 15
3.1.4 Lee *et al.* 17
3.1.5 Turbulent buoyant jet 19
3.2 Vertical impinging jet 21
3.2.1 Large stand-off distance 21
3.2.2 Small stand-off distance 23
3.3 Wall jet 26
3.3.1 Large stand-off distance 27
3.3.2 Small stand-off distance 28
3.4 Concluding remarks 28
4 Threshold of Motion 29
4.1 Hydrodynamic Forces 30
4.2 Stability parameters 31
4.2.1 Shields 32
4.2.2 The Jongeling *et al.* stability parameter 34
4.2.3 The Hofland stability parameter 35
4.2.4 The Hoan stability parameter 36

4.3 Concluding remarks ... 40
5 Rock Properties ... 41
5.1 Rock types ... 41
5.2 Rock mass and sizes ... 42
5.3 Rock grading ... 43
5.4 Rock shapes ... 45
5.4.1 Length-to-thickness ration ... 45
5.4.2 Blockiness ... 45
5.4.3 Cubicity ... 46
6 Dumping of a Single Stone ... 47
6.1 Physical description of the settling process ... 47
6.2 Vertical forces ... 47
6.2.1 Gravitational force ... 47
6.2.1 Buoyance force ... 48
6.2.2 Drag force ... 49
6.2.3 Settling velocity ... 49
6.3 Horizontal forces ... 55
6.3.1 Lift force ... 55
6.3.2 Current ... 58
6.4 Trajectory and motion ... 58
6.5 Seabed interaction ... 59
6.5.1 Bouncing ... 59
6.5.2 Rolling ... 60
6.5.3 Sliding ... 60
7 Dumping of Multiple Stones ... 61
7.1 Settling process of rock groups ... 61
7.1.1 Phase 1: Acceleration of the group ... 61
7.1.2 Phase 2: Deceleration of the group ... 62
7.1.3 Phase 3: Rock front of larger stones ... 63
7.1.4 Phase 4: Settling process according to the SSM ... 64
7.1.5 Phase 5: Radial runoff ... 65

7.2 Hindered settling ... 66
8 Dumping of Stones through a Fallpipe ... 69
8.1 Jet velocity ... 69
8.1.1 Exit velocity ... 69
8.1.2 Centreline velocity ... 71
8.2 Spreading of rock ... 72
9 Built-up of a Berm ... 73
9.1 Single Stone Model ... 73
9.1.1 Berm built-up stages ... 73
9.1.2 Random Walk Model ... 75
9.1.3 Mathematical modelling of the Single Stone model ... 76
9.2 Ring Model ... 76
10 Computational Fluid Dynamics ... 79
10.1 Methodology ... 80
10.1.1 Discretization methods ... 80
10.1.2 Turbulence models ... 81
10.2 CFD Solvers ... 82
10.2.1 Commercial ... 82
10.2.2 Open-source ... 83
List of Figures ... 85
List of Tables ... 87
Bibliography ... 89
Nomenclature ... 93
Abbreviations ... 93
Greek Symbols ... 93
Roman Symbols ... 94
Subscripts ... 97

Tideway Offshore Solutions

FIGURE 2: TIDEWAY OFFSHORE SOLUTIONS' LOGO

Tideway Offshore Solutions, founded in 1991, are a company dedicated to serving the oil and gas industry. Tideway BV is based in Breda in the Netherlands and part of the Belgium based Dredging, Environmental and Marine Engineering (DEME) group of companies. The company is an expert in landfall construction, scour protection and pre- and post-dredging for the support of pipe laying operations. A second line of activity is the precision stone dumping for pipeline crossings, platform approaches and offshore ballasting. Operating three state-of-the-art fallpipe vessels, Tideway executes precision stone dumping up to depths of $2{,}000\,m$.

Rock placement

The company is also an expert in rock placement, with vast experience on projects for the oil and gas operators worldwide. Tideway's hi-tech Dynamic Positioning (DP) Fallpipe Vessels are the equipment of choice and the fleet has a capacity for precision work in depths up to $2000\,m$. Rock placement operations are executed with extremely high precision, even in these extreme water depths. Therefore, an active heave-compensated Remote Operated Vehicle (ROV) is fixed below the fallpipe, facilitating precision steering.

Seabed preparation is a special application for rock placement operations, which includes: pre-lay crossing rock placements, construction of supporting berms for a pipeline in rough terrain or coral area, gravel blankets, ramps for PipeLine End Manifolds and PipeLine End Terminals and building pre-lay free span supports.

Tideway has four DP Rock Placement Vessels: DP Side Stone Dumping Vessel Atlantis ($2{,}000\,t$) and the DP2 Fallpipe Vessels Seahorse ($18{,}500\,t$), Rollingstone ($11{,}500\,t$) and the Ice Class Vessel Flintstone ($20{,}000\,t$).

Landfall construction

The company has extensive experience in installing pipelines in coastal but also in near-shore waters. Tideway is equipped to install pipelines which discharge cooling- or wastewaters for power and water authorities. Depending on the project, the installation method for pipelines from on- to offshore or vice versa, entail pulling by an onshore sheave block from a lay barge winches, pulling by onshore or offshore winches, controlled surface tow or directional drilling.

Power cable installation

Tideway has the specialized knowledge, experience and techniques that are required for the installation of high voltage marine power cables. The company has worked on several world firsts in the power cable installation field. As example, the $576\,km$ high voltage NorNed power cable between Norway and the Netherlands, which has a world record length, was laid by Tideway. Furthermore, interconnecting power cables is a core specialism of Tideway.

Offshore dredging

Tideway operates one of the most modern and versatile dredging fleets in the industry, with vessels in every size and segment, assuring the ultimate flexibility. Offshore dredging encompasses pre-trenching, pre-sweeping, sand wave removal and prior pipe lay and glory hole dredging. All of these activities require high precision and the very highest standards of safety, quality and environmental care, in line with the demands of the oil and gas operators. Offshore dredging requires absolute precision and for this reason all of Tideway's dredgers are equipped with High Precision Dynamic Positioning software, which guarantees precision accuracy.

1

Introduction

Mankind finds itself in a never-ending battle against the influence of water. This has already been the case for centuries because the interface of land and water plays an important role in human activities. Ports were built and coastal protection was needed. For this purpose rock has been used for the construction of dikes, breakwaters, groins and for scour protection. Early on, this rock placement was done from shore and mainly by hand. Further development in the last century made it possible to mechanical dump rock from a vessel. For this offshore subsea rock placement two different types can be distinguished. Shallow water rock placement up to $50\,m$ depth and rock placement for greater water depths, usually ranging from 50 to around $2000\,m$. Rock placement up to $50\,m$ depth is typically used for embankment and coastal protection works and rock placement in deep water is most frequently applied for the offshore oil and gas industry.

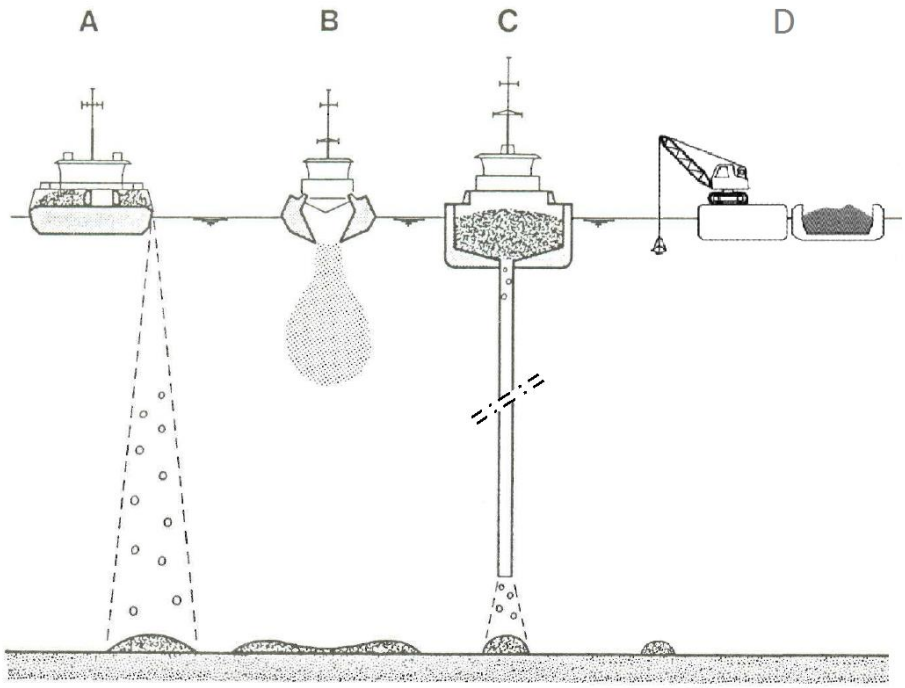

FIGURE 3: A) SIDE STONE DUMPING VESSEL, B) SPLIT HOPPER DREDGER, C) FALLPIPE VESSEL, D) DRAGLINE

The enormous difference in depth makes it interesting to use two kind of methods for rock placement operations. Therefore shallow water rock placement is mainly done by dumping the rock from the water surface after which it will move under free fall to the bottom. For deep water this method of rock placement gives a high spreading of the rock and rather the method of guiding the rock from the water surface to the bed is used.

Besides the different methods wherein rock placement is used also different techniques are used. The four main techniques are: side stone dumping, bottom door dumping, rock placement with the use of a fallpipe and dragline dumping. These four methods are presented in Figure 3 respectively.

Side stone dumping is done by a vessel whereby rock on the deck is pushed over the side with the use of hydraulic sliders. Side stone dumping vessels are self-propelled and can position themselves above the work. For bottom door dumping a split hopper barge or split hopper dredger is used. The difference between the two is that the split hopper dredger is self-propelled and the split hopper barge not. However, the method of dumping is the same, the bottom can split open and in a short time the whole load of rock is dumped. This is done by splitting the port and starboard halves which are hinged at the deck and operated by hydraulic cylinders. Both these techniques, side stone dumping and bottom door dumping, are primarily used in the shallow water region because the accuracy decreases with increasing water depth.

The dragline technique uses a bucket which descends into the water and the rock is placed at the desired location. This technique has a higher accuracy than the previous two, however it is still limited to rather shallow water due to the time consuming method of guiding the rock to the bed. For high precision deep water rock placement operations mainly a fallpipe vessel is used. The rock is dumped into a chute and from thereon guided to the bed by a fallpipe. This fallpipe consists of different sections and can have a total length up to $2000\,m$.

There are currently two different fallpipe systems in operation in the field, one with a flexible fallpipe and one with a closed fallpipe. The flexible fallpipe consists of a string of bottomless, heavy plastic buckets along two chains. For durability purposes a few buckets at the top and bottom of the pipe are made of steel. Due the open structure of this fallpipe a downward directed flow is caused by the dumping process. The closed fallpipe consist of steel pipe sections and therefore, as opposed to the flexible fallpipe, water is not able to enter the pipe over its length. However, in order to prevent the water level in the fallpipe falling too far, water is let into the fallpipe by means of a water inlet section located at the upper end. By this means, just as with the flexible fallpipe, a downward directed flow is caused by the dumping process.

Both fallpipe systems have a Remote Operated Vehicle (ROV) connected at the end of the fallpipe. The ROV is equipped with thrusters to manoeuvre the exit of the fallpipe. This is to assure the high precision of rock placement operations and to monitor the installation process accurately.

2

Rock Placement Operations

As mentioned in the introduction there are two different kind of fallpipe vessels, a flexible fallpipe and a closed fallpipe vessel. This study will further focus on the closed fallpipe vessel. The main advantage of a closed fallpipe over a flexible fallpipe is that the sort of "density current" inside the fallpipe can be better regulated by means of opening or closing the water inlet sections. By opening or closing water inlet sections the amount of water which will enter the fallpipe, and thus the downward directed flow, can be regulated.

Tideway owns three fallpipe vessels, all equipped with a closed fallpipe system. These are the Seahorse ($18{,}500\,t$), Rollingstone ($11{,}500\,t$) and the Flintstone ($20{,}000\,t$). All are equipped with a dynamic positioning system class 2, i.e. DP2, and the Flintstone even has an ice class notation. In this chapter the layout of the Flintstone will be described as well as the application of subsea rock placement.

2.1 The Tideway Flintstone

The "Tideway Flintstone" is called a Dynamic Positioned Fall Pipe vessel. The main activity of this vessel is rock placement operations at large water depths with great accuracy at offshore locations. The rock is guided to the seabed by the closed fallpipe. By doing so the effect of the current and the spreading of the rock can be minimized which guarantees greater accuracy. Besides from rock placement, common operations also consists of surveying, loading rock or sailing between the project site and quarry. In Figure 4 a layout of the Flintstone can be seen.

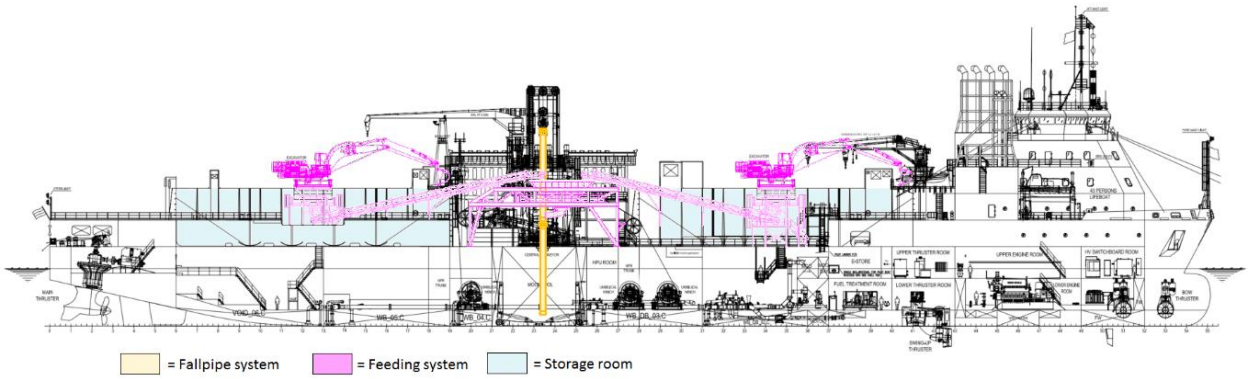

FIGURE 4: LAYOUT OF THE TIDEWAY FLINTSTONE

Three main features of the vessel can be distinguished as: the storage room, the feeding system and the closed fallpipe system. The storage room of the vessel is made out of different holds wherein the material is placed. During rock placement operations, the rock is discharged from the bunkers and thereafter these can be filled with ballast water. This is done to ensure the stability of the vessel and to compensate for an unequally distributed cargo. This process is reversed when new rock is loaded on the vessel at the quarry.

The feeding system consists of rotatable excavators, conveyor belts, a central hopper and inflow chute. The process starts with the rock being scooped from the storage holds. This is done with a bucket or a poly grab. The poly grab is used for extra-large stones to reduce the wear and tear on the excavator. The rock will be placed on a conveyor belt and transferred to the central hopper, also called the buffer hopper. With an adjustable feeder this hopper guides the rock to the central conveyor belt. From there on the rock is dumped in the inflow chute. The chute is a funnel shaped inlet which has a smaller opening than the fallpipe diameter. The reason for this is that a possible blockage caused by stones will occur in the chute rather than in the fallpipe. The chute is located at deck level and therefore easy accessible in comparison to the fallpipe self. After the chute receives the stone that fall from the central conveyor belt, it is led to the fall pipe. In order to built-up the fallpipe system the whole system is lowered through the moonpool, which is a square shaped opening in the vessel with direct access to the water below. In Figure 5 a detailed built-up of the fallpipe is shown.

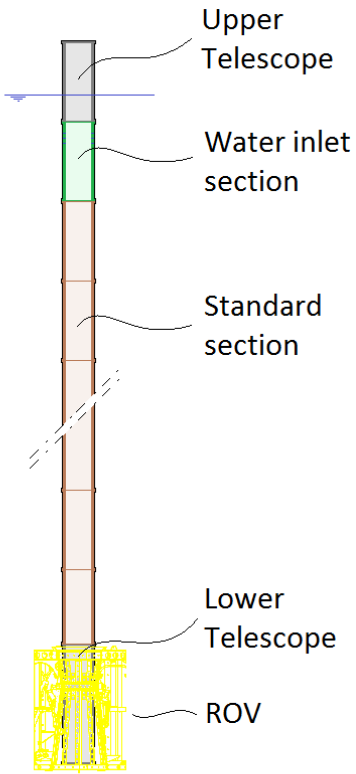

The fallpipe consists of different standard sections which are mounted on top of each other. On top of the standard steel sections the water inlet section is placed. The water inlet is a section of fallpipe which has four rings of variously sized holes. As indicated before, these holes allow a different amount of water to enter the fall pipe due to various combinations. It is very important that water can enter the fallpipe when working at medium range to considerable depths in order to avoid a fallpipe section becoming overstressed from the water pressures and collapsing as a consequence.

The upper telescope, on top of the water inlet section, consists of two pipe sections whereby one section can slide into the other. The upper part is connected with wires to the vessel and the lower part rests on the water inlet section.

All these sections rest upon the lower section which is called the suspension section. This suspension section is connected on top of the lower telescope, this is the part that fits through the Remote Operated Vehicle (ROV). It is equipped with Teflon, a synthetic material, acting as bumper strips in order to absorb the forces between the ROV and the fallpipe during steering.

FIGURE 5: FALLPIPE BUILT-UP

The lowest part of the fallpipe system is the ROV. The function of the ROV is to steer the outer end of the fallpipe, serve as a survey platform and to monitor the rock installation process. The ROV is a cylindrical shaped structure which hangs on three armoured umbilical cables. The umbilicals are equipped with electrical wires, twisted pairs and fibre optic cables in order to power the hydraulic motors and survey equipment. Two deployable arms, attached with different types of instruments, such as cameras, lights and profilers, are connected to the ROV.

Some considerations with respect to the fallpipe operations of the Flintstone [ROLAND, 2012]

- In general at a depth of $2000\,m$ mainly small material is used for insulation of a pipeline or cable. At this depth protection against waves is irrelevant.
- The Flintstone uses pipe sections with a diameter of $0.65\,m$.
- During the dumping of rock, the water surface inside the fallpipe could not be observed due to the mixture level drop. When the dumping of the rock is stopped, and while the system settles, a significant amount of air bubbles appears at the water surface.

2.2 Rock placement

Fallpipe vessel can be used in a large variety of rock placement projects in the offshore industry, which will be explained in this paragraph. However, for all applications of rock placement the height above the seabed which is desired is generally in between 3 and $8\,m$. Usually, the height will be approximately $5\,m$. Rock can be installed from a higher position to attain more dispersal of the stones or lower for precise installation as in remedial rock placement by respectively extending or retracting the upper telescope. For safety reasons is a stand-off distance of $3\,m$ the absolute minimum limit. The advantage of the upper telescope is also that reasonable depth- and tide differences can be easily compensated for.

Pre-lay seabed preparation works

The unevenness of a seabed is levelled with seabed preparation works, also referred to as pre-lay rock installation. An uneven seabed or sharp features on the seabed might damage the pipeline or cable. Pre-lay rock installation can be done in a single long berm or as spot berms. The distance between two spot berms depends on the strength of the pipeline because every pipeline is able to withstand a free span up to a certain length.

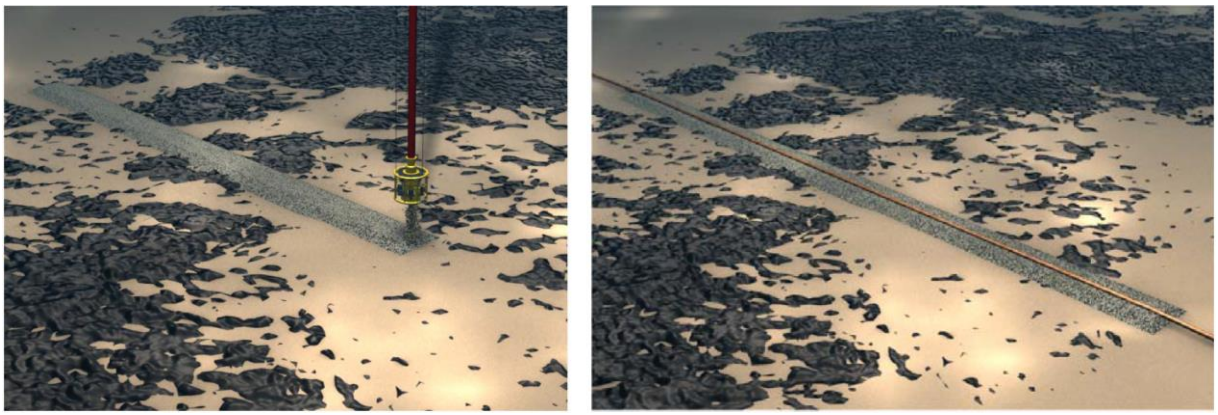

FIGURE 6: SINGLE LONG BERM

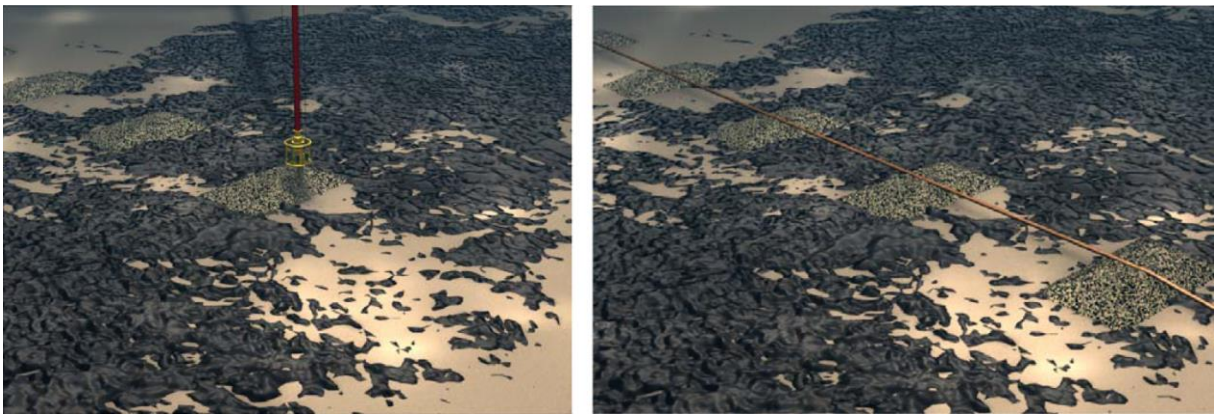

FIGURE 7: SPOT BERMS

Scour protection

When structures are placed on the seabed, such as wind turbine foundations or oil platforms, they are subjected to wave- and current velocities. These wave- and current velocities tend to wash away the sand around the structures. The stability of the foundation is affected by this process and can cause failure of the structure. To prevent such a scour hole, rock can be placed around or underneath structures. For the rock placement underneath structures the normal fallpipe cannot be used due to the lack off room. Because of this a special fallpipe, the inclined fallpipe, will be used.

Pipeline protection

In order to protect a pipeline against fishing trawlers or dragging anchors it can be completely protected by a single long rock berm. This will be often done in places where a lot of sea-going activities take place. When a pipeline or cable needs to be protected against trawling activities, the grading of the rock needs to be smaller than the mesh of the commonly used nets. So that the stones slip nicely through and are not dragged along with the fish in the net. Also subsea structures require protection so that anchors or trawling nets slide smoothly over.

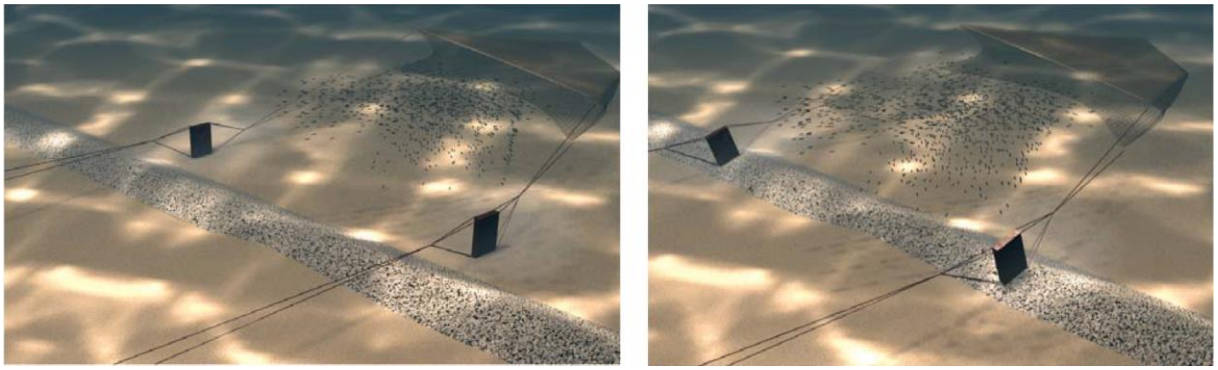

FIGURE 8: PROTECTED PIPELINE AGAINST FISHING TRAWLERS

Upheaval buckling prevention

Upheaval buckling must be prevented because this can cause damage to a pipeline. Upheaval buckling can occur since oil and gas is transported through the pipeline and this can effect in the pipeline to buckle up, due to high temperatures, from the seabed or even from a backfilled trench. As a preventive measure a certain berm design is required, over determined intervals, along the pipeline. When a pipe is already risen from the seabed a corrective intervention can stabilize the pipe in order to avert further damage.

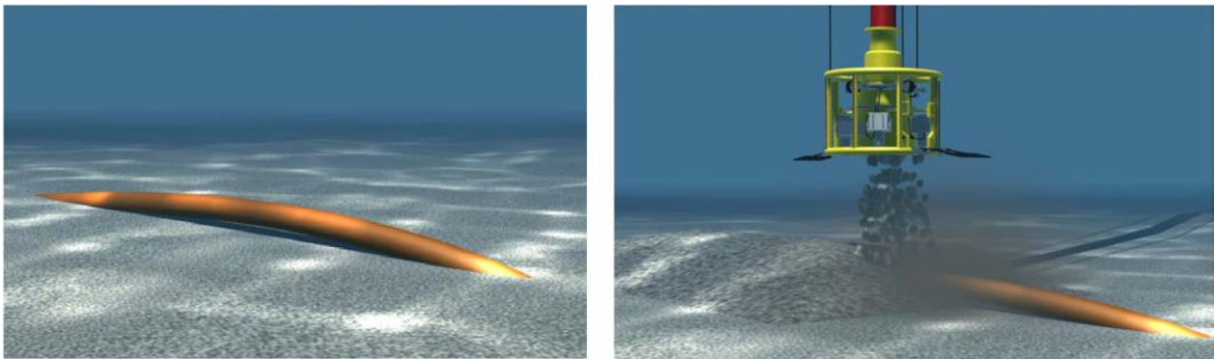

FIGURE 9: UPHEAVAL BUCKLING OF A PIPELINE

Insulation

The fluid which goes through a pipeline often needs to be at a certain predetermined temperature. To maintain this critical temperature pipeline insulation can be used. Generally a mixture of sand and rock is used because of the minor voids. This fine material easily goes into suspension when under water. Therefore it is quite difficult to build a satisfying insulation berm. Possible solutions are to place two supporting rock berms on either side of the pipeline as a sort of an artificial berm or at the quarry a small amount of stones will be loaded on top of the mixture.

Crossings

When a new pipeline needs to cross an existing laid pipeline, rock placement is also used. First, pre-lay rock placement will be performed by creating a gentle slope to assure a safe and stable crossing. This is done by placing a spot berm at either side of the existing pipeline or cable, as well as placing a complete berm over the existing pipeline. Secondly, post-lay rock placement will be performed in order to stabilise the newly installed pipeline or cable and to protect the crossing.

3

Circular Turbulent Jets

A distinction between different kinds of fluid intrusions into other fluids can be made. Nonetheless, in every case, a fluid with some buoyancy (the difference in density) and/or momentum exits from a relative narrow orifice and intrudes into a larger body of fluid with different characteristics, such as a different density or speed. As can be seen in Table 1, a jet is defined as a flow which is driven by the continuous addition of momentum at the source. A plume is defined as a flow which is driven by the continuous addition of buoyancy, and a buoyant jet is driven by the continuous addition of both buoyancy and momentum at the source.

TABLE 1: THE TERMINOLOGY OF TYPES OF FLUID INTRUSIONS

	Continuous injection	Intermittent injection
Momentum only	Jet	Puff
Buoyancy only	Plume	Thermal
Both momentum and buoyancy	Buoyant jet	Buoyant puff

The flow below the fallpipe is both momentum and buoyancy driven and is therefore called a buoyant jet. The jet, just as any fluid flow, can be either turbulent or laminar. If a fluid flow is turbulent or laminar depends on the Reynolds number which is given as:

$$Re = \frac{u * L}{\nu} \tag{3.1}$$

With:

Re	Reynolds number	$[-]$
u	characteristic velocity	$[m/s]$
L	characteristic length	$[m]$
ν	kinematic viscosity	$[m^2/s]$

The exact Reynolds number at which the transition between the laminar and turbulent flow occurs is not predictable, but in general for $Re > 2000$ turbulent flow can be assumed. The behaviour of a turbulent jet is described by [FISCHER *et al.*, 1979] and depends on three classes of parameters: geometrical factors, jet parameters and environmental parameters. The first group refers to the jet's direction, shape and proximity to boundaries or free surfaces. The jet parameters consists of the jet velocity distribution and turbulence level, jet momentum flux, jet mass flux and the flux of the jet tracer material. The third group include ambient factors such as turbulence and currents. These environmental parameters, when present, start to influence the jet at a certain distance from the orifice. The dispersion process of a buoyant jet in a low energetic system, with no background currents, is classified in three categories by [FISCHER *et al.*, 1979].

- **Density current:** the buoyant jet spreads in the water column predominantly as a density current.
- **Dispersion:** The buoyant jet is dispersed and transported by the momentum induced by the exit geometry.
- **Transitional:** The processes of momentum and density current are of the same magnitude. Therefore the plume behaviour does not suit the description of one of the other categories.

Also the characterization of a jet is described by [FISCHER *et al.*, 1979] and depends on three flow parameters: mass flux, specific momentum flux and specific buoyancy flux. The initial values of these fundamental fluxes for a circular jet can be calculated as follows:

$$Q_0 = \frac{1}{4}\pi * D^2 * u_0 \tag{3.2}$$

$$M_0 = \frac{1}{4}\pi * D^2 * {u_0}^2 \tag{3.3}$$

$$B_0 = Q_0 \left(\frac{\rho_m - \rho_f}{\rho_f}\right) g \tag{3.4}$$

With:

Q_0	jet volume flux	$[m^3/s]$
D	diameter of the fallpipe	$[m]$
u_0	initial jet velocity	$[m/s]$
M_0	jet momentum flux	$[m^4/s]$
B_0	jet buoyancy flux	$[m^3/s^3]$
ρ_m	mixture density	$[kg/m^3]$
ρ_f	fluid density	$[kg/m^3]$
g	gravitational acceleration	$[m/s^2]$

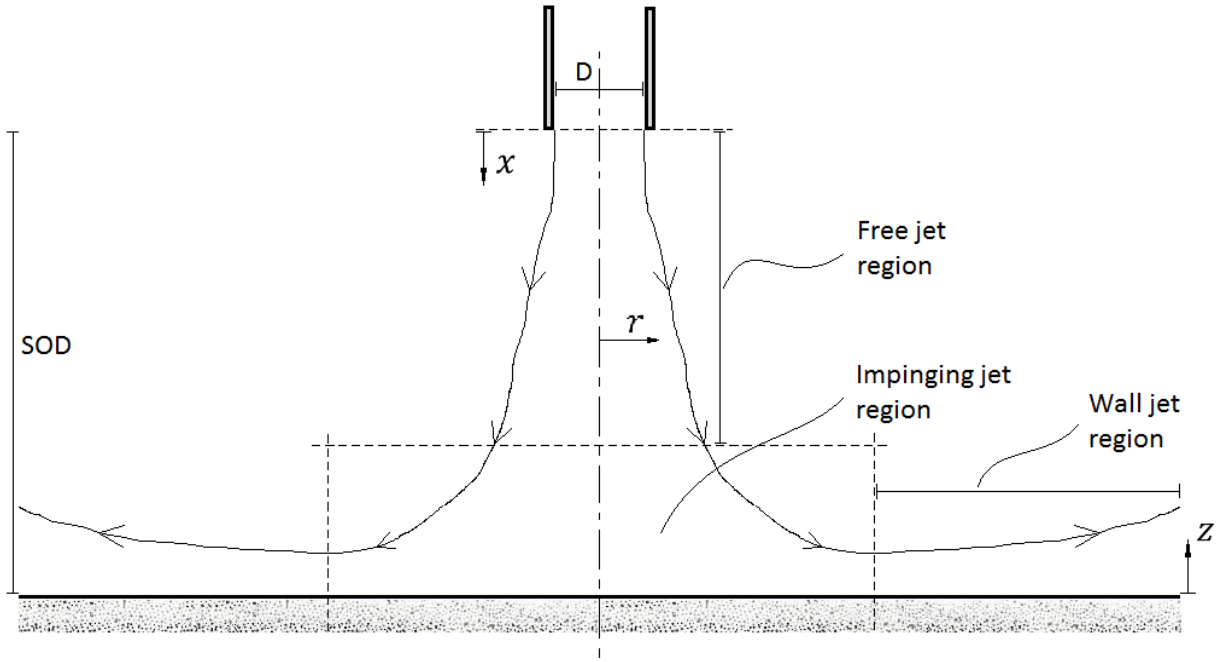

FIGURE 10: DIFFERENT FLOW REGIONS OF A JET BELOW A FALLPIPE

With:	SOD	stand-off distance	$[m]$
	r	radial distance	$[m]$
	x	vertical distance	$[m]$

In addition, the flow inside the fallpipe is restricted by the fallpipe sections. However, when the flow reaches the mouth of the fallpipe it is not restricted by the boundaries anymore and from thereon it is called a free buoyant jet. When the end of the fallpipe has enough height above the bed this turbulent jet will remain a free jet. When this distance is limited the jet will be deflected by the bed, this is defined as the impinging jet region. Therefore the jet below the fallpipe can be divided into three regions: the free jet region, the impinging jet region and the wall jet region. In Figure 10 the different regions are presented and are further elaborated in this chapter.

Without rock being dumped into the chute and going through the fallpipe the density inside the fallpipe will not increase. This means that the density inside the fallpipe is the same as the density outside the fallpipe. Therefore the water level inside the fallpipe will not drop and no downwards directed flow through the fallpipe will be generated because water will not flow through the water inlet sections. Nonetheless, in this chapter will be looked at the characteristics and velocity profile of the jet without any rock present. This is done to get a better understanding of the different processes of a jet involved.

3.1 Free jet

As explained, the flow is no longer restricted by the fallpipe sections when it reaches the mouth and enters the ambient fluid. This is the reason why the turbulent jet is called a free jet. The incompressible submerged jet flow, or the free jet, can be further separated into three zones: the initial region, the fully developed region and the transitional region [LEE *et al.*, 2010]. These three zones are also called the Zone of Flow Establishment (ZFE), Transitional zone and Zone of Established Flow (ZEF) respectively. The different regions are shown in Figure 11. The fallpipe has a circular orifice and therefore the jet spreads out radially, symmetrical to the centreline of the jet.

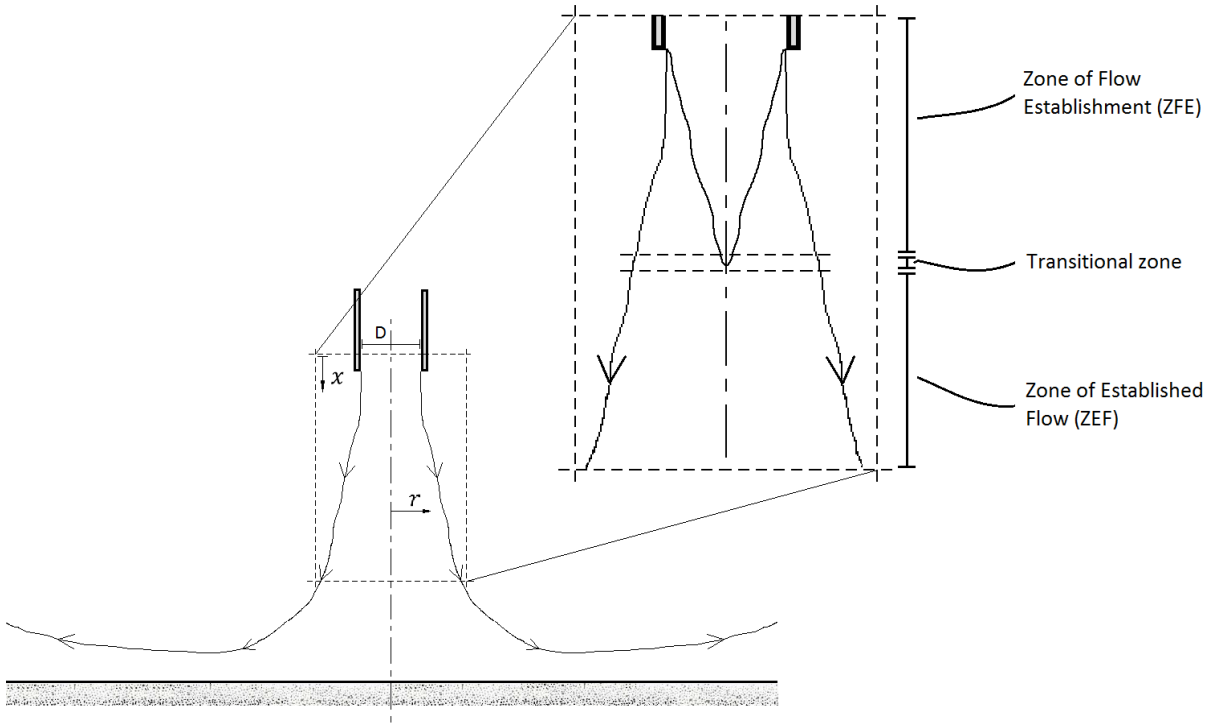

FIGURE 11: THE THREE ZONES OF THE FREE JET

3.1.1 Zone of Flow Establishment

When the turbulence generated on the boundaries, of the non-constricted flow, penetrates to the centre of the jet the mean velocity on this axis begins to decay with distance from section 1 – 1, in Figure 12. Before section 1 – 1, a core of fluid, in the form of a cone, with an undiminished velocity is situated. This cone is known as the potential cone or more often used, the potential core. The zone from the orifice to the end of the potential core is known as the Zone of Flow Establishment (ZFE).

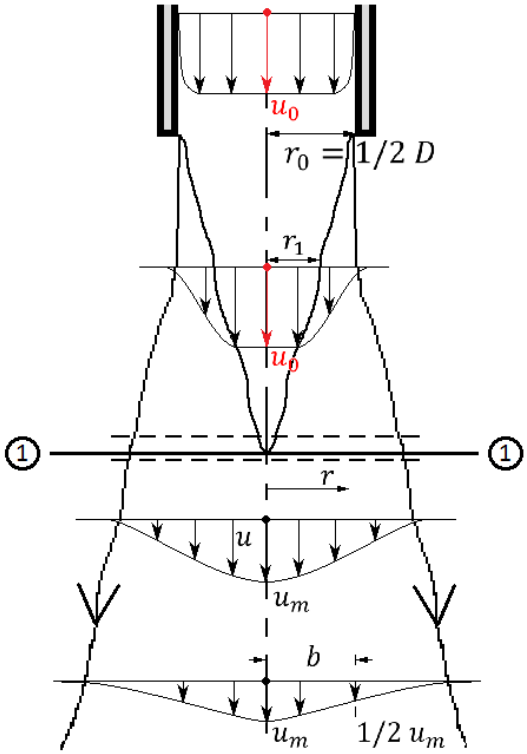

FIGURE 12: FREE JET VELOCITY PROFILE

In 1972 Rajaratnam and Pani [RAJARATNAM, 1976] researched the length of this potential core. They found an empirical equation to describe the relation between the dimensionless radius of the core and the dimensionless distance from the orifice.

$$\frac{r_1}{r_0} = 0.95 - 0.097\frac{\bar{x}}{r_0} \tag{3.5}$$

With:	r_1	distance from centre to the edge of the core	$[m]$
	r_0	radius of the jet	$[m]$
	$\bar{x}$	potential core length	$[m]$

Eq. (3.5) indicates that the length of the potential core is about ten times the radius, or five times the diameter of the orifice. Also, the experimental results of Rajaratnam and Pani in 1972 have shown that the angle of the inner edge of the shear layer is about 5.7° whereas the angle of the outer edge is about 9.0° [RAJARATNAM, 1976].

In general the velocity profile of the cross section of a jet can be expressed as a Gaussian distribution:

$$u = u_m * e^{-\left(\frac{r}{b}\right)^2} \tag{3.6}$$

With:	u_m	maximum velocity	$[m/s]$
	r	radial coordinate	$[m]$
	b	spreading width	$[m]$

The maximum velocity in the flow field of a free jet can be found in the centre of the jet, see Figure 12. In this case is thus the initial and centreline velocity equal to the maximum velocity $(u_0 = u_c = u_m)$. [RAJARATNAM, 1976] found, when $r > r_1$, the velocity field of the ZFE can be calculated with:

$$u = u_0 * e^{-0.693\left(\frac{r-r_1}{b}\right)^2} \tag{3.7}$$

With: $\frac{b}{r_0} = 0.10 + 0.111\frac{\bar{x}}{r_0}$

The distance from the centre to the edge of the core r_1 in Eq. (3.7) can be determined with Eq. (3.5).

In 1950 Albertson *et al.* also developed an equation for the flow rate, and when reduced to an expression containing the entrainment velocity, is written as [RAJARATNAM, 1976]:

$$\frac{v_e}{u_0} = \frac{2r_0}{r_2}\left(0.010 + 0.003\frac{\bar{x}}{2r_0}\right) \tag{3.8}$$

With:

v_e	entrainment velocity	$[m/s]$
r_2	distance from inner to outer edge	$[m]$

The observations of Hill on the entrainment velocity are reproduced in Figure 13 where it is shown that the dimensionless entrainment velocity increases to the fully developed jet value of 0.026 at around four times the dimensionless distance from the orifice.

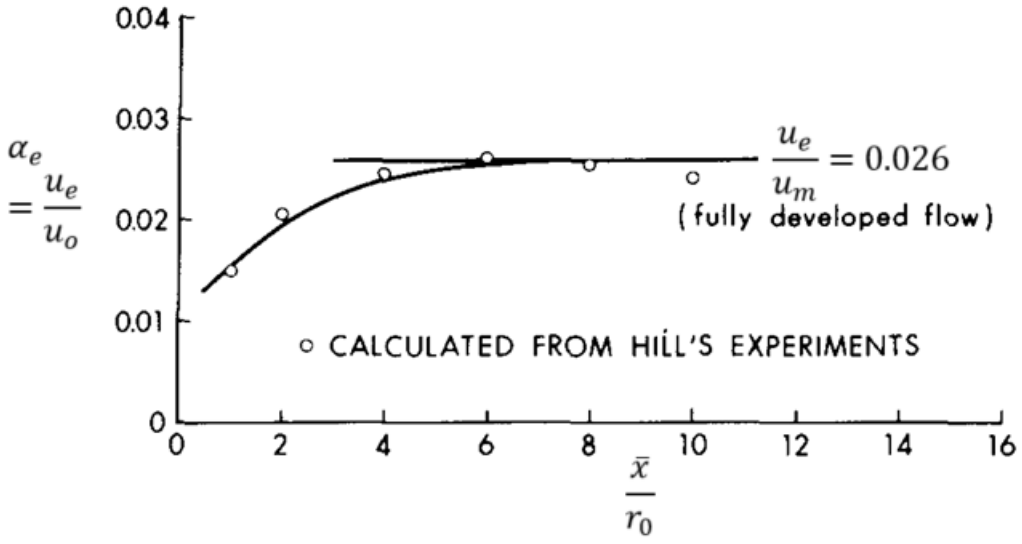

FIGURE 13: ENTRAINMENT COEFFICIENT IN THE ZFE FOR CIRCULAR JETS

3.1.2 Transitional zone

The transitional zone is the small part between the ZFE and ZEF. In literature little can be found on this zone because it is usually neglected. The reason for this is because the influence and length of this zone is small. Therefore no further elaboration in this literature study will be done and this zone will be further neglected.

3.1.3 Zone of Established Flow

The zone away from the end of the potential core is known as the Zone of Established Flow (ZEF). In this zone the velocity decreases, at any section, continuously from a maximum value at the centre of the jet to zero far away from the centre, see Figure 12.

[RAJARATNAM, 1976] gave two solutions for the centreline velocity for the fully developed region. A solution based on the Prandtl mixing length hypothesis, a Tollmien-type solution. And a solution based on the eddy viscosity model of Prandtl, the Goertler-type solution.

Tollmien-type solution
[RAJARATNAM, 1976] derived the Tollmien-type solution and is written as:

$$u_m = u_0 * \frac{0.965 r_0}{\alpha * x} \tag{3.9}$$

With: α coefficient [−]

The Tollmien-type solution describes the experimental observations conducted by Trupel well and it is found that the solution agrees better for the outer regions. For a nozzle, with uniform velocity distribution, taking $\alpha = 0.066$, the relation for the centreline velocity becomes:

$$u_m = 14.64 u_0 * \frac{r_0}{x} \tag{3.10}$$

Goertler-type solution
[RAJARATNAM, 1976] also derived the Goertler-type solution and is written as:

$$u_m = u_0 * \frac{\sigma}{1.61} * \frac{r_0}{x} \tag{3.11}$$

With: σ constant [−]

Near the axis of the jet, the Goertler-type solution is slightly superior to the Tollmien curve. When $\sigma = 18.5$ is taken, as was determined using the experimental observations of Reichardt, the equation for the centreline velocity becomes:

$$u_m = 11.5 u_0 * \frac{r_0}{x} \tag{3.12}$$

[RAJARATNAM, 1976] made a comparison between the above mentioned solutions of the velocity field for the fully developed region. It was suggested, for practical purposes, that the following equation is used for the centreline velocity:

$$u_m = 12.6 u_0 * \frac{r_0}{x} \tag{3.13}$$

The solutions for the centreline velocity of the previously mentioned expressions agree well with the length of the potential core which can be calculated with (3.5). This relation indicates that the length of the potential core is about 10 times the radius of the jet, for the formulae (3.11), (3.12) and (3.13) this is between 11.5 and 14.64 times the radius. In the graph below a comparison between the predicted centreline velocities by the Tollmien-type, Goertler-type, Rajaratnam and Lee *et al.* is presented.

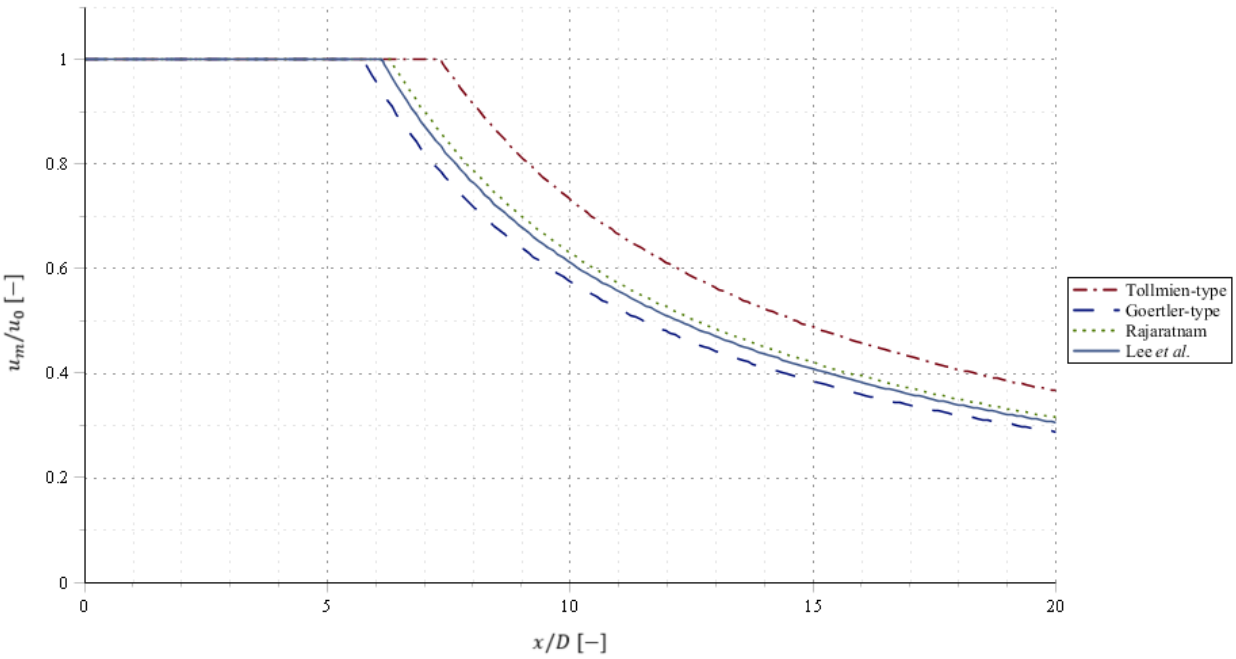

FIGURE 14: CENTRELINE VELOCITIES FOR THE DIFFERENT EXPRESSIONS

Now, with the use of the maximum velocities, which are the centreline velocities, the jet velocity for the ZEF can be calculated. The general form of the Gaussian distribution given in (3.6) was adapted by [RAJARATNAM, 1976] to this end:

$$u = u_m * e^{-0.693\left(\frac{r}{b}\right)^2} \tag{3.14}$$

Different values for b for the ZEF are found by experiments, however, for practical use the following relation can be used according to [RAJARATNAM, 1976]

$$b = 0.10x \tag{3.15}$$

Jet velocity of a free jet

In the previous sections the jet velocity for the ZFE and ZFE are determined. In Figure 15 the normalized jet velocity is plotted versus the radial coordinate for several distances. It is easily noticed that the jet velocity still equals the initial velocity to a certain distance, i.e. the flow is still in the ZFE (3.7). After this, the ZEF (3.14) is reached and the normalized jet velocity experience quite some dispersion.

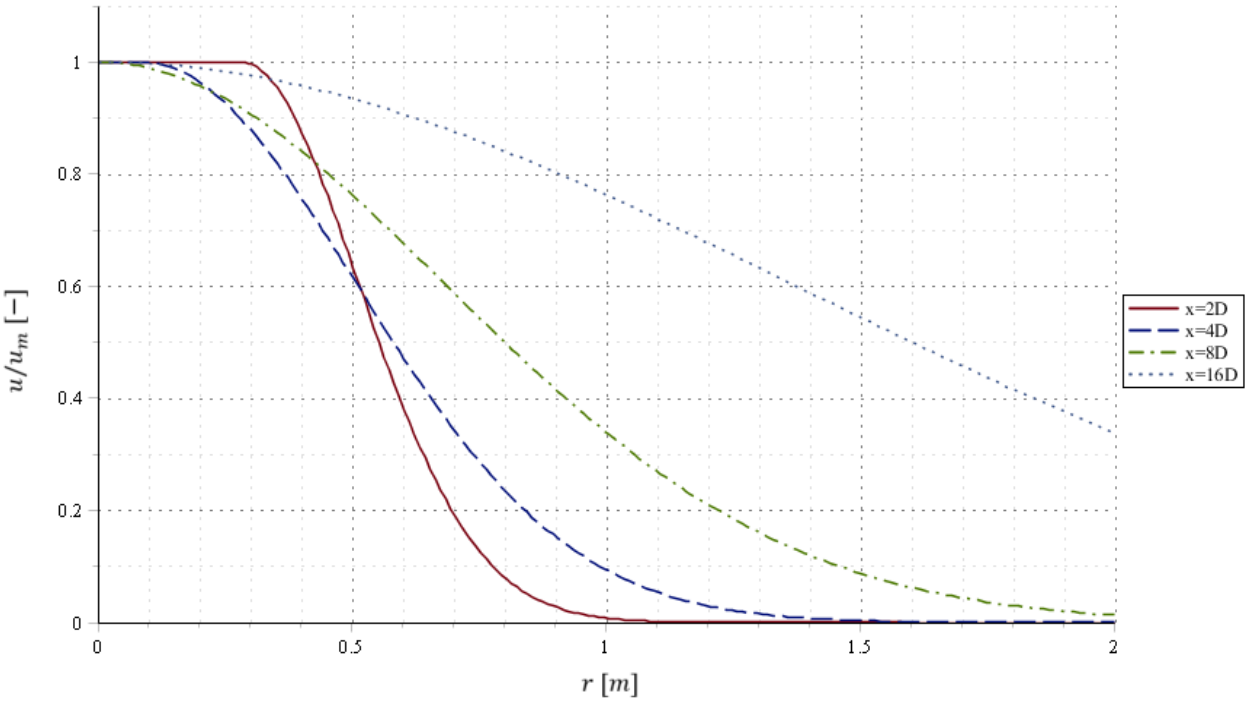

FIGURE 15: JET VELOCITY AS FUNCTION OF THE RADIAL COORDINATE FOR A FREE JET BY RAJARATNAM

3.1.4 Lee *et al.*

[LEE *et al.*, 2009] wrote a paper on the establishment of a new formula to describe the velocity profile of a jet flow in the case of the initial region being long enough not able to be neglected. Especially when the jet flow has a large orifice. As mentioned before, usually the velocity profile of a submerged turbulent jet with a small exit can be expressed as a Gaussian distribution, see (3.6).

[LEE *et al.*, 2009] proposed a new formula to describe the velocity profile when the ZFE cannot be neglected. By this, the velocity profile also cannot be expressed in a Gaussian distribution, however, the profile still answers for axial symmetry in the ZFE. The formula proposed by Lee et al. is written as:

$$u = u_m * e^{-\left[\left(\frac{r}{b^*}\right)^2\right]^{\xi(x)}} \tag{3.16}$$

With:			
	$\xi(x)$	radial adjusting coefficient	$[-]$
	b^*	spreading width by Lee *et al.*	$[m]$

The radial adjusting coefficient for a submerged circular jet is given as:

$$\xi(x) = e^{\frac{x^\Delta}{x}} \tag{3.17}$$

With:			
	x^Δ	characteristic length of a circular round jet	$[m]$

The characteristic length of a submerged circular jet is given as:

$$x^{\Delta} = 6.11D\left(\frac{u_{\infty} + u_0}{u_0}\right) \tag{3.18}$$

With: u_{∞} ambient flow velocity $[m/s]$

The whole centreline velocity of a free jet flow can hereby be rewritten as:

$$u_m = \begin{cases} u_0 & 0 \le x \le x^{\Delta} \\ \dfrac{x^{\Delta}}{x} * u_0 & x \ge x^{\Delta} \end{cases} \tag{3.19}$$

In the first part, the centreline velocity is equal to the initial jet velocity. Further away from the orifice the centreline velocity decays with $1/x$ dependence. It should be noted that this expression is only valid for high Reynolds numbers, so for a jet in the turbulent regime. At low Reynolds numbers the flow will be laminar with a higher distance from the mouth of the fallpipe. This will result in a larger characteristic length than given by (3.18). The spreading width of the jet flow velocity, for the determination of (3.6) and (3.16), is given as [LEE *et al.*, 2009]:

$$b^* = \frac{D}{2} * \left[\frac{(u_0^2 + 2u_0 * u_{\infty})}{2u_m * u_{\infty} * A_1 + 1.1u_m^2 * A_2}\right]^{\frac{1}{2}} \tag{3.20}$$

With:

$$A_1 = \sum_{n=0}^{\infty}\left[(-1)^n * \frac{1}{n!} * \frac{(\ln 100)^{-\left(n+\frac{1}{\xi}\right)}}{(\xi * n + 1)}\right] \quad [-]$$

$$A_2 = \sum_{n=0}^{\infty}\left[(-1)^n * \frac{2^n}{n!} * \frac{(\ln 100)^{-\left(n+\frac{1}{\xi}\right)}}{(\xi * n + 1)}\right] \quad [-]$$

Jet velocity of a free jet

In the previous sections the jet velocity for the entire free jet is determined (3.16). In Figure 16 the normalized jet velocity is plotted versus the dimensionless radial coordinate for several distances. It is easily noticed that the jet velocity still equals the initial velocity to a certain distance, i.e. the flow is still in the ZFE. Besides, as comparison to the jet velocity by Rajaratnam the jet velocity by Lee *et al.* still has an increasing dispersion after reaching the ZEF.

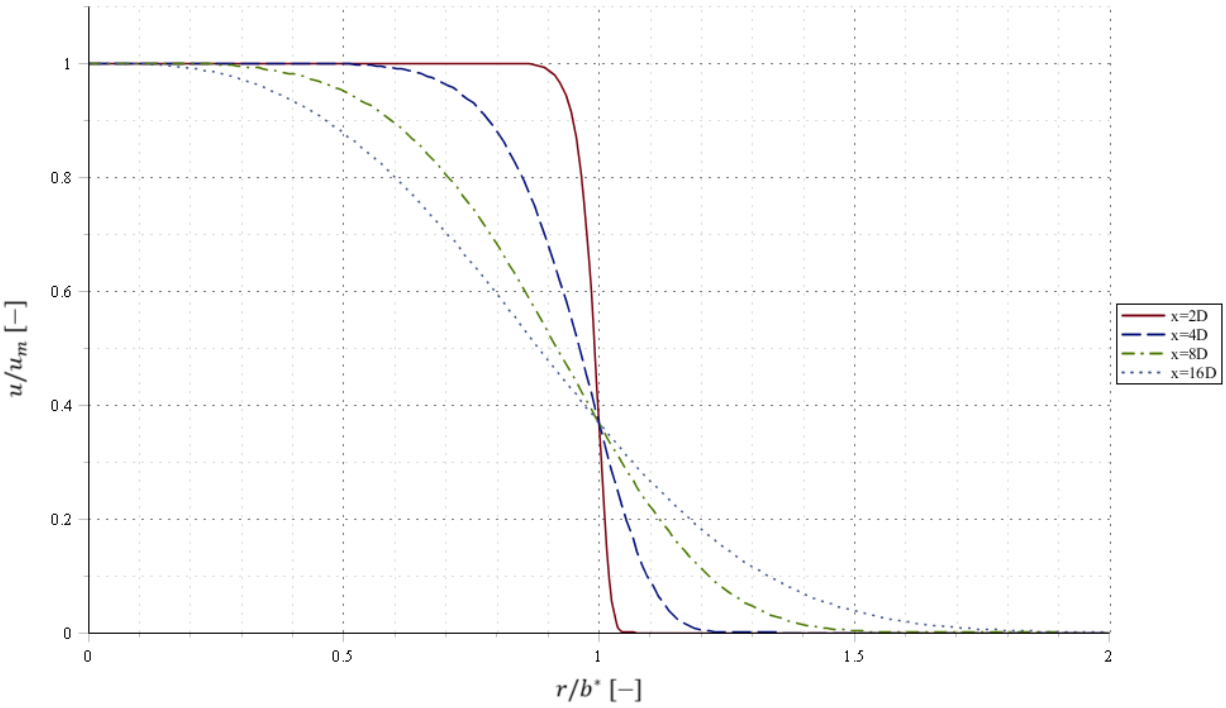

FIGURE 16: JET VELOCITY AS FUNCTION OF THE NORMALIZED RADIAL COORDINATE FOR A FREE JET BY LEE *ET AL.*

3.1.5 Turbulent buoyant jet

In the previous sections the free jet region of the turbulent buoyant jet was divided in the three mentioned zones. In addition, the turbulent buoyant jet can also be divided when looking at the jet flow parameters given in (3.2), (3.3) and (3.4). With the use of these jet flow parameters several length scales were defined by [FISCHER *et al.*, 1979].

Length scales

For a simple turbulent round jet a characteristic length scale for the jet can be derived from the volume flux (3.2) and momentum flux (3.3). When this characteristic length scale is made dimensionless it is given as [FISCHER *et al.*, 1979].

$$\frac{L_Q}{SOD} = \frac{Q_0}{SOD * M_0^{1/2}} \tag{3.21}$$

With: L_Q discharge-momentum length scale $[m]$

The fully developed region of the jet is reached when the discharge-momentum length scale over the stand-off distance is $\gg 1$. While the exit geometry still plays an important role when the discharge-momentum length scale over the stand-off distance is $\mathcal{O}(1)$.

A buoyant jet, as defined by Table 1, behaves like a jet depending on its initial volume and momentum fluxes. The plume-like behaviour is depending on its initial buoyancy flux. When the stand-off distance is large enough, i.e. enough free distance is given, a buoyant jet will always turn into a plume. Therefore a length scale which indicates the location where the transition from momentum dominated behaviour to buoyant dominated behaviour can be derived. It is assumed that the flow has both a momentum and buoyancy flux, but no initial volume flux. This momentum-buoyancy length scale, when made dimensionless, is given as [FISCHER *et al.*, 1979]:

$$\frac{L_{MB}}{SOD} = \frac{M_0^{3/4}}{SOD * B_0^{1/2}} \tag{3.22}$$

With: L_{MB} momentum-buoyancy length scale $[m]$

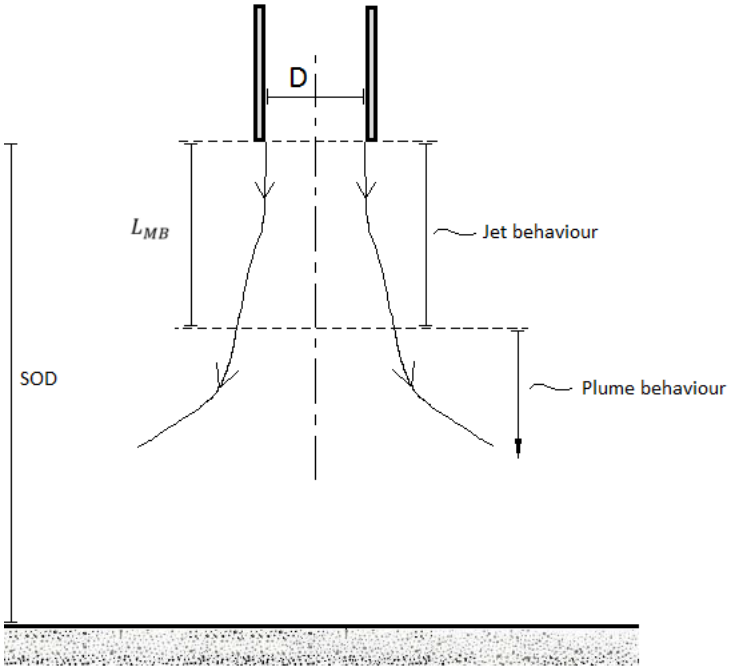

FIGURE 17: BUOYANT JET BEHAVIOUR

When the momentum-buoyancy length scale over the stand-off distance is $\ll 1$ the flow is dominated by the momentum flux (Jet behaviour). On the other hand, when the momentum-buoyancy length scale over the stand-off distance is $\gg 1$ the flow is dominated by the buoyancy flux (Plume behaviour), see Figure 17.

As already stated, when (3.21) is $\ll 1$ the fully developed region of the jet is reached. While the exit geometry still plays an important role when (3.21) is $\mathcal{O}(1)$. Thus, if the discharge-momentum and momentum-buoyancy length scale are in the same order then the flow will be very similar to a plume from the orifice. The ratio between these two length scales is called the jet Richardson number and is given for a round jet as [FISCHER *et al.*, 1979]:

$$R_0 = \frac{L_Q}{L_{MB}} = \frac{Q_0 * B_0^{1/2}}{M_0^{5/4}} = \frac{1}{4}\pi^{1/4} * \frac{1}{F_d} \tag{3.23}$$

With: R_0 jet Richardson number $[-]$
F_d jet densimetric Froude number $[-]$

If the Richardson number is $\ll 1$, buoyancy is unimportant in the flow while if the Richardson number is $\gg 1$ buoyancy is dominant. The flow is likely to be buoyancy driven when the Richardson number is $\mathcal{O}(1)$.

3.2 Vertical impinging jet

The impingement of turbulent jets on solid boundaries has been studied extensively in the past, for example by Poreh and Cermak in 1959, Tani and Komatsu in 1964, Hrycak *et al.* in 1974 and Beltaos and Rajaratnam in 1974 [Beltaos and Rajaratnam, 1977]. The free jet treated in the previous paragraph remains a free jet when the flow is not restricted by a boundary, i.e. when the orifice has enough height above the bed. This distance between the jet orifice and seabed is often called the impingement height (H) or stand-off distance (SOD). When the SOD is limited the jet will be deflected by the bed, this is defined as the impinging jet region. However, in most the previously mentioned studies the impingement distance was greater than about $10D$. For these studies this means that the jet flow already reached the ZEF, as given in Figure 10. Therefore [Beltaos and Rajaratnam, 1977] researched the effects of an impinging jet still in the ZFE. A distinction was made between large and small stand-off distances by [Beltaos and Rajaratnam, 1977]. It was proposed in their research that values of the SOD less than approximately $5.5D$ be considered as small. For a SOD greater than $8.3D$ the distance is considered large, with the range $5.5D \lesssim SOD \lesssim 8.3D$ being transitional. In the following two paragraphs the impinging jet for a large and small SOD, respectively, will be treated.

3.2.1 Large stand-off distance

The free jet region extends from the orifice for x/SOD up to about 0.86 for a large SOD, i.e. $SOD > 8.3D$, this was found by Beltaos and Rajaratnam in 1974 [Rajaratnam and Mazurek, 2005]. After this the impingement region starts with a height of $0.14SOD$ above the seabed. Just as for the free jet, the maximum velocity in the flow field of an impinging jet can be found at the centre. The centreline velocity of the jet flow in this impingement region was found by Beltaos and Rajaratnam in 1974 and can be approximated by [Ravelli, 2012]:

$$\frac{u_m}{u_{mf}} = 3.10\eta_i\sqrt{1-\eta_i} \tag{3.24}$$

With: u_{mf} corresponding centreline velocity of free jet without a boundary $[m/s]$
η_i factor for impinging jet $[-]$

The reduction factor can be calculated with:

$$\eta_i = \frac{x}{SOD} \tag{3.25}$$

As stated, the flow of the impinging jet is deflected by the boundary, i.e. the seabed, and will go over in the wall jet region as given in Figure 10. The horizontal distance which depicts the end of this impinging jet region is given by [RAJARATNAM AND MAZUREK, 2005] as:

$$r_{im} = 0.22SOD \tag{3.26}$$

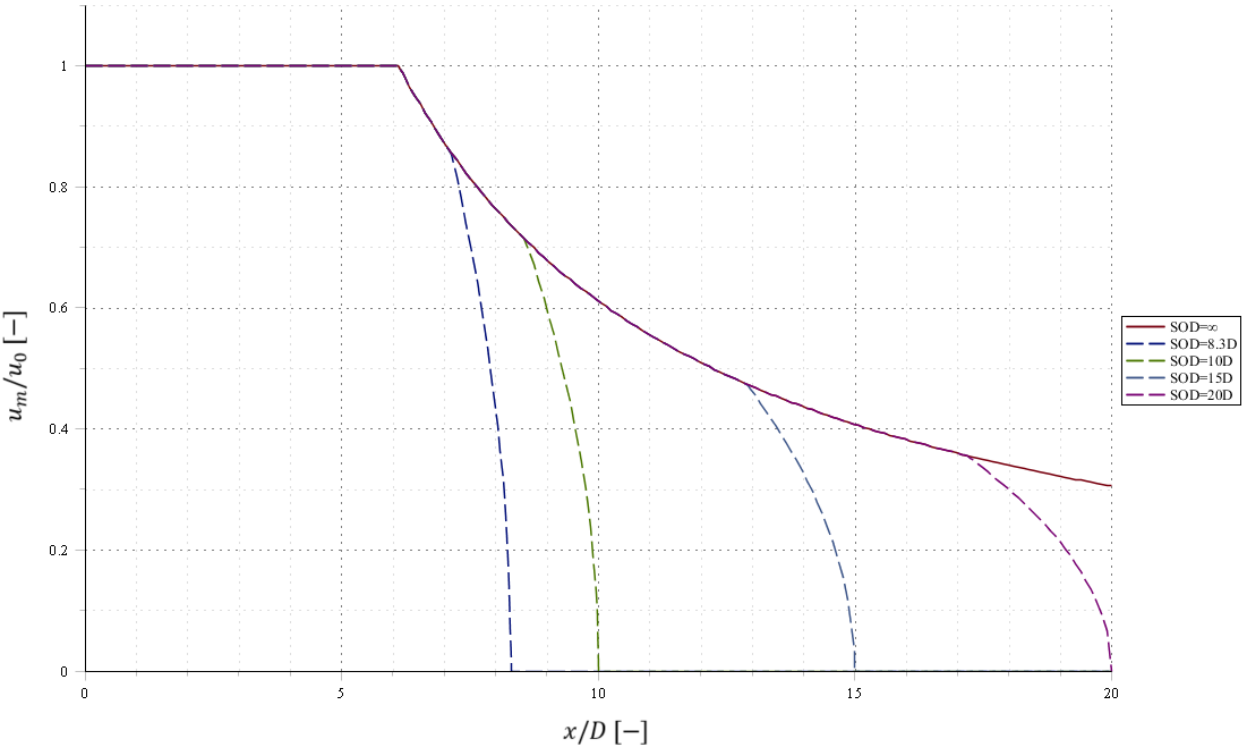

FIGURE 18: CENTRELINE VELOCITY FOR LARGE STAND-OFF DISTANCES

In Figure 18 the centreline velocity in the impinging region for different large values of the SOD is shown. The relation of [LEE *et al.*, 2009] is used for the corresponding centreline velocity in the free jet region in (3.24). This relation includes the entire flow field in the free jet region and is given by (3.19).

Jet velocity of an impinging jet

The jet velocity of an impinging jet with large $SODs$ can now be determined with the use of the centreline velocity (3.24) and the adapted general form of the Gaussian distribution (3.14), see also Figure 15.

3.2.2 Small stand-off distance

The region were r is greater than r_1 but less than r_2 is the annular shear layer.

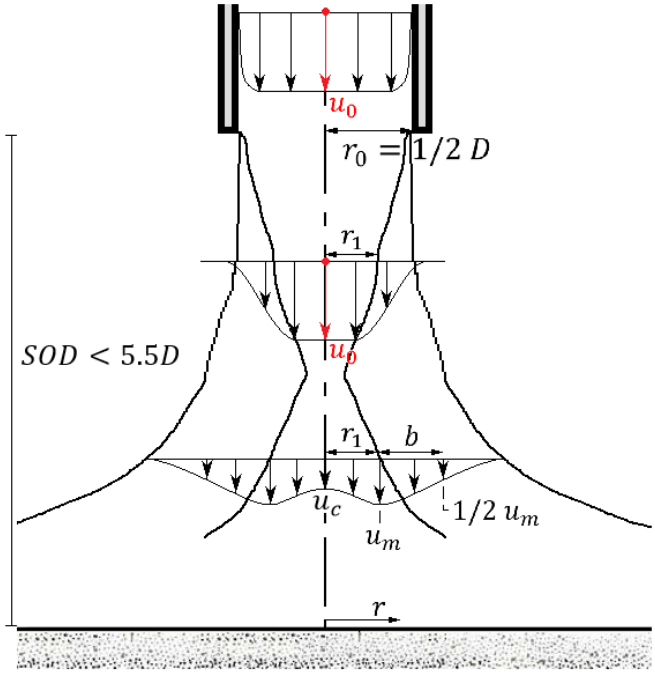

FIGURE 19: IMPINGING JET VELOCITY PROFILE

As can be seen in Figure 19, in comparison to the flow field of the free jet or for an impinging jet with a large SOD, the maximum velocity is not found at the centre of the jet. [BELTAOS AND RAJARATNAM, 1977] found with their research that the centreline velocity of the impinging jet, with a small SOD, is equal to:

$$u_c = u_0 * \frac{z/D}{1.1}\left(2 - \frac{z/D}{1.1}\right) \tag{3.27}$$

With: z vertical distance from the seabed $[m]$

Centreline velocity comparison

In literature little can be found on the velocity profile or centreline velocity of the flow field for the transitional range, i.e. $5.5D \lesssim SOD \lesssim 8.3D$. Therefore a comparison between the centreline velocities for large and small $SODs$, with different values for the SOD, is presented Figure 20. It is easily noticed that for a large SOD the centreline velocity is already decreased before reaching the impinging jet region. For a small SOD the velocity starts to decrease when the impinging jet region is reached, this is at $z/D = 1.1$.

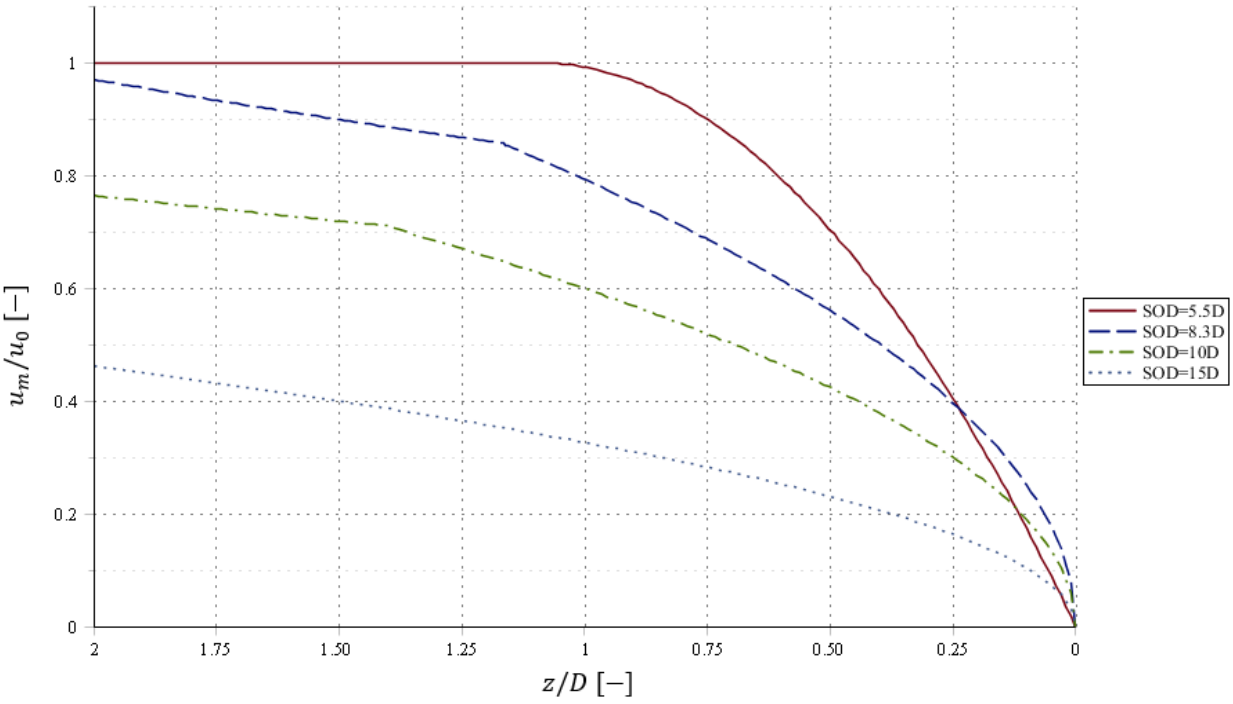

FIGURE 20: COMPARISON OF THE CENTRELINE VELOCITY FOR LARGE AND SMALL STAND-OFF DISTANCES

A remark must be made here. The dimensionless distance used in Figure 20 is with the use of the distance above the seabed, as given as the parameter z in Figure 10. In comparison, the dimensionless distance used in Figure 18 is with the use of the distance below the orifice of the fallpipe, this is given as the parameter x, also given in Figure 10.

Jet velocity for an impinging jet

Now, with the centreline velocity, an expression for the velocity field of the impinging jet with a small SOD can be derived. It was found by [BELTAOS AND RAJARATNAM, 1977] that the relation between the centreline velocity and maximum velocity is proportional to:

$$u_m = 1.15u_c \tag{3.28}$$

With this maximum velocity, the jet velocity in the shear layer ($r_1 < r < r_2$) can expressed as [BELTAOS AND RAJARATNAM, 1977]:

$$u = u_m * e^{-0.693\eta^2} \tag{3.29}$$

With: $\eta = \dfrac{(r - r_1)}{b}$ [−]

$b = 0.115D + 0.087x$ [m]

The distance from the centre of the jet to the edge of the core in this region is also determined by [BELTAOS AND RAJARATNAM, 1977]

$$r_1 = (0.5D - \frac{0.069SOD}{D}) * \left(\frac{z}{D}\right)^{-1/4} \tag{3.30}$$

For the zone where $r < r_1$, i.e. in the core of the jet, a rough approximation of the velocity field is given by [BELTAOS AND RAJARATNAM, 1977]:

$$u = \lambda^2(2-\lambda^2)(u_m - u_c) + u_c \tag{3.31}$$

With: $\lambda = \dfrac{r}{r_1}$ $[-]$

In Figure 21 the normalized jet velocity is plotted versus the radial coordinate for two impinging jets with small $SODs$, namely $SOD = 5.5D$ and $SOD = 2D$. The non-uniform radial distribution of the jet velocity is easily noticed.

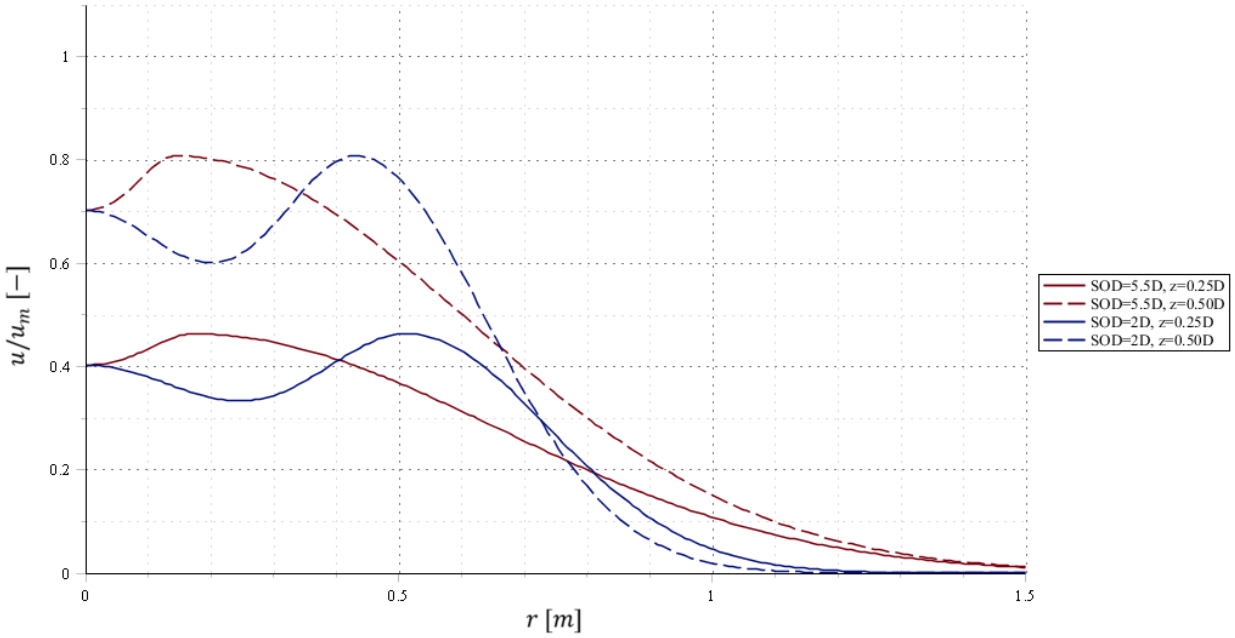

FIGURE 21: JET VELOCITY AS FUNCTION OF THE RADIAL COORDINATE FOR AN IMPINGING JET WITH A SMALL SOD

Radial velocity

The radial component of the velocity in the impingement region is expressed by [BELTAOS AND RAJARATNAM, 1977] as:

$$v = v_1 * \frac{\lambda}{1.15}[1 + 0.15\lambda^2(2-\lambda^2)] \tag{3.32}$$

With: v_1 radial velocity at $r = r_1$ $[m/s]$

v radial velocity $[m/s]$

This expression is valid for $0 \le r \le r_1$ and is an approximation of the values found in the experiments. For the radial velocity at $r = r_1$ [BELTAOS AND RAJARATNAM, 1977] also found an approximation based on their experiments. This approximation agrees quantitative well for the region $z/D < 0.5$, outside this region the deviation becomes considerable. The approximation is given as:

$$v_1 = \frac{u_0 * r_1}{D} * \frac{0.294}{\sqrt{(z/D) - 0.07}} \tag{3.33}$$

In Figure 23 and Figure 22, both the radial velocity at $r = r_1$, depending on the distance above the bed, and the normalized total radial velocity, depending on the radial distance, are plotted respectively.

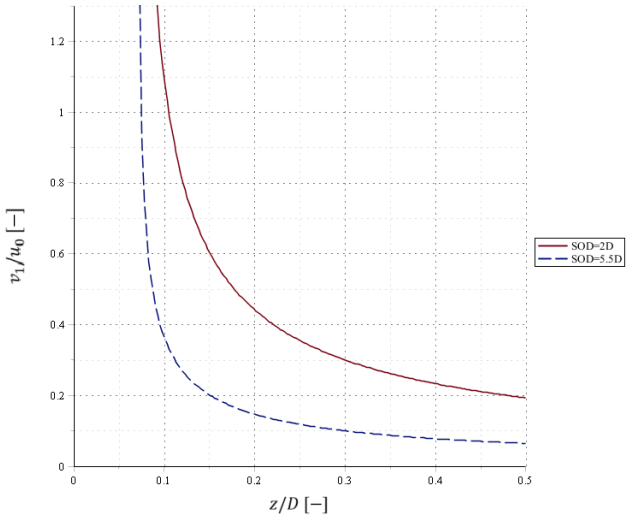

FIGURE 23: RADIAL VELOCITY AT $r = r_1$

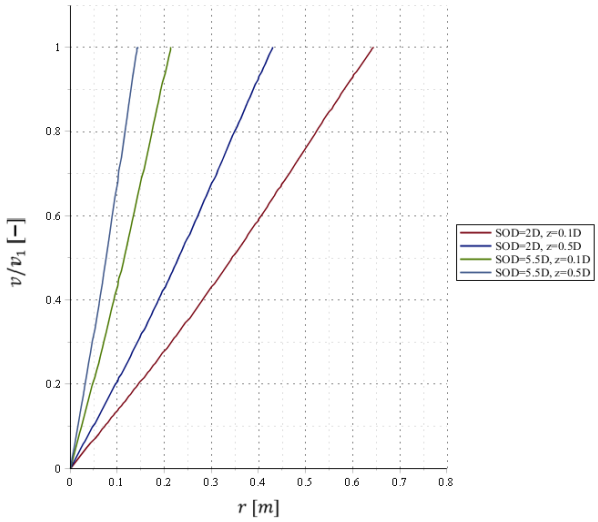

FIGURE 22: RADIAL VELOCITY AS FUNCTION OF RADIAL COORDINATE

3.3 Wall jet

Due to the normally impingement of a circular jet on a boundary, a radial spreading of the jet will be seen. This radial wall jet has an axisymmetric characteristic and quite some experiments have be done on this type of wall jet. For example by Poreh and Cermak in 1959, Love in 1961 and Verhoff in 1963 [RAJARATNAM, 1976]. However, just as for the studies on the impinging jet, for most studies experiments with large $SODs$, as defined in the previous paragraph, were executed. Therefore also experiments for small $SODs$ were performed by [BELTAOS AND RAJARATNAM, 1977]. In the following two paragraphs the impinging jet for a large and small SOD, respectively, will be treated. In Figure 24 the flow field of the wall jet region is shown.

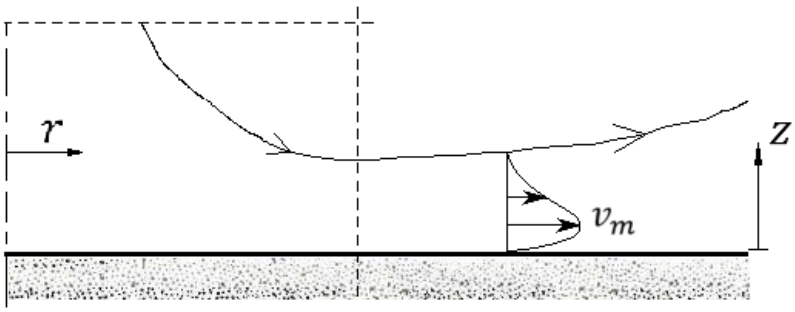

FIGURE 24: WALL JET VELOCITY PROFILE

3.3.1 Large stand-off distance

As can be seen from Figure 24 the maximum radial velocity in the velocity profile of a wall jet is not found at the centreline of the jet. [BELTAOS AND RAJARATNAM, 1977] found with their research that the maximum velocity of the wall jet, with a large SOD, is equal to:

$$v_m = u_0 * \frac{1.03}{r/D} \tag{3.34}$$

With: v_m maximum radial velocity $[m/s]$

It is easily noticed from the above equation that the flow characteristics in the wall jet region for large $SODs$ is independent of the height above the seabed.

With this maximum radial velocity an expression for the flow field is found by Verhoff in 1963 [RAJARATNAM, 1976] and is noted as:

$$v = v_m * 1.48\eta_w^{1/7}[1 - erf(0.68\eta_w)] \tag{3.35}$$

With: η_w factor for wall jet $[-]$

The factor of the wall jet and the spreading width can be determined with:

$$\eta_w = \frac{z}{b} \tag{3.36}$$

$$b = 0.087r \tag{3.37}$$

In Figure 25 the normalized radial velocity as function of the distance above the seabed of the wall jet is plotted. The radial velocity is given for different radial distances from the impingement point and clearly quite some dispersion can be noticed.

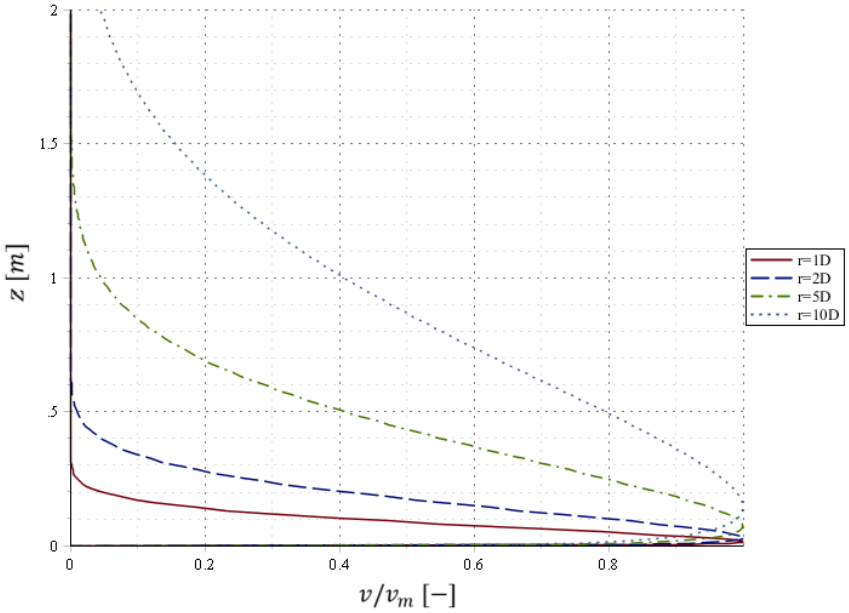

FIGURE 25: RADIAL VELOCITY FOR A WALL JET

3.3.2 Small stand-off distance

Just as for large $SODs$ the flow characteristics in the wall jet region for small $SODs$ are independent of the height above the seabed. For the calculation of the shear stress in the wall jet region the following equation was found adequate by [BELTAOS AND RAJARATNAM, 1977]:

$$u_* = u_0 * \frac{0.0794}{\frac{r}{D} - 0.3} \tag{3.38}$$

With: u_* shear velocity $[m/s]$

For the maximum velocity in the wall jet region a factor of around 1 instead of 1.03, for equation (3.34), is found by [BELTAOS AND RAJARATNAM, 1977].

3.4 Concluding remarks

All the empirical relations mentioned in this chapter are based on multiple experiments carried out for a circular turbulent jets, with a range of SODs. The distance between the seabed and the orifice of the fallpipe when executing a rock placement operation is however not constant. As mentioned in (2.2 Rock placement) the absolute minimum of SOD is $3\,m$ due to safety reasons and the maximum height above the bed is possible large. From practical experience it is noted that the SOD is within a rough range of $5D < SOD < 20D$. This range is quite well covered by the executed experiments.

Furthermore, for a fluid flow to be turbulent depends on the Reynolds number, roughly $Re > 2000$. The Reynolds number used in the experiments was of a high order, including experiments with $Re \approx 5 * 10^4$. The Reynolds number depends on the velocity, a length scale and viscosity. A range of different pipe diameter was used in the experiments, however many of them relatively small compared to the diameter of a fallpipe. On the other hand also a range of exit velocities was tested, including velocities an order higher than experienced with a rock placement operation. Nonetheless, a quick calculation with input parameters from practice learns that the Reynolds number of the closed fallpipe system is approximately 2 orders higher. However, [RAVELLI, 2012] states when taking into account the discharge-momentum length scale, which can be calculated with equation (3.21), and comparing the system used in this thesis with the experiments similar results are obtained. Thus, it is adopted that the type of flow from the experiments and in this thesis are equal, although the Reynolds numbers deviate from each other.

4

Threshold of Motion

A critical or threshold condition for flow over an erodible bed has been reached when the hydrodynamic force is balanced by the resisting force. The particles, e.g. sand or stone, will erode and will continue to erode until this condition is restored. The hole created by this process will continuously enlarge until the force of the jet is insufficient to move the particles. Already for various times the threshold of motion of particles and the corresponding transport formula have been researched. This has been proven to be a very difficult task because still no conclusive physical relation and formula have been found. Therefore, numerous experiments have been performed to find an empirical formula for this transport.

The definition of the threshold of motion is not very well defined either and thus different definitions can be given. Definitions based on critical stability parameters, number of particles displaced per area and time (e.g. Breusers and Schukking in 1971; Graf and Pazis in 1977; [Tromp, 2004]; Dessens in 2004 [Hoan, 2008] and through visual observation.

A visual observation method for the bed movement is defined by Kramer in 1932 [Hoan, 2008]:

1. None.
2. Weak ("… several of the smallest particles are in motion, in isolated spots, and in countable numbers.")
3. Medium ("… grains of main diameter are in motion in numbers too large countable […] movement is no longer local in character. It is not strong enough to affect bed configuration and does not result in transportation of an appreciable quantity of material.")
4. General ("… grains up to and including the largest are in motion […]. It is sufficiently vigorous to change the bed configuration […]. There is an appreciable quantity of material transported …")

Another definition of the bed movement suggested by WL|Delft Hydraulics in 1972 can be described as [Schiereck, 2012]:

0. no movement at all
1. occasional movement at some locations
2. frequent movement at some locations
3. frequent movement at several locations
4. frequent movement at many locations

5. frequent movement at all locations
6. continuous movement at all locations
7. general transport

In 1936 Shields pioneered the dimensionless critical shear stress to define incipient motion of a particle [HOAN, 2008]. Since then, the dimensionless critical shear stress is called the critical Shields stability parameter and is used by many researchers to study the threshold conditions. In this chapter will first be looked at the hydrodynamic forces on a stone. Then the different researchers and their modification on the critical Shields stability parameter will be further elaborated.

4.1 Hydrodynamic Forces

Let us consider a stone lying on the bed which is exposed to a fluid flow. For this situation the forces acting on a stone are shown in Figure 26.

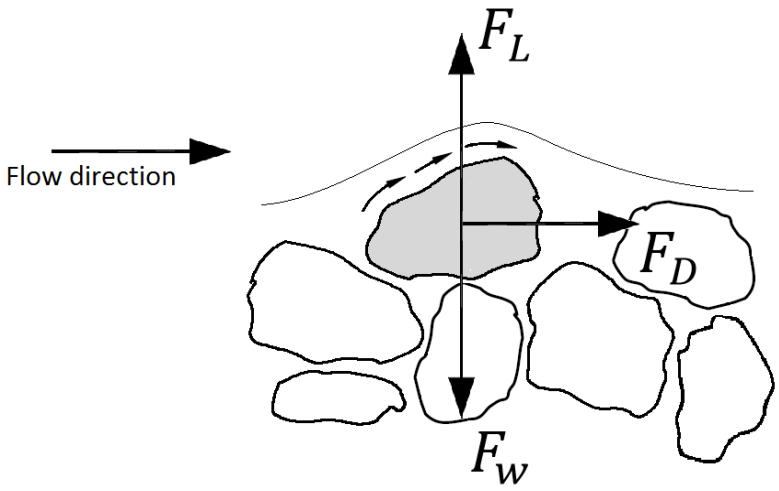

FIGURE 26: FORCES ACTING ON A STONE LYING ON THE BED

A frictional force is presented on the rough surface of the stone and due to a pressure difference between the front and the back surface of the particle, a resistance is formed. The frictional force is for high particle Reynolds numbers, larger than 500, negligible [HOAN, 2008]. The resultant of the frictional and resistance force is the driving force on the particle and is called the drag force. In general form this drag force can be written as:

$$F_D = \frac{1}{2} * C_D * A_D * \rho_f * u|u| \tag{4.1}$$

With:			
	F_D	drag force	$[kgm/s^2]$
	C_D	drag coefficient	$[-]$
	A_D	surface area exposed to drag	$[m^2]$

A lift force is caused due to a higher velocity at the top than at the bottom of the stone. In general form this lift force can be written as:

$$F_L = \frac{1}{2} * C_L * A_L * \rho_f * u|u| \tag{4.2}$$

With:			
	F_L	lift force	$[kgm/s^2]$
	C_L	lift coefficient	$[-]$
	A_L	surface area exposed to lift	$[m^2]$

The submerged weight of the stone is the counteracting force of the lift force as can be seen in Figure 26. The submerged weight of the stone, in general form, is:

$$F_w = V * (\rho_s - \rho_f) * g \tag{4.3}$$

With:			
	F_w	submerged weight	$[kgm/s^2]$
	V	volume	$[m^3]$
	ρ_s	density of solids	$[kg/m^3]$

At the moment just before the rock starts to move, the hydrodynamic force is still in equilibrium with the resisting force. This equilibrium is written as:

$$F_D = \mu * (F_w - F_L) \tag{4.4}$$

With:			
	μ	friction coefficient	$[-]$

4.2 Stability parameters

A stone transport formula should present a method of determining the bed response, i.e. the bed damage level, as function of all the variables involved [HOAN, 2008]. Such variables are: the bed shear stress, velocity, stone size, turbulence and specific submerged density of stone. This specific submerged density of stones is given by:

$$\Delta = \frac{(\rho_s - \rho_f)}{\rho_f} \tag{4.5}$$

With:			
	Δ	relative density	$[-]$

The bed shear stress has been widely used as the only governing variable representing the flow forces. It can be used to define the threshold condition at which the stones start to move. In this paragraph first the definition of Shields for the dimensionless critical shear stress is treated, including an analytical derivation of the threshold of motion by [MIEDEMA, 1981]. Then adaptations of the Shields formula by Jongeling in 2003 and [HOFLAND, 2005] will be further elaborated. Furthermore, [HOAN, 2008] executed a comparative research and adjustment on the stability parameters of Jongeling *et al.* and Hofland and introduced his own stability parameter. All the stability parameters treated in the last sections of this chapter are Shields-like stability parameters.

4.2.1 Shields

As already stated, Shields was the first to define the incipient motion of a particle with the dimensionless critical shear stress. It was assumed that the factors in determining the stability of the particles on a bed are the bed shears tress and the submerged weight of the particles. With these two quantities the dimensionless shear stress is formed and is now known as the Shields stability parameter.

$$\Psi_s = \frac{load}{strength} = \frac{\tau_b * d^2}{g * (\rho_s - \rho_f) * d^3} = \frac{\tau_b}{\rho_f * \Delta * g * d} \tag{4.6}$$

With:			
	Ψ_s	Shields parameter	$[-]$
	τ_b	bed shear stress = $\rho_f * u_*^2$	$[kg/ms^2]$
	u_*	particle diameter	$[m/s]$
	d	particle diameter	$[m]$

In this literature study the median nominal diameter (d_{n50}) will be used as the governing diameter for particles. The median nominal diameter is further elaborated in Chapter 5.

Thus for the determination of the required stone size formula (4.6) becomes:

$$d_{n50} = \frac{u_*^2}{\Delta * g * \Psi_s} \tag{4.7}$$

In Figure 27 the original Shields curve is displayed, whereby the marked area shows the critical shear stress as a function of the particle Reynolds number. With (3.1) the particle Reynolds number can be defined as:

$$Re_p = \frac{u_e * d_{n50}}{\nu} \tag{4.8}$$

The particle Reynolds-number indicates whether the grain protrudes into the turbulent boundary layer or stays within the viscous sub-layer [SCHIERECK, 2012]. This number is different from the normal Reynolds-number given in (3.1) and says nothing about the flow characteristics of the flow as a whole.

It should be noted that the Shields curve is developed for uniform open-channel flow and turbulence is not explicitly accounted for. Its effect is incorporated implicitly through the empirically estimated values of the Shields parameter. This is a valid approach for uniform flows, for which the ratio of turbulence intensity to the shear velocity is virtually constant [HOFLAND, 2005]. However, the turbulence also plays an important role and therefore it is questionable whether the bed shear stress should be used as the only parameter representing the flow forces.

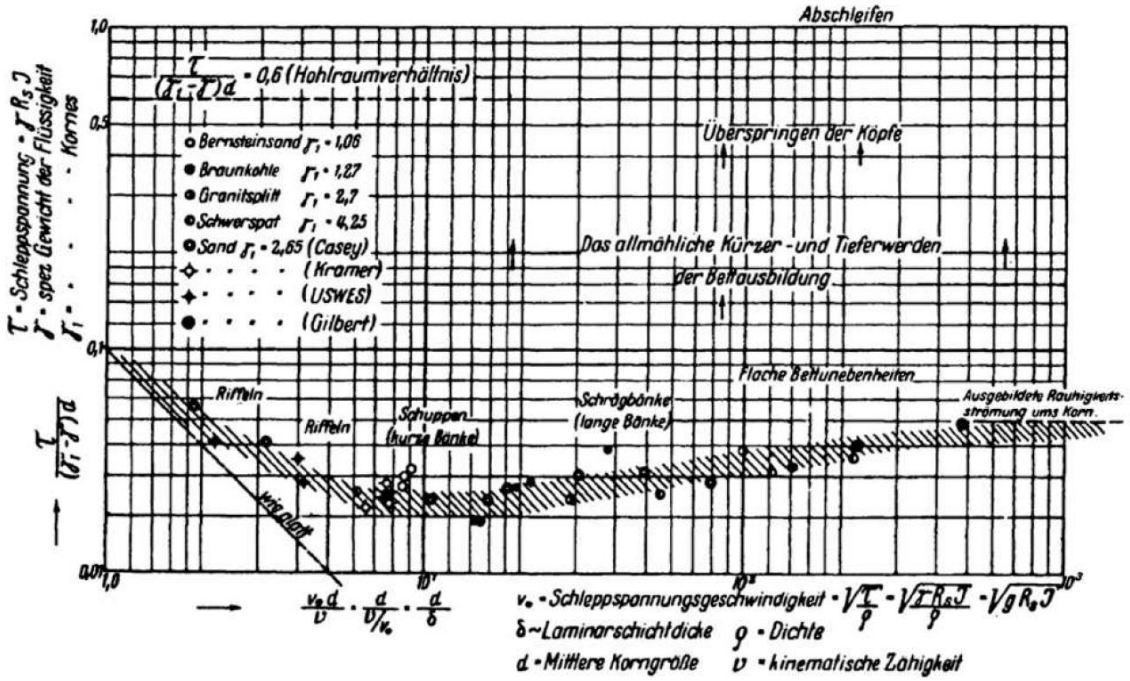

FIGURE 27: ORIGINAL SHIELDS CURVE

When considering large grains, larger than the viscous sub-layer, a turbulent flow will exist around the grain. In this case the Shields parameter is no longer dependent on the particle Reynolds number and becomes constant with a value of about 0.055, as can be seen in the right part of Figure 27.

The analytical expression by Miedema

[MIEDEMA, 1981] derived an analytical expression to determine the threshold of motion with a Shields approach. The general form of the forces acting on a stone lying on a bed, (4.1), (4.2) and (4.3), were adjusted for a spherical grain. This is done by adjusting the velocity near a grain in the shear velocity with a certain coefficient. The coefficient is used to modify the shear velocity so that it forms the characteristic flow velocity past the grain:

$$u = \alpha * u_* \tag{4.9}$$

With: α shear velocity modification coefficient $[-]$

For the surface areas which are exposed to drag and lift, half of the spherical area is taken. Also, a certain coefficient is introduced, this is done because only a fraction of the area is subjected to drag and lift:

$$A_D = A_L = \frac{1}{4} * \beta * \pi * d^2 \tag{4.10}$$

With: β surface area coefficient $[-]$

The volume of particle in question is taken as the volume of a sphere:

$$V_s = \frac{1}{6} * \pi * d^3 \tag{4.11}$$

With: V_s volume of a sphere $[m^3]$

With these alterations of the general form of the forces the following equation is derived [MIEDEMA, 1981]:

$$\Psi_{cr} = \frac{u_*^2}{\Delta * g * d} = \frac{4}{3} * \frac{\mu}{\beta} * \frac{1}{\alpha^2} * \frac{1}{C_D + \mu * C_L} \tag{4.12}$$

With: Ψ_{cr} critical stability parameter $[-]$

The original Shields curve contains on both axis the shear velocity and this parameter is usually unknown. Therefore this makes the Shields graph not convenient to use and the axis system was transformed by [MIEDEMA, 2008] to make the graph explicit. This is done with the use of the dimensionless grain diameter, the so-called Bonneville parameter, and is defined as:

$$D_* = d \sqrt[3]{\frac{\Delta * g}{\nu^2}} \tag{4.13}$$

With: D_* Bonneville parameter $[-]$

With the use of the Bonneville parameter, [MIEDEMA, 2008] found for (4.12) functions (an upper limit, an average and a lower limit) which cover the entire Shields graph. The function for the average Shields parameter as derived by [MIEDEMA, 2008] is given in equation (4.14) and thus the stone diameter be determined with equation (4.15):

$$\Psi_{cr} = \frac{0.2285}{D_*^{1,02}} + 0.0575 * (1 - e^{-0.0225 * D_*}) \tag{4.14}$$

$$d_{n50} = \frac{u_*^2}{\Delta * g * \frac{0.2285}{D_*^{1,02}} + 0.0575 * (1 - e^{-0.0225 * D_*})} \tag{4.15}$$

The corresponding critical velocity can be calculated if the relation between the shear velocity and the ambient flow velocity is known. [BELTAOS AND RAJARATNAM, 1973] show that the ratio of the shear velocity and the ambient flow velocity for a plane impinging jet is constant when the horizontal distance from the centre of the jet over the SOD is larger than 0.2 and then is equal to approximately 0.06.

4.2.2 The Jongeling *et al.* stability parameter

A combination of turbulence distributions over a certain water column above the bed and velocity is used to quantify the flow forces in 2003 by Jongeling *et al.* for determining the damage of bed protections. The method was developed by using the outputs of numerical computations. The turbulence is incorporated to account for the peak values of the forces that occur in the flow. The stability parameter is expressed as [HOAN, 2008] (see also Figure 28):

$$\Psi_{WL} = \frac{\langle (\bar{u} + \alpha * \sqrt{k})^2 \rangle_{hm}}{\Delta * g * d} \tag{4.16}$$

With:

Ψ_{WL}	Jongeling *et al.* stability parameter	$[-]$
α	empirical turbulence coefficient	$[-]$
k	turbulent kinetic energy	$[m^2/s^2]$
$\bar{u}$	stationary mean part of u	$[m/s]$
$\langle \dots \rangle_{hm}$	spatial average over a distance hm above the bed	

A stability threshold concept is used to determine the empirical turbulence magnification factor for the new stability parameter and its critical value thereof. First, experiments were carried out at incipient conditions for various flow configurations. Then, numerical flow models were used to simulate these experiments. At last, with the use of the outputs from a numerical flow model the new stability parameter, with several combinations of the empirical turbulence magnification factor and the distance above the bed, were computed. To formulate the stability parameter, the values of the empirical turbulence magnification factor and the distance above the bed, that give more or less equal values for the critical value of the stability parameter, at incipient motion for all considered geometries, were chosen. The least variation of the critical stability parameter was found after mutual comparison of the various geometries by $\alpha = 6$.

The method of choosing the empirical turbulence magnification factor and the distance above the bed is questionable because there is no proof that the critical stability parameter has to be a constant value. Though, the advantage of this approach is that the turbulence effect is explicitly modelled. It is also pointed out by [HOFLAND, 2005] that using a subjective definition of incipient motion will not yield consistent design criteria.

According to [HOAN, 2008] it appears that in 2006 Jongeling *et al.* defined the incipient of motion by the visual observation method since the flow conditions in their experiments are described as: "In all cases the bed was protected with stones and the flow conditions were such that individual stones were now and then moved by the flow (*incipient motion* condition)". Therefore, it was found by [HOAN, 2008] that the link between the critical stability parameter and the stability state of bed material is not clear.

4.2.3 The Hofland stability parameter

[HOFLAND, 2005] proposed a method for evaluating the stability of bed protections under non-uniform flow using output of a 3D RANS model. A local stability parameter was formulated with the use of the profiles of the mean velocity and turbulent kinetic energy in the water column above the bed.

A Shields-like stability parameter was proposed and is written as (see also Figure 28):

$$\Psi_{Lm} = \frac{max\left[\langle \bar{u} + \alpha * \sqrt{k} \rangle_{Lm} \frac{L_m}{z}\right]^2}{\Delta * g * d} \tag{4.17}$$

With:

Ψ_{Lm}	Hofland stability parameter	$[-]$
L_m	Bakhmetev mixing length $= \kappa z\sqrt{1 - z/h}$	$[m]$
κ	Von Karman constant	$[-]$
h	water depth	$[m]$
$\langle \ldots \rangle_{Lm}$	moving average with varying filter length Lm	

[HOAN, 2008] analysed the data of Jongeling *et al.* and de Gunst, from 2003 and 1999 respectively, to determine the correlation between the Hofland stability parameter and the bed damage. Just as for the Jongeling *et al.* stability parameter, a value of $\alpha = 6$ was visually found as the best fit for the given data.

4.2.4 The Hoan stability parameter

[HOAN, 2008] investigated the stability of granular bed protections under flowing water. The bed protections were defined as hydraulic rough granular beds under non-uniform flow. A detailed set of measurements were carried out in a laboratory flume. This detailed set of measurements include, the bed response (quantified by a dimensionless entrainment rate) as well as the flow field (velocity and turbulence intensity distributions). The flow configuration within the flume was chosen in such a way that a high turbulence intensity was created.

Mobility parameters

When assessing the stability of a granular bed it is essential to have a clearly defined and quantified measure of damage, and is often referred to as mobility parameter. In 1998 Mosselman and Akkerman [HOAN, 2008] distinguished two ways of defining the mobility of particles: the number of particles that is transported through a cross-section per unit time or the number of pick-ups per unit time and area. The two ways are often called bed load transport and (volume) entrainment rate respectively. It is however important for non-uniform flow that the mobility parameter is dependent on the local hydrodynamic conditions. Therefore the dimensionless entrainment rate could be used as a bed damage indicator because it is completely dependent on the local hydrodynamic parameters [HOFLAND, 2005], contrary to the bed load transport. The dimensionless entrainment rate is expressed as [HOAN, 2008]:

$$\Phi_E = \frac{E}{\sqrt{\Delta * g * d}} \tag{4.18}$$

With:

Φ_E	entrainment parameter	$[-]$
E	entrainment rate	$[m/s]$

Experiments by Hoan

The evaluation of the stability parameters, of Shields, Jongeling *et al.*, Hofland and the newly proposed stability parameter, done by [HOAN, 2008] is elaborated in this section. A correlation analysis was made and the coefficient of determination gives the quantitative confirmation of the validity of these parameters. A graphical comparison of the Shields, *Jongeling et al.,* Hofland and Hoan stability parameters is given in Figure 28.

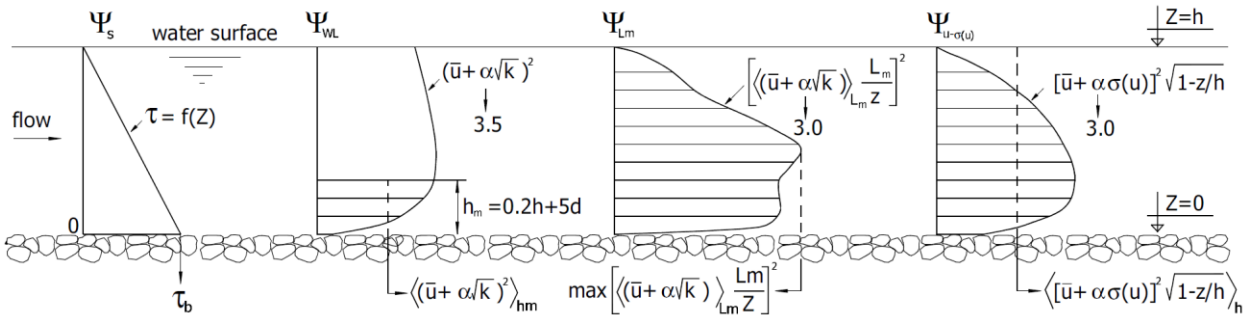

FIGURE 28: TYPICAL DISTRIBUTIONS OF THE KEY PARAMETERS ACCORDING TO (4.6), (4.16), (4.17) AND (4.21) [HOAN, 2008]

Figure 29 shows the correlation between the Shields stability parameter (4.6) and the dimensionless entrainment rate for all data from the experiments performed by [HOAN, 2008]. It can be clearly seen that almost no correlation exists between the two parameters for non-uniform flow. The analysis also clearly shows that the bed shear stress alone is not sufficient to quantify the flow forces acting on the bed [HOAN, 2008].

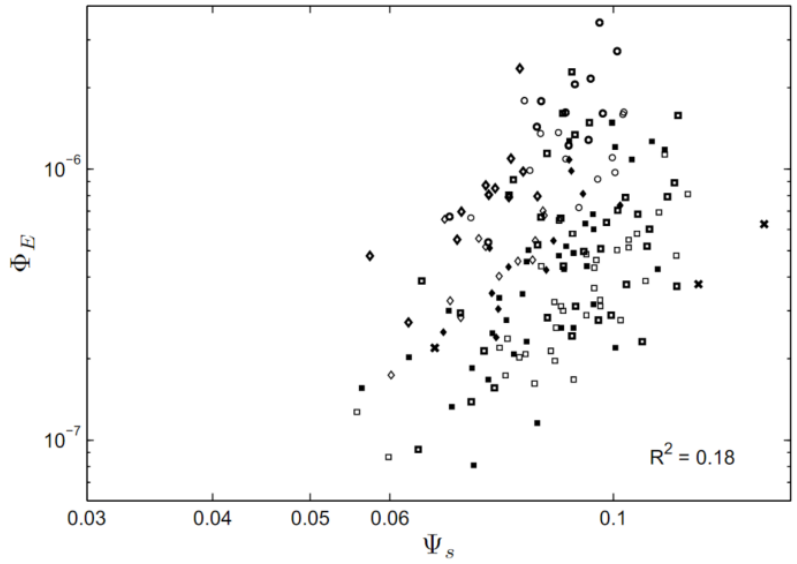

FIGURE 29: MEASURED Ψ_s VERSUS MEASURED Φ_E [HOAN, 2008]

As mentioned in section 4.2.2, for the Jongeling *et al.* stability parameter the turbulence magnification factor of 6 was found and suggested after mutual comparison of the various geometries. However, in the analysis by [Hoan, 2008] a value of the turbulence magnification factor of $\alpha = 3.5$ was found as the best correlation between the stability parameter and the dimensionless entrainment rate. In contrast to the Shields stability parameter, Figure 29 the measured Jongeling *et al.* stability parameter is strongly correlated to the measured dimensionless entrainment parameter, see Figure 30.

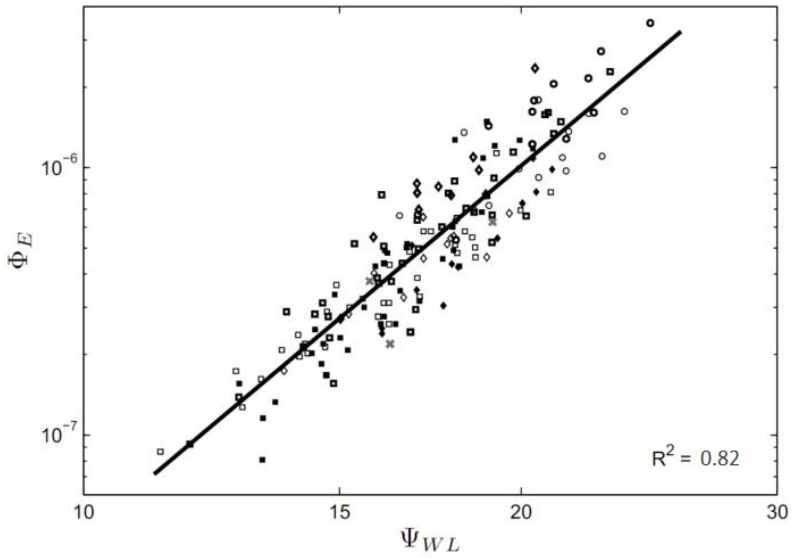

FIGURE 30: MEASURED Ψ_{WL} VERSUS MEASURED Φ_E [HOAN, 2008]

The correlation analysis leads to the following stone transport formula for the Jongeling *et al.* stability parameter [HOAN, 2008]:

$$\Phi_E = 1.16 * 10^{-12} * \Psi_{WL}^{4.57} \qquad for\ 11 < \Psi_{WL} < 25 \tag{4.19}$$

As indicated in section 4.2.3, for the Hofland stability parameter the turbulence magnification factor also of 6 was visually found as the best fit for the given data. However, in the analysis by [HOAN, 2008] a value for the turbulence magnification factor of $\alpha = 3$ was found as the best correlation between the stability parameter and the dimensionless entrainment rate. In contrast to the Shields stability parameter, Figure 29, the measured Hofland stability parameter is strongly correlated to the measured dimensionless entrainment parameter, see Figure 31.

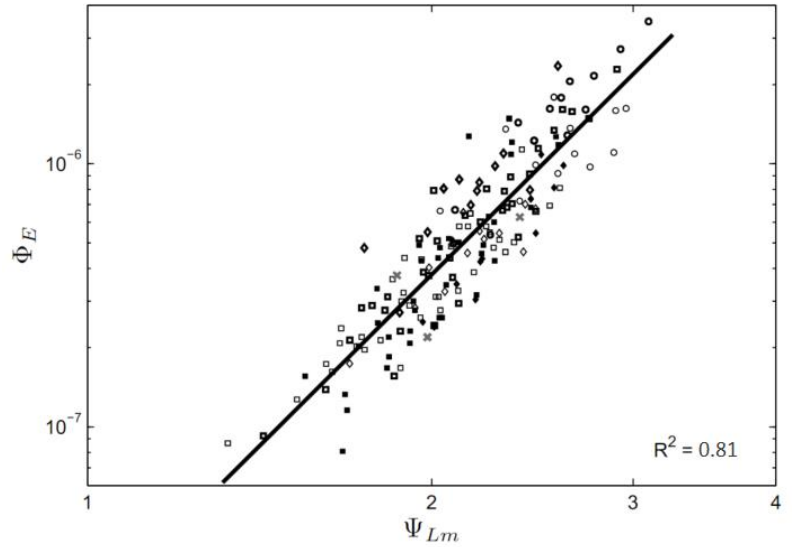

FIGURE 31: MEASURED Ψ_{Lm} VERSUS MEASURED Φ_E [HOAN, 2008]

The correlation analysis leads to the following stone transport formula for the Hofland stability parameter [HOAN, 2008]:

$$\Phi_E = 1.15 * 10^{-9} * \Psi_{Lm}^{4.53} \qquad for\ 1.3 < \Psi_{Lm} < 3.2 \tag{4.20}$$

Besides the comparison and analysation of the Jongeling *et al.* and Hofland stability parameter, [HOAN, 2008] also proposed his own stability parameter. This new stability parameter incorporates the influence of turbulence sources above the bed. This is done by a turbulence quantity $\sigma(u)$. This turbulence component can be calculated directly from the instantaneous velocity data. The stability parameter is expressed as [HOAN, 2008]:

$$\Psi_{u-\sigma[u]} = \frac{\langle [u + \alpha * \sigma(u)]^2 * \sqrt{1 - z/h} \rangle_h}{\Delta * g * d} \tag{4.21}$$

With:

$\Psi_{u-\sigma[u]}$	Hoan stability parameter	$[-]$
$\sigma(u)$	turbulence quantity	$[m/s]$
$\langle \dots \rangle_h$	average over water depth	

The best correlation between the stability parameter and the dimensionless entrainment rate was found for a turbulence magnification factor of $\alpha = 3$ for the newly-proposed stability parameter by [HOAN, 2008]. Just as the previous two stability parameters, the measured Hoan stability parameter is strongly correlated to the measured dimensionless entrainment parameter, see Figure 32.

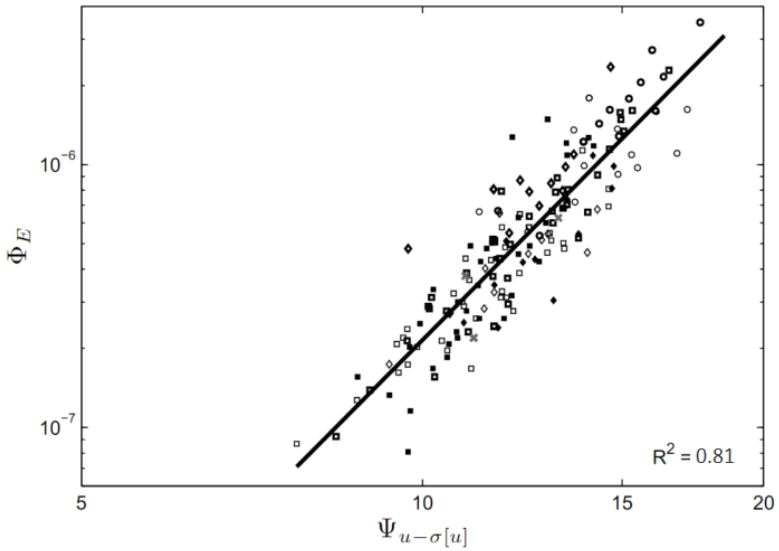

FIGURE 32: MEASURED $\Psi_{u-\sigma[u]}$ VERSUS MEASURED Φ_E [HOAN, 2008]

The correlation analysis leads to the following stone transport formula for the Hoan stability parameter [HOAN, 2008]:

$$\Phi_E = 9.6 * 10^{-12} * \Psi_{u-\sigma[u]}^{4.35} \qquad for\ 7.5 < \Psi_{u-\sigma[u]} < 18 \tag{4.22}$$

The coefficient of determination for the Jongeling *et al.* stability parameter is equal to 0.82. For the Hofland stability parameter this is 0.81 and for the Hoan stability parameter also 0.81. Therefore the three stability parameters perform similarly well. This is however only the case when the appropriate values of the turbulence magnification factor are used, proposed by [HOAN, 2008], for the Jongeling *et al.* and Hofland stability parameter.

Required stone diameter

[HOAN, 2008] recommended to use the critical values of the corresponding stability parameters, translated from a subjectively chosen low value of the entrainment as a consistent design criteria to determine the stone size in designing a bed protection. The required stone diameter, with the use of (4.21), (4.17) and (4.16), can now be determined as:

$$d_{n50} = \frac{\langle [u + \alpha * \sigma(u)]^2 * \sqrt{1 - z/h} \rangle_h}{\Delta * g * \Psi_{u-\sigma[u],c}} \qquad with\ \alpha = 3.0 \tag{4.23}$$

$$d_{n50} = \frac{\langle (\bar{u} + \alpha * \sqrt{k})^2 \rangle_{hm}}{\Delta * g * \Psi_{WL,c}} \qquad with\ \alpha = 3.5 \tag{4.24}$$

$$d_{n50} = \frac{max\left[\langle \bar{u} + \alpha * \sqrt{k} \rangle_{Lm} \frac{L_m}{z}\right]^2}{\Delta * g * \Psi_{Lm,c}} \qquad with\ \alpha = 3.0 \tag{4.25}$$

With:

$\Psi_{u-\sigma[u],c}$	critical Hoan stability parameter	$[-]$
$\Psi_{WL,c}$	critical Jongeling *et al.* stability parameter	$[-]$
$\Psi_{Lm,c}$	critical Hofland stability parameter	$[-]$

4.3 Concluding remarks

The stability parameters and the corresponding transport formulas mentioned in this chapter are all based on multiple experiments. The used flow in these experiments is classified as a turbulent flow with a Reynolds number from roughly $Re \approx 5 * 10^4$ up to $Re \approx 10^5$. The main similarity between the different experiments is that they were all conducted in a laboratory flume simulating different open channel flows, including but not limited to a long and short sill, a gate and increased large-scale turbulence. These results were compared and fitted with results from computational fluid dynamics simulations.

As mentioned in (3.4 Concluding remarks) the Reynolds number of the used jet at the orifice of the fallpipe is roughly $Re \approx 2 * 10^6$. However near the seabed this value will decrease due to the decreasing jet velocity and therefore it is assumed that the impinging jet has the same order of Reynolds number as used in the experiments. Nonetheless, the experimental relations for the damage of the bed are based on a long lasting hydraulic loads whereas the impinging jet caused by a rock placement operation is an incidental, short lasting and abrupt hydraulic load.

5

Rock Properties

All materials can be characterized by their properties, for rock this is the same. A lot of different characteristics of rock can be recognised. However, in this chapter the focus lies on rock types, mass and sizes, grading, and shapes. These will be further explained and are also all described in the "Manual on the use of Rock in Hydraulic Engineering" [CUR/RWS 169, 1995] or "The Rock Manual" [CIRIA/CUR/CETMEF, 2007].

5.1 Rock types

Rock types can be classified by their mineral and chemical composition, texture of the constituent particles and formation process. When rock types are divided by geologists they are generally looking on their mode of formation. There are three different groups when looking on the mode of formation, namely: igneous rock, sedimentary rock and metamorphic rock. It is possible for these groups to be split-up into 20 rock types, which all have their own characteristics. Typically, rock materials are obtained by conventional quarrying operations.

Igneous rock
Igneous rock is formed by the crystallisation and solidification of a molten silicate magma. All types of rock within the igneous group are usable as armour, filter as well as core filling. Two well-known types of igneous rock are granite and basalt. Granite is one of the most popular building materials and because of its hardness and toughness it has gained widespread use throughout the human history. Basalt rock is also widely used in the Netherlands, as revetment on dikes, breakwaters and quay walls. This is due to the shape of the basalt columns and therefore can be placed as a puzzle.

Sedimentary rock
Sedimentary rock is formed by sedimentation and subsequent lithification of mineral grains, either under water or more rarely on an ancient land surface. This type of rock is less suitable as armour, filter or as core filling and generally has a lower density than igneous rock. Two examples of sedimentary rock are: sandstone and limestone.

Metamorphic rock

Metamorphic rock is formed by the effect of heat and pressure on igneous, metamorphic or sedimentary rock for geological periods of time, resulting in new minerals and textures developing within the pre-existing rock. Temperatures higher than $150\ to\ 200\ °C$ and pressure over $1500\ bar$ is needed for this metamorphic process. Because this type of rock is formed from other types of rock the differences are large. A highly-known and used type of metamorphic rock is marble.

5.2 Rock mass and sizes

In a normal grain size distribution the value of d_{50} is used, which is the median grain size. This median grain size is determined by sieving a sample. However, for larger stones is sieving rather difficult and instead the simplest measurement is its mass. When the weight of individual stones is determined also the median weight is known. For both the median diameter and the median weight means that 50% exceeds the value and 50% is below this value. Nevertheless in most design formulas not the weight, but the diameter is used. Considering stones have irregular shapes it is not easily done to convert the weight into the diameter. Because of this the nominal diameter is internationally used and is defined as:

$$d_{n50} = \left(\frac{M_{50}}{\rho_s}\right)^{\frac{1}{3}} \tag{5.1}$$

With:			
	d_{n50}	median nominal diameter	$[m]$
	M_{50}	median mass	$[kg]$

Still, considering that the shape of most rock is more-or-less the same, a relation between the median and median nominal diameter exists. This relation can be noted as a shape factor times the median diameter:

$$d_{n50} = F_s * d_{50} \tag{5.2}$$

With:			
	d_{50}	median diameter	$[m]$
	F_s	shape factor	$[-]$

According to [LAAN, 1982] this shape factor is around 0.84, and this value is widely applied in hydraulic engineering practice. Furthermore the research by Laan in 1981 [SCHIERECK, 2012] shows that in nearly all cases the shape factor is between 0.70 and 0.90. The values for the shape factor are based on a report published by Laan in 1981, however, the concerned report is missing from the libraries and unfortunately Laan passed away. For this reason [WITTEMAN, 2015] researched the shape factor of quarry rock again and found a value of 0.86, which differs relatively little from the commonly applied value. Nonetheless, [WITTEMAN, 2015] recommends to apply the newly derived value of 0.86 in hydraulic engineering practice because for this value a theoretical justification is provided. The median sieve size, the median nominal diameter and the median mass are thus related using the following conversion factor:

$$F_s^* = \left(\frac{M_{50}}{\rho_s * d_{50}^3}\right) = 0.84^3 \cong 0.60 \tag{5.3}$$

With:			
	F_s^*	conversion factor	$[-]$

The assumption of that the conversion factor = 0.60 is considered best practice and compares well with the values in the field, which vary from 0.34 *to* 0.72. Also values of 0.66 *to* 0.70 are found for model-scale armour stone materials used in hydraulics laboratories [CIRIA/CUR/CETMEF, 2007].

It should be noted that the "nominal" diameter is not related to a certain exceedance value.

5.3 Rock grading

In a certain sample of rock produced at a quarry a range of stone weights will be observed. It can be said that all rock materials are therefore, to some extent, graded. The difference between the bigger and smaller rock says something about the grading width of the sample. The three main grading widths which are recommended are given in Table 2.

TABLE 2: RECOMMENDED GRADING WIDTHS

	$(W_{85}/W_{15})^{1/3}$ *or* d_{85}/d_{15}	W_{85}/W_{15}
Narrow or "single-sized" gradation	Less than 1.5	1.7 – 2.7
Wide gradation	1.5 – 2.5	2.7 – 16.0
Very wide or "quarry run" gradation	2.5 – 5.0+	16 – 125+

Rock from a quarry, or for that matter any kind of rock, comes in all kind of sizes. Therefore it has a big advantage to have some sort of grading classes for practical use. The producer of rock, i.e. quarries, are encouraged to produce the graded products because designers will use these standard classes whenever possible. European standards [EN 13242, 2008] and [EN 13383, 2002] define gradings for larger rock, i.e. armour stone, and smaller rock respectively. Stones smaller than $CP_{45/125}$, see Table 4, are not defined in [EN13383, 2002] because they cannot be applied in hydraulic engineering works in unbounded form as armour layer. However, they can be used for offshore works in deep water as an insulation layer or as filter layers. In the European standards, gradings are defined by a lower sieve class and upper sieve class.

In [EN 13242, 2008] no special classes are defined, but it has been defined how classes need to be described. The stones are defined by their size, e.g. stones 20/40 means that the stones have a "minimum" of a lower sieve class of $20\,mm$ and a "maximum" of the upper sieve class of $40\,mm$. $G_{c,85/20}$ means that 85% of the stones is smaller than the upper sieve class and 20% of the stones is smaller than the lower sieve class [SCHIERECK, 2012]. In Table 3 the standard gradings of course material are shown.

TABLE 3: COURSE GRADINGS [EN 13242, 2008]

aggregate	size	percentage passing by mass					category
		$2d_{lcl}$	$1.4d_{lcl}$	d_{lcl}	d_{ucl}	$d_{ucl}/2$	G
coarse	$d_{ucl}/d_{lcl} < 2$ *or* $d_{ucl} < 11.2\,mm$	100	98 to 100	85 to 99	0 to 20	0 to 5	$G_c85/200$
		100	98 to 100	85 to 99	0 to 20	0 to 5	$G_c85/200$

With: d_{lcl} lower sieve class $[mm]$
d_{ucl} upper sieve class $[mm]$
G_c course gradings $[-]$

For larger rock special classes are defined, these standard classes of rock grading are given in Table 4:

TABLE 4: STANDARD CLASSES OF ROCK GRADING [EN 13383, 2002]

Class Name	described in EN 13383		$d_{50}(cm)$	d_{85}/d_{15}	$d_{n50}\,(cm)$	Layer thickness $1.5d_{n50}(cm)$	Minimal dumping quantity with layer of $1.5d_{n50}(kg/m^3)$
	range	range of M_{50} for category "A" (kg)					
CP45/125	$45/125\ mm$	0.4-1.2	6.3-9.0	2.8	6.4	20	300
CP63/180	$63/180\ mm$	1.2-3.1	9.0-12.5	2.8	9	20	300
CP90/250	$90/250\ mm$	3.1-9.3	12.5-18	2.8	12.8	20	300
CP45/180	$45/180\ mm$	0.4-1.2	6.3-9.0	4.0	6.4	20	300
CP90/180	$90/180\ mm$	2.1-2.8	11-12	2.0	9.7	20	300
LMA 5-40	$5-40\ kg$	10-20	18-23	1.7	17	25	500
LMA 10-60	$10-60\ kg$	20-35	23-28	1.5	21	32	550
LMA 40-200	$40-200\ kg$	80-120	37-42	1.5	43	52	850
LMA 60-300	$60-300\ kg$	120-190	42-49	1.5	38	57	950
LMA 15-300	$15-300\ kg$	45-135	30-44	2.7	31	46	700
HMA 300-1000	$300-1000\ kg$	450-690	65-75	1.4	59	88	1325
HMA 1000-3000	$1-3\ ton$	1700-2100	103-110	1.4	90	135	2050
HMA 3000-6000	$3-6\ ton$	4200-4800	138-144	1.2	118	177	2700
HMA 6000-10000	$6-10\ ton$	7500-8500	167-174	1.2	144	216	3250

Besides the European standard grading, a different grading is mainly used in the offshore industry. These different requirements for rock grading are set by [STATOIL TR1370, 2009] and are intended for subsea rock installation.

TABLE 5: ROCK GRADING BY [Statoil TR1370, 2009]

Class	Rock size	Target (mm)	Min (mm)	Max (mm)
1 – 3" $(75\ mm\ rock)$	d_m	--	--	100
	d_{90}	75	60	90
	d_{50}	50	40	60
	d_5	22	16	32
1 – 4" $(100\ mm\ rock)$	d_m	--	--	125
	d_{90}	100	90	115
	d_{50}	60	50	70
	d_5	22	16	32
1 – 5" $(125\ mm\ rock)$	d_m	--	--	150
	d_{90}	125	110	135
	d_{50}	75	60	90
	d_5	22	16	32

Furthermore according to [STATOIL TR1370, 2009] crushed rock shall comply with the following:

- Project design requirements for design strength parameters (friction angle and attraction), grading, specific density and bulk density
- Chemically stable
- Not flaky

5.4 Rock shapes

The shape of rock is quite important for hydraulic engineering. This is because the shape has an influence on the stability, shear strength, permeability and filtering properties of a layer of rock. For typical angular rock sources, two uncorrelated rock shape descriptors are described by Newberry and Stewart *et al.* in 2003. These are the length-to-thickness ratio and blockiness, one is for form and the other relates to compactness. Both are practical and sufficiently reproducible [CIRIA/CUR/CETMEF, 2007]. Both rock shape descriptors will be described in this paragraph.

5.4.1 Length-to-thickness ration

The length-to thickness-ratio (l/d) is also referred to the aspect ratio sometimes. It is defined as the maximum length of a single stone, divided by the minimum width. This minimum width is the distance between two parallel lines whereby the rock would just pass, see Figure 33. In [EN 13383, 2002] this from is also defined and therefore the industry standard.

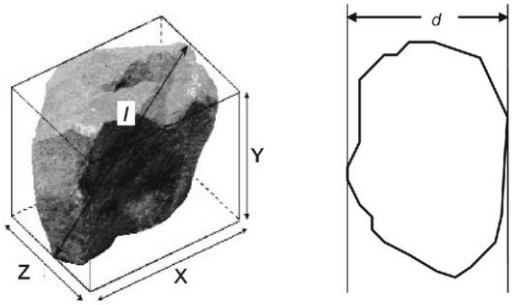

FIGURE 33: MEASUREMENT SYSTEM FOR STONE SHAPES [CIRIA/CUR/CETMEF, 2007]

5.4.2 Blockiness

Blockiness (BLc) of a stone is defined as the percentage of the volume with reference to an orthogonal XYZ *box* with minimum volume, see Figure 34. It can also be said that it is a volume reduction factor because it is the difference of volume between the stone and the box. Blockiness relates to compactness and correlates well with the packing behaviour of placed stones. The density, numbers of contact points and thus interlock qualities are dependent on the blockiness of a stone. And with a higher blockiness of a stone these qualities are improved.

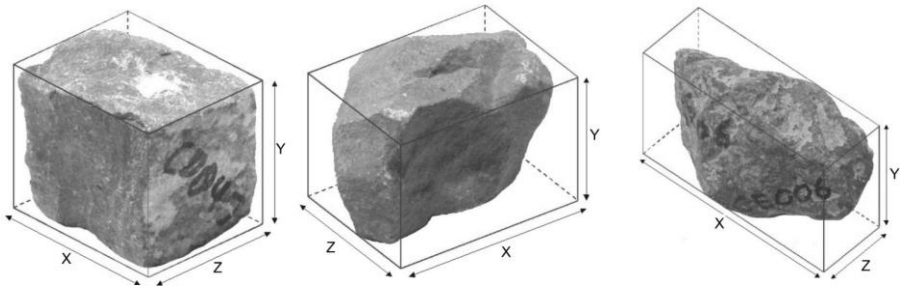

FIGURE 34: BLOCKINESS (FROM LEFT TO RIGHT, BLC = 80%, 60% *and* 40%) [CIRIA/CUR/CETMEF, 2007]

The blockiness of a stone can be calculated with the following formula:

$$BLc = \left(\frac{M}{\rho_s} * \frac{1}{X * Y * Z}\right) * 100 \tag{5.4}$$

With: BLc Blockiness [%]

The orthogonals X, Y *and* Z of the box are determined by measuring the maximum, the intermediate and minimum dimensions respectively of the smallest hypothetical box that would enclose the block. To help find the X, Y *and* Z dimensions, Z is set parallel to d, see Figure 33, and X *and* Y are then defined by the axes of the perpendicular plane with projected minimum area.

5.4.3 Cubicity

Another way to quantify the shape of a rock is the cubicity, or form index which is used in France. The cubicity of a stone can be calculated with the following formula:

$$Cubicity = \frac{L + I}{2S} \tag{5.5}$$

With:
	L	longest orthogonal	$[m]$
	I	intermediate orthogonal	$[m]$
	S	shortest orthogonal	$[m]$

The cubicity differs from the blockiness of a stone because the dimensions of X, Y *and* Z are different from L, I *and* S. For the cubicity the longest orthogonal, L, is first defined and then both the orthogonals G *and* E. Cubicity can be more objectively measured for highly irregular shapes than blockiness. However, X, Y *and* Z are more relevant for quantifying the shape of blocky pieces since Z is the longest side of the enclosing box and L would be close to the longest dimension of the box, i.e. its diagonal.

6

Dumping of a Single Stone

To get a better understanding of what happens with rock falling through a fallpipe and settling below the fallpipe, first the dumping of a single stone in stagnant water will be looked at. This is done to get a better insight of the forces and processes involved when an object or rock is falling through water. There are three different forces working on a single stone which is falling through water. Forces in the same direction as the settling direction and forces in the opposite direction as the settling direction (the vertical forces) and forces perpendicular of the settling direction (the horizontal forces).

6.1 Physical description of the settling process

When a single rock is falling through stagnant water it will be subjected to an acceleration due to the gravitational force. The settling velocity of a single rock will increase until the terminal, or equilibrium, velocity is reached. This equilibrium velocity is caused by the fact that the resisting force will increase with an increasing settling velocity and thus the acceleration decreases. Therefore this equilibrium will be reached when the gravitational force is the same as the resistance force.

6.2 Vertical forces

As mentioned before, when a single stone is falling through water it is subjected to a downwards directed force, the gravitational force. The upwards directed forces are the drag force, caused by the falling rock through the water and the buoyance force, caused by density difference between the water and the settling stone. The manner in which the three different vertical forces act on a single rock falling through water can be seen in Figure 35 and will be further elaborated in this paragraph.

6.2.1 Gravitational force

The downwards directed gravitational force is the product of the mass of an object and the gravitational acceleration. So the gravitational force is equal to:

$$F_z = M * g \tag{6.1}$$

With:	F_z	gravitational force	$[kgm/s^2]$
	M	mass	$[kg]$

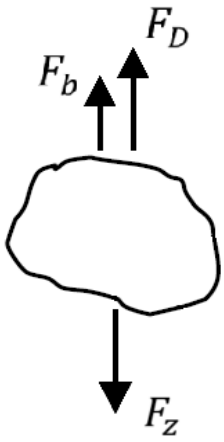

FIGURE 35: VERTICAL FORCES ON A SINGLE STONE FALLING THROUGH WATER

The mass of a sphere depends on the volume and density. The volume of a sphere is given in (4.11), for convenience given here again:

$$V_s = \frac{1}{6} * \pi * d^3 \tag{6.2}$$

Therefore the mass is given as:

$$M = \frac{1}{6} * \pi * d^3 * \rho_s \tag{6.3}$$

Substituting (6.3) in (6.1), and the gravitational force becomes:

$$F_z = \frac{1}{6} * \pi * d^3 * \rho_s \tag{6.4}$$

6.2.1 Buoyance force

Buoyance is an upward directed force exerted by a fluid that opposes the weight of an immersed object. This is due to the difference in density between the settling object, i.e. the settling sphere, and the ambient fluid. The buoyance force for a sphere is written as:

$$F_b = -\frac{1}{6} * \pi * d^3 * \rho_f * g \tag{6.5}$$

With: F_b buoyancy force $[kgm/s^2]$

The difference between the gravitational force and the buoyance force is also denoted as the submerged weight of a particle, the general form of this equation is given in (4.3). For a sphere the submerged weight is written as:

$$F_w = \frac{1}{6} * \pi * d^3 * (\rho_s - \rho_f) * g \tag{6.6}$$

With: F_w submerged weight of a sphere $[kgm/s^2]$

6.2.2 Drag force

Let us consider an object with a relative motion compared to the fluid wherein it is moving. This fluid could be an ideal fluid whereby the viscous effects are not taken into account. Which means no resulting drag force is applied on the object. However, for an object falling in stagnant water, the fluid needs to be characterized as a non-ideal fluid. A counteracting force in opposite direction of the velocity vector will therefore be experienced by the object, the drag force. This drag force is the result of two effects, the frictional force on the rough surface of the stone and due to a pressure difference between the front and the back of an object. The friction on the object, or the shear stress, is determined by the flow separation point. Boundary layer theory can predict this separation point, but the pressure distribution in the separation region cannot be predicted. The actual contribution of the two effects is difficult to determine and depends on the geometry of the object and the type of flow. The total drag coefficient is often expressed as a function of the Reynolds number and the shape of the object. The general form of the drag force is given in (4.1). The surface area exposed to drag for a sphere is equal to:

$$A_s = \frac{1}{4} * \pi * d^2 \tag{6.7}$$

With: A_s surface area exposed to drag/lift for a sphere $[m^2]$

Substituting (6.7) in (4.1) and the expression for the drag force for a sphere falling through water thus becomes:

$$F_D = \frac{1}{8} * \pi * d^2 * C_D * \rho_f * (u_f - u_s) * |u_f - u_s| \tag{6.8}$$

With: u_f velocity of the fluid $[m/s]$
u_s velocity of the solids $[m/s]$

6.2.3 Settling velocity

The combination of the three vertical forces and with the help of Newton's law of motion the differential equation is given as:

$$F_z + F_b + F_D = M * a_v \tag{6.9}$$

With: α_v vertical acceleration of a particle $[m/s^2]$

When solving (6.9), with substituting (6.4), (6.5) and (6.8), the functions of the settling velocity with respect to time and distance can be derived. The expression for a sphere, falling through stagnant water, with respect to time and distance are given in (6.10) and (6.11) respectively.

$$u(t) = \sqrt{\frac{4 * g * d * (\rho_s - \rho_f)}{3 * C_D * \rho_f}} * \tanh\left(\sqrt{\frac{3 * C_D * g * \rho_f}{8 * d * (\rho_s - \rho_f)}} * t\right) \tag{6.10}$$

With: t time $[s]$

$$u(x) = \sqrt{\frac{4 * g * d * (\rho_s - \rho_f)}{3 * C_D * \rho_f}} * \left(1 - e^{\frac{-3 * C_D * \rho_f}{2 * d * \rho_s} * x}\right) \tag{6.11}$$

In Figure 36 the velocity of the settling sphere is presented as function of time.

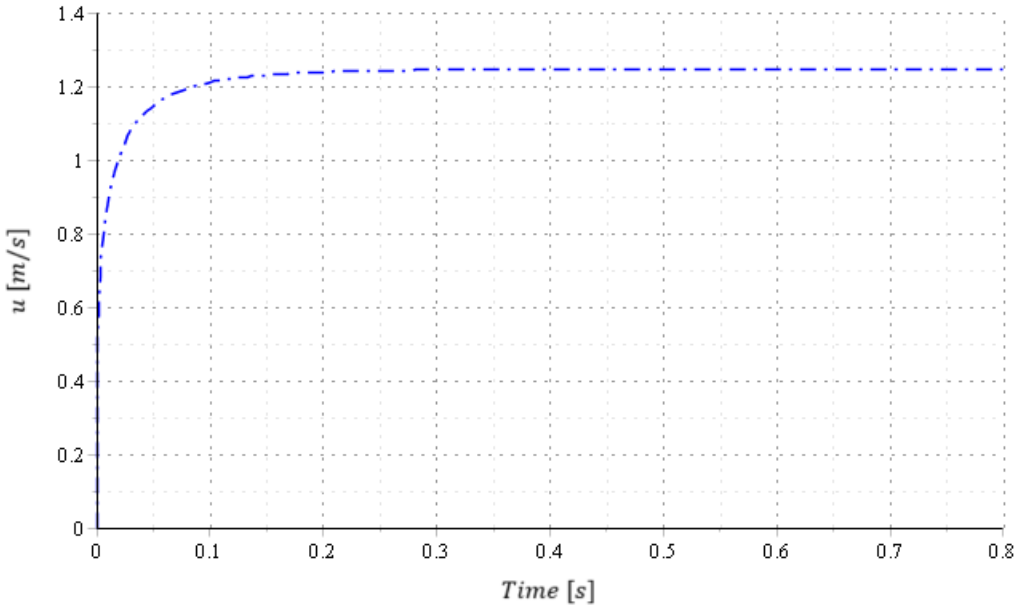

FIGURE 36: VELOCITY OF A SETTLING SPHERE AS FUNCTION OF TIME

In Figure 37 the velocity of the settling sphere is shown as function of distance.

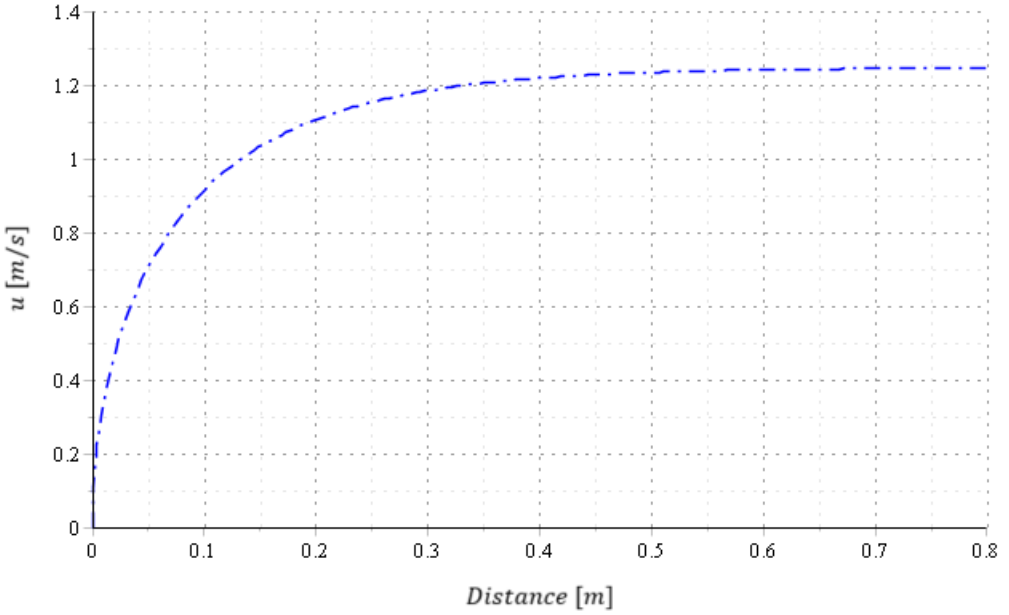

FIGURE 37: VELOCITY OF A SETTLING SPHERE AS FUNCTION OF DISTANCE

For this graphical illustration, the diameter of the sphere is assumed on $0.075\,m$, a commonly used median nominal diameter of a stone in the offshore industry. Furthermore, the drag coefficient is set on 1, the density of the fluid is assumed on $1025\,kg/m^3$ and the density of the solids on $2650\,kg/m^3$.

It is easily noticed from both graphs that the settling velocity reaches an equilibrium quite fast. With the used parameters this equilibrium is reached after around $0.4\ s\ or\ 0.6\ m$ and the terminal velocity is then equal to $1.25\ m/s$. This equilibrium velocity is reached when the downward force is equal to the upward force. That is, the submerged weight of a particle is equal to the drag force. By equating (4.2) and (4.3) the equilibrium settling velocity of a particle, through stagnant water, can be easily obtained:

$$u_e = \sqrt{\frac{2 * \mathrm{V} * g * \Delta}{A_D * C_D}} \tag{6.12}$$

With: u_e equilibrium settling velocity $[m/s]$

Doing the same for (6.6) and (6.8) the equilibrium settling velocity of a sphere is obtained. Equation (6.12) and (6.13) are equal to each other when the surface area and volume, (6.7) and (4.11) respectively, of a sphere are taken.

$$u_e = \sqrt{\frac{4 * g * d * \Delta}{3 * C_D}} \tag{6.13}$$

In 1982 van Mazijk determined that the depth on which a settling object reaches the equilibrium settling velocity can be calculated with [DE REUS, 2004]:

$$x = -\frac{1}{\varphi_m} ln\,(1 - \epsilon^2) \tag{6.14}$$

With: φ_m coefficient of the equilibrium velocity equation by van Mazijk $[m^{-1}]$
ϵ certain fraction of the equilibrium velocity $[-]$

The coefficient of the equilibrium settling velocity equation by van Mazijk can be calculated with:

$$\varphi_m = 1.5 * \frac{C_D * \rho_f}{d * \rho_s} \tag{6.15}$$

Drag coefficient for rock

The determination of the drag coefficient for rock is quite ambitious because even for a sphere this is rather difficult. However, several empirical relationships between the drag coefficient and the Reynolds number for a sphere are in use. The most common formulae for the laminar, or Stokes, transitional and turbulent regime are respectively [VAN RHEE, 2002]:

$$C_D = \frac{24}{Re_p} \qquad Re_p \leq 1 \tag{6.16}$$

$$C_D = \frac{24}{Re_p} + \frac{3}{\sqrt{Re_p}} + 0.34 \qquad 1 < Re_p < 2000 \tag{6.17}$$

$$C_D = 0.4 \qquad 2000 \leq Re_p < 200000 \tag{6.18}$$

The particle Reynolds number is noted in (4.8), however for convenience given here again.

$$Re_p = \frac{u_e * d_{n50}}{\nu} \tag{6.19}$$

The kinematic velocity of water depends on the temperature. The following relation between the kinematic viscosity and temperature is often used [VAN RHEE, 2002]:

$$\nu = \frac{40 * 10^{-6}}{20 + T} \tag{6.20}$$

With: T temperature $[°C]$

In Figure 38 the relationship between the drag coefficient for a smooth sphere and the particle Reynolds number is shown as given in 1990 by Battjes [ROOK, 1994].

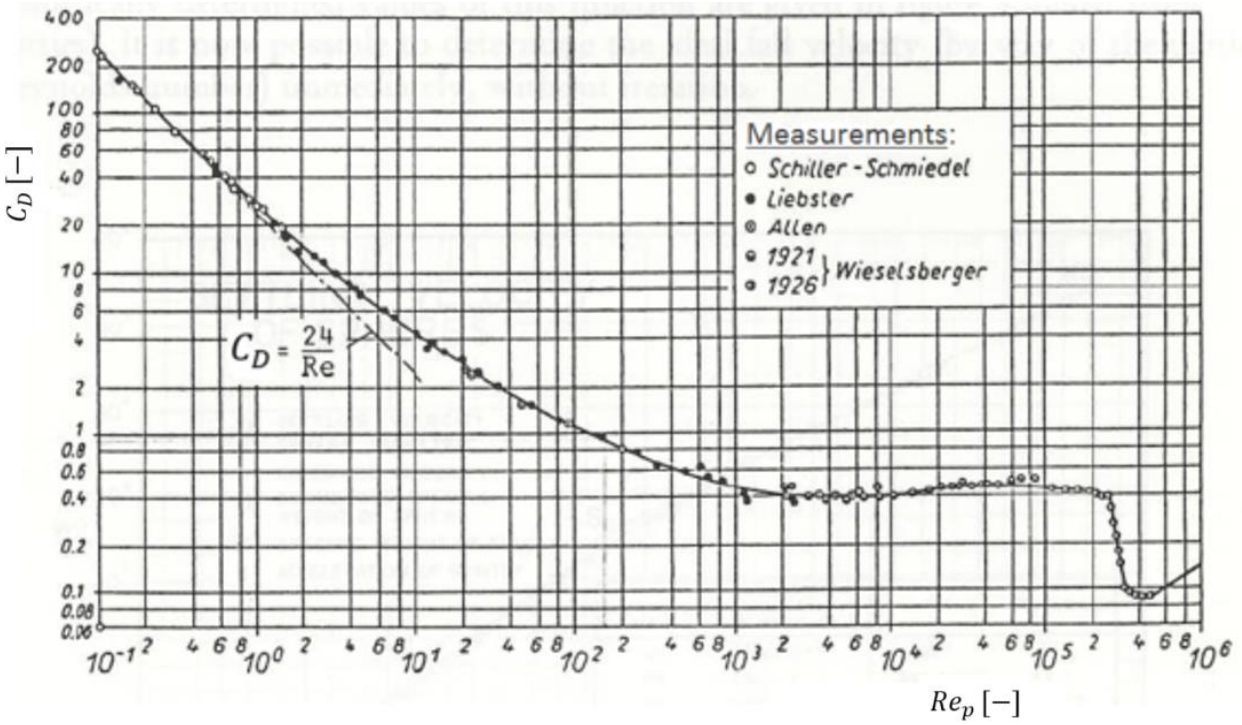

FIGURE 38: RELATIONSHIP DRAG COEFFICIENT FOR SPHERES AND THE PARTICLE REYNOLDS NUMBER [ROOK, 1994]

The drag coefficient for rock is researched quite extensively and several empirical expressions are derived, for example by Kniess in 1981, [VAN DER WAL, 2002] and [DE REUS, 2004]. The drag coefficient defined by Kniess in 1981, based on stones with an average diameter of $270\ mm$, is [RAVELLI, 2012]:

$$C_{D,Kniess} = \frac{2 * \Delta * g * 0.245 * l}{0.25 * \pi * u_e^2} \tag{6.21}$$

The weighted average value for the drag coefficient found by Kniess in 1981 was 0.81 ± 0.25 while the drag coefficient for stones with a nominal diameter between $0.017\ m\ and\ 0.25\ m$ was constant: 0.7 ± 0.15 [RAVELLI, 2012].

[VAN DER WAL, 2002] showed that (6.21) is inaccurate for the calculation of the drag coefficient when the shape of rock deviates from a certain margin. This was found due to a calculated higher equilibrium velocity for relative flat stones $(l/d \geq 2)$ and a calculated lower equilibrium velocity for relative angular stones $(l/d \leq 1.5)$.

It is also noted by [DE REUS, 2004] that the drag coefficient determined by Kniess in 1981 is difficult to compare to other drag coefficients due to a deviating definition of the diameter. Besides, the results of Kniess were based on a small amount of measurements.

[VAN DER WAL, 2002] concludes from his research that the drag coefficient of rock in stagnant water follows a normal distribution, independent of the diameter. This distribution is given by:

$$f_{C_D}(C_D) = \frac{1}{\sqrt{2\pi} * \sigma_{C_D}} * e^{-\frac{\left(C_D - \mu_{C_D}\right)^2}{2\sigma_{C_D}^2}} \tag{6.22}$$

With:
- f_{C_D} probability density function of the drag coefficient
- μ_{C_D} mean value of the drag coefficient [−]
- σ_{C_D} standard deviation of the drag coefficient [−]

An improvement of around **10%** for the accuracy of the drag coefficient can be achieved if the length-to-thickness ratio is used for the determination of the mean value of the drag coefficient. It was further suggested that the angularity of rock also could influence the drag coefficient, but not included in the study.

[DE REUS, 2004] concluded from his research that the drag coefficient for rock will be around 1.6 in practice. This is based on the found mean value of the drag coefficient for two sizes of rock used in his experiments. The stone diameters researched are $d_{n50} = 0.016\,m\ and\ 0.077\,m$, with corresponding mean values of the drag coefficient of $\mu_{C_D} = 1.43\ and\ 1.64$ respecively. However, the l/d ratio in practice will be larger than the l/d ratio of the smaller stone, which causes a higher drag coefficient. It is furthermore noted that the boundary layer will be in the turbulent regime for a stone with a larger diameter than $0.15\,m$, which causes a lower drag coefficient. Also the average l/d ratio will decrease in practice for increasing stone size, which also causes a lower drag coefficient.

Equilibrium settling velocity of rock

With the drag coefficient of rock, the equilibrium settling velocity, i.e. terminal velocity, can be determined. [VAN DER WAL, 2002] recommended the following method to do so:

1. Determination of the mass of the stone;
2. Determination or estimation of the density of the stone;
3. Calculation of the median nominal diameter with (5.1);
4. Determination of (l/d);
5. Calculation of the equilibrium settling velocity with:

$$u_e = \sqrt{2 * \Delta * d_n * \frac{g}{C_D}} \tag{6.23}$$

This method for calculating the equilibrium settling velocity assumes that the surface exposed to the drag is equal to the square of the nominal diameter.

The drag coefficient can be determined with the use of (6.20). When the length-to-thickness ratio is used the mean value and standard deviation of the drag coefficient are given as [VAN DER WAL, 2002]:

$$\mu_{C_D} = 0.54 * \frac{l}{d} + 0.42 \tag{6.24}$$

$$\sigma_{C_D} = 0.30 \tag{6.25}$$

When the (l/d) ratio is not used the mean value and standard deviation of the drag coefficient are given as:

$$\mu_{C_D} = 1.42 \tag{6.26}$$

$$\sigma_{C_D} = 0.33 \tag{6.27}$$

6. Correction with a shape factor, needs to be determined.

As mentioned in the previous section, [DE REUS, 2004] also conducted research into the settling behaviour of rock. The same method, as the method of [VAN DER WAL, 2002], for determining the settling velocity was used. Though, he found different values for the mean value and standard deviation of the drag coefficient. For larger stone sizes, which are used in the offshore industry, it was found:

$$\mu_{C_D} = 1.64 \tag{6.28}$$

$$\sigma_{C_D} = 0.30 \tag{6.29}$$

Additionally, [DE REUS, 2004] also found a relation for the terminal velocity which is only dependent on the l/d ratio and the nominal diameter of the stone.

$$u_e = 6.425 \sqrt{\frac{d_{n50}}{l/d}} \tag{6.30}$$

In Figure 39 a comparison of the terminal velocity as function of the length-to-thickness ratio is shown. For this end six different expressions for the drag coefficient of rock are used to calculate the equilibrium velocity. These are the terminal velocity given by: 1. a smooth sphere (6.13); 2. Kniess (6.21); 3. van der Wal dependent on the l/d ratio (6.22); 4. van der Wal independent on the l/d ratio (6.22); 5. de Reus (6.22) and 6. de Reus only dependent on the l/d ratio and d_{n50} (6.30). For the determination of the drag coefficient for methods 3, 4 and 5 the different corresponding mean values and standard deviations of the drag coefficient are used. The other parameters needed for this graphical illustration are assumed as: the diameter of the stone on $0.075\,m$, the density of the fluid on $1025\,kg/m^3$ and the density of the solids on $2650\,kg/m^3$.

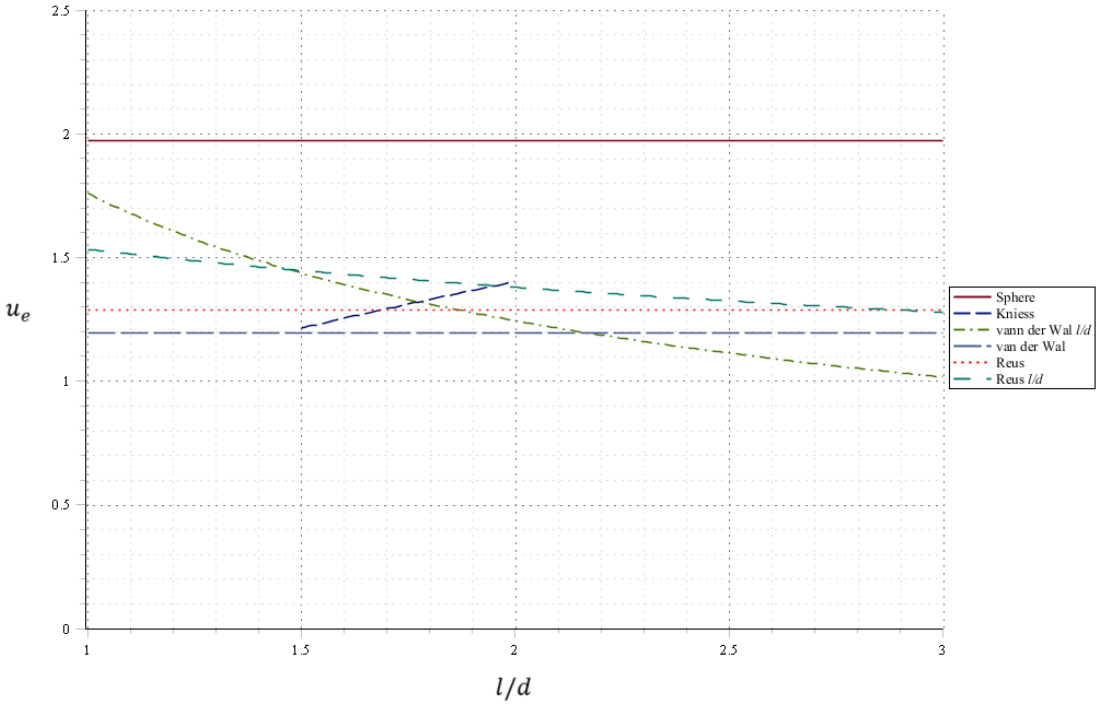

FIGURE 39: COMPARISON OF THE DIFFERENT TERMINAL VELOCITIES FOR ROCK BY DIFFERENT DRAG COEFFICIENTS

Time scale

In the previous sections the equilibrium velocity of a stone falling through water is treated. Now, with this knowledge a timescale for settling can be derived. The time a particle takes to settle is the distance to cover divided by the total velocity, or given in formula form as:

$$T_s = \frac{SOD}{u_e + u_f} \tag{6.31}$$

With: T_s timescale for settling $[s]$

6.3 Horizontal forces

When considering a stone falling through water, the stone will not settle entirely in vertical direction. Also a horizontal displacement, caused by different forces, will be noticed. This horizontal displacement can be caused by a lift force and due to a horizontal flow in the water column, such as an ambient current. The manner on how the two different horizontal forces act on a single rock falling through water can be seen in Figure 40 and will be further elaborated in this paragraph.

6.3.1 Lift force

In literature the lift force is often mentioned as a force which can cause a horizontal displacement of a stone Lift forces are the result of an asymmetric flow field around objects or stones, which can be caused by an irregular shape of the objects or stones. The lift force, based on the general formulation of the resistance force by Stuckrath *et al.* in 1996 [WEUSTINK, 1998], is given in (4.2).

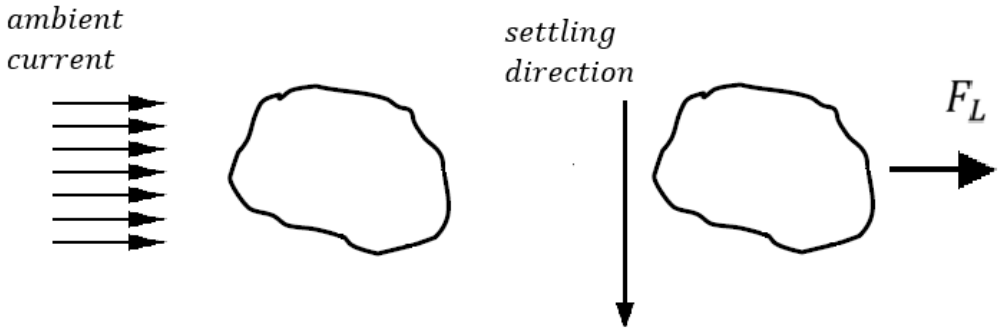

FIGURE 40: HORIZONTAL FORCES ON A SINGLE STONE FALLING THROUGH WATER

Just as for the drag coefficient, the lift coefficient also depends on the influence of the flow velocity in relation with the viscosity expressed in the Reynolds number. Further, the shape and size of a stone also influence the magnitude of the lift coefficient. It is assumed by [WEUSTINK, 1998] that the lift force is the resulting force of the resistance force of the fluid and is determined by three phenomena. The direction of the lift force, as shown in Figure 40, is defined as perpendicular to the moving direction of the stone. The three phenomena also act perpendicular on the settling direction. This phenomena will be further elaborated in this section and are: vortex shedding, the Magnus-effect and asymmetric boundary layer separation.

Vortex shedding

Consider a flow around an object, when the Reynolds number is higher than around 4000, a more or less regular oscillating flow will be situated behind the object. This is caused by flow separation and occurs alternating on one and then on the other side of the object [VAN DER WAL, 2002], see Figure 41.

FIGURE 41: VON KARMAN VORTEX STREET [RAKESH *ET AL.*, 2014]

Von Karman conducted a theoretical research on this effect and concluded that only one stabile asymmetric configuration is possible [DE REUS, 2004]. Often, this phenomena is therefore called the von Karma vortex street. The frequency of this vortex shedding can be described with the Strouhal number:

$$St = \frac{\omega * d}{u} = \frac{2\pi * d}{T_{vs} * u} \tag{6.32}$$

With:	St	number of Strouhal	$[-]$
	ω	radial frequency	$[s^{-1}]$
	T_{vs}	period of vortex shedding	$[s]$

Comprehensive research is done into the principle of the vortex shedding for the situation of a falling stone through water. When the terminal velocity and the number of Strouhal are constant expression (6.32) can be rewritten as given in equation (6.33), and the vortex shedding period is obtained. This period is equal to the alternating acceleration direction in the lift force direction [VAN DER WAL, 2002].

$$T_{vs} = \frac{2\pi}{St\sqrt{\frac{2\Delta * g}{C_D}}} * \sqrt{d} \tag{6.33}$$

From (6.35) can be concluded that the period of the vortex shedding between the two alternating sides is proportional to the square root of the diameter of the stone. The random walk model is based on this principle by Vrijling *et al.* in 1995 [DE REUS, 2004]. This random walk model is further elaborated in (9.1.2 Random Walk Model).

Magnus-effect

Consider an object moving, and at the same time, rotating through a fluid. As a result of these translation and rotation movements a lift force, perpendicular to the falling direction, will act on the object. This effect is called the Magnus-effect and the explanation of the cause is visualized in Figure 42, defined by Stuckrath *et al.* in 1996 [WEUSTINK, 1998],[VAN DER WAL, 2002].

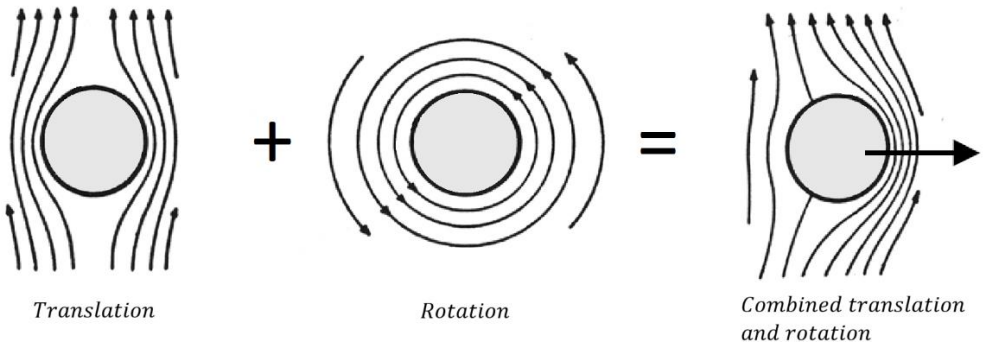

FIGURE 42: MAGNUS-EFFECT

The visualisation is given for a sphere in a fluid. The fluid wants to adapt the rotational movement of the sphere due to a friction between both. By this, the flow velocity on the one side of the sphere is increased while on the other side it will decrease, causing a pressure difference. This pressure difference results in the lift force perpendicular to the falling direction. Furthermore, also a gyroscopic moment is caused by the rotation of the object which results in a, much slower, rotation in direction perpendicular on the initial rotation. As a result of these two rotations a spiral shaped trajectory towards the seabed will be followed by the falling object.

Asymmetric boundary layer separation

Asymmetric boundary layer separation is caused by a similar effect as the Magnus-effect. When looking at natural rock it is fast concluded that stones are not comparable to a perfectly smooth sphere. Due to the shape and the variating roughness on sides of a stone asymmetric boundary layer separation will occur. Flow on a rougher side of a stone will separate sooner from the rock in comparison to flow on a smoother side. As a result of this asymmetric boundary layer separation, an asymmetric pressure distribution will develop which causes a lift force, also perpendicular to the falling direction [VAN GELDEREN, 1998].

6.3.2 Current

In most cases a current is present when looking at natural environments, for example caused by tide or river flow. If rock is dumped in such environments the horizontal component of the settling velocity of a stone will be equal to the current velocity of the surrounding water in the equilibrium situation. A graphical representation is presented in Figure 43.

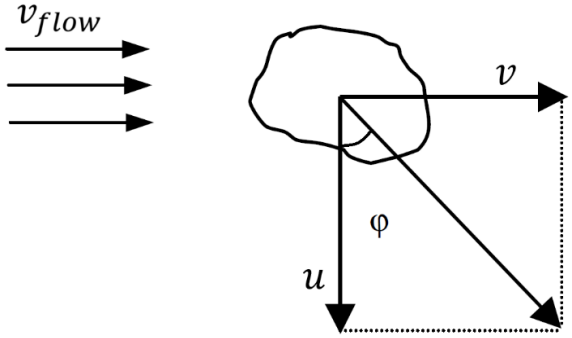

FIGURE 43: CURRENT ON A SINGLE STONE FALLING THROUGH WATER

[VAN DER WAL, 2002] derived an equation which describes the movement of the settling rock for this equilibrium situation:

$$tan(\varphi) = \frac{v}{u} = \frac{v_{flow}}{u} \tag{6.34}$$

With:	φ	angle between the vertical and resultant velocity	[°]
	v_{flow}	velocity of the ambient fluid	$[m/s]$

As explained, this method is only valid when the horizontal component of the settling velocity is equal to the velocity of the surrounding water. When a stone reaches the seabed before this equilibrium situation the velocity can be calculated according to the following differential equation [VAN DER WAL, 2002]:

$$V * (\rho_s - \rho_f) * \frac{dv}{dt} = \frac{1}{2} * C_L * A_L * \rho_f * (v - v_{flow})^2 \tag{6.35}$$

6.4 Trajectory and motion

[VAN GELDEREN, 1999] gives an overview of the knowledge and research done on the trajectory and motion of settling stones at that time. In this paragraph a short summary of his overview will be given.

The research on the settling velocity of rock done in 1968 by Alger and Simons describes the trajectory and motion of different stones. The shape of the stone was defined with a modified Corey shape factor and it was found that a stone with a particle Reynolds number lower than 100 has a more or less vertical trajectory and will fall in a relative stable orientation. When looking at a stones with particle Reynolds numbers larger than 2000 a fully developed tipping and sliding motion is showed. The tipping-sliding motion is characterized by oscillations in the horizontal plane. These oscillations will increase with time until they will pass the threshold for tipping. After this, the stone will rotate along its axis and returns suddenly to the oscillating motion. The time between these two phases and the number of rotations seems completely random. For stones with a particle Reynolds number in between 100 and 2000 a transitional region exists.

For an increasing value of the modified Corey shape factor a decrease in the tipping-sliding motion was noticed, however an increase in rotation was concluded by Alger and Simons in 1968 [VAN GELDEREN, 1999]. When the shape factor increases, the geometry of the rock will be more like a cube. The observations in 1968 by Alger and Simons are thus completely in line with the settling velocities of the basic geometries [VAN GELDEREN, 1999]. It was furthermore concluded that the shape factor has a big advantage due to the fact the determination of the area of a rock can only be done in a laboratory and is thus not suitable for practical applications.

[WEUSTINK, 1998] tried to categorize the settling behaviour of rock based on the particle Reynolds number and the dimensionless moment of inertia. To determine the moment of inertia for natural rock is virtually impossible and quite ambitious. This in comparison to the basic geometries wherefore this calculation is quite easy. If the rock was modelled as a sphere, the dimensionless moment of inertia is not related to the particle Reynolds number. It is assumed that no prediction of the settling trajectory could be made based on the dimensionless moment of inertia [VAN GELDEREN, 1999].

[VAN GELDEREN, 1999] concluded in his own research that the trajectory and movement of a settling stone is a combination of the movements of a cube, sphere, cylinder and disc due to the diversity of the rock shape.

Within the rock grading [VAN DER WAL, 2002] used for his experiments the horizontal spreading of the stones is just shy of agreeing with a Rayleigh-distribution. This confirms the results [VAN GELDEREN, 1999] obtained from his research. The cube-shaped stones particularly do not comply with the Single Stone Model (SSM) this is due the possibility of rotation caused by the Magnus-effect.

6.5 Seabed interaction

When considering the built-up of a berm it is generally assumed that the position of the stone will be the position of impact. Soon the phenomena of bouncing and rolling are going to play a part. Moreover, when a certain steepness of the slope of the newly built rock berm is exceeded, which is defined by the maximal angle of inclination, the slopes become unstable and sliding will occur. Therefore when a rock reaches the seabed it is not likely it will immediately come to a standstill. These three phenomena will be further elaborated in the coming sections.

6.5.1 Bouncing

Consider a stone reaching the seabed, then there is a possibility the stone will bounce away when hitting the bed or on previously dumped stones. The horizontal displacement was defined by [VAN OORD, 1996] as:

$$S_h = v * t = \frac{2 * u_{bounce}^2 * \cos(\phi) * sin(\phi)}{g} \tag{6.36}$$

With:			
	S_h	maximum horizontal displacement	$[m]$
	u_{bounce}	bouncing velocity	$[m/s]$
	ϕ	angle of deflection	[°]

A constant settling velocity of the stone, no hindrance by water or any other object and a flat stiff collision area is assumed. It is furthermore assumed that the stone will bounce off under a certain angle, and with the same velocity as the vertical settling velocity, see Figure 44.

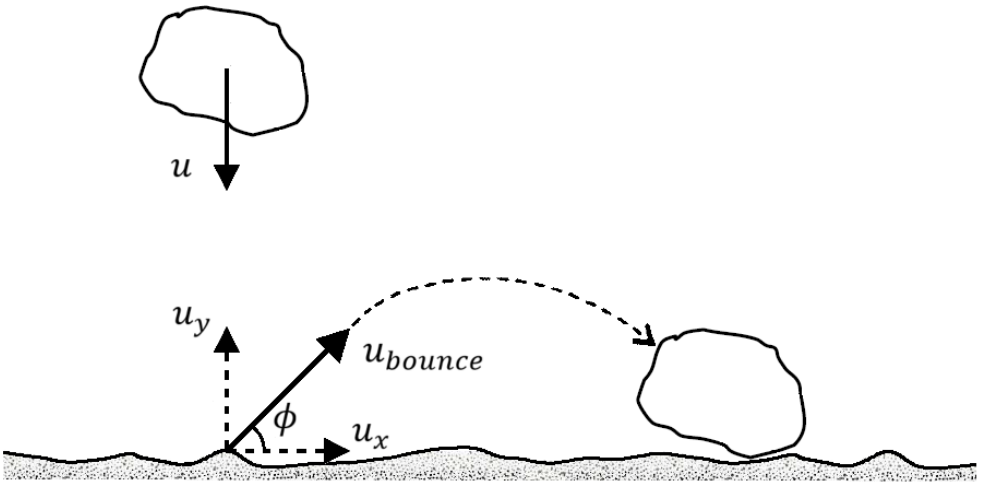

FIGURE 44: SCHEMATIZATION OF THE BOUNCING OF A STONE ON THE SEABED

The maximum distance a stone can travel when bouncing away can be calculated by taking an angle of deflection of 45 degrees and assuming the bouncing velocity equal to the maximum settling velocity of a stone. Substituting (6.13), with a drag coefficient of 1 and a relative density of 1.65, in (6.36), the maximal horizontal displacement of a bouncing stone becomes 2.2 times its own diameter. For industrial rock placement operations, with the diameter of the most commonly used stone of around 7.5 cm, this will be in de order of 10's of centimetres.

6.5.2 Rolling

Again, consider a stone reaching the seabed. When a stone lands on a slope there is a possibility of rolling off. This will happen when the horizontal component of the gravitational force is larger than the counteracting frictional force which acts on the stone due to the seabed or other stones. It is very complicated to model the rolling behaviour because of the varying roughness of the stone. Every part of the stone has a different roughness whereby the rolling acting is determined, to a large degree, by the roughness interaction between the seabed and the part of the stone which touches the seabed. There is currently no model which describes the probability if a stone will start to roll, was mentioned by [RAVELLI, 2012].

6.5.3 Sliding

The occurrence of sliding is mainly dependent on the steepness of the berm, but also on the angle of attack at which the rock will hit the berm, the settling velocity of the stones. Also the shape of the part of the stone which reaches the slope first, including the local roughness. Very little research is done on the occurrence of sliding slopes of a rock berm [VAN OORD, 1996].

7

Dumping of Multiple Stones

In the previous chapter the dumping of a single stone is elaborated. However, in practice, when a rock placement operation with a fallpipe vessel is executed a large amount of rock is dumped. Production rates of $2300\ t/h$ are not uncommon by the Flintstone for industrial purposes. In this chapter will therefore be looked at the dumping of multiple stones, and the influence on each other.

7.1 Settling process of rock groups

[VAN DER WAL, 2002] defined five different phases, based on his experiments, for the settling process of rock groups. The five phases include all possible mechanisms which can occur. Not all phases actually have to occur during the settling process. For example, when looking at a large group of stones, the group can settling according to phase 1, 2 and 3 and reaching the bed before the start of phase 4, the settling behaviour described by the Single Stone Model (SSM). However, for a small group of stones this is possibly the other way around. Phases 1, 2 and 3 will not occur but the group will follow the settling behaviour described by the SSM. Each of the five phases are described in this paragraph.

7.1.1 Phase 1: Acceleration of the group

Consider a group of stones falling, closely together, through water. Water is hereby trapped inside the group. This entrainment of water can be seen as added-mass. To schematize this group, to describe the settling process, it is now assumed as a single body with a group volume and group density. The acceleration of an object with a constant volume and density is described by van Mazijk in 1982 [VAN DER WAL, 2002]. The derivation shows that the final velocity of a single stone is quite fast reached and after a limited depth. Just as with a single stone, the acceleration or deceleration of a stone group is caused by the difference between the drag force and the resulting force in the settling direction. In comparison with the derivation of van Mazijk for a single stone, [VAN GELDEREN, 1998] found that the acceleration/deceleration of a group of stones is less. This is due to the fact that the magnitude of the acceleration depends on the inertia of mass of the group. The inertia of mass for the group of stones not only depends on the density of the stones but also on the added-mass. Furthermore the maximum settling velocities for a stone group are higher than the terminal velocity, and no equilibrium velocity will be reached.

The drag force on the stone group increases with increasing depth caused by the increasing cross section of the group front and increasing settling velocity. The settling velocity is maximal when the increasing drag force is equal to the force in the settling direction. From this point water is still entrained within the group and therefore the volume of the group is still increasing. Due to this effect the acceleration turns into a deceleration. This tipping point is the start of phase 2.

The depth over which the acceleration takes place seems dependent on the total mass of the group, the starting density of the group as whole and the velocity with which the width and height of the front increases, according to [VAN GELDEREN, 1998]. There is little influence on the acceleration phase by the characteristics of single stones within the group. The same acceleration process and group velocity of stone groups with a constant total stone mass but with different stone diameters is noticed by [VAN GELDEREN, 1998].

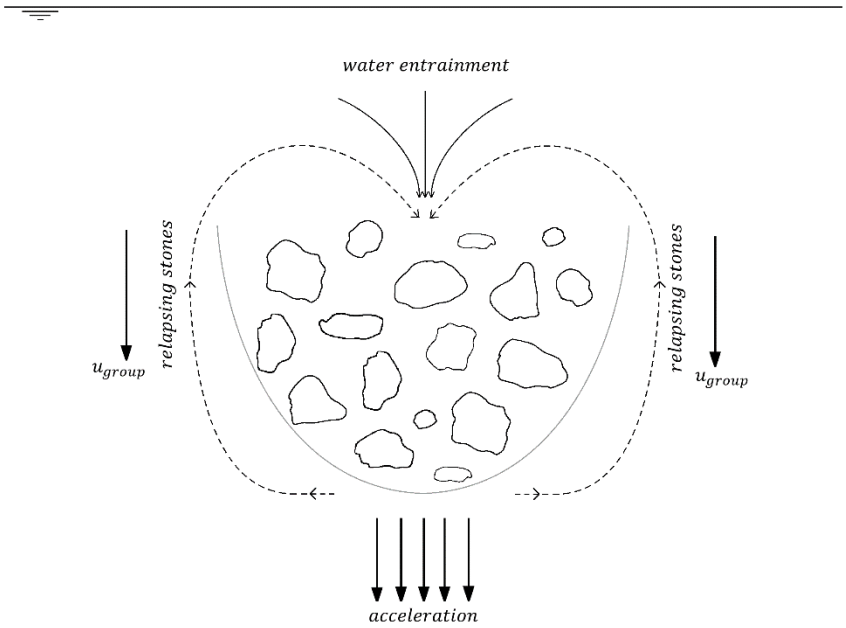

FIGURE 45: PHASE 1: ACCELERATION OF THE GROUP

7.1.2 Phase 2: Deceleration of the group

In phase 2 the acceleration is now inverted into a deceleration. This deceleration will continue, by cause of the same effects as in phase 1, until the terminal velocity of the larger stones is reached. At this point the larger individual stones will "fall-through" the group and phase 3 will start. During the acceleration, as well as the deceleration process (phase 1 and phase 2), the stones are circulating within the group. When a stone is situated at the front it will decelerate in comparison to other stones. This is caused by the increased resistance, and then the stone moves to the side of the group. From there it will relapse aside the group until it reaches the tail. At the tail of the group the stone will experience less resistance because it is now situated in the wake of the group. Therefore the stone will go through the middle to the front of the group again.

The circulation process also exists when a group of stones with a certain grading is settling. However, the smaller stones within the group behave different in comparison to the larger stones. The larger stones will stay longer at the front of the group, and will re-join the group sooner when relapsing aside the group. Therefore they will appear back at the front sooner than the smaller stones. Furthermore, the group velocity is lower than the velocity of the individual stones and water within the group, [VAN GELDEREN, 1998] concluded. In phase 2 only the total mass of the group and volume over which this mass is divided is of significance, so the geometric form of the stones is of low importance.

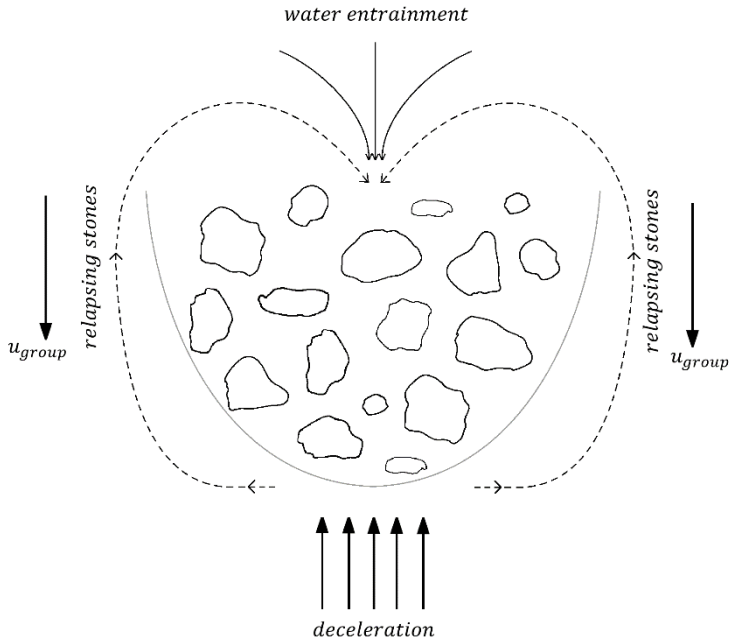

FIGURE 46: PHASE 2: DECELERATION OF THE GROUP

7.1.3 Phase 3: Rock front of larger stones

As mentioned, phase 3 starts when the settling velocity of the group is decreased until it reaches the terminal velocity of the largest stones within the group. From this moment the largest stones will "fall-through" the group and water is no longer entrained within the group. This falling through process is self-amplified. The added-mass water is left behind and the kinetic energy of the added-mass is dissipated by the ambient fluid. The smaller stones will follow in the wake of the front of the larger stones. Phase 4 will start when mutual influence is too small for the smaller stones to follow the front of the larger stones.

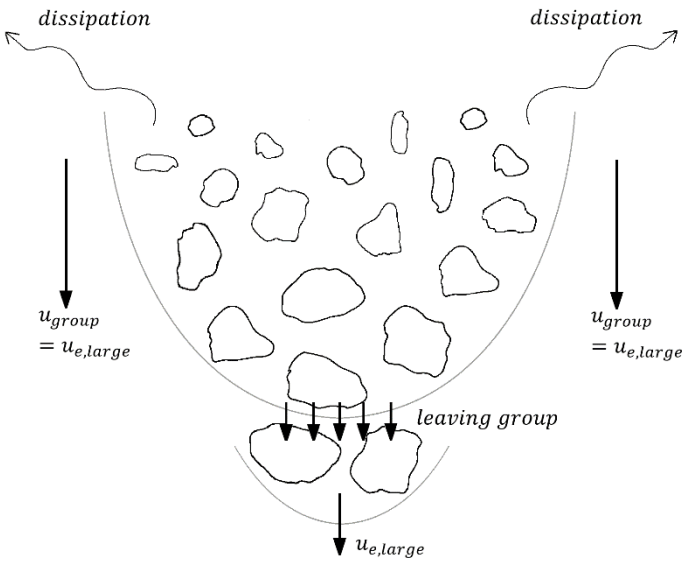

FIGURE 47: PHASE 3: ROCK FRONT OF LARGER STONES

7.1.4 Phase 4: Settling process according to the SSM

When the mutual influence of the stones is too small they will further settle as individual stones. This settling behaviour is described by the SSM. According to this model stones will develop arbitrarily, alternating, horizontal movements caused by alternating lift forces on the stones. These horizontal movements will result in a normal distributed horizontal spreading at the bed.

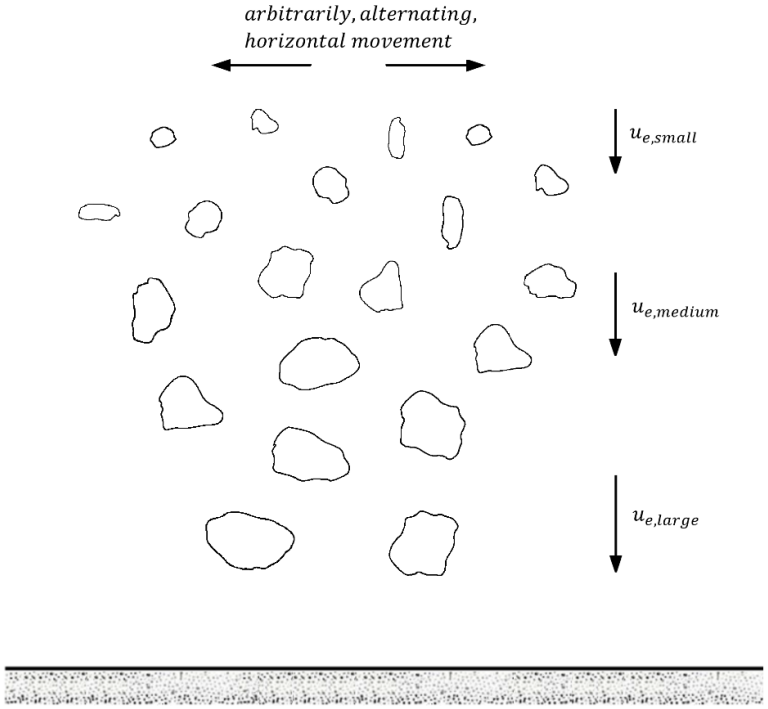

FIGURE 48: PHASE 4: SETTLING PROCESS ACCORDING TO THE SSM

The group density at which phase 4 start is not the same for every stone group, this was noticed by [VAN GELDEREN, 1998]. The mutual influence of a stone group with a larger total stone mass is longer in comparison to stone groups with a lower mass. This is caused by a longer entrainment of water and due a higher inertia of mass for larger groups.

7.1.5 Phase 5: Radial runoff

A radial runoff of water will develop when the settling process of phase 1 or 2 occurs close enough to the bed. The radial velocity will first increase rapidly from the centre to the outside, to gradual decrease subsequently. Stones are transported away from the group centre by this flow. The horizontal distance a single stone will travel depends on the mass, flow speed, diameter and roughness of the bed. The radial runoff is governed by the velocity at which the group will reach the bed and the total mass of the group.

[VAN DER WAL, 2002] researched the settling process of stone groups. Figure 49 gives the result of one of the measurements and illustrates the principle of radial runoff. For this measurement two stone groups with an equal stone diameter but a different mass are used (left: a higher mass, right: a lower mass). As mentioned, the horizontal distance a single stone will travel depends amongst others on the mass, this difference is clearly shown in Figure 49.

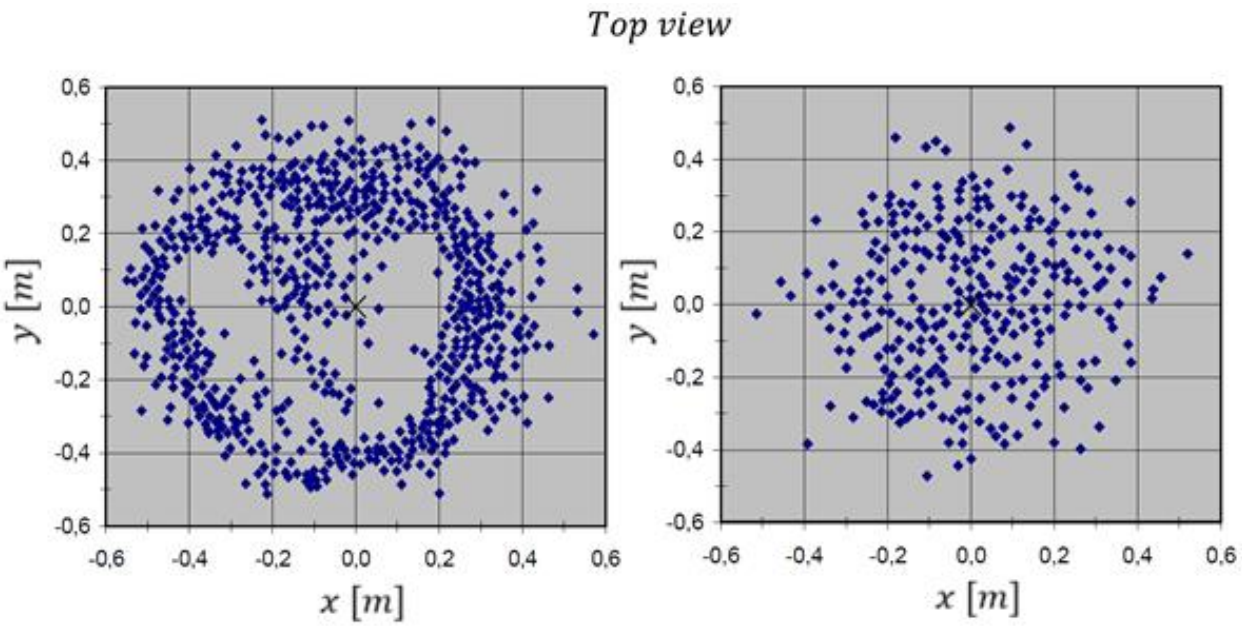

FIGURE 49: RADIAL RUNOFF FOR TWO STONE GROUPS WITH EQUAL DIAMETER BUT DIFFERENT MASS [VAN DER WAL, 2002]

It should be noted again that not all phases have to occur during the settling process of stone groups.

7.2 Hindered settling

When particles are continuously dumped in stagnant water the mutual influence of the particles decreases the settling velocity. This effect is called hindered settling and is caused by an increased drag coefficient, due to the proximity of other particles, particle collision and the returning water flow as it is displaced by the descending particles. The hindered effects are mainly caused by the concentration of particles in a cloud, and is generally written as:

$$u_{hs} = f(C_v)u_e \tag{7.1}$$

With:			
	u_{hs}	hindered settling velocity	$[m/s]$
	C_v	volume concentration	$[-]$

A series of experiments on hindered settling were carried out by Richardson and Zaki in 1954 and they proposed the following empirical function based on their experiments [VAN RHEE, 2002]:

$$u_{hs} = u_e * (1 - C_v)^{\beta} \tag{7.2}$$

With:			
	β	coefficient	$[-]$

They found for a particle Reynolds number less than 0.2 and greater than 500 that the influence of the particle Reynolds number is negligible. In 1954 Richardson and Zaki found the following values for factor β [ROOK, 1994]:

$$\beta = 4.65 + 19.5\frac{d}{D} \qquad for \quad Re_p < 0.2 \tag{7.3}$$

$$\beta = \left(4.35 + 17.5\frac{d}{D}\right) * Re_p^{-0.03} \qquad for \quad 0.2 < Re_p < 1 \tag{7.4}$$

$$\beta = \left(4.45 + 18.5\frac{d}{D}\right) * Re_p^{-0.1} \qquad for \quad 1 < Re_p < 200 \tag{7.5}$$

$$\beta = 4.45Re_p^{-0.1} \qquad for \quad 200 < Re_p < 500 \tag{7.6}$$

$$\beta = 2.39 \qquad for \quad Re_p > 500 \tag{7.7}$$

The description of the exponent with five different functions does not lead to a smooth behaviour. A smooth presentation can be achieved using the logistic curve [VAN RHEE, 2002]. By this, the empirical exponent β can be approximated by the following general equation:

$$\beta = \frac{(a + bRe_p^{\alpha})}{1 + cRe_p^{\alpha}} \tag{7.8}$$

For the different coefficients in (7.2) the following values are reported:

TABLE 6: DIFFERENT COEFFICIENTS FOR DETERMINING THE EMPIRICAL EXPONENT β

Author(s)	Re_p	Concentration	a	b	c	α
Garside (1977) [VAN RHEE, 2002]	$0.001 < Re_p < 3 * 10^4$	$0.04 < C_v < 0.55$	5.1	0.27	0.1	0.9
Rowe (1978) [VAN RHEE, 2002]	$0.2 < Re_p < 10^3$	$0.04 < C_v < 0.55$	4.7	0.41	0.175	0.75
Di Felice (1999) [VAN RHEE, 2002]	$0.01 < Re_p < 1 * 10^3$	$0 < C_v < 0.05$	6.5	0.3	0.1	0.74
[RAVELLI, 2012]	-	$0 < C_v < 0.3$	4.7	0.705	0.253	0.687

The different approaches are compared in Figure 50. It is easily noticed that the expression according to Rowe from 1978 is a smoothed representation of the original Richardson and Zaki relations [VAN RHEE, 2002]. Furthermore the approach reported by [RAVELLI, 2008] for the determination of the empirical exponent corresponds well with the original Richardson and Zaki relations for the lower particle Reynolds numbers. The particle Reynolds number of the particles used in rock placement operations are in the order off around 10^3. When looking at this range, the empirical exponent is bounded at $2.39, 2.70, 2.41, 3.0$ *and* 2.8 for Richardson and Zaki, 1954, Garside, 1977, Rowe, 1978, Di Felice, 1999 and [RAVELLI, 2008] respectively.

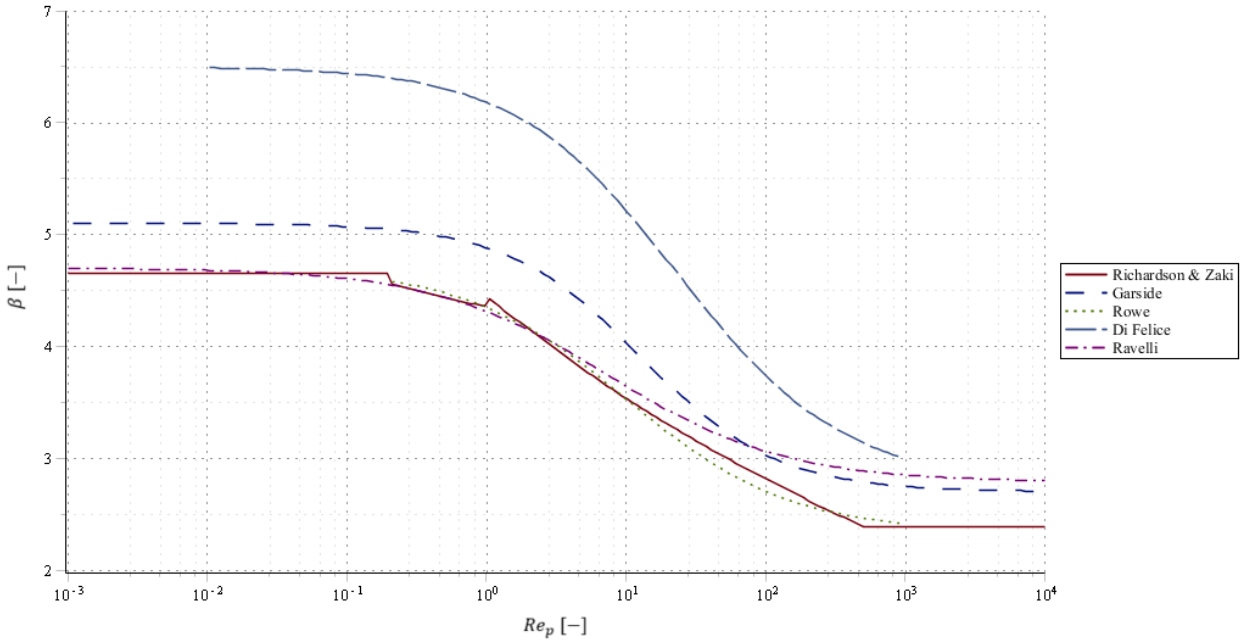

FIGURE 50: DIFFERENT APPROACHES FOR THE VALUE OF THE EXPONENT FOR HINDERED SETTLING

8

Dumping of Stones through a Fallpipe

In the previous two chapters the dumping of a single stone and multiple stones is elaborated. This is done to get a better understanding of the different processes involved. However, for rock placement operations in practice the stones are dumped through the fallpipe and not at the water surface. In this chapter first will be looked at the jet velocity of the rock and water mixture at the end and below the fallpipe. This velocity will be different than the equilibrium velocity determined in the previous two chapters due to the downward directed flow in the fallpipe. Also the jet velocity will be different from the velocity determined in Chapter 3. The downward directed flow is caused by the dumping process whereby the density of the mixture in the fallpipe is higher than the surrounding fluid. By this, the water level in the fallpipe will fall and in order to prevent this, water is let into the fallpipe by means of a water inlet section located at the upper end. In the second paragraph of this chapter, the spreading of rock below the fallpipe will be discussed based on the research done by [Ravelli, 2012].

8.1 Jet velocity

As mentioned, the rock and water mixture has a higher density than the surrounding water and therefore a different jet velocity in comparison with a plain water jet will be noticed. In this paragraph first two methods for the determination of the exit velocity are treated, i.e. at the end of the fallpipe. After this the centreline velocity, i.e. below the fallpipe, based on [van Rhee, 2002] will be elaborated.

8.1.1 Exit velocity

Author's note: This information is confidential.

8.1.2 Centreline velocity

Author's note: This information is confidential.

8.2 Spreading of rock

In the research done by [Ravelli, 2012] it was investigated which parameters are governing for the spreading of rock below a flexible open fallpipe. The most promising variables were selected base on his literature survey and are: initial jet velocity, height above the seabed where the stones are released and rock diameter. To investigate the effect of these parameters on the spreading, a numerical model was developed whereby the circular turbulent jet was simplified into a two dimensional plane jet. It was furthermore assumed that the dumping process was stationary and at a fixed location, the shape of the stones as a sphere and the lift force was neglected. In the model the fluid and solid motions were uncoupled which means that the motions of the stones and fluid were calculated separately.

It was concluded that the spreading, expressed in the standard deviation, increases approximately linear with the water depth but the releasing location had no effect. Furthermore, the developed model was unable to predict the correct standard deviation for all configurations. The given reason for this was expected to be the type of velocity field that was used as input to the simulations. The used velocity field consisted only of mean velocities, where the experiments showed that the jet flow was highly turbulent [Ravelli, 2012].

9

Built-up of a Berm

A predetermined shape is designed for the execution of a rock berm placement operation. This is a theoretical and perfect berm which secures the minimum coverage of a pipeline or cable with the least amount of stone. A better insight in the process when building a berm with the use of a rock placement operation will be given in this chapter. First will be looked at the different models which are known for the built-up of a berm. This includes the Single Stone Model, Ring Model and Combination Model. In the last paragraph of this chapter, different berm types which are seen in the field and their shape will be further elaborated.

9.1 Single Stone Model

The Single Stone Model (SSM), so called by [CREGTEN, 1995], is an analytical model to determine the position of a falling stone, through water, at the end of its settling process. The settling motion of a rock is in fact characterised by a diffusion process. This settling motion is statistically described by the Random Walk Model, which is further elaborated in section 9.1.2.

9.1.1 Berm built-up stages

When rock is dumped from a point in water, through a fallpipe or any other dumping method, different stages are noticeable. In theory twee different stages can be distinguished when looking at the process of the built-up of a berm, see Figure 51.

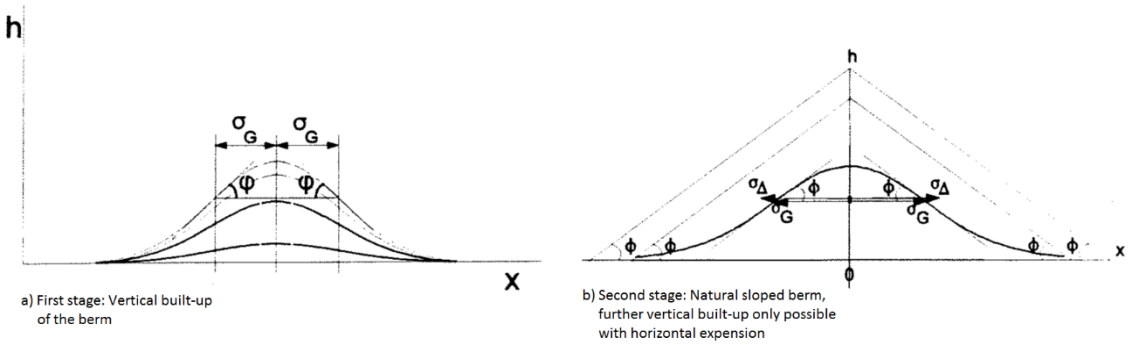

FIGURE 51: DIFFERENT STAGES OF THE BUILT-UP OF A ROCK BERM

In the first stage of the process, the built-up of the berm will only increase in the vertical direction without an increase of the base width. The radius of gyration, σ_G in Figure 51, the square root of the moment of inertia divided by the cross section of the berm, is a measure for the spreading of stones around their average position on the seabed. This radius of gyration is constant during the first stage of the built-up process as long as the stand-off distance and the diameter of the stones will remain constant and without turbulence included. The first stage of the built-up process will end when, on an arbitrary point on the berm profile, the angle of repose is reached. From this moment the transition stage will begin, whereby the angle of repose will be reached on an increasing part of the berm. [CREGTEN, 1995] researched this transition between the first and second stage. The influence of the transition stage on the built-up of the berm showed to be little.

When on every part of the berm the angle of repose is reached the second stage will start. The profile of the berm is then equal to an isosceles triangle, see Figure 51. This shape will be preserved during further increase of the berm. Therefore the height of the berm, or vertical increase, will only be obtained when the width of the berm base is also increased. The radius of gyration of this isosceles triangle is now independent of the stand-off distance. In this stage the radius only depends on the amount of dumped stones. A derivation of this radius of gyration of an isosceles triangle is done in 1995 by Vrijling *et al.* [VAN GELDEREN, 1999]. The final result of this derivation is:

$$\sigma_\Delta = \sqrt{\frac{A}{6 * tan(\varphi)}} \tag{9.1}$$

With:

σ_Δ	standard deviation of the isosceles triangle	$[-]$
φ	angle of repose	$[°]$

When the above given theory is correct, experiments will show corresponding lines as given in Figure 52, which is reproduced from [VAN GELDEREN, 1999]. The horizontal line in this figure shows that the radius of gyration of the isosceles triangle is independent of the water depth. The curved line shows that the radius of gyration of the Gauss profile proportional to the square root of the water depth. In reality the sharp angle between the two zones would not occur because a transitional zone would exist. However, this transitional zone is quite small [CREGTEN, 1995].

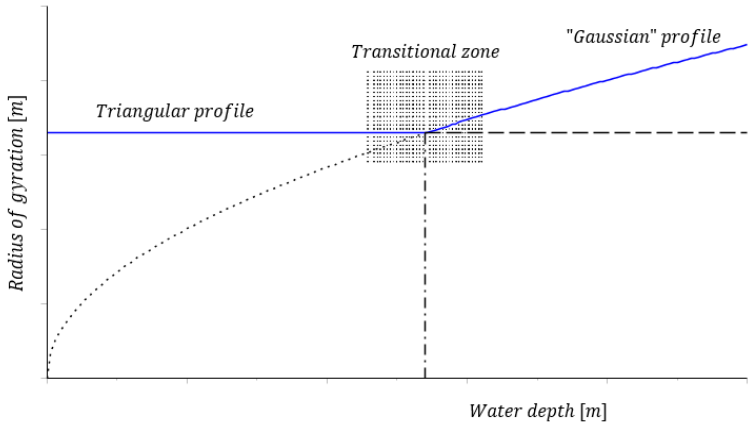

FIGURE 52: RELATION BETWEEN RADIUS OF GYRATION AND WATER DEPTH, REPRODUCED FROM [VAN GELDEREN, 1999]

In practice however, in contrary to the isosceles triangle shape of the berm, the crest of the berm is rounded as result of the built-up process itself. Furthermore stones will not be immediately at a standstill when they land on one of the slopes but will roll further downwards. A Gaussian profile, which will be elaborated further in 0, is therefore more likely to form than the triangular shape.

9.1.2 Random Walk Model

As explained before, the Random Walk Model (RWM) is a statistical description of the settling motion of a single rock. The set-up of the SSM from the RWM was made possible because for the physical derivation three important assumptions were made:

1. The change in direction of the acceleration of the stones in the direction perpendicular to the direction of movement is determined by the change in pressure due to alternating separation of flow;

2. The Strouhal number is also applicable for 3-dimensional flow;

The Strouhal number is defined in (6.32), but for convenience given here again:

$$St = \frac{2\pi}{T_{vs}}\frac{d}{u} \tag{9.2}$$

3. The flow separation at the surface of the stones is random, due to the irregular shape and rotation of the stone during its settling movement. For this reason it is assumed that the direction and magnitude of the divergence in the next step is undependable of the previous step.

This derivation was also done in 1995 by Vrijling *et al.* [VAN GELDEREN, 1999]. The final result of this derivation is:

$$\sigma_G = \frac{\gamma''}{\sqrt{St^3}} * \frac{\rho_f}{\rho_s} * C_L * \sqrt{h * d} \tag{9.3}$$

With:	σ_G	standard deviation of the Gaussian profile	$[-]$
	h	height	$[m]$
	γ''	constant	$[-]$

It was assumed in 1995 by Vrijling *et al.* that (9.3) can be simplified to the following equation [VAN GELDEREN, 1999]:

$$\sigma_G = c * \sqrt{h * d_{n50}} \tag{9.4}$$

In the research of [WEUSTINK, 1998] the density of the fluid and solids is explicitly used in the equation for the determination of the standard deviation of the Gaussian profile for the horizontal displacement. Furthermore, the median sieve size instead of the nominal median diameter was used for the equation:

$$\sigma_G = c * \frac{\rho_f}{\rho_s} * \sqrt{h * d_{50}} \tag{9.5}$$

9.1.3 Mathematical modelling of the Single Stone model

[MEERMANS, 1998]: researched the falling behaviour of rock when dumped from a fixed location. In his thesis the 3-dimensional falling behaviour of stones was simplified by assuming the stones settle between parallel plates. A mathematical derivation of the Gaussian probability density was conducted. This 2-dimensional probability density of the Gaussian profile is given as [MEERMANS, 1998]:

$$f_{ssm_{2d}}(x) = \frac{1}{\sqrt{2\pi} * \sigma_G} * e^{-\frac{1}{2}\left(\frac{x}{\sigma_G}\right)^2} \tag{9.6}$$

With: $f_{ssm_{2d}}$ 2-D probability density function Single Stone Model [−]

In reality, rocks will not fall in the 2-dimensional plane, but in the 3-dimensional plane. For the derivation of this 3-dimensional probability density of the Gaussian profile it was assumed that the motions in the horizontal plane are independent and have an equal probability. By this, the 3-dimensional probability density is obtained by multiplying the probability densities in the horizontal plane, rewriting to polar coordinates gives [MEERMANS, 1998]:

$$f_{ssm_{3d}}(r) = \frac{r}{\sigma_G^2} * e^{-\frac{r^2}{2\sigma_G^2}} \tag{9.7}$$

With: $f_{ssm_{2d}}$ 3-D probability density function Single Stone Model [−]

9.2 Ring Model

The ring model is a calculation model whereby it is assumed that objects settle with an averaged, in direction and magnitude, constant horizontal force. In comparison to the SSM, the rock will settle under an angle resulting in a circular shaped berm, see figure Figure 53.

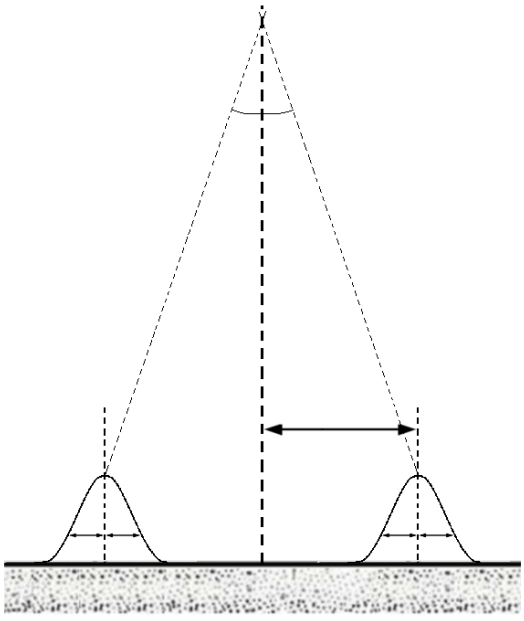

FIGURE 53: RING MODEL

For a 2-dimensional situation the combined probability density that a rock will end at a certain distance y from the releasing point is given for the combined probability as [MEERMANS, 1998]:

$$f_{rm}(y) = \frac{e^{-\frac{1}{2}\left(\frac{\sqrt{x^2+y^2}+\mu_{rm}}{\sigma_{rm}}\right)^2} + e^{-\frac{1}{2}\left(\frac{\sqrt{x^2+y^2}-\mu_{rm}}{\sigma_{rm}}\right)^2}}{2\pi\left[2\sigma_{rm}^2 * e^{-\frac{1}{2}\left(\frac{\mu_{rm}}{\sigma_{rm}}\right)^2} + \mu_{rm} * \sigma_{rm}\sqrt{2\pi} * erf\left(\frac{\mu_{rm}}{\sigma_{rm} * \sqrt{2}}\right)\right]} \tag{9.8}$$

With: f_{rm} 2-D probability density function Ring Model [−]

10 Computational Fluid Dynamics

Fluid flows, both gas and liquid, are governed by partial differential equations (PDE) which represent conservation laws. These conservation laws consists of conservation of mass, conservation of momentum and conservation of energy. Computational Fluid Dynamics (CFD) replaces such PDE systems by a set of algebraic equations which can be solved by using a computer. CFD gives an insight into flow patterns that are otherwise expensive, difficult or impossible to study using traditional, experimental, techniques. These experimental techniques give a quantitative description of flow phenomena using measurements based on a certain time, a laboratory-scale model and a limited range of problems. CFD, however, provides a prediction of fluid flows by means of mathematical modelling, numerical methods and software tools. Therefore it is possible to model all desired quantities, with high resolution in space and time and almost any problem. The difference between an experiment and a CFD simulation is shown in figure Figure 54.

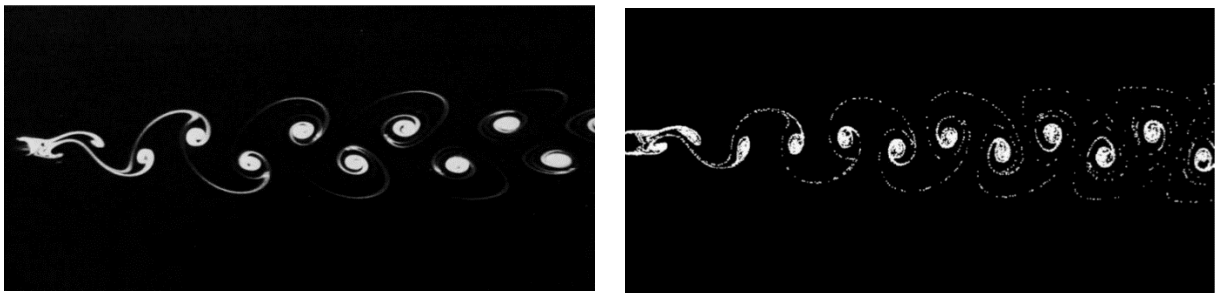

FIGURE 54: A) REAL EXPERIMENT B) CFD SIMULATION [RAKESH *ET AL.*, 2014]

The Navier-Stokes equations, which define any single-phase fluid flow, are the fundamental basis of almost all CFD problems. These equations describe how the pressure, velocity, density and temperature of a moving fluid are related, and can be simplified, obtaining the Euler equations. This is done by removing terms describing viscous actions, the viscosity and thermal conductivity terms. The full potential equations can then be obtained from the Euler equations by removing the terms describing vorticity. And when the full potential equations are linearized the linearized potential equations will be left.

The full 3D Navier-Stokes equations are formulated as:

$$\frac{\delta\rho}{\delta t}+\frac{\delta\rho u}{\delta x}+\frac{\delta\rho v}{\delta y}+\frac{\delta\rho w}{\delta z}=0 \qquad \textit{Continuity equation} \tag{10.1}$$

$$\frac{\delta\rho u}{\delta t}+\frac{\delta(\rho u^2)}{\delta x}+\frac{\delta(\rho uv)}{\delta y}+\frac{\delta(\rho uw)}{\delta z}=-\frac{\delta p}{\delta x}+\nu\left(\frac{\delta^2 u}{\delta x^2}+\frac{\delta^2 u}{\delta y^2}+\frac{\delta^2 u}{\delta z^2}\right) \tag{10.2}$$

$$X-\textit{Momentum equation}$$

$$\frac{\delta\rho v}{\delta t}+\frac{\delta(\rho uv)}{\delta x}+\frac{\delta(\rho v^2)}{\delta y}+\frac{\delta(\rho vw)}{\delta z}=-\frac{\delta p}{\delta y}+\nu\left(\frac{\delta^2 v}{\delta x^2}+\frac{\delta^2 v}{\delta y^2}+\frac{\delta^2 v}{\delta z^2}\right) \tag{10.3}$$

$$Y-\textit{Momentum equation}$$

$$\frac{\delta\rho w}{\delta t}+\frac{\delta(\rho uw)}{\delta x}+\frac{\delta(\rho vw)}{\delta y}+\frac{\delta(\rho w^2)}{\delta z}=-\frac{\delta p}{\delta z}+\nu\left(\frac{\delta^2 w}{\delta x^2}+\frac{\delta^2 w}{\delta y^2}+\frac{\delta^2 w}{\delta z^2}\right) \tag{10.4}$$

$$Z-\textit{Momentum equation}$$

$$\frac{\delta\rho E}{\delta t}+\frac{\delta(\rho uE)}{\delta x}+\frac{\delta(\rho vE)}{\delta y}+\frac{\delta(\rho wE)}{\delta z}=-\frac{\delta pu}{\delta x}-\frac{\delta pv}{\delta y}-\frac{\delta pw}{\delta z}+S \tag{10.5}$$

$$\textit{Energy equation}$$

In this chapter, first the methodology of CFD will be given, with different discretization methods and turbulence models. In the second part different available CFD solvers will be treated.

10.1 Methodology

All the approaches, described in this paragraph, are following the same basic procedure. The procedure can be divided into three stages, that is: pre-processing, simulation and post-processing. For pre-processing the geometry, or the physical bounds, of the problem are defined. Also the mesh is created, this is done by dividing the volume occupied by the fluid into discrete cells. Furthermore the physical modelling and boundary conditions are defined. After this the simulation is started and the equations are solved iteratively as a steady-state or transient. In the last stage a postprocessor is used for the analysis and visualization of the solution.

10.1.1 Discretization methods

In this section three numerical methods for discretization of the Navier-Stokes equations will be considered. These are the finite volume, finite element and finite difference methods. More methods for the discretization exists however these are the most well-known and most used. For all three methods the values are calculated at discrete places on a meshed geometry.

Finite volume method

The Finite Volume Method (FVM) is one of the most common used and versatile discretization techniques used in CFD. FVM uses a volume integral formulation of a problem with a finite set of volumes to discretize the partial differential equations. This discretization guarantees the conservation of fluxes through a particular control volume, and makes this a conservative method. Another advantage is the easy formulation of the FVM which allows the use of unstructured meshes.

Finite element method
The Finite Element Method (FEM) uses division of the whole domain of the problem into simpler parts, called finite elements. Furthermore it uses variation methods from the calculus of variations to solve the problem by minimizing an error function. Finite element spaces can be constructed on general triangulations, i.e. grids, and this method is able to handle complex boundaries and geometries. Generally speaking, FEMs is the method of choice in all types of analysis for elliptic equations in complex domains. It is more stable than FVM, however, FEM can require more memory and has slower solution times than the FVM.

Finite difference method
The Finite Difference Method (FDM) is used in some specialized codes. Codes which can handle complex geometry with high efficiency and accuracy. The FDM consists of replacing each derivative by a difference quotient in the partial differential equations. It is simple to code and economic to compute. The drawback of the FDM is accuracy and flexibility. Standard FDMs require more regularity of the solution and the triangulation, e.g. uniform grids. Difficulties also arises in imposing boundary conditions.

10.1.2 Turbulence models

For engineering designs, whereby the fluid velocity is under interest, turbulence models are required because virtually all applications in engineering are turbulent. For turbulent flows, the range of length scales and complexity of the phenomena involved in turbulence make most other modelling approaches impossible or too expensive. In this section some commonly-used computational models for turbulent flows are given.

Reynolds-averaged Navier-Stokes
The Reynolds-averaged Navier-Stokes (RANS) equations are the oldest approach to turbulence modelling and are time-averaged equations of motion for fluid flow. By Reynolds averaging of the Navier-Stokes equations new apparent stresses are introduced, the so called Reynold stresses. Thereafter the objective of the turbulence models for the RANS equations is to compute these Reynolds stresses.

Large eddy simulation
Large Eddy Simulation (LES) is also a technique widely used for the simulation of turbulent flows. Kolmogorov's theory of self-similarity says that the large eddies of the flow are dependent on the geometry while the smaller scales are more universal. So, by using subgrid-scale models this allows the smallest scale, and their effect, to be removed. This is done by a filtering operation and then the largest and most important scales, i.e. the large eddies, of the turbulence can be resolved. The velocity representing the small scales, and their effect on the resolved field, is then included through the subgrid-scale model. By doing so the computation cost caused by the smallest scales are reduced greatly. However, the LES method requires greater computational resources than RANS methods, but it is cheaper than DNS.

Detached eddy simulation
The Detached Eddy Simulation (DES) is a modification of a RANS model and a LES model, or a so-called hybrid model. The best of both models are used whereby near-wall regions are treated in a RANS-like manner and the rest of the flow in a LES-like manner.

Direct numerical simulation
Direct Numerical Simulation (DNS) is a solver whereby the Navier-Stokes equations are solved numerical without a turbulence model. DNS solves the entire range of turbulent length in the computational mesh. Turbulence models are therefore not needed, but this a quite expensive manner because the computational cost are proportional to the Reynolds number to the third power.

Linear eddy model
The Linear Eddy Model (LEM) can be applied across a wide range of length scales and Reynolds numbers and therefore primarily used in one-dimensional representations of turbulent flow. This model is generally used as a building block for more complicated flow representations, as it provides high resolution predictions that of a large range of flow conditions. Specifically, it provides a mathematical way to describe the interactions of a scalar variable within the vector flow field.

10.2 CFD Solvers

There are a lot of different CFD solvers on the market, commercial as well as open-source. At the moment, the best known commercial CFD software are probably ANSYS CFX, ANSYS Fluent and Flow 3D. For the open-source software these are probably OpenFOAM and Stanford University Unstructured (SU2). The different CFD solvers will be further elaborated in this paragraph.

10.2.1 Commercial

ANSYS CFX
CFX is a commercial CFD program developed by ANSYS Inc. It is a general purpose, high-performance solver that has been applied to solve wide-ranging fluid flow problems including laminar to turbulent, incompressible to fully compressible and single fluids to mixtures of fluids. CFX uses a unique hybrid finite element/finite volume method approach for discretizing the Navier-Stokes equations. Furthermore, CFX is a vertex-centred solver, which means that every variable is stored in a mesh vertex, or node, instead of a cell centroid, see figure Figure 55.

ANSYS Fluent
Fluent is another commercial CFD program developed by ANSYS Inc. The software contains the broad physical modelling capabilities needed to model, for example, flow, turbulence and heat transfer. Fluent's interactive solver set-up, solution and post-processing make it easy to examine results. The solver uses a classical FVM and has many options for Pressure-Velocity (PV) coupling. Fluent uses a cell centroid solver to store every variable, in contrary to CFX which used a vertex-centred solver, see Figure 56.

Flow 3D
Flow 3D is developed by the company Flow Science Inc. which was founded by Dr. C.W.T. Hirt. Hirt was known for having pioneered the volume of fluid method (VOF) for tracking and locating the free surface or fluid-fluid interface. This method, VOF, was used for the development of Flow 3D and therefore the solver is very capable for problems containing free surface flows.

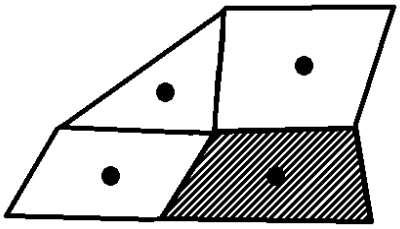

FIGURE 56: CELL CENTRED

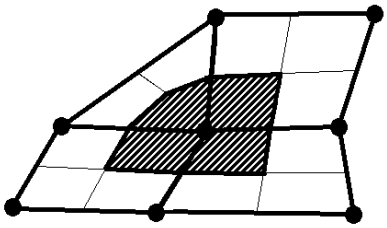

FIGURE 55: VERTEX-CENTRED

10.2.2 Open-source

OpenFOAM [GREENSHIELDS, 2015]

OpenFOAM is a software package developed by OpenCFD Ltd at ESI Group. OpenFOAM uses FVM to solve systems of PDE ascribed on any 3D unstructured mesh of polyhedral cells. The software is first and foremost a C++ library, used primarily to create executables, known as applications. The toolbox contains numerous solvers and utilities covering a wide range of problems and is supplied with pre- and post-processing environments. The overall structure of OpenFOAM is presented in Figure 57. One of the strengths of OpenFOAM is that new solvers and utilities can be created by its users. Just as ANSYS Fluent is OpenFOAM a cell-centred solver, see Figure 56.

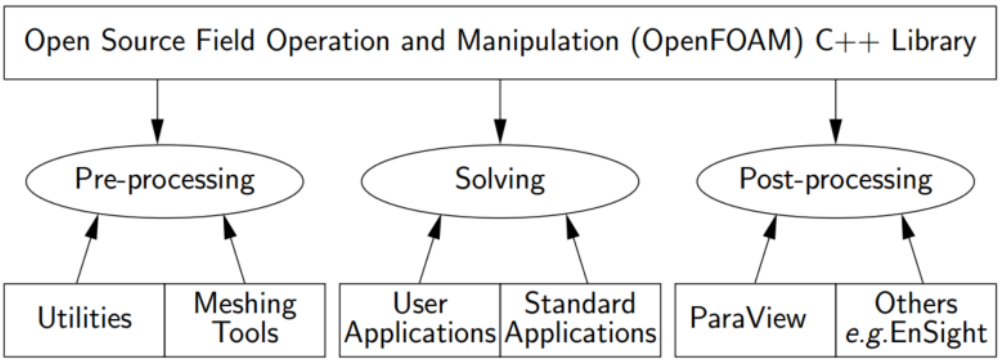

FIGURE 57: OVERVIEW OF OPENFOAM STRUCTURE [GREENSHIELDS, 2015]

Stanford University Unstructured (SU2) [PALACIOS *et al.*, 2013]

SU2 has been developed using ANSI C++ and only relies on widely-available, well-supported, open-source software. As such, SU2 is able to run on any computing platform for which a C++ compiler is available. SU2 is under active development in the Aerospace Design Lab (ADL) of the Department of Aeronautics and Astronautics at Stanford University. The SU2 software suite specialize in high-fidelity PDE analysis and in the design of PDE-constrained systems on unstructured meshes. The suite itself is composed of several C++ analysis modules that handle specific jobs. Both FVM and FEM solvers and their corresponding ad joint systems are applicable. Also, if needed, multi-physics solvers that can combine both approaches are developed. Just as ANSYS CFX is SU2 a vertex-centred solver, see Figure 55

List of Figures

Figure 1: Flowchart of the layout of the literature study IV
Figure 2: Tideway Offshore Solutions' logo IX
Figure 3: A) Side stone dumping vessel, B) Split hopper Dredger, C) Fallpipe Vessel, D) Dragline 1
Figure 4: Layout of the Tideway Flintstone 3
Figure 5: Fallpipe built-up 4
Figure 6: Single long berm 5
Figure 7: Spot berms 6
Figure 8: Protected pipeline against fishing trawlers 6
Figure 9: Upheaval buckling of a pipeline 7
Figure 10: Different flow regions of a jet below a fallpipe 11
Figure 11: The three zones of the free jet 12
Figure 12: Free jet velocity profile 13
Figure 13: Entrainment coefficient in the ZFE for circular jets 14
Figure 14: Centreline velocities for the different expressions 16
Figure 15: Jet velocity as function of the radial coordinate for a free jet by Rajaratnam 17
Figure 16: Jet velocity as function of the normalized radial coordinate for a free jet by Lee *et al.* 19
Figure 17: Buoyant jet behaviour 20
Figure 18: Centreline velocity for large stand-off distances 22
Figure 19: Impinging jet velocity profile 23
Figure 20: Comparison of the centreline velocity for large and small stand-off distances 24
Figure 21: Jet velocity as function of the radial coordinate for an impinging jet with a small SOD 25
Figure 22: radial velocity as function of radial coordinate 26
Figure 23: radial velocity at $r = r1$ 26
Figure 24: Wall jet velocity profile 26
Figure 25: Radial velocity for a wall jet 27
Figure 26: Forces acting on a stone lying on the bed 30
Figure 27: Original Shields curve 33
Figure 28: Typical distributions of the key parameters according to (4.6), (4.16), (4.17) and (4.21) [Hoan, 2008] 37
Figure 29: Measured Ψs versus measured ΦE [Hoan, 2008] 37
Figure 30: Measured ΨWL versus measured ΦE [Hoan, 2008] 38
Figure 31: Measured ΨLm versus measured ΦE [Hoan, 2008] 38
Figure 32: Measured $\Psi u - \sigma[u]$ versus measured ΦE [Hoan, 2008] 39
Figure 33: Measurement system for stone shapes [CIRIA/CUR/CETMEF, 2007] 45
Figure 34: Blockiness (from left to right, BLc $= 80\%, 60\%$ *and* 40%) [CIRIA/CUR/CETMEF, 2007] 46
Figure 35: Vertical forces on a single stone falling through water 48
Figure 36: Velocity of a settling sphere as function of time 50

Figure 37: Velocity of a settling sphere as function of distance 50
Figure 38: Relationship drag coefficient for spheres and the particle Reynolds number [Rook, 1994] 52
Figure 39: Comparison of the different terminal velocities for rock by different drag coefficients..... 55
Figure 40: Horizontal forces on a single stone falling through water..... 56
Figure 41: Von Karman vortex street [Rakesh *et al.*, 2014] 56
Figure 42: Magnus-effect 57
Figure 43: Current on a single stone falling through water..... 58
Figure 44: Schematization of the bouncing of a stone on the seabed 60
Figure 45: Phase 1: Acceleration of the group 62
Figure 46: Phase 2: Deceleration of the group 63
Figure 47: Phase 3: Rock front of larger stones 64
Figure 48: Phase 4: Settling process according to the SSM..... 64
Figure 49: Radial runoff for two stone groups with equal diameter but different mass [van der Wal, 2002]..... 65
Figure 50: Different approaches for the value of the exponent for hindered settling..... 67
Figure 51: Different stages of the built-up of a rock berm 73
Figure 52: Relation between radius of gyration and water depth, reproduced from [van Gelderen, 1999].. 74
Figure 53: Ring model 76
Figure 54: a) Real experiment b) CFD simulation [Rakesh *et al.,* 2014]..... 79
Figure 55: Vertex-centred..... 83
Figure 56: Cell centred 83
Figure 57: Overview of OpenFOAM structure [Greenshields, 2015]..... 83

List of Tables

Table 1: The terminology of types of fluid intrusions 9
Table 2: Recommended grading widths 43
Table 3: Course gradings [EN 13242, 2008] 43
Table 4: Standard classes of rock grading [EN 13383, 2002] 44
Table 5: Rock grading by [Statoil TR1370, 2009] 44
Table 6: Different coefficients for determining the empirical exponent β 67

Bibliography

ADERIBIGBE, O.O., RAJARATNAM, N. (1996) Erosion of loose beds by submerged circular impinging vertical turbulent jets. *Journal of Hydraulic Research*, 34:1, 19-33

ANSYS, INC. (2013) ANSYS Fluent theory guide, *Canonsburg*

BEEMSTERBOER, T.N. (2013) Modelling the immediate penetration of rock particles in soft clay during subsea rock installation, using a flexible fallpipe vessel. *Master's thesis, Delft University of Technology*

BELTAOS, S. (1976) Oblique impingement of circular turbulent jets. *Journal of Hydraulic Research*, 14:1, 17-36

BELTAOS, S., RAJARATNAM, N. (1973) Plane turbulent impinging jets. *Journal of Hydraulic Research*, 11:1, 29-59

BELTAOS, S., RAJARATNAM, N. (1977) Impingement of axisymmetric developing jets. *Journal of Hydraulic Research*, 15:4, 311-326

BREDBERG, J. (2000) On the wall boundary condition for turbulence models. *Internal report 00/4, Chalmers University of Technology*

BRENNAN, D. (2001) The numerical simulation of two-phase flows in settling tanks. *PhD thesis, University of London*

CHOI, L., TU, J. (2006) Flow and particle deposition patterns in realistic human double bifurcation airway model. *CSIRO, Fifth International Conference on CFD in the Process Industries*

CIRIA/CUR/CETMEF (2007) The Rock Manual. *C683, CIRIA, London*

CREGTEN, H.J. (1995) Het gebruik van probabilistische methoden bij het beoordelen van het stortresultaat van een zijstorter. *Master's thesis, Delft University of Technology*

CUR/RWS 169 (1995) Manual on the use of Rock in Hydraulic Engineering. *Ministry of transport, public works and water management, Gouda*

DUIJNHOVEN, J.A.F. VAN (2005) The results of dumping stones on a slope by a side stone-dumping vessel. *Master's thesis, Delft University of Technology*

FISCHER, H.B., LIST, E.J., KOH, R.C.Y., IMBERGER, J., BROOKS, N.H. (1979) Mixing in Inland and Coastal Waters. *Academic Press, Inc., San Diego*

FURBO, E. (2010) Evaluation of RANS turbulence models for flow problems with significant impact of boundary layers. *Master's thesis, Uppsala Universitet*

GELDEREN, P.J.G. VAN (1999) Het Enkele Steen Model. *PhD thesis, Delft University of Technology*

GREENSHIELDS, C.J. (2015) OpenFOAM: The Open Source CFD Toolbox User Guide. *OpenFOAM Foundation Ltd.*

HOAN, N.T. (2008) Stone stability under non-uniform flow. *PhD thesis, Delft University of Technology*

HOFLAND, B. (2005) Turbulence-induced damage to granular bed protections. *Master's thesis, Delft University of Technology*

LAAN, G.J. (1982) Kwalitieit en kwaliteitscontrole van breuksteen voor de waterbouw. *Report MAW-R-81054, WKE-R-82002, Rijkswaterstaat, DWW, Delft*

ISHII, M., HIBIKI, T. (2006) Thermo-fluid dynamics of two-phase flow. *Springer Science+Business Media, Inc., New york*

LEE, J., LU, T., SUN, H., MIAO, G. (2010) A novel formula to describe the velocity profile of free jet flow. *Archive of Applied Mechanics*, 81:3, 397-402

MEERMANS, W. (1997) Steenstorten: Voorspelling van het stort als gestort wordt vanuit een vast punt. *Internal report, Delft University of Technology*

MENTER, F.R. (1994) Two-Equation Eddy-Viscosity Turbulence models for Aerodynamic Flows. *AIAA journal,* 32:8, 1598-1605

MIEDEMA, S.A. (1981) The flow of dredged slurry in and out hoppers and the settlement process in hoppers. *Master's thesis, Delft University of Technology*

OORD, G. VAN (1996) Spreiding van steen in het stortproces van schuifstorters. *Master's thesis, Delft University of Technology*

OPENFOAM FOUNDATION (2012) OpenFOAM: The open source CFD tool user guide. *Version 3.0.1 edition.*

OPENCFD LTD (2010) OpenFOAM: The open source CFD toolbox. Advanced training. *Version 1.7.1 edition.*

PALACIOS, F., COLONNO, M.R., ARANAKE, A.C., CAMPOS, A., COPELAND, S.R., ECONOMON, T.D., LONKAR, A.K., LUKACZYK, T.W., TAYLOR, T.W.R., ALONSO, J.J. (2013) Stanford University Unstructured (SU2): An open-source integrated computational environment for multi-physics simulation and design. *AIAA Paper, 2013-0287*

RAJARATNAM, N. (1976) Turbulent Jets. *Elsevier Scientific Publishing Company, Amsterdam*

RAJARATNAM, N., BERRY, B. (1977) Erosion by circular turbulent wall jets. *Journal of Hydraulic Research*, 15:3, 277-289

RAJARATNAM, N., MAZUREK, K.A. (2005) Impingement of circular turbulent jets on rough boundaries. *Journal of Hydraulic Research*, 43:6, 689-695

RAKESH, M., SOORAJ, J., VISHNU V.K. (2014) Subsonic flow analysis of a tailless aircraft by using CFD. *Bachelor's thesis, Dhanalakshmi Srinivasan Engineering College*

RAVELLI, F.D.C. (2012) Improving the efficiency of a flexible fallpipe vessel. *Master's thesis, Delft University of Technology*

REUS, J.S. DE (2004) Het valgedrag van stortsteen onder invloed van stroming. *Master's thesis, Delft University of Technology*

RHEE, C. VAN (2002) On the sedimentation process in a trailing suction hopper dredger. *PhD thesis, Delft University of Technology*

ROLAND, G. (2012) Simulating the dynamics of concentrations in turbulent slurry flow in a fallpipe by means of a computational model for use in the offshore rock dumping. *Master's thesis, Delft University of Technology*

ROOK, D.B. (1994) Fall pipe fluid mechanics. *Master's thesis, Delft University of Technology*

SCHIERECK, G.J. UPDATED BY VERHAGEN, H.J. (2012) Introduction to bed, bank and shore protection. *VSSD, Delft*

SCHLICHTING, H. (1979) Boundary layer theory. *McGraw Hill book company, New York*

STATOIL TR1370 (2009) Subsea Rock Installation. *Concept development and engineering*

STEENSTRA, R.S. (2014) Incorporation of the effects of accelerating flow in the design of granular bed protections. *Master's thesis, Delft University of Technology*

TRANG, V.T (2013) The physics and sediment containment phenomenon of a silt screen. *PhD thesis, Nanyang Technological University*

TROMP, M. (2004) Influences of fluid accelerations on the threshold of motion. *Master's thesis, Delft University of Technology*

VERSTEEG, H.K., MALALASEKERA, W. (1995) An introduction to computational fluid dynamics: The finite volume method. *Longman Scientific & Technical, Essex*

VUIK, C., BEEK, P. VAN, VERMOLEN, F., VAN KAN, J. (2006) Numerieke methoden voor differentiaalvergelijkingen. *VSSD, Delft*

WAL, J.R. VAN DER (2002) Het valgedrag van steengroepen. *Master's thesis, Delft University of Technology*

WEUSTINK, O.W.A. (1998) De vlakheid van steenbestortingen. *Master's thesis, Delft University of Technology*

WITTEMAN, D. (2015) The shape factor of quarry rock. *Master's thesis, Delft University of Technology*

ZIJLEMA, M. (2012) Computational modelling of flow and transport. *Delft University of Technology, Delft*

Nomenclature

Abbreviations

CFD	Computational Fluid Dynamics
DES	Detached Eddy Simulation
DNS	Direct Numerical Solution
DP	Dynamic Positioning
FDV	Finite Difference Method
FEM	Finite Element Method
FVM	Finite Volume Method
LES	Large Eddy Simulation
PDE	Partial Differential Equation
RMS	Root Mean Square
ROV	Remote Operated Vehicle
RWM	Random Walk Model
SOD	Stand-Off Distance
SSM	Single Stone Model
$SU2$	Stanford University Unstructured
VOF	Volume Of Fluid
ZEF	Zone of Established Flow
ZFE	Zone of Flow Establishment

Greek Symbols

α	coefficient	[−]
β	coefficient	[−]
γ''	constant	[−]
Δ	relative density	[−]
ϵ	certain fraction of the equilibrium velocity	[−]

ζ	friction loss coefficient	$[-]$
η	factor	$[-]$
κ	von Karman constant	$[-]$
μ	mean value/friction coefficient	$[-]$
ν	kinematic viscosity	$[m^2/s]$
ξ	radial adjustment coefficient	$[-]$
ρ	density	$[kg/m3]$
ρ_m	mixture density	$[kg/m3]$
σ	standard deviation/constant	$[-]$
$\sigma(u)$	turbulence quantity	$[m/s]$
τ	shear stress	$[kg/ms^2]$
τ_b	bed shear stress	$[kg/ms^2]$
φ	angle between the vertical and resultant velocity/angle of repose	$[°]$
ϕ	angle of deflection	$[°]$
Φ_E	entrainment parameter	$[-]$
φ_m	coefficient by van Mazijk	$[m^{-1}]$
Ψ	stability parameter	$[-]$
Ψ_{cr}	critical stability parameter	$[-]$
Ψ_s	Shields stability parameter	$[-]$
Ψ_{Lm}	Hofland stability parameter	$[-]$
$\Psi_{u-\sigma[u]}$	Hoan stability parameter	$[-]$
Ψ_{WL}	Jongeling *et al.* stability parameter	$[-]$
ω	radial frequency	$[s^{-1}]$

Roman Symbols

A	surface area	$[m^2]$
a_v	acceleration	$[m/s^2]$

b	spreading width	$[m]$
b^*	spreading width by Lee *et al.*	$[m]$
B_0	jet buoyancy flux	$[m^3/s^3]$
BLc	blockiness	[%]
B_u	decay coefficient	$[-]$
C_D	drag coefficient	$[-]$
$C_{D,Kniess}$	drag coefficient	$[-]$
C_L	lift coefficient	$[-]$
C_v	volume concentration	$[-]$
d	particle diameter	$[m]$
D	diameter of the fallpipe	$[m]$
D_*	Bonneville parameter	$[-]$
d_{n50}	nominal median diameter	$[m]$
d_{50}	median diameter	$[m]$
E	entrainment rate	$[m/s]$
F_D	drag force	$[kgm/s^2]$
F_d	densimetric Froude number	$[-]$
F_b	buoyancy force	$[kgm/s^2]$
F_g	gravitational force	$[kgm/s^2]$
F_L	lift force	$[kgm/s^2]$
F_r	Froude number	[]
F_s^*	conversion factor	$[-]$
F_s	shape factor	$[-]$
F_w	submerged weight	$[kgm/s^2]$
F_z	gravitational force	$[kgm/s^2]$
g	gravitational acceleration	$[m/s^2]$
G_c	coarse gradings	$[-]$

h	height	$[m]$
I	intermediate orthogonal	$[m]$
k	turbulent kinetic energy	$[m^2/s^2]$
L	characteristic length	$[m]$
L_m	Bakhmetev mixing length	$[m]$
L_{MB}	momentum-buoyancy length scale	$[m]$
L_Q	discharge-momentum length scale	$[m]$
l/d	length-to-thickness ration	$[-]$
M	mass	$[kg]$
M_{50}	median mass	$[kg]$
M_0	jet momentum flux	$[m^4/s]$
P_r	production rate	$[kg/s]$
$p_{driving}$	driving force	$[kg/ms^2]$
$p_{loss,total}$	frictional force	$[kg/ms^2]$
Q_0	jet volume flux	$[m^3/s]$
r	radial distance	$[m]$
R_0	Richardson number	$[-]$
r_0	radius of the jet	$[m]$
r_1	distance from the centre to the edge of the core	$[m]$
r_2	distance from inner to outer edge	$[m]$
Re	Reynolds number	$[-]$
Re_p	particle Reynolds number	$[-]$
S	shortest orthogonal	$[m]$
S_h	maximum horizontal displacement	$[m]$
SOD	stand-off distance	$[m]$
St	Strouhal number	$[-]$
t	time	$[s]$
T	temperature	$[°C]$

T_s	timescale for settling	$[s]$
T_{vs}	period of vortex shedding	$[s]$
u	velocity	$[m/s]$
$\bar{u}$	stationary mean part of u	$[m/s]$
u_*	shear velocity	$[m/s]$
u_{bounce}	bouncing velocity	$[m/s]$
u_c	centreline velocity	$[m/s]$
u_e	equilibrium settling velocity	$[m/s]$
u_{exit}	exit velocity	$[m/s]$
u_{hs}	hindered settling velocity	$[m/s]$
u_{mf}	corresponding centreline velocity without boundary	$[m/s]$
V	volume	$[m^3]$
V_s	volume of a sphere	$[m^3]$
v	radial velocity	$[m/s]$
v_1	radial velocity at $r = r_1$	$[m/s]$
v_e	entrainment velocity	$[m/s]$
v_{flow}	horizontal velocity of the ambient fluid	$[m/s]$
x	vertical distance	$[m]$
$\bar{x}$	potential core length	$[m]$
x^{Δ}	characteristic length of a circular round jet	$[m]$
z	vertical distance from the seabed	$[m]$

Subscripts

0	initial value
∞	property of ambient fluid
c	critical value
f	property of the fluid
im	property of impinging jet

j	property of the jet
m	maximum value
s	property of the solids
lcl	lower sieve class
ucl	upper sieve class
w	property of wall jet